Search for Dark Matter and Supersymmetry in the single photon events with the ATLAS detector

Mengqing Wu

UNIVERSITÉ DE GRENOBLE

THÈSE

Pour obtenir le grade de

DOCTEUR DE L'UNIVERSITÉ DE GRENOBLE

Spécialité : **Physique Subatomique et Astroparticules**

Arrêté ministériel : 7 Août 2006

Présentée par

Mengqing WU

Thèse dirigée par **Faïrouz Malek**
et **Marie-Hélène Genest**

préparée au sein du **Laboratoire de Physique Subatomique et de Cosmologie de Grenoble**
et de **l'École Doctorale de Physique de Grenoble**

Search for dark matter and supersymmetry in the single photon events with the ATLAS detector

Thèse soutenue publiquement le **30 Juillet 2015**,
devant le jury composé de :

Patrice Verdier
IPNL-Lyon, Président
Pascal Pralavorio
CPPM-Marseille, Rapporteur
Francesco Polci
LPNHE-Paris, Examinateur
Ingo Schienbein
UJF-Grenoble, Examinateur
Faïrouz Malek
LPSC-Grenoble, Directrice de thèse
Marie-Hélène Genest
LPSC-Grenoble, Co-Encadrante de thèse

“Trouver n’est rien, c’est le plan qui est difficile.”

– Fiodor Dostoïevski

Acknowledgements

Firstly, I would like to express my deepest gratitude to my advisers Dr. Marie-Hélène Genest and Dr. Faïrouz Malek for their continuous support of my Ph.D study and related research throughout these three years. I could not have imagined having any better adviser and mentor for my Ph.D study. I remain incredibly indebted to Marie-Hélène Genest for her patience, encouragement and immense knowledge. My sincere thanks also goes to Faïrouz Malek for offering me this great Ph.D project opportunity and all the vital help she provides to me at those most critical periods during my study.

Besides my advisers, I would like to thank the rest of my thesis committee: Dr. Patrice Verdier, Dr. Pascal Pralavorio, Dr. Francesco Polci and Dr. Ingo Schienbein, not only for their insightful comments and encouragement, but also for the hard questions which incited me to widen my research from various perspectives.

I am grateful to Dr. Pierre-Antoine Delsart, Dr. Benjamin Trocme, Dr. Jan Stark, Dr. Fabienne Ledroit-Guillon and Prof. Reinhard Schwienhorst, for those stimulating discussions on writing of this thesis and preparing the defence. Throughout my Ph.D, I sincerely ap- preciate all my fellow labmates from the Laboratory of Subatomic Physics and Cosmology (LPSC), particularly from the ATLAS group for their never-ending support. Thanks to the rich and stimulating ambience created by the people from LPSC, I have greatly enjoyed the time I have spent so far working as part of LPSC.

In addition, I would like to thank Dr. Luca Fabbri for the extremely interesting theoretical courses that he gave me in the first year, and for his kindly guides and advices in helping me complete the theory section of my thesis in the last year. I am also highly grateful to Prof. Ximeng Chen and Researcher Guoshu Zhang for enlightening me the first glance of research.

This thesis would not exist without all the support and encouragement given to me over the years by my family, nor would it exist without Jiang Zhou for his love and support throughout all the challenging moments of the last few years.

Abstract

This thesis presents the search for new physics in the final state containing a single photon and missing transverse momentum. The analysis is performed on $20.3\,\text{fb}^{-1}$ of proton-proton collisions data at a center-of-mass energy of 8 TeV collected by the ATLAS detector at the Large Hadron Collider. Given the good agreement of the data with the Standard Model prediction of such events, an upper limit on the visible cross section produced by new physics is derived. The observed limit at 95% confidence level is 3.64 fb.

In this thesis, the results are also interpreted as limits in the parameter space of two new physics models. The first model is an effective field theory, inspired by Fermi-LAT results, in which dark matter particles couple to photons via a contact interaction vertex. Limits are set on the effective mass scale and depend on the postulated coupling constants. The limits set in this dark matter model provide an effective constraint in the parameter space of the theory compatible with the Fermi-LAT results. The second one is a simplified supersymmetric model describing the first and second generation squark pair production with their subsequent decay into a quark and a neutralino. The photon is emitted as initial or final state radiation and the spectrum is compressed, i.e. the mass difference between the squark and the neutralino is assumed to be small. Limits are set on the production cross-section; squark masses are excluded up to 250 GeV in the very compressed region. As the photon can be radiated from the intermediate squark, this final state would eventually provide the possibility to probe the charge of the squark.

A preliminary study has also been carried out to show the search sensitivity with 13 TeV data, which indicate that the limits presented in this thesis can already be improved by 10% with an integrated luminosity of $5\,\text{fb}^{-1}$.

Résumé

Cette thèse présente une recherche de nouvelle physique avec un état final contenant un seul photon et de l'énergie transverse manquante. L'analyse des données collectées par le détecteur ATLAS au LHC, issues de collisions proton-proton dont l'énergie dans le centre de masse est de 8 TeV, est faite avec $20.3\,\text{fb}^{-1}$ de données. Cette analyse est sensible à la présence de matière noire et/ou à la présence de particules supersymétriques. L'accord entre les données mesurées et les prédictions du modèle standard permet d'établir une limite sur la section efficace de production mesurable. Cette limite est observée à la valeur de 3.64 fb à 95% de niveau de confiance.

Dans cette thèse, la limite expérimentale obtenue est également interprétée comme une limite dans l'espace des paramètres de deux nouveaux modèles.

Le premier est basé sur une théorie des champs effective qui s'inspire des résultats du satellite Fermi-LAT. Dans ce modèle, les particules de matière sombre se couplent aux photons par une interaction de contact. Les limites sur l'échelle de masse effective sont établies et dépendent d'un postulat sur les constantes de couplage. Elles contraignent l'espace des paramètres qui est compatible avec les résultats de Fermi-LAT.

Le second est un modèle supersymétrique simplifié décrivant la production de paires de squarks de première et de deuxième générations se désintégrant en un quark et un neutralino. Dans ce cas, le photon est émis soit dans l'état initial soit dans l'état final. De plus, le spectre en masse est compressé, c'est-à-dire que la différence de masse entre les squarks et les neutralinos est supposée petite. Les limites sont établies sur la section efficace de production. Ces limites montrent une exclusion sur la masse des squarks jusqu'à 250 GeV dans la région la plus compressée de l'espace des paramètres. Le photon pouvant être émis par le squark intermédiaire, cet état final pourrait permettre de déterminer la charge du squark.

Enfin, une étude préliminaire prospective à l'énergie de collision de 13 TeV a également été menée. Elle montre qu'avec une luminosité intégrée de $5\,\text{fb}^{-1}$ de données seulement, les limites peuvent être améliorées de 10%.

Introduction

This thesis presents a search for new physics in a final state of a monophoton and missing transverse momentum, performed on $20.3\,\text{fb}^{-1}$ of proton-proton collisions data at a center-of-mass energy of 8 TeV collected by the A Toroidal LHC Apparatus (ATLAS) detector at the Large Hadron Collider (LHC).

The thesis is arranged in three parts. Part I introduces the theoretical background for the research work of this thesis, including Chapters 1 to 3. Part II introduces the LHC and ATLAS, the data processing chain and the reconstruction of physics objects, covering Chapters 4 to 7. Part III is the core of this thesis; it presents the analysis in detail, a comparison with other analyses, and a preliminary study towards the next LHC run. This part is composed of Chapters 8 to 15. Finally, the thesis will be summarized in the Conclusion.

The Standard Model of particle physics (Chapter 1) is successful in describing the fundamental particles and their interactions. However, it is still far from a complete theory; there are open questions it does not answer, such as the nature of dark matter and the energy scale hierarchy problem, which some theories beyond the Standard Model try to address.

A compelling candidate for dark matter is the weakly interacting massive particle, WIMP. Many experiments (Chapter 2) were sent to space to look for the dark matter annihilation products, or installed deep underground to detect dark matter particles passing through. One can also identify dark matter particles at colliders by producing them in collisions.

Many theories beyond the Standard Model can provide attractive WIMP candidates, such as the lightest neutralino, $\tilde{\chi}_1^0$, from supersymmetry (Chapter 3). Supersymmetry is an internal symmetry, which relates bosons with fermions by a spinorial operator, known as supercharge. Moreover, supersymmetry is able to provide a solution to the energy scale hierarchy problem.

The LHC (Chapter 4), located at CERN, is the largest hadron accelerator and collider in the world at present. It has collided proton beams at a center-of-mass energy of 7 and 8 TeV from 2010 to 2012. One of the four detectors installed at the LHC is ATLAS (Chapter 5), which is composed of various sub-detectors to identify and record particles coming out from the proton-proton collisions.

Monte Carlo simulations produce events which help to study the detector performance, and to provide expectation to compare with the data. There is a full processing chain (Chapter 6) to produce the simulated events, which converges with the data processing at the so-called reconstruction step. The reconstruction step (Chapter 7) characterizes and identifies the physics objects, such as the photons, electrons, muons, jets or missing transverse energy ($E_{\mathrm{T}}^{\mathrm{miss}}$).

Particles from models beyond the Standard Model, such as dark matter or supersymmetric models, can be produced at colliders. One can use an initial state radiation (ISR) signature to probe new particles which are invisible to the detector. A possibility for the ISR signature is the photon, which leads to a final state of $\gamma + E_{\mathrm{T}}^{\mathrm{miss}}$, called the monophoton final state.

The analysis is performed by comparing a background expectation to the experimental observation in order to assess if any significant excess of events (the signal) is produced in the monophoton final state with respect to the Standard Model production (the background). An analysis region is defined with a set of selections in the phase space of the kinematic observables of the physics objects in the $\gamma + E_{\mathrm{T}}^{\mathrm{miss}}$ events, which is called the signal region (SR). The SR is defined (Chapter 10) by a trade-off between maximizing the signal strength and minimizing the background level and the associated uncertainties. The background expectation in the SR (Chapter 11) is derived from a likelihood fit using several 'control regions', each control region being enriched in a given background process. The technique used to estimate the background in the SR is validated (Chapter 11) with a validation region defined kinematically close to the SR but with signal suppressed.

The observed event count in the SR is found to be consistent with the background expectation (Chapter 11), therefore, an upper limit at 95% confidence level (Chapter 12) is set to the visible cross section of new physics, which is the product of cross section, acceptance and selection efficiency ($\sigma \times A \times \varepsilon$) using a Modified Frequentist (CL_S) method. Generally, this result can be applied to any model of interest which can produce a monophoton final state in the same SR.

In this thesis, two new physics models are studied and limits are set to their parameter spaces.

One is an effective field theory describing the interaction between pairs of dark matter particles and photons (Chapter 13). It is inspired by the Fermi-LAT result issued in 2012 which hints at a dark matter particle mass of 130 GeV.

The other is a simplified supersymmetric model with squark pair production in a compressed spectrum scenario (Chapter 13). In this case, the quarks in the decay product of the squarks are too soft to be identified, leading to a monophoton final state.

These two models can also be probed by other analyses in ATLAS with 'monoX' signature, such as the monojet and the monoW/Z analyses, and the possibilities are discussed in this thesis (Chapter 14).

Besides, another analysis using the monophoton final state exists, which uses the Compact Muon Solenoid (CMS) detector at the LHC. It is interesting to cross check the analysis methodology and the result of this CMS analysis, and a discussion is presented in this thesis (Chapter 14).

At the end, a preliminary study projecting toward the next LHC run (run 2) is presented (Chapter 15), which shows the search sensitivity of the monophoton analysis with the data that will be collected at center-of-mass energy of 13 TeV.

Table of contents

Part I

Theoretical Background

Chapter 1

The Standard Model

The Standard Model of particle physics is the actual theory that describes the fundamental constituents of matter, and their interactions governed by three of the four fundamental forces. So far, it has successfully passed all experimental tests and its predictions are well confirmed, such as the existence of the Higgs boson.

Section 1.1 introduces the particle contents described in the Standard Model. The interaction principles are given in Section 1.2. Although the Standard Model has been well-tested to successfully describe particles and their interactions, it still suffers from problems, a few of which are introduced in Section 1.3.

1.1 Particle contents

The fundamental particles described in the Standard Model can be classified into fermions and bosons, which differ by the spin. The Standard Model describes two types of fermions (the quarks and the leptons), four different spin-1 bosons (photon, gluon, W and Z) and one spin-0 boson (the Higgs boson). It is the quarks and leptons who make up the matter and interact by exchanging spin-1 bosons, which are the mediators of the different forces. The Higgs boson is responsible for the mass of both fermions and gauge bosons W and Z.

The fundamental fermions

There are twelve fundamental fermions in the Standard Model: six quarks and six leptons, see Table 1.1 and 1.2. The quarks (leptons) are classified into three generations, and the particle mass increases with generation number, except for the neutrinos as they are massless in the Standard Model. Each particle has its antiparticle, which has the same mass but opposite sign quantum numbers.

There are three lepton flavor number, L_e, L_μ and L_τ, which are equal to $+1$ for the related leptons, -1 for the antileptons and 0 for the other particles. The basic properties of leptons can be found in Table 1.1.

Leptons	L_e, L_μ, L_τ	Charge	Mass
e	1, 0, 0	-1	0.511 MeV
ν_e	1, 0, 0	0	< 2.2 eV
μ	0, 1, 0	-1	105.66 MeV
ν_μ	0, 1, 0	0	< 0.17 MeV
τ	0, 0, 1	-1	1.777 GeV
ν_τ	0, 0, 1	0	< 15.5 MeV

Table 1.1 All six leptons are shown along with the value of their lepton flavor numbers, electric charge and mass (or mass limit for neutrinos).

Unlike leptons, free quarks can never be observed because they carry a color charge that is confined by the strong force, so they are always bounded into either baryons (qqq or $\bar{q}\bar{q}\bar{q}$) or mesons ($q\bar{q}$), both known as hadrons. Table 1.2 summarizes the properties of the quarks.

Quarks	Charge	Mass
u	$\frac{2}{3}$	2.3 MeV
d	$-\frac{1}{3}$	4.8 MeV
c	$\frac{2}{3}$	1.275 GeV
s	$-\frac{1}{3}$	95 MeV
t	$\frac{2}{3}$	173.07 GeV
b	$-\frac{1}{3}$	4.18 GeV

Table 1.2 All six quarks are shown along with their electric charge and mass.

The fundamental forces

There are four fundamental forces responsible for all the phenomena observed in nature: the gravitational, the electromagnetic, the strong and the weak forces. Each force has its own effective range: gravity and electromagnetism are the most familiar ones because of their infinite effective range, while the weak and the strong forces were only discovered when probing the nuclei. Not all the particles interact via all the forces. For example, only electrically charged particles interact electromagnetically. The weak force acts on particles according to their weak isospin, and strong force only applies to color-charged particles including the mediator of the strong force, the gluon, itself.

The interactions governed by the fundamental forces result from exchanging the corresponding intermediate vector bosons: the photon mediates the electromagnetic interactions; the strong force is carried by another massless boson, the gluon; and the weak force is mediated by the massive $W^{\pm}$ and Z^0 bosons. Except for the familiar photon, all other mediator bosons have been discovered at experiments operated at CERN and DESY. However, gravity is still beyond the Standard Model description so far, and its mediator particle, the graviton has yet never been observed. A summary of the fundamental forces can be found in Table 1.3 along with their corresponding effective range and mediator boson.

Force	Effective Range [m]	Charge	Force Carrier	
			Vector Bosons	Mass [1]
Electromagnetism	infinite	electric charge	γ	0
Strong Force	$< 10^{-18}$	color charge	g	0
Weak Force	10^{-15}	weak isospin	$W^{\pm}$	80.385 GeV
			Z^0	91.1876 GeV

Table 1.3 The effective range and the relevant charge of the three fundamental forces are shown, as well as the force carriers with their masses.

1.2 The interactions

Gauge theories

Gauge theories build up the theoretical foundation of the Standard Model . In quantum field theory (QFT), Lagrangians ($\mathscr{L}$) are introduced to describe the dynamics of the fields (ψ): the Klein-Gordon Lagrangian describes scalar (spin-0) fields; the Dirac Lagrangian is built for spinor (spin-$\frac{1}{2}$) fields; the Proca Lagrangian represents vector (spin-1) fields. Gauge theories are built up on these Lagrangians to describe the interactions in the Standard Model .

Lagrangians must be invariant under the global phase transformation:

$$\psi \rightarrow e^{i\theta}\psi, \tag{1.1}$$

where θ is an arbitrary real number. By asking θ to be a function of x, a local phase transformation is introduced:

$$\psi(x) \rightarrow e^{i\theta(x)}\psi(x), \tag{1.2}$$

which is known as a *gauge transformation*. In order to keep Lagrangians invariant under

gauge transformations, massless vector fields $\mathbf{A}_\mu$ must be introduced. These vector fields are called *gauge fields*, and describe the force carriers, called *gauge bosons*. Such a gauge transformation forms a continuous symmetry group, called *gauge group*, and the group generator relates to the charge of the force. A new Lagrangian can be written, including a description of the particles interacting with the gauge fields.

Starting with a singlet spinor ψ, its Lagrangian follows the Dirac equation and is written as

$$\mathscr{L} = i\bar{\psi}\gamma^\mu \partial_\mu \psi - m\bar{\psi}\psi. \tag{1.3}$$

Imposing gauge invariance $\psi \to U\psi$ ($U^\dagger U = 1$ and $U = e^{i\theta}$) to the field ψ, one needs to insert a massless vector field A_μ described by a Proca Lagrangian. The gauge field transforms as $A_\mu \to A_\mu + \partial_\mu \lambda$, where $\theta(x) = -q\lambda(x)$, and q is a constant referring to the electric charge. Finally, the complete Lagrangian for QED invariant under U(1) symmetry is written as [2]:

$$\mathscr{L} = [i\bar{\psi}\gamma^\mu \partial_\mu \psi - m\bar{\psi}\psi] - \left[\frac{1}{16\pi} F^{\mu\nu}F_{\mu\nu}\right] - (q\bar{\psi}\gamma^\mu\psi)A_\mu, \tag{1.4}$$

where $F^{\mu\nu}$ is the commutator defined as $F^{\mu\nu} = [\mathscr{D}_\mu, \mathscr{D}_\nu]$, and $\mathscr{D}_\mu = \partial_\mu + iqA_\mu$ which is called *covariant derivative*. The massless gauge field dynamics is given by the second term of the Lagrangian, and the third term describes interactions between the Dirac fields (spinors in QED) and the Maxwell field (photon). This abelian U(1) gauge symmetry group sees only electrically charged singlet described by the Dirac Lagrangian, namely generating all the interactions for electrically charged particles.

In addition to the U(1) symmetry discussed above, another internal symmetry in the isospin rotation space can be introduced starting with a spinor isospin doublet:

$$\psi = \begin{pmatrix} \psi_1 \\ \psi_2 \end{pmatrix}. \tag{1.5}$$

The corresponding Lagrangian can be written as

$$\mathscr{L} = i\bar{\psi}\gamma^\mu \partial_\mu \psi - \bar{\psi}M\psi, \tag{1.6}$$

where M is a diagonal mass matrix.The local SU(2) transformation can be written as:

$$S = e^{-ig\tau\lambda(x)}, \tag{1.7}$$

where τ is the generator of SU(2), and its elements refer to the Pauli spin matrices. In order to force the SU(2) gauge invariance onto the Lagrangian described in Equation (1.6), one needs to add additional new massless gauge fields: $\mathbf{A}^\mu = (A_1^\mu, A_2^\mu, A_3^\mu)$ by substituting the

derivative of $\mathscr{L}$ with the covariant derivative:

$$\mathscr{D} = \partial_\mu + ig\tau\mathbf{A}_\mu, \tag{1.8}$$

where g is a coupling constant. Therefore, the complete Lagrangian based on the spinor doublet is:

$$\mathscr{L} = [i\bar{\psi}\gamma^\mu\partial_\mu\psi - m\bar{\psi}\psi] - \left[\frac{1}{16\pi}\mathbf{F}^{\mu\nu}\mathbf{F}_{\mu\nu}\right] - (g\bar{\psi}\gamma^\mu\tau\psi)\mathbf{A}_\mu, \tag{1.9}$$

which is called a Yang-Mills Lagrangian [2], and describes the weak interactions with conservation of the weak isospin.

Similarly, one can impose gauge invariance on the Lagrangian of a color triplet:

$$\psi = \begin{pmatrix} \psi_r \\ \psi_b \\ \psi_g \end{pmatrix} \tag{1.10}$$

The invariance requires new gauge fields $\mathbf{A}_\mu$ corresponding to the eight gluons, which mediate the strong force. This QCD gauge sector can be written with the same procedure, including in the Lagrangian the free gluon dynamics and the strong interactions in terms of the strong coupling constants. Gell-Mann matrices λ are used in this case instead of the Pauli matrices τ which are used for the SU(2) sector.

The Glashow-Weinberg-Salam model [2] unifies electromagnetic and weak descriptions into an electroweak description under the symmetry of $U(1)\times SU(2)_L$ in the hypercharge space. This unification was born in terms of the *chirality* of fermions: the left handed fermion is described using $\psi_L = \frac{1}{2}(1-\gamma^5)\psi$ with $chirality = -1$, while the right handed fermion with $chirality = +1$ is $\psi_R = \frac{1}{2}(1+\gamma^5)\psi$; and the opposite for the antiparticles.

The covariant derivatives depending on the generators of both U(1) and SU(2) can be defined as [2]

$$\mathscr{D}_\mu\psi_{L,R} = \left[\partial_\mu + iq\tau_{L,R}\mathbf{W}^\mu + ig\frac{Y_{L,R}}{2}B^\mu\right]\psi_{L,R}, \tag{1.11}$$

where the B^μ gauge field is introduced by the U(1) gauge group; whilst $\mathbf{W}^\mu$ represents the gauge fields under the SU(2) gauge group; and the $Y_{L,R}$ refers to the hypercharge, where the subscript indicates the chirality of particles. The hypercharge Y is related to the electric charge (Q) and weak isospin (I_3) by $Q = I_3 + \frac{1}{2}Y$.

Based on the values found in Table 1.4 and an Equation (1.11), one can see that ψ_L and ψ_R transform differently, and only left-handed particles interact weakly. As a consequence,

the gauge invariance would be broken by the fermion mass term $m\bar{\psi}\psi = m\bar{\psi}_R\psi_L + m\bar{\psi}_L\psi_R$. Fermions are hence massless in the un-broken Lagrangian.

Fermions	Q	I_3	Y
$\binom{\nu_e}{e}_L$, $\binom{\nu_\mu}{\mu}_L$, $\binom{\nu_\tau}{\tau}_L$	$\binom{0}{-1}$	$\binom{+\frac{1}{2}}{-\frac{1}{2}}$	$\binom{-1}{-1}$
e_R, μ_R, τ_R	-1	0	-2
$\binom{u}{d}_L$, $\binom{c}{s}_L$, $\binom{t}{b}_L$	$\binom{\frac{2}{3}}{-\frac{1}{3}}$	$\binom{+\frac{1}{2}}{-\frac{1}{2}}$	$\binom{\frac{1}{3}}{\frac{1}{3}}$
u_R, c_R, t_R	$\frac{2}{3}$	0	$\frac{4}{3}$
d_R, s_R, b_R	$-\frac{1}{3}$	0	$-\frac{2}{3}$

Table 1.4 Electroweak charges for chiral fermions.

The Higgs boson: the last fundamental family member

It was noted above that mass terms for the weak mediator bosons and the fermions would break the gauge invariance. As most of them are massive, then the query of a mechanism to give them masses arose. An SU(2) doublet of complex scalar fields was hence introduced, namely the *Higgs field*:

$$\phi = \begin{pmatrix} \phi^+ \\ \phi^0 \end{pmatrix} = \frac{1}{\sqrt{2}} \begin{pmatrix} \phi_1 + i\phi_2 \\ \phi_3 + i\phi_4 \end{pmatrix}, \tag{1.12}$$

in which each ϕ_n ($n = 1,2,3,4$) is a scalar field described by the Lagrangian

$$\mathscr{L} = \frac{1}{2}(\partial_\mu \phi)(\partial^\mu \phi) - V(\phi), \tag{1.13}$$

where the potential term $V(\phi)$ is

$$V(\phi) = -\frac{1}{2}\mu^2\phi^2 + \frac{1}{4}\lambda^2\phi^4, \tag{1.14}$$

where μ and λ are constant[1].

Given this potential $V(\phi)$, the ground state, which is called vacuum expectation value (VEV), occurs at $\phi = \pm\sqrt{\frac{\mu^2}{\lambda}}$ but not at $\phi = 0$. A small perturbation of the initial state will lead to a non-zero VEV and break the initially symmetric configuration, as shown in Figure 1.1. This is known as *spontaneous symmetry breaking* [3–6].

[1] μ relates to the particle mass described by the scalar field Lagrangian, and λ is a new coupling constant accounting for the self coupling term.

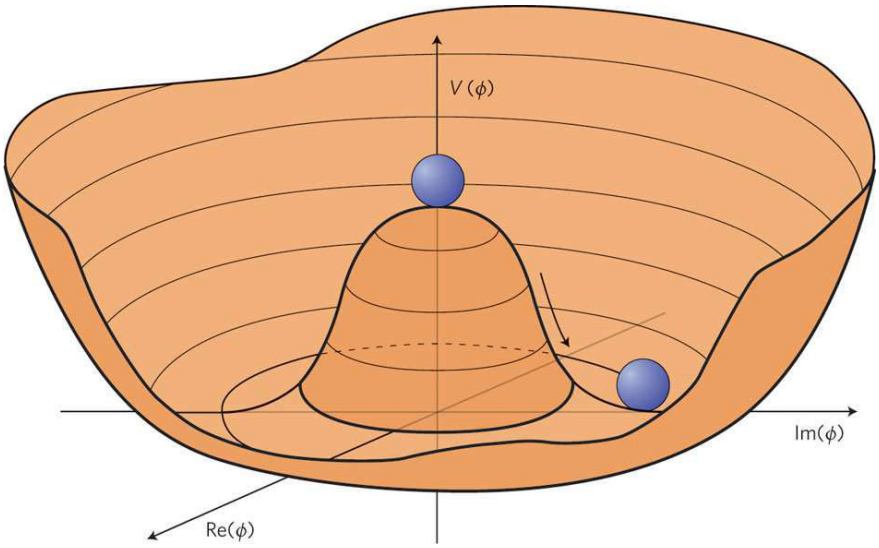

Fig. 1.1 The Mexican hat of the Higgs potential [7].

By using the idea of spontaneous symmetry breaking and applying the gauge invariance to the Higgs field doublet, three of the four degrees of freedom of the Higgs doublet are used to construct mass terms for the W and Z gauge bosons, with one degree of freedom remaining as a physical massive scalar boson: the Higgs boson. The fermion mass terms are different from the ones of the weak bosons, in that they achieve their mass terms by Yukawa couplings with the physical Higgs boson; their coupling constant is proportional to their mass.

The Higgs boson was discovered in 2012 by ATLAS and CMS at the LHC at CERN, and its mass, as measured, is $125.09 \pm 0.21(stat) \pm 0.11(syst)$ GeV [8].

The Standard Model (SM) is a renormalizable gauge theory [2], based on a symmetry group $U(1) \times SU(2) \times SU(3)$, where the U(1) symmetry group describes QED, SU(2) describes the weak interaction and SU(3) represents QCD. The full SM Lagrangian describes the three generations of fermions, the gauge bosons that mediate three of the four fundamental forces, and the Higgs mechanism which gives masses to the particles and gives rise to the spin-0 massive Higgs boson.

1.3 Standard Model Limitations

So far, the Standard Model has remarkable successes at describing the currently known particle phenomena. However, it is still far from a complete theory and has some open questions (see [2] for more details), as it does not explain, for example, the three generations of quarks and leptons, the neutrino oscillation, the asymmetry between matter and antimatter,

the hierarchy problem, or the nature of dark matter. This section will concentrate on the hierarchy problem and the nature of dark matter.

The gauge hierarchy problem

The strong interaction starts to play an important role at an energy around 200 MeV [9], the scale which determines the masses of hadrons made of light quarks such as the π^0. The energy scale of the electroweak interactions is on the order of the vacuum expectation value of the Higgs boson, $vev \approx 246$ GeV [1]. A large gap on the order of 10^{17} GeV is found between the electroweak energy scale and the Planck energy scale ($\sim 10^{19}$ GeV) where the gravitational effect needs to be considered.

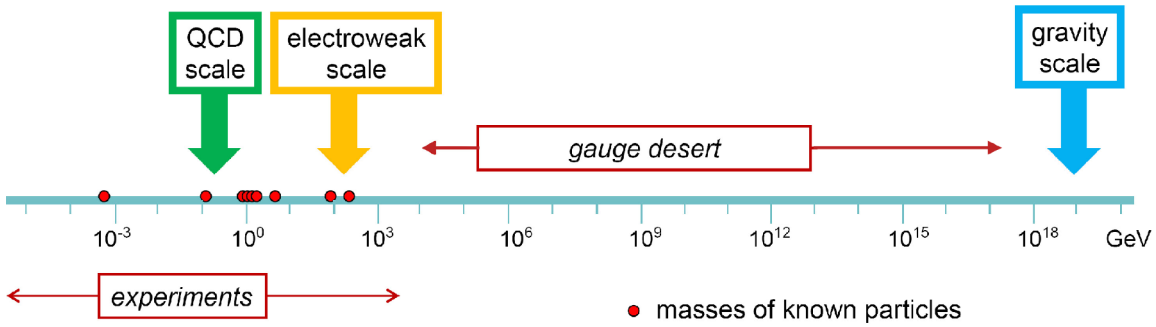

Fig. 1.2 The hierarchy of scales of gauge interactions [9].

The gauge hierarchy problem [10–12], coming from the gap between the energy scales shown in Figure 1.2, can be seen in the radiative corrections to the Higgs mass, when allowing the Standard Model to be valid up to the Planck scale.

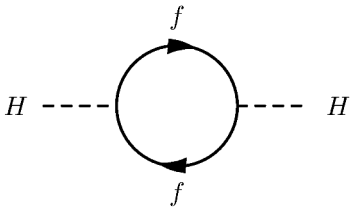

Fig. 1.3 One-loop quantum correction to the Higgs squared mass parameter m_H^2, contributed by a Dirac massive fermion f.

The observable Higgs mass, $m_{exp,H}$, is composed of the tree-level Higgs mass, m_H, and of 'self-energy' terms coming from virtual particle loops, Δm_H, as shown in Figure 1.3.

$$m_{exp,H}^2 = m_H^2 + \Delta m_H^2. \tag{1.15}$$

However, these radiative corrections are quadratically divergent because the momentum of those virtual particles can take the highest energy scale at which the theory stops to be valid. For example, if the Standard Model is believed to be suitable up to the reduced Planck scale [13]

$$M_p = (8\pi G)^{-\frac{1}{2}} = 2.4 \times 10^{18}\ \text{GeV}, \tag{1.16}$$

where the impact of quantum gravity should be strong, then the radiative corrections $\Delta m_H^2 \sim M_p^2$, and the tree level Higgs mass must become unnaturally large and fine-tuned, as it is known from the experimental measurements that $m_{exp,H}^2 \simeq (125\ \text{GeV})^2$.

As a conclusion, the Standard Model suffers from an unnatural Higgs mass tuning due to the scale hierarchy. A solution to constrain the divergent term is to lower the Planck scale, by adding more dimensions. Another solution could be given by proposing a new theory called, supersymmetry, which will be described in section 3.

Dark matter

Dark matter was named 'dark' not only for its luminous darkness for detectors, but also for its unknown nature. Its existence was proven by many cosmological experiments, such as the measure of galaxy rotation curves and the study of gravitational lensing effect.

When measuring the rotation tangential velocity (v) of objects as a function of the distance (r) from the galactic center, the velocity is expected to increase starting from the center of the galaxy and then to decrease as $v = \sqrt{GM_r/r}$ when the radius r is larger than the edge of the galaxy, resulting from Newton's equation $F = G\frac{m_1 m_2}{r^2}$. If the rotation curve becomes flat as is observed, it implies the existence of an unknown massive matter contributing to M_r which is non-luminous and has a mass density proportional to $\frac{1}{\sqrt{r}}$. As an example, Figure 1.4 gives the experimental rotation curve measured for a dwarf spiral galaxy [14]. The observed data can be explained by adding to the luminous and gas components a dark matter contribution.

On top of the compelling evidence for dark matter introduced above, there are other experiments which not only offer evidence but also measure the total amount of dark matter in the Universe. As announced by Planck [15], an experiment analyzing the Cosmic Microwave Background (CMB), there is only 4.9% ordinary baryonic matter in the Universe, while dark matter occupies 26.8%, and the rest of the energy is known as dark energy.

Dark matter would interact neither electromagnetically nor strongly, as it is found to be non-luminous and non-baryonic. However, the possibility for dark matter to interact only weakly is still allowed. In other words, massive particles who are neutral and interact weakly are likely candidates to dark matter. There is no such candidate in the Standard

Model. Solutions to this problem will be introduced in Section 2.

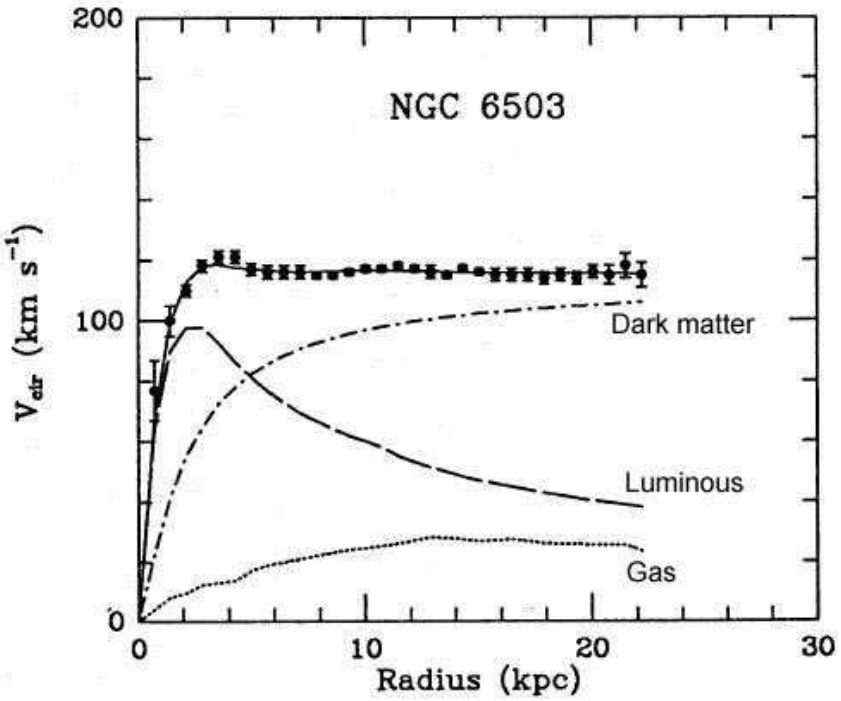

Fig. 1.4 Rotation curve of NGC 6503, which is a dwarf spiral galaxy located in a region of space called the Local Void. The experimental measurement of the rotation curve is represented by the dots with error bar, with a three parameter fit drawn in solid line. The three simulated distribution of dark matter, luminous components and gas are shown in dash-dotted, dashed and dotted lines respectively [14].

Chapter 2

Dark matter

2.1 Introduction

The existence of a non-baryonic dark matter is proven by many astrophysical observations, as discussed in Section 1.3, although its nature is yet unknown. Dark matter candidates are usually classified as hot, warm and cold in astrophysics depending on their thermal velocity in the early universe. According to the important role dark matter plays in the galaxy formation and evolution, the dark matter candidate should be cold (more details can be found in References [16, 17]). This forms a Lambda cold dark matter (ΛCDM) model, which is tested via experiments measuring the cosmic microwave background (CMB), such as Planck [15, 18].

An appealing candidate for the cold dark matter is a weakly interacting massive particle (WIMP), noted as χ, as it can provide a relic density of dark matter compatible with experimental observation, which is known as the *WIMP miracle*. Many theories beyond the Standard Model, such as supersymmetry or extra dimensions, can provide compelling candidates for a WIMP.

2.2 Dark matter detection

Experimental detection of dark matter can be classified into different categories according to their detection mechanism. One can directly measure the elastic scattering cross section between WIMPs and a target nucleon, which is often called the *direct detection* method. The *indirect detection* method looks for the annihilation products of WIMPs such as photons or positrons. Finally, the *collider detection* method hunts for WIMPs production in the collision of Standard Model particles. All these three detection methods are illustrated

in Figure 2.1.

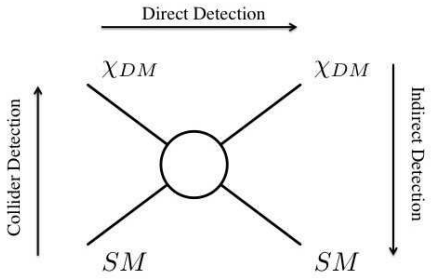

Fig. 2.1 A schematic diagram to show the various Dark Matter detection methods.

Each detection method introduced above can lead to different detectable final states depending on the interactions between the WIMPs and the Standard Model particles, which will be introduced below.

Direct detection

As observed in CMB experiments, the galaxy should be filled with dark matter particles. From time to time, dark matter particles passing through the Earth can interact with nucleons in very sensitive detectors, generating nuclear recoils which can be analyzed.

In order to reject cosmic ray backgrounds and thus increase the signal sensitivity, these detectors are usually located deeply underground. Such experiments are setting limits on the elastic scattering cross section of WIMPS on nucleons, if there is no significant signal found.

Many experiments have been built using different techniques to measure the nuclear recoil in a complementary way, such as SuperCDMS [19], LUX [20], ELDELWEISS [21], XENON100 [22] or PICASSO [23]. For example, the LUX (Large Underground Xenon) experiment, which is located at the Sanford Underground Research Facility in the USA, uses liquid Xenon as target material. The LUX detector was completed in the spring of 2012 and its first and latest result [24] published in 2013 using 85.3 live-days of data can be found in Figure 2.2. As shown in this figure, LUX is more sensitive in the high WIMP mass region.

Indirect detection

The indirect detection of dark matter aims at detecting the flux of annihilation products from dark matter particles. These detectors are usually set to focus on the areas where the dark matter density should be high, such as the galactic center.

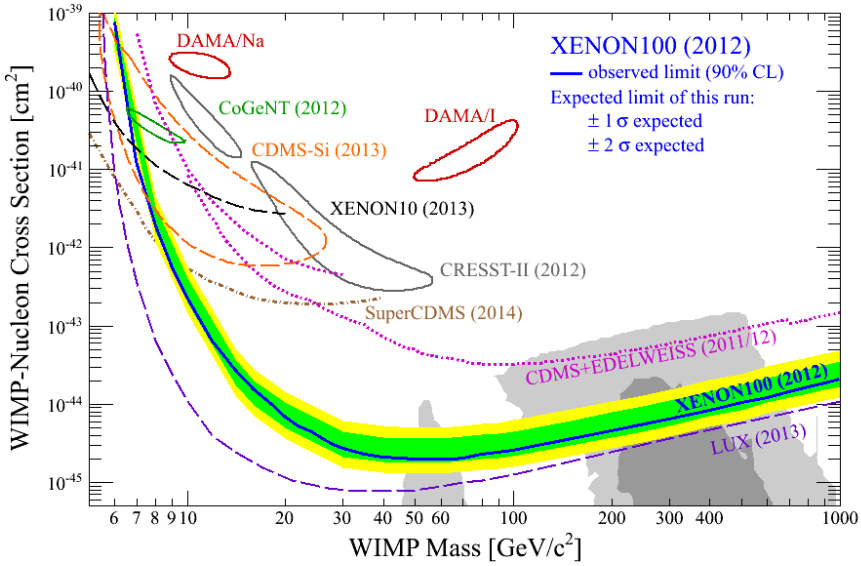

Fig. 2.2 The observed upper limits at 90% CL are set on spin-independent elastic WIMP-nucleon cross-section as a function of the WIMP mass [25], the results are obtained by different but complementary dark matter experiments.

Depending on the final annihilation products, these dark matter experiments either look for neutrinos such as the IceCube [26] detector, charged anti-particles (like positrons and anti-protons) such as AMS-02 [27], or deviations in the gamma-ray spectrum like the Fermi Large Area Telescope (Fermi-LAT) [28]. Considering that the analysis presented in Section 13.1 uses a dark matter model inspired by the Fermi-LAT result, it is useful to introduce in more details this indirect detection experiment.

The Large Area Telescope (LAT) is the principal instrument on the Fermi Gamma-ray Space Telescope mission, which was launched into a near-earth orbit on June 11^{th} 2008 with a designed lifetime of 5 years. This gamma-ray telescope covers the energy range from below 20 MeV to more than 300 GeV.

One of the aim of the Fermi-LAT experiment is to detect the gamma-ray flux coming from dark matter annihilation. The observed flux intensity ϕ of gamma-rays at a given energy, coming from the annihilation of dark matter from a point-like source, can be written as [29]

$$\frac{d\phi}{dEdV} = \frac{1}{4\pi d^2}\frac{dN}{dE}\frac{\langle\sigma v\rangle}{2m_\chi^2}\rho_{DM}^2, \tag{2.1}$$

where $\langle\sigma v\rangle$ refers to the mean value of the dark matter annihilation cross-section multiplied by velocity, dN/dE denotes the photon spectrum per annihilation, m_χ and ρ_{DM} are the mass and mass density of the dark matter source, and d refers to the distance from the source to the detector. The integral of Equation (2.1) over a solid angle α gives the gamma-ray

flux of a given energy observed within α. If the dark matter particle is not its anti-particle, Equation (2.1) should be reduced by a factor of two.

The gamma-ray spectrum produced by the dark matter annihilation at a given mass can either be continuous, with a cutoff at the mass of the dark matter particle as shown in Figure 2.3a, or a line at the dark matter mass shown in Figure 2.4, depending on the annihilation process.

There is no continuous gamma-ray spectra observed when fitting the data to the background flux estimation, and thus limits are set to the phase space of $\langle\sigma v\rangle$ versus m_χ for different secondary particles, such as limits shown in Figure 2.3b in the $\chi\chi \to \tau^+\tau^-$ case.

At the time the work on the thesis started, a gamma-ray line indicating the existence of a dark matter particle at a mass around 130 GeV had been published [30], where the excess events showed a local significance of $4.6\,\sigma$ which dropped to $3.2\,\sigma$ when taking into account the look-elsewhere effect, see Figure 2.4 [1]. This result was obtained using 43 months of public data from the Fermi-LAT. Another result was issued later, using 44.4 months of data [31]: the $3.3\,\sigma$ local significance at $m_\chi = 133$ GeV translated into a global significance of $1.5\,\sigma$. The dark matter interpretation of the gamma-ray line at around 130 GeV was hence disfavored by the latter result.

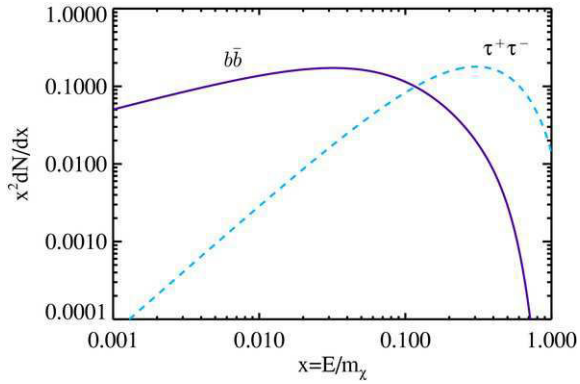

(a) Continuous photon spectra coming from different annihilation processes for a dark matter of $m_\chi = 500$ GeV [32].

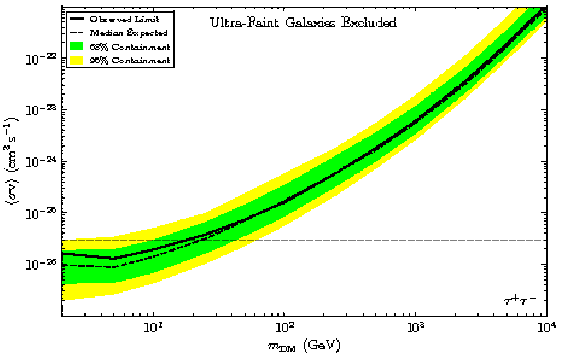

(b) Observed limits set on the dark matter annihilation cross section, $\langle\sigma v\rangle$, versus the dark matter mass, m_{DM}, in the $\chi\chi \to \tau^+\tau^-$ channel [33].

Fig. 2.3 Expected continuous photon spectra at a given dark matter mass (a), and observed limits set to the dark matter annihilation cross-section in the $\chi\chi \to \tau^+\tau^-$ channel (b).

[1] The discovery of dark matter at a given mass could be claimed if the excess events at the gamma-ray line had a significance over 5 standard deviations (5σ).

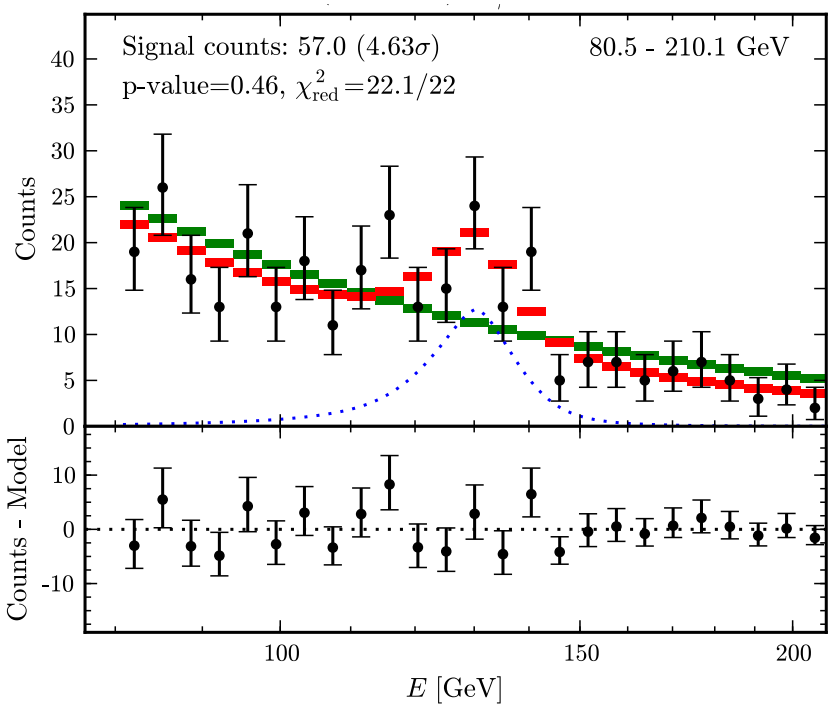

Fig. 2.4 A spectral gamma-ray flux measured by Fermi-LAT, where an excess of events around 130 GeV is clearly visible in the data [34]. The blue dotted line in the upper indicates the line flux component only, the red dashed line shows the best-fit DM model and the green dashed line do not include any DM model.

Collision production detection

With the high energy and large number of collisions produced in colliders, such as the Large Hadron Collider (LHC) which will be introduced in Chapter 4, it may be possible to produce dark matter particles from Standard Model particle collisions [35, 36].

One can use an accurate model, or a more model-independent Effective Field Theory (EFT) [37–41], in which the mediator mass $M_{med} = \sqrt{g_q g_\chi} M_*$ (where M_* is the effective energy scale) is assumed to be much heavier than the transferred momentum q_{tr}, resulting in an effective operator [38, 39].

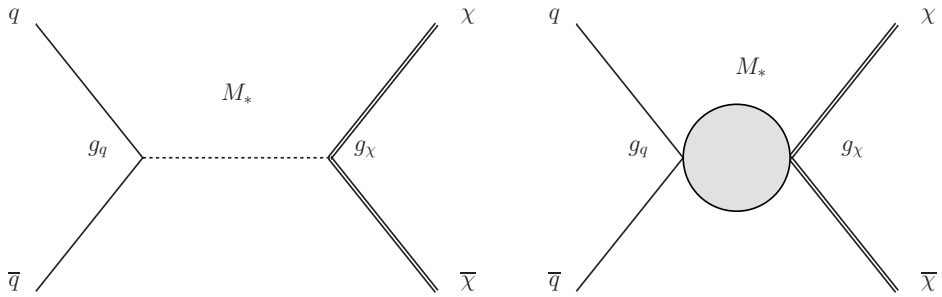

Fig. 2.5 The Feynman diagrams for $q\overline{q} \to \chi\overline{\chi}$, with a s-channel heavy mediator exchange (left panel) and its effective operator (right panel).

Figure 2.5 illustrates the $q\overline{q} \to \chi\overline{\chi}$ process with an s-channel mediator exchanged in a simplified model (left). The mediator can be integrated out to give a contact interaction (right) if the following EFT condition is valid

$$M_* > \frac{q_{tr}}{\sqrt{g_q g_\chi}}. \tag{2.2}$$

This EFT validity requirement can be written as $M_* > \frac{m_\chi}{2\pi}$ to satisfy the conditions of $q_{tr} > 2m_\chi$ for an s–channel model, and the perturbativity of the couplings $g_{q,\chi} < 4\pi$ [41].

Detectors such as ATLAS, which will be introduced in the following Chapter 5, can not identify the dark matter particles as they interact only weakly. Hence the experimental signal to probe the dark matter production is the detectable signatures of initial state radiation (ISR) emitted by the colliding Standard Model particles. This ISR can either be a gluon, a W, a Z, or a photon, leading to various final states to analyze. The data analysis presented in this thesis uses a final state containing a single photon as illustrated in Figure 2.6.

The EFT dark matter limits obtained by an LHC experiment can be translated into limits in the same parameter space as the one used by direct detection experiments, which is shown in Figure 2.2. However, this is model-dependent, as one needs to choose certain operators

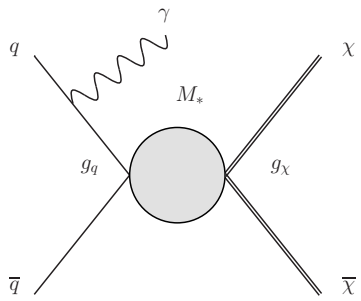

Fig. 2.6 The Feynman diagram for $q\overline{q} \to \chi\overline{\chi}\gamma$, where the photon is radiated from initial state quarks.

and couplings [39] and take into account the validity of the EFT [41, 42]. The comparison between the two kinds of results is hence not so straightforward if only limits are placed. However, once a dark matter signal is discovered, it could help finding out the nature of the dark matter.

The dark matter particles can be produced at colliders even if it is very light; the collision production detection is very sensitive to the very low dark matter mass region. The direct detection is highly sensitive in the high mass region due to the detecting mechanism (elastic scattering between the WIMP and nucleon) but is not sensitive in the very low mass region. The two results are hence complementary.

Chapter 3

Supersymmetry

3.1 Motivation and general idea

Symmetries play an important role in modern particle physics. The isometric group of Minkowski space is called the *Poincaré group*, and includes translations, rotations and boosts in 4–dimensional space. In addition to space-time symmetries, there are also internal symmetries as introduced in Section 1.2. Due to the restriction of the no–go theorem [43], supersymmetry (SUSY) was introduced as the only possible extension of the Poincaré group which combines it with an internal symmetry, SUSY, relating bosons with fermions as:

$$\begin{aligned} Q|fermion\rangle &= |boson\rangle, \\ Q|boson\rangle &= |fermion\rangle, \end{aligned} \tag{3.1}$$

where this spinorial operator Q, known as supercharge, generates transformations between states differing by half a unit of spin. Together with its Hermitian conjugate $Q^\dagger$, they satisfy the SUSY algebra with fundamental anti-commutator and commutator relations:

$$\begin{aligned} \{Q_a, Q^\dagger_{\dot{a}}\} &= 2\sigma^\mu_{a\dot{a}} P_\mu, \\ [P_\mu, Q_a] &= [P_\mu, Q^\dagger_{\dot{a}}] = 0, \end{aligned} \tag{3.2}$$

where P_μ refers to the four-momentum generator of the Poincaré group.

All the particles are in the irreducible representations of the SUSY algebra, called supermultiplets, which can be basically classified as chiral supermultiplet fields each containing a spin $\frac{1}{2}$ fermion and a spin 0 boson, and gauge supermultiplet fields each containing a spin 1 vector and a spin $\frac{1}{2}$ fermion. In SUSY, each Standard Model particle acquires a supersymmetric partner, called a sparticle. Since the supercharge commutes with the squared

mass operator $P^2 \equiv P^\mu P_\mu$, as well as the gauge generators, particles in the same supermultiplet should be degenerated in mass and the other gauge charges, such as electric charges, weak isospin and color charge. Accordingly, sparticles interact similarly to their Standard Model partners; they only differ by their spin.

If supersymmetry is an unbroken theory, the Lagrangian should be invariant under a SUSY transformation. As there is no spartner found with the same masses as the Standard Model particles, it is necessary to consider supersymmetry as a broken symmetry.

The supersymmetric Lagrangian can be broken either by adding supersymmetry breaking terms as free parameters, or by introducing given scenarios, such as a gravity-mediation in the SUGRA model. For further discussion on the breaking models, see Section 3.3.

As introduced before, supersymmetry was naturally developed as a general extension to the Poincaré group, but must be broken. It is still attractive as it can offer solutions to many problems of the Standard Model , such as the hierarchy and the dark matter problems introduced in Section 1.3.

Given the fact that fermion loops and boson loops contribute to the Higgs radiative corrections with opposite signs, the large radiative corrections Δm_H^2 would be canceled by the new loops introduced in supersymmetry, see Figure 3.1.

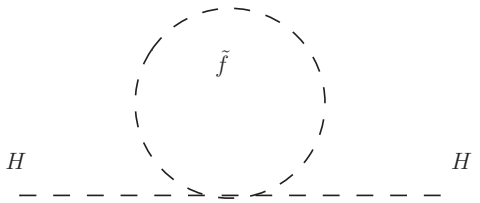

Fig. 3.1 One-loop quantum corrections to the Higgs squared mass parameter m_H^2 due to a scalar $\tilde{f}$

Supersymmetry can also offer a weakly interacting candidate for dark matter (see Section 3.2) and it can also help to unify the running gauge couplings at higher energy scale [44].

Many analyses have been set to look for evidence of SUSY, using data from detectors at different colliders, such as the Tevatron at FermiLab, or Large Hadron Collider (LHC) at CERN. A brief overview of SUSY analyses at LHC will be given in Section 3.4.

3.2 Particle contents and interactions

Particle contents

The sparticles introduced here represent the minimal supersymmetric extension of the Standard Model , and form the so-called Minimal Supersymmetric Standard Model (MSSM) [45–49].

The nomenclature of sparticles has the following logic: the bosonic spartners of SM fermions are named with a prefix of 's' (for example, the selectron is the spartner of the electron), whilst the fermionic spartners of the bosons have a suffix 'ino' instead, (for example, the gluino is the spartner of the gluon). In addition, sparticles are written by adding a tilde on top of the symbols of their SM partners, such as $\tilde{q}$ for squarks.

As detailed in Reference [13], two Higgs doublets need to be introduced in the MSSM in order to be able to construct mass terms for the SM massive fermions and to avoid introducing a gauge anomaly. The relevant two Higgs supermultiplet are constructed with weak hypercharge Y of $\frac{1}{2}$ and $-\frac{1}{2}$, respectively. After the electroweak symmetry breaking, five physical Higgs bosons are left: two charged Higgses ($H^{\pm}$), one pseudo-scalar Higgs (A) and two scalar Higgses (h and H^0). Furthermore, the lightest scalar Higgs h has a mass constraint in the MSSM, it should not be more than ~ 150 GeV [13], in agreement with the experimental Higgs mass discovered at $125.09 \pm 0.21(stat) \pm 0.11(syst)$ GeV [8].

After electroweak symmetry breaking, the spartners of the electroweak gauge and Higgs bosons form mass eigenstates known as *charginos*: $\tilde{\chi}_1^{\pm}, \tilde{\chi}_2^{\pm}$, and *neutralinos*: $\tilde{\chi}_1^0, \tilde{\chi}_2^0, \tilde{\chi}_3^0, \tilde{\chi}_4^0$, where the subscripts of charginos and neutralinos are ordered in increasing mass.

As a summary, Table 3.1 shows the mass eigenstates of the sparticles introduced in this section, together with their spin and partners.

Names	Symbol	Spin	Partners
squarks	$\tilde{u}, \tilde{c}, \tilde{t}$ $\tilde{d}, \tilde{s}, \tilde{b}$	0	u, c, t d, s, b
sleptons	$\tilde{e}, \tilde{\mu}, \tilde{\tau}$ $\tilde{\nu}_e, \tilde{\nu}_\mu, \tilde{\nu}_\tau$	0	e, μ, τ ν_e, ν_μ, ν_τ
charginos	$\tilde{\chi}_1^{\pm}, \tilde{\chi}_2^{\pm}$	$\frac{1}{2}$	$H^{\pm}, W^{\pm}$
neutralinos	$\tilde{\chi}_1^0, \tilde{\chi}_2^0, \tilde{\chi}_3^0, \tilde{\chi}_4^0$		h, A, H, Z, γ
gluino	$\tilde{g}$		g
gravitino	$\tilde{G}$	$\frac{3}{2}$	G

Table 3.1 The MSSM particles along with their spin and partner. The charginos ($\tilde{\chi}_i^{\pm}$) and the neutralinos ($\tilde{\chi}_i^0$) are mixture of gauginos and Higgsinos.

Decays and interactions

Sparticles have the same couplings as their SM partners, and accordingly will have the same types of interactions. Another quantum number is introduced in SUSY, called R-parity. It is defined as $(-1)^{3(B-L)+2s}$ [13], where B refers to baryonic number, L is the leptonic number and s refers to the spin. It has a value of 1 for Standard Model particles and -1 for sparticles.

In models for which R-parity is not conserved, the lightest sparticle can decay into SM particles via a lepton number violating vertex, or a vertex with baryon number violation.

On the other hand, if R-parity is conserved, the lightest sparticle which is often the weakly interacting $\tilde{\chi}_1^0$, is predicted to be stable, satisfying the properties of dark matter particles in ΛCDM model. Besides, if R-parity is conserved, sparticles must be generated in pairs, and the decay production of a sparticle should always contain another lighter sparticle.

3.3 SUSY breaking and proposed solutions

As discussed in Section 3.1, SUSY must be broken to allow different mass terms for the sparticles. In the general MSSM, the breaking mechanism is not specified, and leaves many parameters free and independent. One can also introduce a given breaking mechanism, like in Gauge-Mediated SUSY Breaking (GMSB) [50–55] and Supergravity (SUGRA) [56–61] models; they are less generic than the MSSM but have fewer free parameters.

Another approach is the simplified model, which is not a complete model but a basic building block of the supersymmetry. It usually concerns a given Feynman diagram such as the diagram shown in Figure 3.2: the generation and decay modes are set and the sparticle masses are fixed. Therefore, the cross section of this diagram can be calculated without fixing the full supersymmetric Lagrangian.

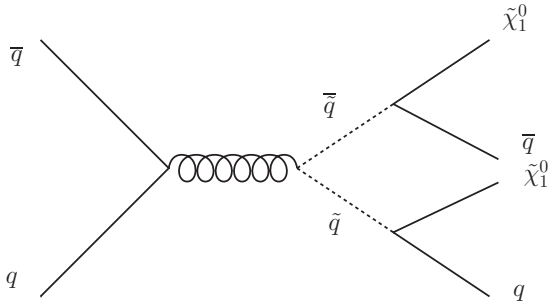

Fig. 3.2 Pair production of squarks, followed by decay into quarks and neutralinos.

Experimental limits based on simplified models can eventually be translated into com-

plete supersymmetric models.

3.4 Experimental signals

Different supersymmetric models predict different masses, production and decay modes for the sparticles. For this reason, sparticles such as gluinos, squarks, charginos or neutralinos could be generated and decay differently, and thus lead to many different *final states* for experimental analyses; for example, in models with R-parity violation (RPV), the lightest neutralino $\tilde{\chi}_1^0$ can decay to Standard Model particles identified in the detectors, whereas in models with R-parity conservation, $\tilde{\chi}_1^0$ will not decay and escape the detectors as missing energy which can be measured in the transverse plane.

Given that no sparticle was discovered so far, all these SUSY searches are presently confined to setting limits on sparticle masses. In the ATLAS experiment at the LHC, various supersymmetry analyses have been developed according to different final states. As discussed in Section 3.1, SUSY is expected to solve the hierarchy problem by introducing new massive particles. This requirement implies rather light charginos, neutralinos and the third generation squarks; supersymmetric models respecting this constraint are said to have a natural spectrum. Due to this specific interest, dedicated analyses are arranged to search for the third generation squarks and the electroweak SUSY in ATLAS.

A representative selection of the available mass limits from the supersymmetric searches in ATLAS, together with the model and searching channel used, are shown in the summary Figure 3.3. Besides the dedicated channels related to the natural spectrum, there are R-parity conserving inclusive searches for production of strongly interacting sparticles, 'exotics-like' searches for long-lived sparticles and R-parity violating searches.

This figure also shows the SUSY model result presented in this thesis, which gives an exclusion of the first and second generation squark mass up to 250 GeV in the inclusive search for the simplified model of $\tilde{q} \rightarrow q\tilde{\chi}_1^0$ in a compressed mass spectrum where the mass difference between $\tilde{q}$ and $\tilde{\chi}_1^0$ is very small on the order of 10 GeV .

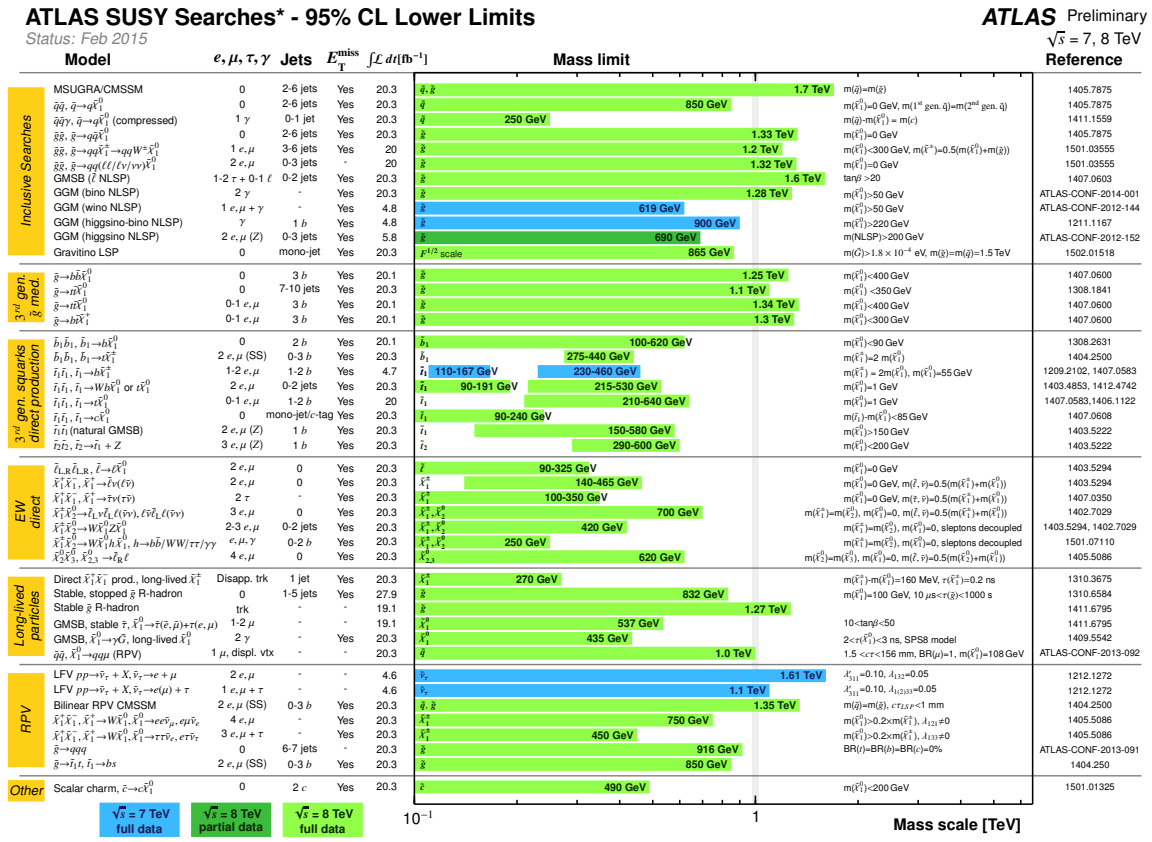

*Only a selection of the available mass limits on new states or phenomena is shown. All limits quoted are observed minus 1σ theoretical signal cross section uncertainty.

Fig. 3.3 Mass reach of ATLAS searches for supersymmetry. Only a representative selection of the available results is shown [62].

Part II

Experimental Setup

Chapter 4

The Large Hadron Collider

The *Large Hadron Collider* (LHC) is a hadron accelerator and collider, built in the existing 27 km underground tunnel of the LEP machine at CERN, which is located at the border of France and Switzerland, close to Geneva.

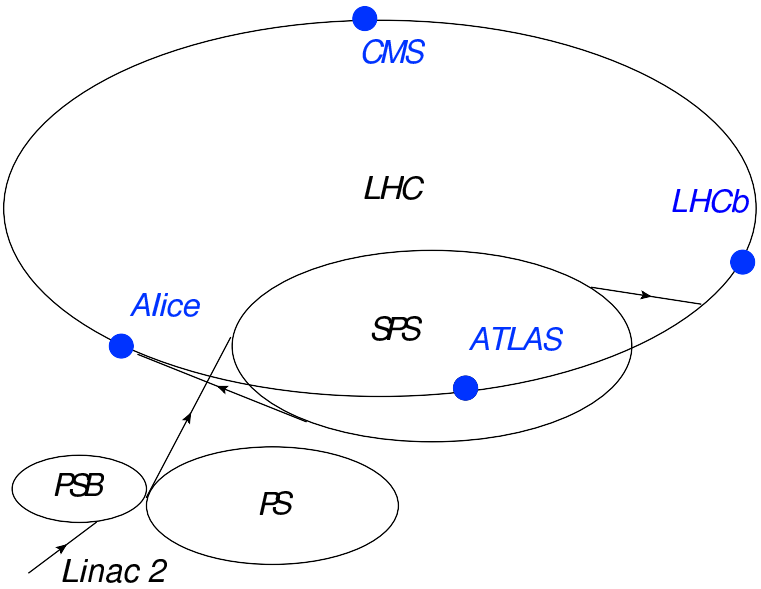

Fig. 4.1 The LHC accelerator complex.

4.1 Accelerator complex

The LHC is an accelerator complex composed of a few different accelerators, as shown in Figure 4.1. Protons first start from a single bottle of hydrogen gas from which they are extracted by an electric field, and they are first accelerated to an energy of 50 MeV by

the LINAC 2, which is the first element of the complex; then with the help of the Proton Synchrotron Booster (PSB), the energy of the proton beam is pushed to 1.4 GeV, and later increased up to 25 GeV via the Proton Synchrotron (PS); finally the proton beam reaches 450 GeV after the Super Proton Synchrotron (SPS) and is injected into the last element of the complex, which is the circular Large Hadron Collider.

The LHC does the final acceleration of the proton beam to a designed maximum energy of 7 TeV, using radiofrequency (RF) cavities. The proton beam is not continuous but is divided among discrete *bunches*, thus each collision is called a *bunch collision* and the interval between two bunch crossings is designed to be 25 ns.

A high degree of vacuum in an accelerator system is crucial, otherwise, protons might interact with gas molecules and thus create background.

4.2 Hadron collider

The LHC accelerates the two proton beams in two separate rings in opposite direction and collides them at 4 crossing points, where particle detectors are installed as shown in Figure 4.1: *A Toroidal LHC Apparatus* (ATLAS), *Compact Muon Solenoid* (CMS), *A Large Ion Collider Experiment* (Alice) and *Large Hadron Collider beauty experiment* (LHCb). Both ATLAS and CMS are symmetric detectors around the interaction point which were designed to search for the Standard Model Higgs boson and new physics beyond Standard Model such as supersymmetry, dark matter, and extra dimensions; LHCb is designed for bottom quark physics studies in terms of precision measurements of CP violation as well as some new physics searches; and Alice is targeting at heavy-ion collisions for the quark-gluon plasma study.

At each collision point the control of the magnetic system allows to bend the path of the proton beams to collide them (dipole magnets), and squeeze the proton beams (quadrupole magnets) to increase the absolute *luminosity*, noted as L (in $cm^{-2}s^{-1}$). The absolute luminosity allows to characterize the number of collisions per second, namely the interaction rate R:

$$R = \sigma \times L, \tag{4.1}$$

where σ is the cross-section. The luminosity can be given as [63]:

$$L = \frac{N^2 k_b f_{rev} \gamma F}{4\pi \varepsilon_n \beta^*}. \tag{4.2}$$

In the numerator, N is the number of particles contained per bunch, k_b is number of bunches,

γ is the usual relativistic factor, f_{rev} refers to the accelerator revolution frequency, and F is the geometric luminosity reduction factor due to the crossing angle at the interaction point. In the denominator, ε_n is the normalized emittance giving a measure of the spread of the beam in transverse phase space and β^* parameterizes the squeeze process at the interaction point (IP) which is proportional to the square root of the beam size. The value of these performance related parameters during the LHC operations from 2011 to 2012 can be found in Table 4.1 where they are compared to the design values.

The integral luminosity, $\int L\mathrm{d}t$, has inverse unit of cross-section, and is often used at the LHC to characterize the size of the collected data. Considering the limitation of increasing the number of protons per bunch and the numbers of bunches per ring, the LHC is designed to run at a maximum luminosity of $10^{34}\,\mathrm{cm}^{-2}\mathrm{s}^{-1}$.

Parameter	2011	2012	Design
β^* [m]	1.5	0.6	0.55
Bunch interval [ns]	50	50	25
Number of bunches	1380	1380	2808
Max. protons per bunch	1.45×10^{11}	1.7×10^{11}	1.15×10^{11}
Normalized emittance at start of fill [mm.mrad]	2.4	2.5	3.75

Table 4.1 An overview of the performance related parameters during LHC operations from 2011 to 2012, compared to the design values [64].

Another obstacle to the increase of luminosity is the pile-up which will change with the number of protons per bunch or the bunch interval. Within one bunch crossing, multiple secondary 'soft' interactions can occur, which is counted as the *in-time pile-up* and can pollute the interesting interaction for analyses. Another type of pile-up comes from collisions of previous bunch crossings, which add on top of one another in the detector, due to the fact that the intervals between bunch crossings are shorter than the detector response time; this is called the *out-of-time pile-up*.

Collisions step by step

In terms of center-of-mass energy ($\sqrt{s}$) of proton-proton (p-p) collisions, the LHC has so far experienced 3 stages from 2009 to 2012: it started colliding proton beams at $\sqrt{s} =$ 900 GeV in late November 2009; its center-of-mass energy rose up to 7 TeV in 2010 and 2011, and finally reached 8 TeV in 2012. The relevant instantaneous luminosity evolution along time from 2010 to 2012 is shown in Figure 4.2 (bottom). The number of colliding bunches in ATLAS is also shown in this figure (top).

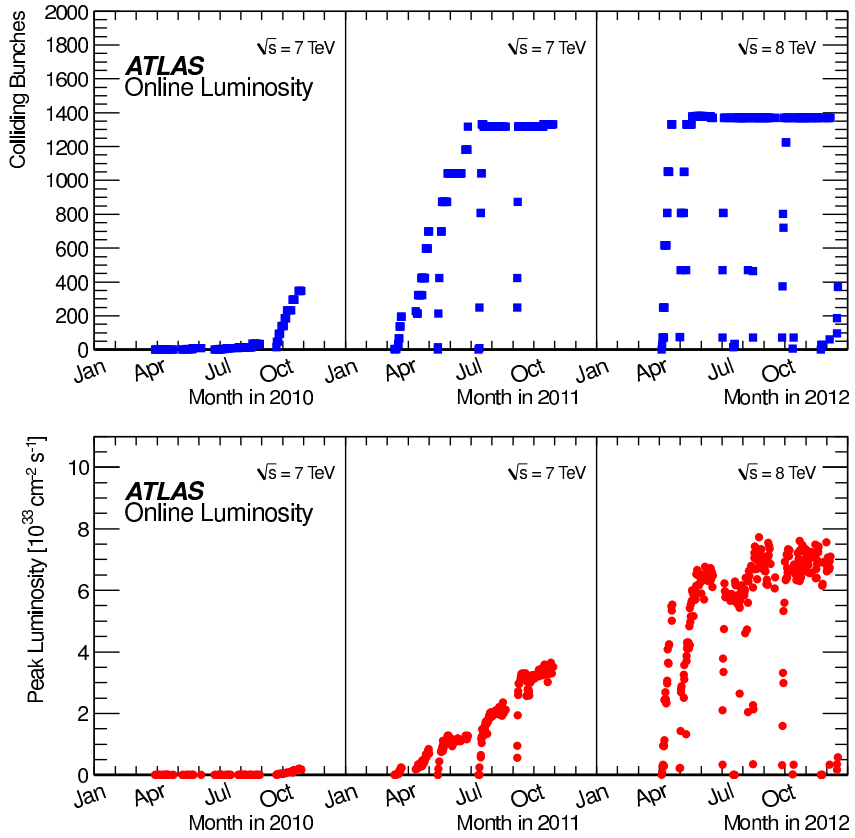

Fig. 4.2 The number of colliding bunches in ATLAS (top) and the peak instantaneous luminosity delivered to ATLAS per day (bottom), versus time during the p-p runs of 2010, 2011 and 2012 [65].

The cumulative integrated luminosity versus time from 2011 to 2012 is shown in Figure 4.3. Three categories are shown: the delivered luminosity from the LHC, the luminosity recorded by ATLAS, and the luminosity corresponding to the data which is of good quality to be used for analyses.

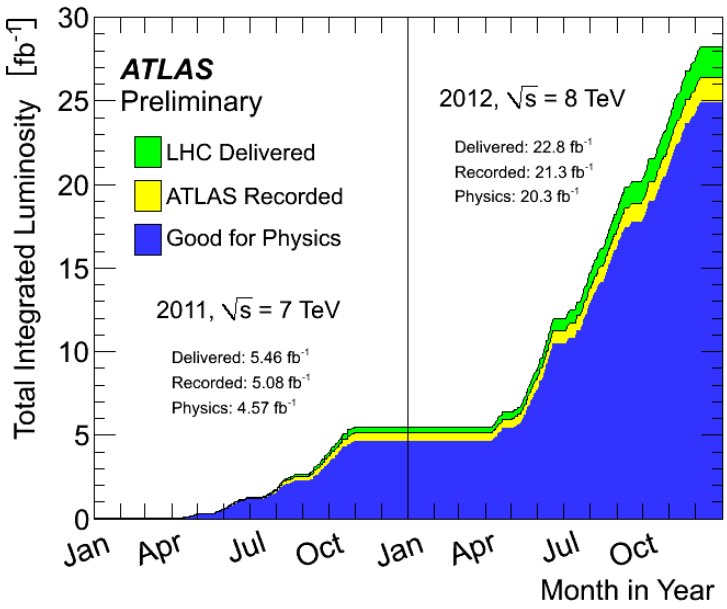

Fig. 4.3 Cumulative luminosity versus time from 2011 to 2012. The delivered luminosity (green) accounts for all the luminosity the LHC delivered to ATLAS, while ATLAS only records a subset shown as the yellow area. The luminosity finally used by physics analysis (blue) refers to that recorded when the ATLAS detector is performing optimally [65].

The mean number of interactions per crossing, $\langle\mu\rangle$, corresponds to the mean of the Poisson distribution of the number of interactions per crossing, μ, calculated for each bunch, and μ is proportional to the instantaneous luminosity per bunch and the inelastic cross section. It is shown in Figure 4.4. The inelastic cross-section used to compute the μ for data collected at center-of-energy of 7 TeV and 8 TeV are 71.5 mb and 73.0 mb, respectively.

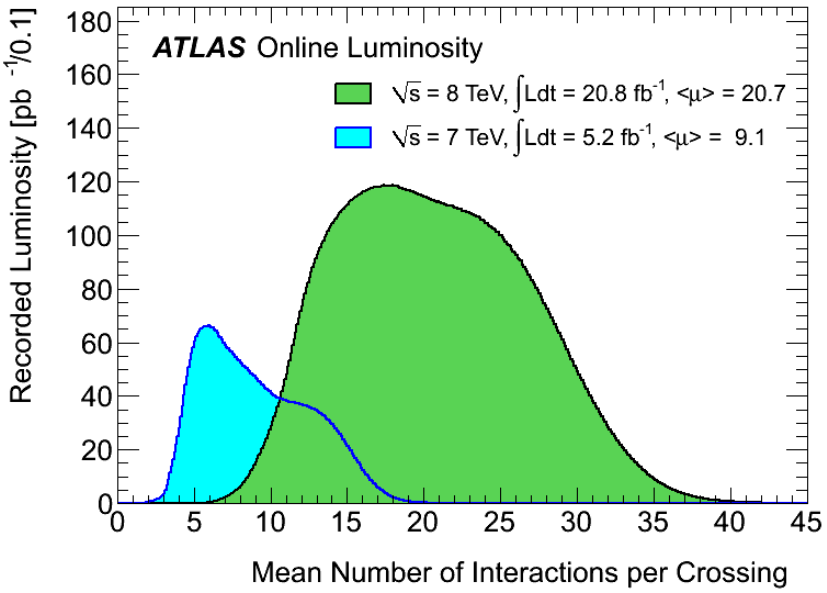

Fig. 4.4 Luminosity-weighted distribution of the mean number of interactions per crossing for the 2011 and 2012 data [65].

Chapter 5

The ATLAS detector

5.1 Introduction

The ATLAS experiment is a general-purpose particle detector installed at the LHC, which records collision events for various physics analyses. It is 46 m long, 25 m high, 25 m wide and weighs 7000 tons. It is operated by an international collaboration with thousands of scientists from all over the world: more than 3000 scientists from 174 institutes in 38 countries work on the ATLAS experiment.

The coordinate system of ATLAS

ATLAS describes collision events using right-handed spherical coordinates, with the origin defined as the nominal interaction point, the z-axis along the beam direction and the transverse x-y plane composed of the positive x-axis pointing at the center of the LHC ring and the positive y-axis pointing upwards. Therefore, a vector can be described using the azimuthal angle ϕ, the polar angle θ and the radius r, as shown in Figure 5.1.

Instead of using θ in the y-z plane, it is usual to take the *pseudorapidity* η defined as

$$\eta = -\ln\tan(\frac{\theta}{2}); \tag{5.1}$$

its absolute value varies from 0, corresponding to the vector being along the y-axis, to infinity, referring to the vector being along the z-axis. Using the pseudorapidity-azimuthal angle space, the distance ΔR between two objects can be defined using

$$\Delta R = \sqrt{\Delta\eta^2 + \Delta\phi^2}. \tag{5.2}$$

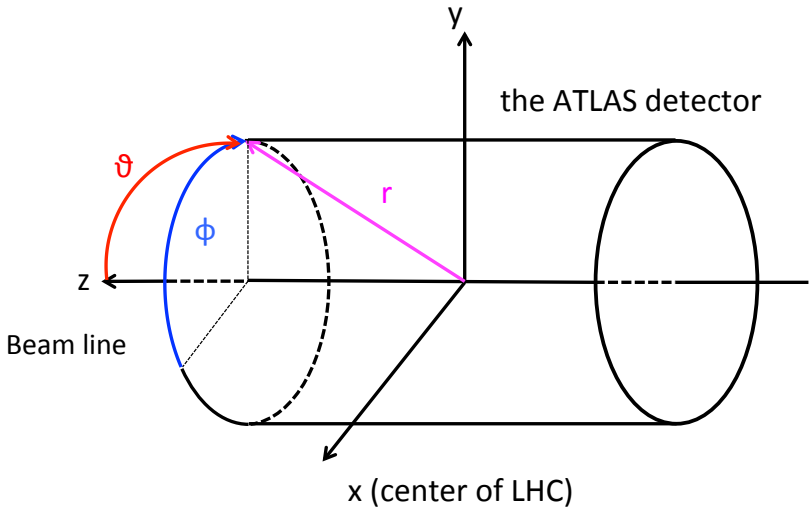

Fig. 5.1 The coordinate system of ATLAS.

The hadron collisions at the LHC are in fact parton collisions. The partons carry a fraction of the hadron's momentum which can not be evaluated on a collision-by-collision basis. Given the initial momentum in the transverse x-y plane is zero, the transverse missing energy $E_{\mathrm{T}}^{\mathrm{miss}}$ is defined in this plane and the transverse momentum p_{T}, and the transverse energy E_{T}, which are more often used in analyses.

The layout of the ATLAS detector

The overall layout of the ATLAS detector is illustrated in a cut-away view in Figure 5.2. It is built with a cylindrical symmetry around the interaction point; it is geometrically divided into a *barrel* region (low η region), two *end-cap* regions (medium η region), and two *forward* regions (high η region). The ATLAS detector is a laterally symmetric detector centered on the interaction point.

The full detector is made up of a chain of sub-detectors, that are designed to identify and record the particles coming out of the proton-proton collisions. From inwards to outwards, these sub-detectors form three systems: the **inner detector** (ID), the **calorimeters** and the **muon spectrometer**. Besides, a central solenoid surrounds the ID to provide a 2 T magnetic field, whilst toroids support magnetic fields of approximately 0.5 T and 1 T in the barrel and end-caps sections of the muon spectrometer.

Particles produced from the proton-proton collisions firstly arrive in the inner detector which covers the region of $|\eta| < 2.5$. The charged particles will interact with different layers of the detector and form discrete hits which will be used to reconstruct their trajectory.

The momenta and charge of these charged particles can be measured, as their trajectories

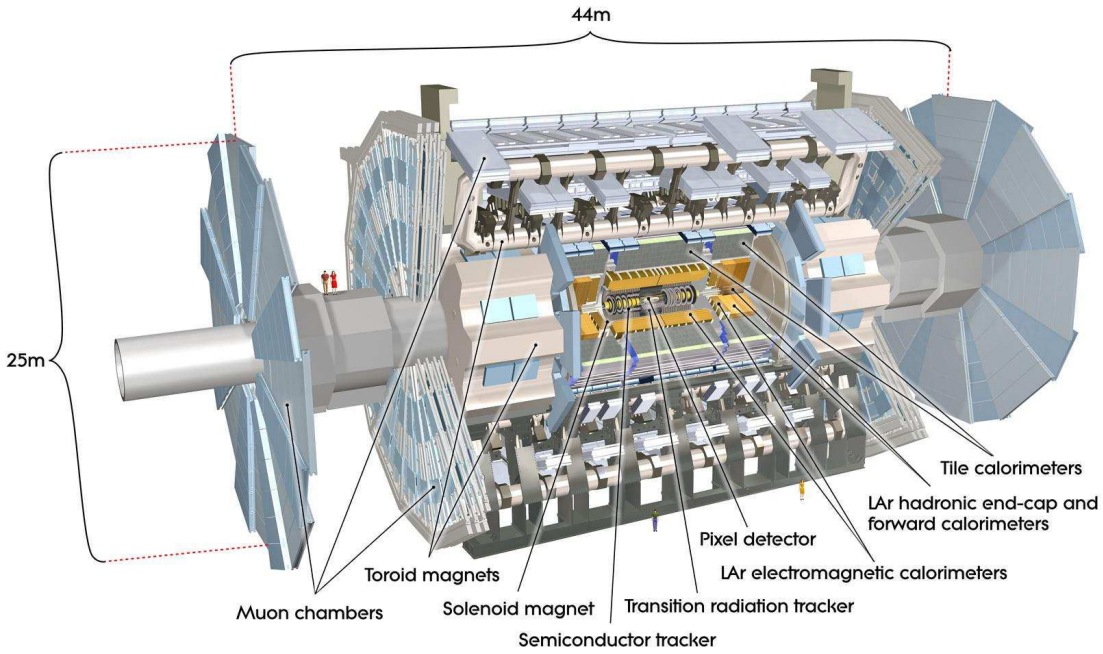

Fig. 5.2 An overall layout of the ATLAS detector [66].

are bent by the 2 T magnetic field provided by the central solenoid. As the innermost layer of ATLAS, the ID provides essential information, such as the recognition of first and second vertices. The ID is therefore designed to have a high granularity with intrinsic accuracy varying from $\sim O(10)$ micrometers to $\sim O(100)$ micrometers and a high momentum measurement resolution which is measured as $\sigma_{p_{\mathrm{T}}}/p_{\mathrm{T}} = (4.83 \pm 0.16) \times 10^{-4}\ \mathrm{GeV}^{-1} \times p_{\mathrm{T}}$ [67]. In order to meet the performance requirement, semiconductor detectors are used for precise measurement close to the beam (the *pixel detector* and the *semiconductor tracker*); and a noble gas detector is used in the outer layer (the *transition-radiation tracker*), as shown in Figure 5.2.

Further away from the collision point are the calorimeters, composed of the *hadronic calorimeters* and the *electromagnetic calorimeters*, which are designed to identify hadrons or electron/photon respectively and measure their energy and coordinates. The incident particles can interact with the instrumented material of the calorimeters via electromagnetic or strong processes, and produce a shower of secondary particles. The energy information will eventually be recorded by collecting the charge or the light produced by the shower. The position information is obtained by segmenting the calorimeters longitudinally and laterally. Sampling calorimeters are composed of an absorber made of dense material to develop the shower, and of an active medium to develop the signal.

The calorimeters will not stop muons as they interact very little with the calorimeter absorber. Muons will pass through the full detector and arrive in the outermost layer of the ATLAS detector, which is the muon spectrometer designed to record and identify the muons. The muon spectrometer contains four types of muon chambers: two types of precision tracking chambers providing position and momentum measurement, and two types of trigger chambers to provide fast and robust information for the hardware-based trigger decision making.

Figure 5.3 illustrates the detector response to different particles, using a transverse section view of the ATLAS detector.

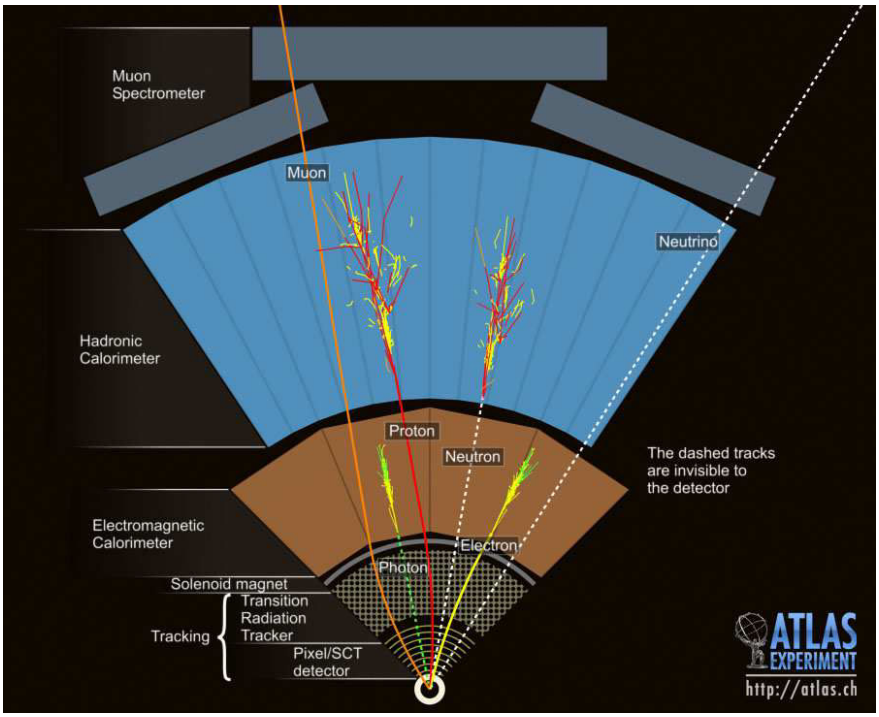

Fig. 5.3 A sector view in the transverse plane of the ATLAS detector, which illustrates how the different particles interact with the detector [68].

5.2 Inner detector

The ID is placed closest to the beam line, therefore its design must allow excellent radiation hardness and long-term stability in addition to ensure adequate performance. The full ID is a cylinder of 6.2 m long and 2.1 m diameter with coverage of $|\eta| < 2.5$, and is segmented into cylindrical layers in the barrel region, and coaxial disks in the end-cap regions, as shown in Figure 5.4. The structural arrangement of the layers of the ID in

the barrel region is shown in Figure 5.5, whilst one end-cap side of the ID is illustrated in Figure 5.6. The basic geometrical parameters of each layer are also given in these two figures.

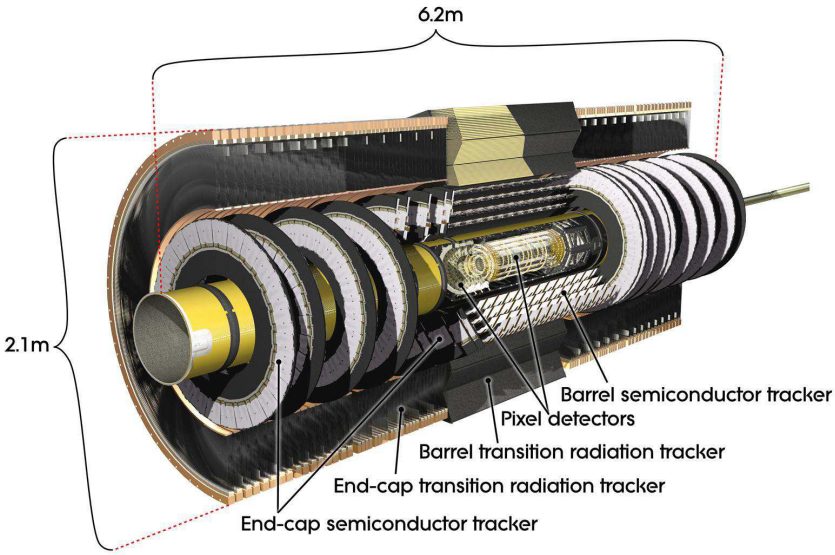

Fig. 5.4 A cut-away view of the ATLAS inner detector [66].

The main parameters of each sub-detector are summarized in Table 5.1, including the η coverage, the number of layers/disks/tubes, the number of hits left per track, the dimension of the basic element and the hit resolution.

	Hits/track	Element size	Hit resolution [μm]
Pixel, $\lvert\eta\rvert < 2.5$ 3 barrel layers 2×3 end-cap disks	3	$50 \times 400\,\mu\text{m}^2$	$10(R-\phi)$, 115 (z) $10(R-\phi)$, 115 (R)
SCT, $\lvert\eta\rvert < 2.5$ 4 barrel layers 2×9 end-cap disks	8	$80\,\mu\text{m}$	$17(R-\phi)$, 580 (z) $17(R-\phi)$, 580 (R)
TRT, $\lvert\eta\rvert < 2.0$ 73 barrel tubes 160 end-cap tubes	~ 30	d=4 mm, l=144 cm d=4 mm, l=37 cm	130/straw

Table 5.1 Summary of the characteristics for each sub-detector of the inner detector [69].

Pixel Detector: In order to have good vertex performance, the pixel detector is designed to have the finest granularity, as shown in Table 5.1. The element size shown in the table is the minimal size of the pixel, 47232 of which build up one pixel detector. The first layer

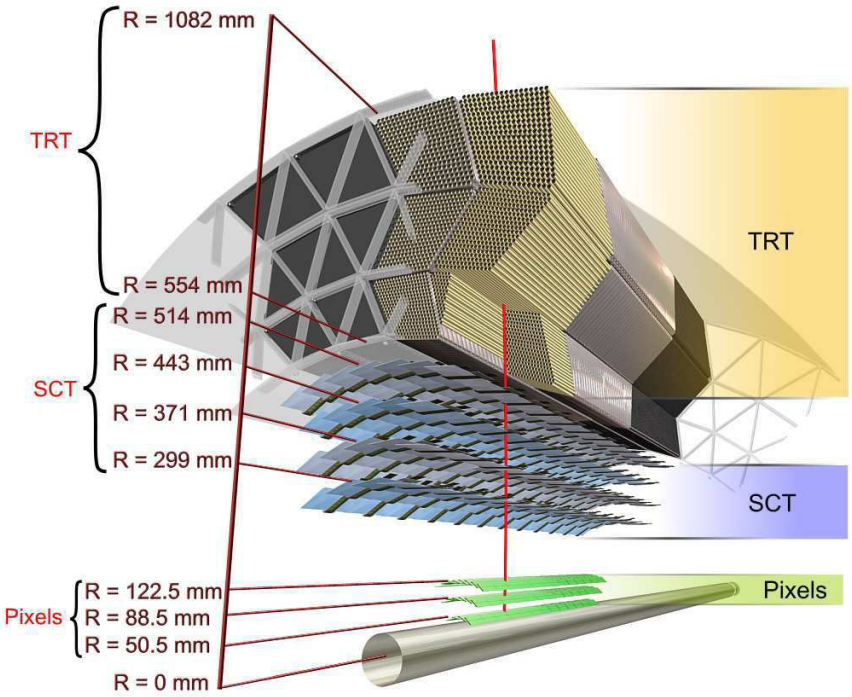

Fig. 5.5 A three-dimensional drawing illustrating the structural arrangement of the ID layers in the barrel region, with their radii [66].

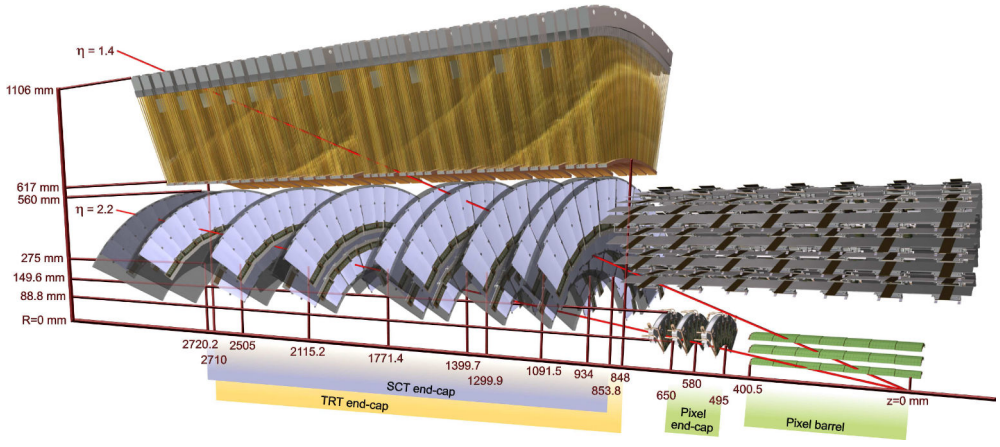

Fig. 5.6 A three-dimensional drawing illustrating the structural arrangement of the ID layers in one end-cap region, with their radii and z-axial distance (using the detector center as origin) [66].

of the pixel detector in the barrel region is known as the "B-layer" since it contributes to the secondary vertex measurement performance, for reconstruction of τ leptons and bottom quarks. As the first element facing the collision point, the B-layer has to be replaced after a few years operation at the designed luminosity of $10^{34}\,\mathrm{cm}^{-2}\mathrm{s}^{-1}$.

Semiconductor Tracker: In each SCT layer, it has two sets of SCT strips. In order to measure both lateral and longitudinal coordinates, the two sets of strips are glued back-to-back with an angle of 40 mrad in between, i.e. one set is either parallel, or perpendicular to the beam line.

Transition Radiation Tracker: The TRT detector is packaged in straw tubes made of polyamide, and uses a Xenon-based (70%) gas mixture with CO_2 (27%) and O_2 (3%). It measures only one coordinate with $z-$axis or radius information missing in barrel or end-caps due to their axial or radial placement. The TRT occupies the largest space of the ID and provides the majority of hits per track, and hence it contributes most to the momentum measurement. Although the TRT has lower precision compared to the silicon precision detectors, it offers longer measurements of tracks to retrieve the momentum information.

The tracks left by the charged particle in the ID can be reconstructed using two main algorithms. One is the baseline inside-out algorithm designed for the reconstruction of primary tracks left by the charged particles originating from the p-p collisions. It starts from three point seeds from the silicon detectors (both Pixel and SCT), and adds the successive hits using a combinatorial Kalman-fitter [70]. The other algorithm is the outside-in algorithm which is designed for the reconstruction of the secondary tracks orginating from secondary particles in decays of primary or other secondary particles in the ID. The outside-in algorithm extends the reconstructed TRT segment [70] by adding the silicon hits with the combinatorial Kalman-fitter as the inside-out does. The TRT segments which do not have any extension in the silicon detectors will be reconstructed as the TRT standalone tracks. The reconstruction efficiency of a track can be measured in simulated events by taking the ratio of the tracks matched to charged particles to the number of generated charged particles; the efficiency varies as a function of p_{T} and η. For example, for primary tracks with $p_{\mathrm{T}} = 10$ GeV, the efficiency is 92% when averaged over η [71].

The primary vertices are reconstructed from the reconstructed tracks using specific finding algorithm with a χ^2 fit [72]. For a single interaction with at least two primary tracks, the vertex reconstruction efficiency is rather high at around 90% [71].

5.3 Calorimeters

The calorimeters should contain the showers initiated by the incident particles and have good segmentation for space-point measurements. Besides, the calorimeters must have sufficient coverage for both η and ϕ to be able to measure well the total energy. The design of the ATLAS calorimeters thus includes an overall pseudorapidity up to $|\eta| = 4.9$, and a full ϕ coverage without cracks around the beam line. The overall layout of the calorimeters in ATLAS is shown in Figure 5.7.

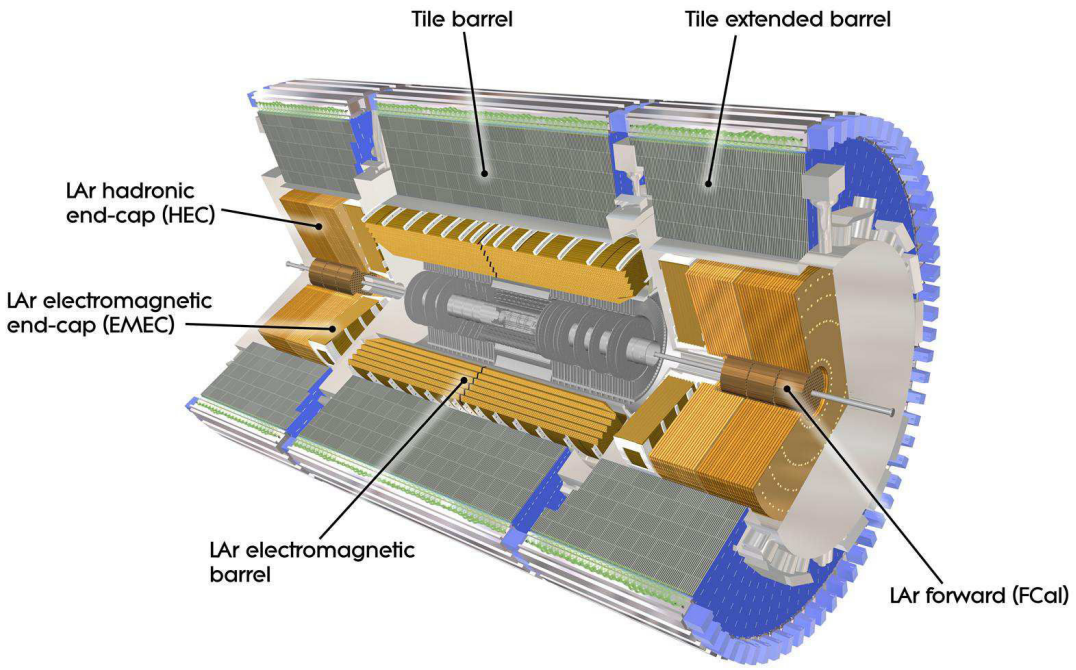

Fig. 5.7 A cut-away view of the ATLAS calorimeter system [66].

The inner part of the calorimeter system is composed of *LAr electromagnetic calorimeters* (EM Calo), in the barrel (EMB), the end-cap (EMEC) and the forward (FCal) regions. The hadrons not stopped in the EM Calo will reach the hadronic calorimeters, consisting of *tile calorimeters* in the barrel and extended barrel regions, the *liquid argon (LAr) hadronic end-cap calorimeter* (HEC) and the *LAr forward calorimeters* (FCal).

The full calorimeter system must provide a good hermeticity to fully contain the electromagnetic and hadronic showers. The total depth of the material up to the end of the calorimeter in ALTAS is shown in unit of interaction length as a function of $|\eta|$ in Figure 5.8, where the amount of material before the first active layer of the muon system (up to $|\eta| < 3.0$) is also given.

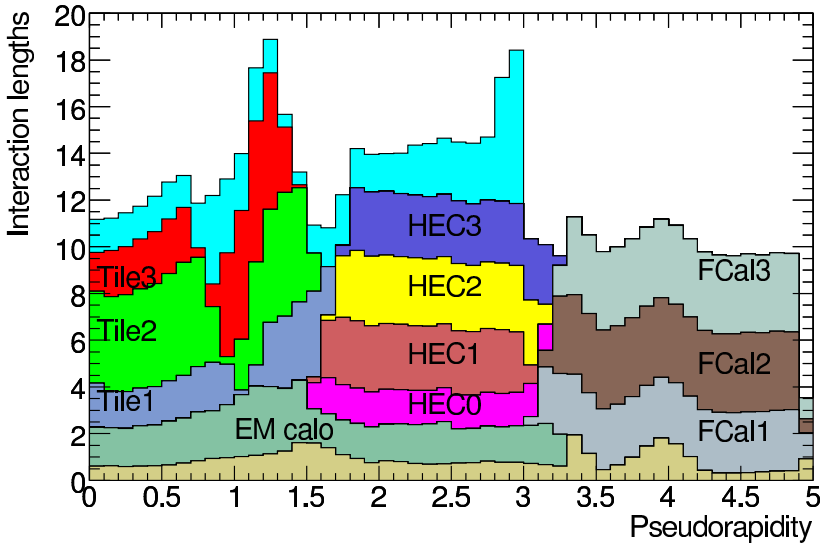

Fig. 5.8 The total depth of the material in front of the EM Calo, of the EM Calo itself, of each hadronic layer and of the cumulative amount of material between the outmost hadronic layer and the first active layer of the muon spectrometer up to $|\eta| < 3.0$ [66]. It is shown in unit of interaction length as a function of $|\eta|$.

The ATLAS calorimeters are sampling calorimeters using different absorber (lead, copper or iron) and media (plastic scintillator or liquid argon), and the resolution of sampling calorimeters can be written as:

$$\frac{\sigma_E}{E} = \frac{a}{\sqrt{E}} \oplus \frac{b}{E} \oplus c. \tag{5.3}$$

The first term is called the *stochastic (sampling) term*, coming from the fact that the secondary particle shower has intrinsic fluctuations due to the interleaved layers of the absorber and the active medium. The second term is known as the *noise term* which mainly comes from the electronic noise of the readout channels. The last *constant term* depends mainly on the detector mechanics and readout system, besides, it can be affected by the temperature gradients, detector aging and radiation damage.

The electromagnetic calorimeter is measured to have a resolution of $\sigma_E/E = 10\%/\sqrt{E} \oplus (1.2 \pm 0.1^{+0.5}_{-0.6})\%$ [73] in the barrel region, while the resolution for the hadronic calorimeter in barrel and end-caps is measured varying from 0.13 to 0.06 [74] when jet (LCW+JES calibration) p_{T} increases; the FCal for electromagnetic measurements is measured to have $\sigma_E/E = 100\%/\sqrt{E} \oplus (2.5 \pm 0.4^{+1.0}_{-1.5})\%$ [66, 73].

5.3.1 Electromagnetic calorimeter

The EM Calo is a LAr sampling calorimeter. LAr was chosen as the active medium for its stability of the response over time and its intrinsic radiation-hardness. The EM Calo is arranged into three cylindrical layers of EMB and two co-axial wheels for each EMEC, covering a pseudorapidity up to $|\eta| = 3.2$. Lead was chosen as absorber for EMB and EMEC for its short radiation length (X_0), which enables the calorimeter to have a compact size while containing the showers.

The lead plates and the copper electrodes are all shaped in an *accordion* geometry, as shown in Figure 5.9, which allows the EM Calo to have a full ϕ coverage measurement. The EM Calo is divided into three layers in depth perpendicular to the beam axis; they differ in terms of radiation length and resolution ($\Delta\phi \times \Delta\eta$) in the $\phi - \eta$ plane. Besides, another single thin liquid argon layer of 11 mm, the presampler, provides measurement of the energy loss before the EM Calo.

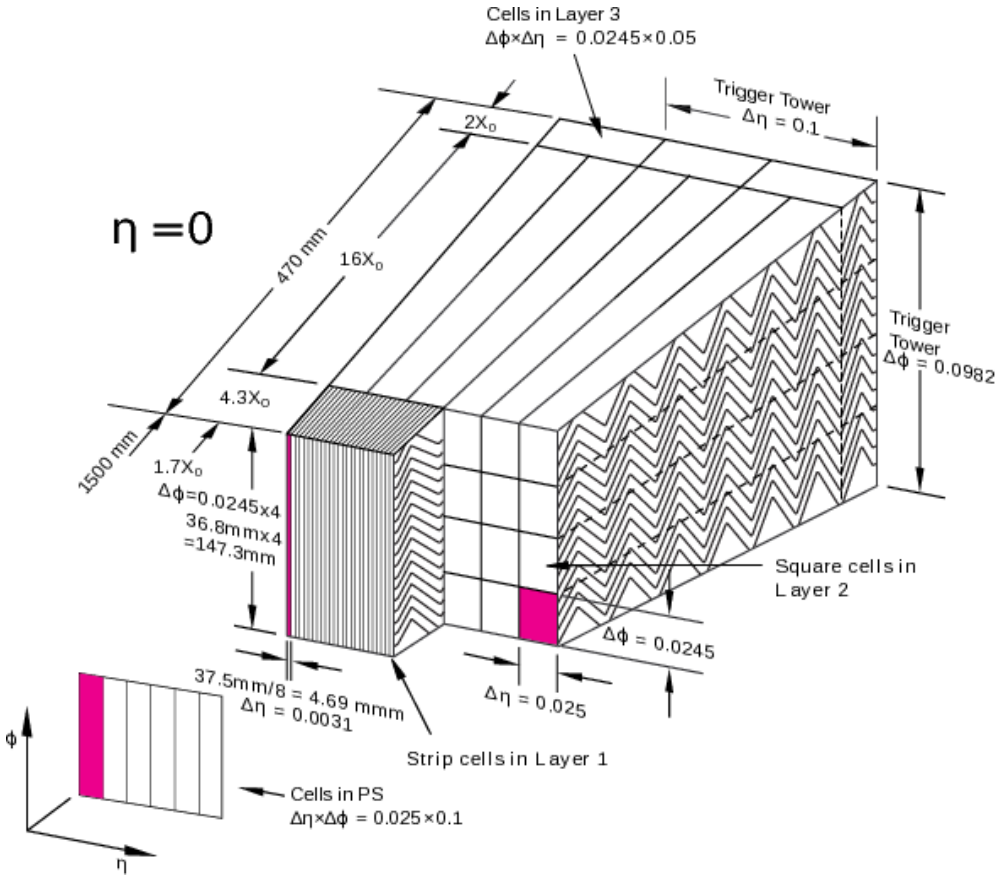

Fig. 5.9 A sketch of a barrel module of the electromagnetic calorimeter illustrating the different layers [66].

Figure 5.9 summarizes the geometry of a barrel module, showing the three accordion

layers and the presampler:

Presampler It is segmented in the $\phi - \eta$ plane with identical resolution of $\Delta\eta \times \Delta\phi = 0.025 \times 0.1$ for all its coverage of $0 < |\eta| < 1.8$.

1st layer This layer is the closest layer to the interaction point after the presampler. It is arranged in strip cells of approximately $\Delta\eta \times \Delta\phi = (0.025/8) \times (0.0245 \times 4)$ in size. It has a relative short depth of $4.3X_0$.

2nd layer It is the largest layer, with $16X_0$ deep, in which the incident particles deposit most of their energy. Electrons and photons are mainly reconstructed from the energy deposited (clusters) in this layer. The second layer is segmented into square cells of $\Delta\eta \times \Delta\phi = 0.025 \times 0.0245$. Combined with the first layer, it can provide a good separation of photons from π^0.

3rd layer As most electrons and photons are absorbed in the second layer, the third layer has a short depth of $2X_0$. Cells in the third layer have a coarse granularity of $\Delta\eta \times \Delta\phi = 0.05 \times 0.0245$ as it only contains the tail of the EM shower. Only the EMB and part of the EMEC outer wheel ($1.5 < |\eta| < 2.5$) are equipped with a third layer.

The total thickness of accordion layers in the barrel region ($0 < |\eta| < 1.475$) is over $22\,\mathrm{X}_0$. The cumulative amount of material in front of the presampler and in front of the accordion layers is shown in Figure 5.10. This material will have an impact on the reconstruction of some physics objects, such as the photons, as will be discussed in Section 7.1.

The η coverage and the dominant granularity of each layer within the EMB and EMEC calorimeters are summarized in Table 5.2. The 1st and 2nd layers get coarser granularities for regions where the presampler is not installed or instrumental transition regions between EMB and EMEC or between EMEC and FCal1. In this case, only the best granularities of the 1st and 2nd samples are shown in the table.

Finally, the first layer of the forward LAr calorimeter (FCal1) uses copper as the absorber and can be used to measure electromagnetic showers; the FCAL will be described in the next section.

5.3.2 Hadronic calorimeters

Tile calorimeter The tile calorimeter is longitudinally segmented into three layers with different granularities as shown in Table 5.3. It uses steel as absorber and scintillator as the active medium in which the hadronic shower's energy information will be converted into photons collected by photo-multiplier tubes. It covers up to $|\eta| = 1.0$ in the barrel region,

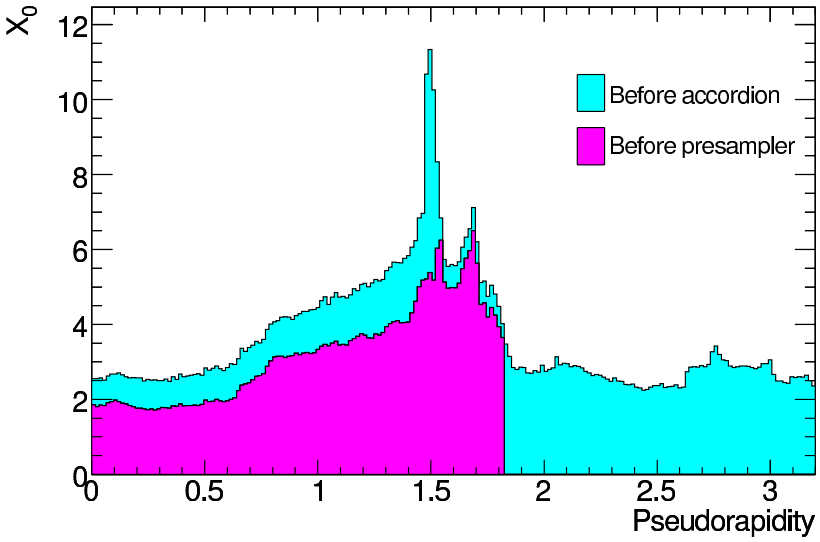

Fig. 5.10 The cumulative amount of material in unit of radiation length X_0 as a function of pseudorapidity η in front of the electromagnetic calorimeter [66].

		Presampler	Layer 1st	Layer 2nd	Layer 3rd
EMB	Coverage	$\lvert\eta\rvert < 1.52$	$0 < \lvert\eta\rvert < 1.475$		$0 < \lvert\eta\rvert < 1.35$
	Granularity ($\Delta\eta \times \Delta\phi$)	0.025×0.1	$0.025/8 \times 0.1$	0.025×0.025	0.05×0.25
EMEC	Coverage	$1.5 < \lvert\eta\rvert < 1.8$	$1.375 < \lvert\eta\rvert < 3.2$		$1.5 < \lvert\eta\rvert < 2.5$
	Granularity ($\Delta\eta \times \Delta\phi$)	0.025×0.1	$0.025/8 \times 0.1$	0.025×0.025	0.05×0.25

Table 5.2 A list of the main parameters of the EMB and EMEC calorimeters [66]. The granularities of the 1st and 2nd layers are varied with η, as shown in Reference [66], therefore only the best values are shown here.

and from $|\eta| = 0.8$ to $|\eta| = 1.7$ in two extended barrel regions. Radially, it is placed between 2.28m and 4.25m.

LAr hadronic end-cap calorimeter The hadronic end-cap calorimeter (HEC) is a liquid argon sampling calorimeter with copper as absorber. It covers the region of $1.5 < |\eta| < 3.2$, with a relatively fine granularity of $\Delta\eta \times \Delta\phi = 0.1 \times 0.1$ which decreases to 0.2×0.2 for $|\eta| > 2.5$. It is formed of two wheels at each end-cap, and each wheel is divided into two sections in depth, that form four layers in total for each end-cap. Its main parameters are summarized in Table 5.3.

LAr forward calorimeter The forward calorimeter is composed of three layers for each side, with liquid argon as active medium because of the high radiation environment in the

forward regions. All three FCal layers form an overall coverage of $3.1 < |\eta| < 4.9$, see its layout in Figure 5.7. The first layer next to the interaction point is the electromagnetic forward calorimeter (FCal1) which uses copper as absorber to optimize the resolution, followed by the two hadronic forward LAr calorimeters, FCal2 and FCal3, which use tungsten to develop the showers. The forward calorimeter helps providing good $E_{\mathrm{T}}^{\mathrm{miss}}$ measurement by extending the η-coverage of the whole calorimeter system,

5.4 Muon system

The muon system is the outermost layer of ATLAS. It is designed to measure the momentum of muons in $|\eta| < 2.7$. It contains a muon spectrometer and a toroid magnet system which consists in three large superconducting air-core toroid magnets. In addition to tracking the muons, the muon system contains trigger chambers with timing resolution of the order of 1.5-4 ns.

The layout of the ATLAS muon system is shown in Figure 5.11. It is composed of various gas detectors: Monitored drift tubes (MDT's), Cathode strip chambers (CSC's), Resistive plate chambers (RPC's) and thin gap chambers (TGC's). The four components can be classified by function into precision tracking chambers and trigger chambers. In the barrel region, the chambers form layers in cylinders that are placed at radii of approximately 5m, 7.5m and 10m, and in the transitions and end-caps they are formed in wheels at a distance from the interaction point of approximately 7.4m, 10.8m, 14m and 21.5m.

Precision tracking chambers The precision tracking measurement by the muon system combines the output of the MDT chambers and the CSC chambers.

The MDT chambers are made up of aluminum tubes placed transverse to the beam axis, and filled with mixed Ar/CO_2 gas. They are designed to provide precision measurement of hit over $|\eta| < 2.0$ with resolution of approximately $80\,\mu$m in $r-\phi$. There are 1150 MDT chambers in total, and they are arranged in cylindrical layers in the barrel region and end-cap

	Tile	**HEC**
Coverage	$\|\eta\| < 1.0$ barrel $0.8 < \|\eta\| < 1.7$ extended barrel	$1.5 < \|\eta\| < 3.2$
Longitudinal segmentation	3 layers	4 layers
Lateral($\Delta\eta \times \Delta\phi$) granularity	Layers 1&2, 0.1×0.1 layer 3, 0.2×0.1	$1.5 < \|\eta\| < 2.5$, 0.1×0.1 $2.5 < \|\eta\| < 3.2$, 0.2×0.2

Table 5.3 The main parameters of the Tile calorimeter and HEC.

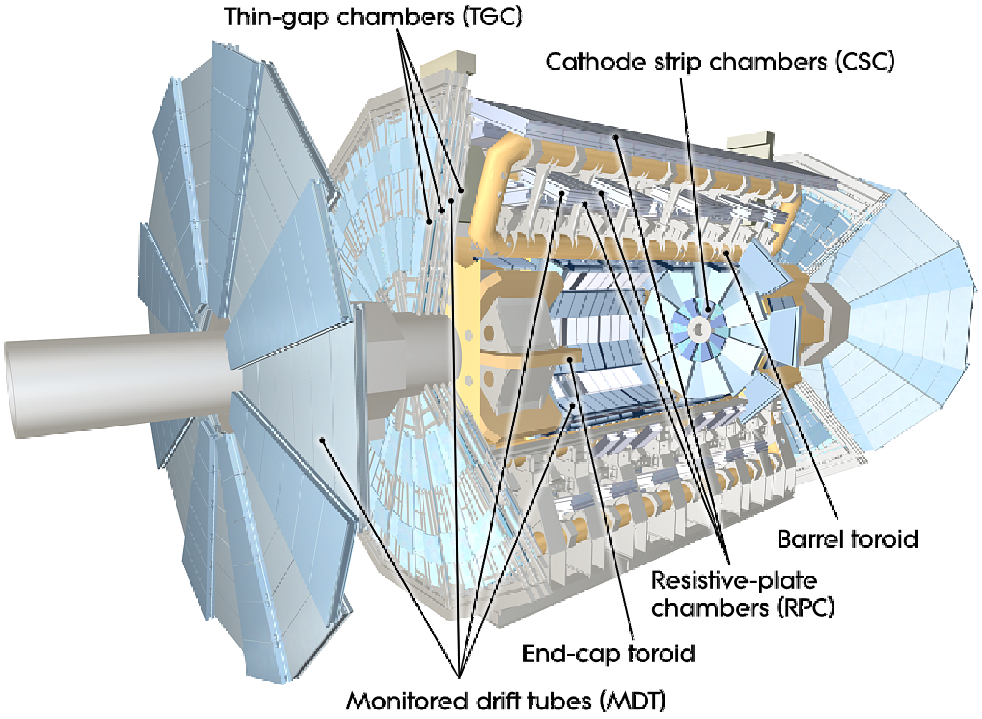

Fig. 5.11 A cut-away view of the ATLAS muon system [66].

wheels as shown in Figure 5.11.

The CSC's are filled with mixed Ar/CO_2 gas and the basic element is a plane of perpendicular cathodes strips with multiple anode wires. They are placed in the region $2.0 < |\eta| < 2.7$, forming the two innermost wheels in the end-cap region, as shown in Figure 5.11. Each wheel contains four small and four large chambers which comprise four CSC's planes each, leading to four independent measurements on both coordinates (ϕ, η) per track. The CSC's provide a resolution of $\sim 60\,\mu$m in $r-\phi$ per CSC plane.

Trigger chambers The trigger chambers of the muon system are composed of RPC's in the barrel region ($|\eta| < 1.05$) and TGC's in the end-caps ($1.05 < |\eta| < 2.7$). They are designed to provide fast muon information for Level 1 trigger determination, as well as timing information for bunch-crossing identification, within $|\eta| < 2.4$. In addition, the trigger chambers provide a second coordinate measurement complementary to the MDT's up to $|\eta| = 2.7$.

The RPC is made of parallel electrode plates separated by a 2 mm gap filled with mixture of $C_2H_2F_4$, isobutane and SF_6. The RPC's are constructed into three barrel layers: the two inner layers (RPC1 and RPC2) enable the trigger to select low-p_T tracks of 6–9 GeV, and the outer layer (RPC3) provides information for higher momentum tracks of 9–35 GeV for the trigger. All three layers are placed next to the MDT barrel layers in order to provide the

second azimuthal coordinate to complement the MDT measurement, and it provides time measurement with a resolution of approximately 1.5 nanoseconds.

The other trigger chamber, TGC, is a multi-wire proportional chamber, with a gas mixture of CO_2 and n-pentane. It also helps providing coordinate measurement complementary to the MDT. Besides, it provides time measurement with a resolution of 4 nanoseconds.

To summarize, the whole muon system is designed to recognize muons within $|\eta| < 2.7$ with a threshold of $p_{\mathrm{T}} > \sim 3$ GeV, as lower–p_{T} muons will mostly loose their energy before entering the muons chambers. The muon spectrometer is measured to be able to provide stand-alone muon p_{T} resolution of approximately 20% at 1 TeV [75]. The magnetic field leads to a maximum accessible muon momenta determination of around 3 TeV. In addition to the momentum measurement, the muon system provides good position and charge measurements.

5.5 Trigger system

At the designed luminosity of $10^{34}\,\mathrm{cm}^{-2}\mathrm{s}^{-1}$, the rate of collisions is approximately 1 GHz. However, only ~ 300 Hz can be recorded due to limited resources. In order to effectively operate an online reduction of the data to be recorded, a multi-level trigger system is used, which is a chain of three levels of triggers: the Level-1 (L1), the Level-2 (L2) and the event-filter (EF) triggers. A schematic illustration of the trigger flow used in the ATLAS experiment is shown in Figure 5.12, with the event rate at each step.

The L1 triggers are hardware-based only, and they must take a decision in less than 2.5 microseconds using the information directly from customized front-end electronics, provided from the muon system and calorimeters only, with a relatively coarse resolution. The L1 triggers effectively reduce the data rate to 50 kHz. Before parsing events to next level trigger, Regions-of-Interest (RoI's) in (η, ϕ) are defined containing the potential particle candidates found by the L1 triggers.

The L2 and EF triggers make up the High-Level Trigger (HLT), which lowers the data recording rate to the objective of 300 Hz. Unlike the L1 triggers, the HLT takes full-granularity measurement from all detectors using algorithms running on computers, and thus the HLT operates slower than the L1 triggers. The L2 triggers use CPU farms to process data from RoI's, and it takes the L2 triggers an average of 40 milliseconds to lower the rate from ~ 50 kHz to ~ 5 kHz. As the last element of this trigger chain, the EF uses algorithms close to the offline ones, and operates on the complete information from events to reach the final data rate within one second in average.

The *trigger menu* contains a list of physics signatures (*trigger chains*), each of which

specifies the thresholds and selection criteria on selected physics objects implemented throughout the trigger system. The trigger chain names follow a given convention defined in ATLAS indicating the trigger level and the criteria, for example, the 'EF_g120_loose' trigger represents a HLT chain selecting events with at least one loose photon of $p_{\mathrm{T}} > 120$ GeV.

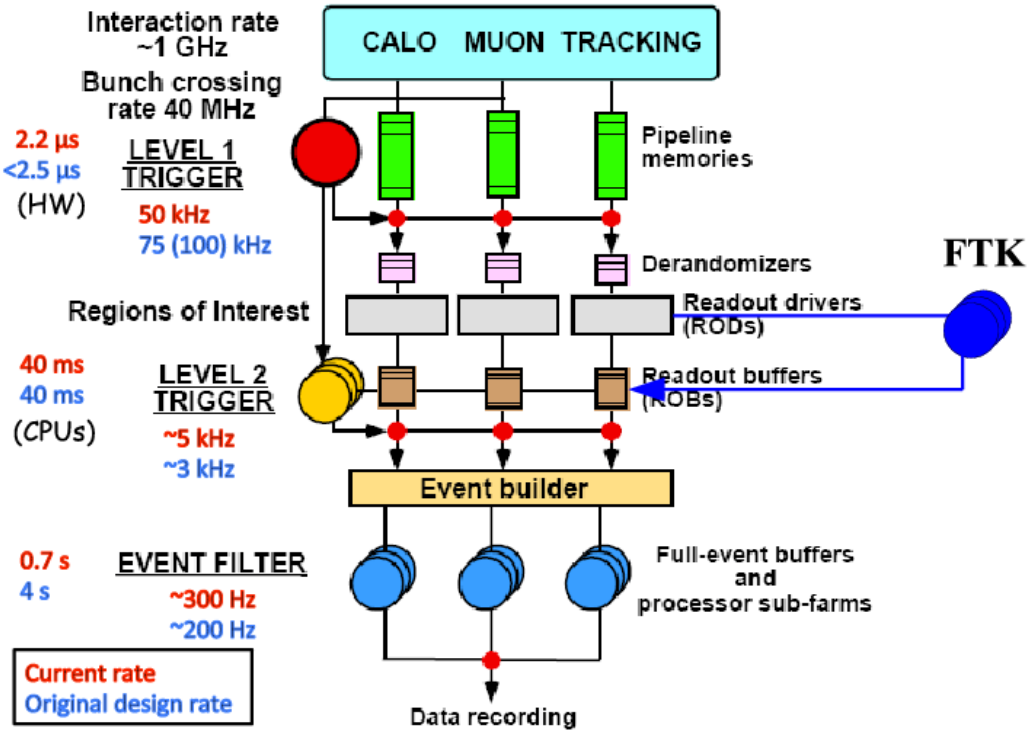

Fig. 5.12 The trigger system [76].

Chapter 6

Data preparation and simulation

6.1 Simulated data processing

The simulated data aims at providing a good description of given processes in a format similar to that of the real data taking from the ATLAS detector. A multi-step processing scheme is developed, which is conceptually illustrated in Figure 6.1. Each step is shown as an orange rectangle with its production output in a blue ellipse below, and the arrow indicates the sequence.

The first step in the full simulation chain is the **Generation**, producing physics objects with four-vectors from given physics processes, for example, a Z boson produced with a photon and its decay to two electrons, $Z(e\bar{e}) + \gamma$.

As the proton-proton collisions are in fact parton-parton collisions, the generation products depend on the parton momentum, which is however not accessible within the experiment. Many studies [78–80] were performed to give descriptions on the *parton distribution function* (PDF) which describe the probability density $xf(x,Q^2)$ as a function of the momentum portion x each parton carries at a given energy scale factor Q. Relevant theoretical parameters and the center-of-mass energy of the proton-proton collisions are parsed to the generator, and the cross-section can be computed by summing over all the possible Feynman diagrams of leading order (LO) or next-to-leading order (NLO) depending on the generator.

In the generation step, the following effects are also included: the cascades of radiation from the QCD processes, known as *parton shower*; the *hadronization* processes to form hadrons, and the *underlying event* (UE) coming from the interactions of the residual components of the two protons from one hard scattering event. In order to provide optimal MC description of the QCD processes, several simulation parameters sets, named 'tunes' [81], are developed by comparing relevant kinematic distributions to data, and are used with different generators.

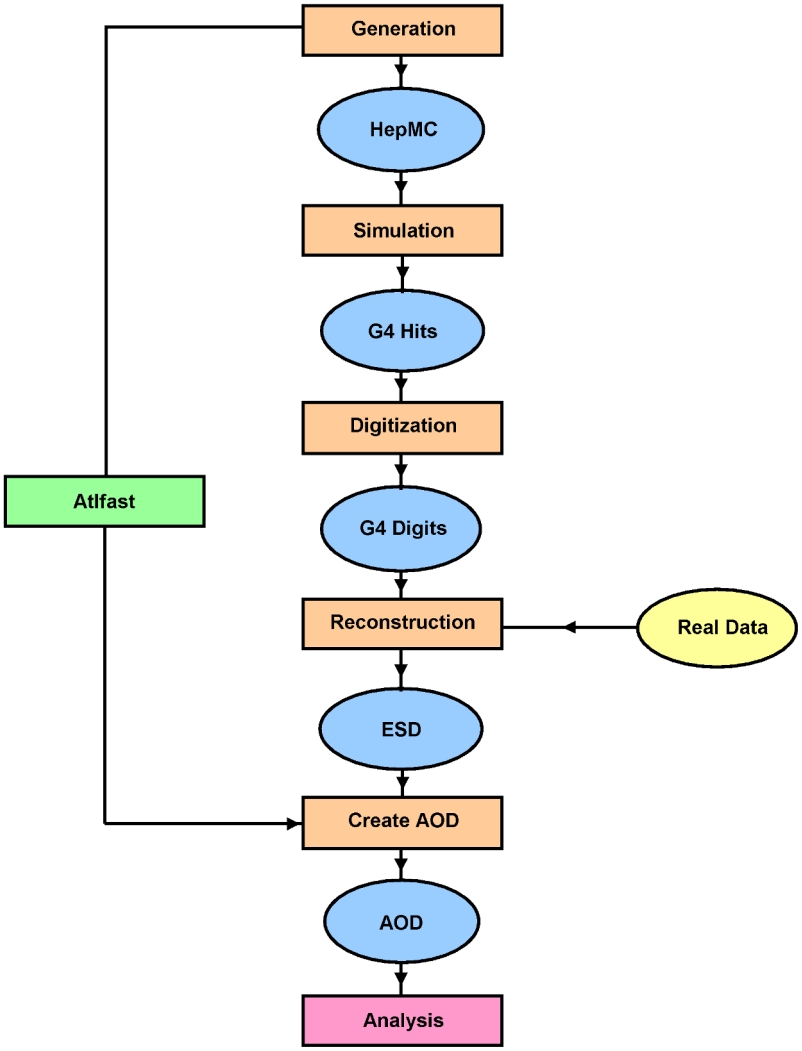

Fig. 6.1 The concept of the full simulation chain is shown in a schematic form [77].

The generation products will be parsed to the **Simulation** software to obtain the corresponding ATLAS detector responses, such as the tracking hits and the calorimeter showers. The simulation software used is `Geant4` [82], which uses as inputs a detailed ATLAS detector geometry and physics lists describing the possible interactions between incident particles and the detector materials. Since it needs a lot of time and resource to produce the full detector simulation, a fast simulation, known as `Atlfast` [83] was developed. It uses the full `Geant4` simulation of the tracker and the muon spectrometer, but a parameterized response for the calorimeters.

The **Digitization** transforms the simulated analog detector response (`Geant4` hits) to digits (`Geant4` digits). At digitization level, pile-up is added by overlaying *minimum bias* events generated with PYTHIA 8 [84] onto the hard-scattering process, according to the distribution of $\langle\mu\rangle$, see Figure 4.4.

The processing chains from the simulation and the real data now converge, and the next step for both is the **Reconstruction**, where physics objects will be identified and characterized using digitization outputs, see more details in Chapter 7. The reconstruction outputs are stored in the format of *Event Summary Data* (ESD), which contains information sufficient to identify particles, and apply fast tuning to the reconstruction algorithms and calibrations of physics objects.

In order to have a rather concise data format with sufficient information on reconstructed events for common analyses, one needs to transform the ESD into the *Analysis Object Data* (AOD).

The full data production scheme is summarized in Figure 6.1, and further details on the ATLAS simulation scheme are given in Reference [85].

6.2 Physics validation

The programs used in each procedure shown in Figure 6.1, are packaged into a software framework, ATHENA [86]. Modifications in the software of the generation, simulation, digitization, or reconstruction lead to a new ATHENA release tag.

Each new release version needs to be validated on physics variables at analysis level. A physics validation group in the ATLAS collaboration is organized to take care of such work, for changes related to the steps starting at simulation or after in the processing chain. This group is composed of people from the different combined performance (CP) groups, such as the Egamma group, and from physics analysis groups such as the supersymmetry (SUSY) working group.

The validation task is performed by comparing the validation samples, which are pro-

duced with un-validated new caches, to reference samples, which are processed with previously validated caches. For example, the new release version could include a geometry of the ATLAS detector with an added new pixel insertable B-layer (IBL), while the reference sample would be produced with the nominal ATLAS detector. In this case, it is expected at the analysis level that the b-jets differ in events between the validation and the reference samples, while other objects, such as non-tagged jets, leptons and photons, are not expected to be affected.

The author has been in charge of the physics validation for the SUSY working group for a year (2012–2013). Beside the normal validation tasks, since the validation code is built up within the ATHENA framework and the ATHENA release can be different from sample to sample, the validation work includes technical upgrades and maintenance of the code. The SUSY validation group is looking at ~ 400 hundreds of kinematic variables covering all objects which could be interesting in SUSY analyses, including jets, leptons, missing transverse energy or photons. In addition, cutflows of some SUSY analyses are checked.

As an example, one of the validation tasks performed was to check, for the Geant4 simulation, if a new description of the geometry of the pixel insertable B-layer (IBL) [87] installed in ATLAS for run-2 was behaving as expected. Figure 6.2 shows this validation example. In this figure, the test sample, with the updated IBL geometry description, was compared to the reference sample A, which used a previous IBL description, and to another reference sample B, which corresponded to the well-validated ATLAS run-1 geometry description. The test sample was an update to the description used in the reference sample A; the latter had been found to be problematic in an earlier validation task, as it led to unexpected differences in the photon energy resolution spectrum when comparing it to the reference sample B. Therefore, the test sample was expected to agree with the reference B but differ from the reference A for this variable, as shown in Figure 6.2. The test sample was found to be in good agreement with the reference sample B, validating the geometry description update.

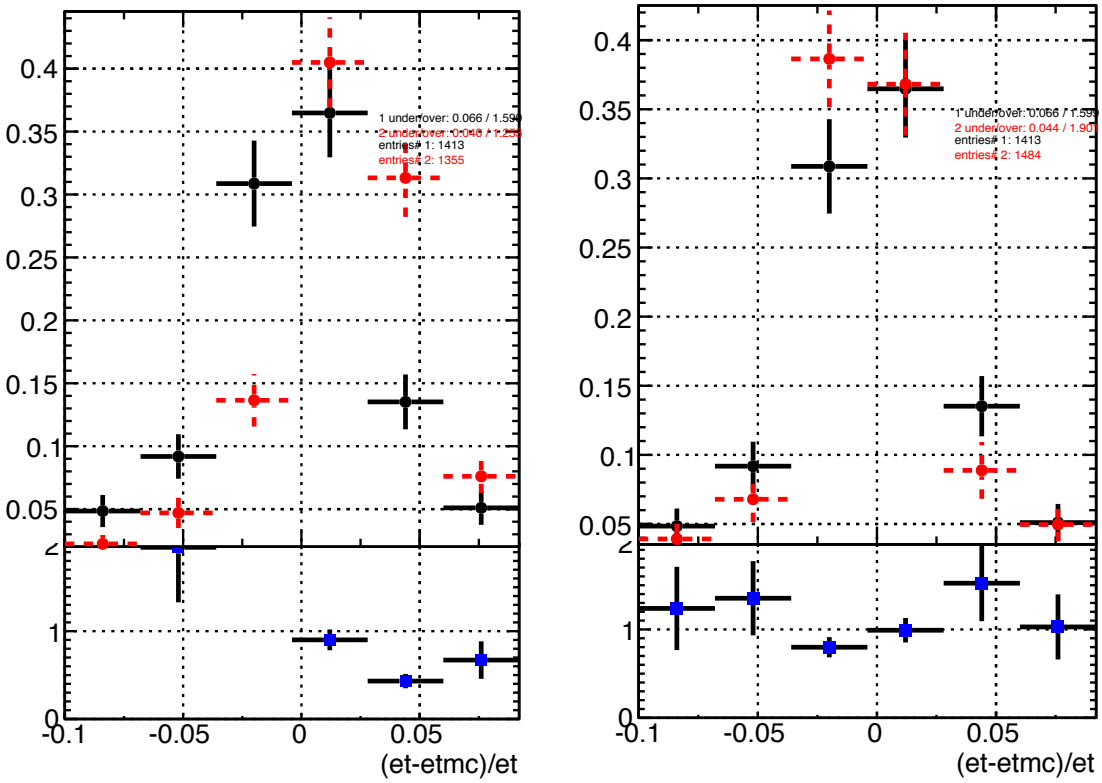

(a) The test sample (black) compared to the reference sample A (red).

(b) The test sample (black) compared to the reference sample B (red).

Fig. 6.2 Physics validation plots of the distribution of the photon energy resolution (normalized to unity) for the test and reference samples described in the text.

Chapter 7

Reconstruction of physics objects

The reconstruction of the physics objects used in this thesis is introduced in this chapter. All the reconstructed objects are calibrated using dedicated methods, then identified by various criteria applied on relevant discriminating variables. The systematic uncertainty sources related to the reconstruction, calibration and identification processes of the objects are introduced here and will be considered in the analysis described in Part III.

7.1 Photons

7.1.1 Reconstruction

A photon can be reconstructed from the EM energy deposit (cluster) and tagged either as *unconverted photon* without any matched track from the ID, or as *converted photon* with one or two matched tracks originating from a conversion vertex. Unconverted photons pass through the ID without leaving tracks and deposit energy in the EM Calo, as shown in Figure 5.3. A photon converted into a pair of electron and positron leaves two tracks (or one track only if the other one is mis-reconstructed) in the ID starting from the conversion vertex, and finally deposits energy in the EM Calo. Figure 5.10 shows the amount of material before the EM Calo varies with the pseudorapidity, and the fraction of converted photons F_{conv} is related to the radiation length $\frac{X}{X_0}$ of the local material via [88]:

$$F_{conv} = 1 - e^{-\frac{7}{9}\frac{X}{X_0}}. \tag{7.1}$$

The fraction of photons converted in the inner tracker (which covers up to a radius of 115 cm), is shown in Figure 7.1 as a function of $|\eta|$.

The EM clusters are reconstructed based on the second EM layer using a 'sliding-

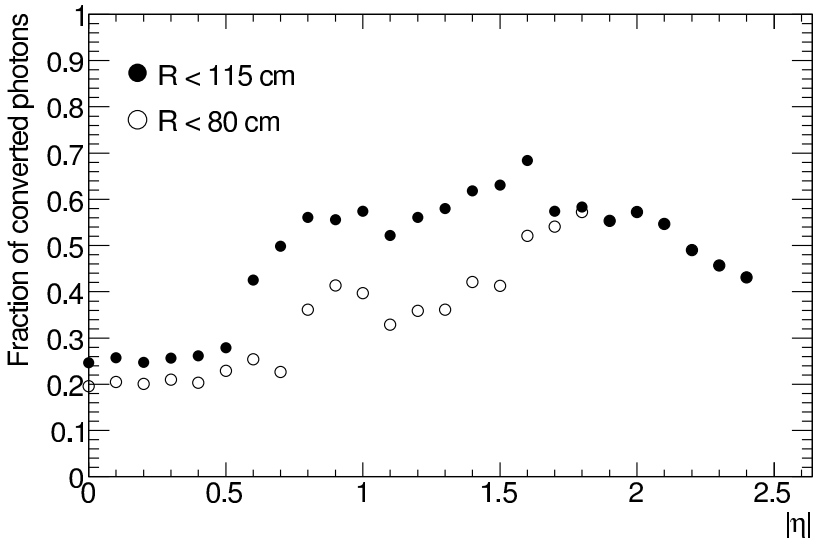

Fig. 7.1 Fraction of photons converting within a radius of 115 cm (80 cm) in full (open) circles as a function of $|\eta|$ [66].

window' algorithm [89], which clusters calorimeter cells within fixed-size rectangles. In order to construct such a 'window', the full EM Calo is divided into a grid of $N_\eta \times N_\phi$ towers based on the size of the cell in the second EM layer, which is $\Delta\eta \times \Delta\phi = 0.025 \times 0.025$. In the barrel, the unconverted photons are reconstructed from clusters in a window size of 3×5, while it is 3×7 for the converted photons. In the end-cap regions, all the photons are reconstructed from clusters with a size of 5×5 towers. Photons are reconstructed from clusters with E_{T} of at least 2.5 GeV [90].

The ϕ information is given by the energy-weighted barycenter of the EM cluster in the second EM layer, while the η coordinate is given by combining the measurements from both first and second EM layers.

The energy information is derived by summing up all the energy deposited inside the EM cluster; for further studies on the cluster energy measurements, see References [90–92]. Taking into account the lateral leakage to the EM cells outside the cluster and the longitudinal leakage to neighbor instruments of the EM Calo, the energy will be eventually corrected by dedicated calibration processes, introduced in Section 7.1.3.

The conversion vertices must be reconstructed at a radius smaller than 800 mm. Depending on the number of tracks in the conversion vertex, there can be double-track conversions or single-track conversions. The single-track conversions can happen if two tracks are too close to be discriminated, or if one of the decay product is mis-reconstructed, for example, its momentum is too small (less than 0.5 GeV) to be reconstructed. The single track left

must be reconstructed only by hits found after the B-layer, and quite a few single-track conversions are reconstructed using hits found in TRT only. Therefore single-tracked photon candidates are poorly reconstructed in terms of momentum and η information. Besides, there is a large overlap between single-tracked photons and electrons, since the EM clusters are also used to reconstruct electrons by matching a single track from the ID as introduced in Section 7.2.

From time to time, some readout channels can randomly produce noise which can be reconstructed as a signal with fake transverse momentum above the threshold of 2.5 GeV. A database recording the known noisy cells has been used to mask these problematic channels, and additional cleaning cuts are developed to reject new noisy channels at the reconstruction level. These cleaning cuts are designed to flag out those photon candidates with very narrow energy deposit, because this kind of fake photons are usually reconstructed from a cluster containing only one cell.

7.1.2 Identification

A set of identification criteria has been developed to discriminate photons from backgrounds, such as clusters polluted by residual jet-component or di-photon decay products from neutral hadrons such as π^0. As an example, Figure 7.2 illustrates the simulation of the energy showers left by one single photon and one neutral pion in the EM Calo. A pair of energetic photons produced from π^0 decay can be very close to each other as shown on the right-hand side. Comparing to the shower left by one single photon on the left-hand side, neutral pions can be discriminated from the photon by checking the lateral width in the second layer of the EM Calo and the energy deposit shape in the first layer.

Given the fact that EM Calo shower shapes can be used as discriminant variables to identify photons, two sets of cuts are built according to their background rejection power. Respectively, they are *loose* cuts and *tight* cuts.

The loose photon cuts are developed based on hadronic leakage, evaluating the fraction of the EM Calo shower leaking into the hadronic layers, and the EM Calo cluster shape in the second layer. Depending on the η region, the hadronic leakage of an EM cluster can be evaluated, either as the ratio of the E_{T} in the hadronic calorimeter to the E_{T} of the EM cluster for central η region, noted as R_{had}, or as the ratio of the E_{T} found in the 1st hadronic sampling to the E_{T} of the EM cluster in other η regions, noted as R_{had1}. The variables related to the EM Calo cluster shape in the 2nd EM layer used for the loose cuts include the lateral width of the cluster, $w_{\eta 2}$, and the energy-weighted lateral width of the cluster, quantified as the energy ratio from rectangular regions ($N_\eta \times N_\phi$) of 3×7 cells to that of 7×7 cells, noted as R_η. As an example to show how the photon differs from the background

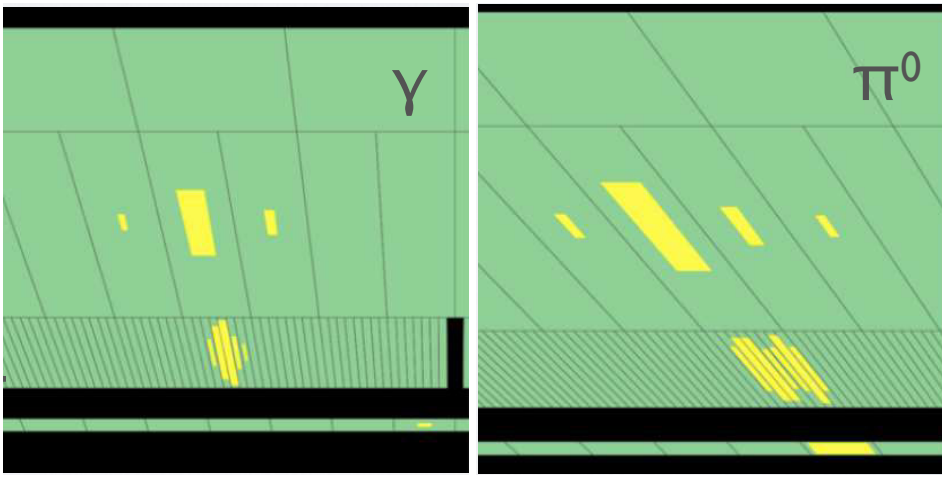

Fig. 7.2 An example to illustrate the calorimeter shower shapes of the photon (left) and the π^0 (right) [65].

jets with these discriminant variables, Figure 7.3 illustrates the distributions of variables of R_{had} and R_η of converted and unconverted photons and of the corresponding fake-photon jet candidates.

The tight photon criteria set tighter cuts on the variables used in the loose criteria, with more requirements set for the shape in the 1st and 2nd EM layers. It further checks the energy fraction of the central cells in 2nd EM layer along ϕ, by defining R_ϕ as the energy ratio from regions of 3×3 cells to that of 3×7 cells. Due to the fine segmentation along η in the 1st EM layer, the tight criteria is able to build up better separation of photon and pions, as implied in Figure 7.2.

Table 7.1 summarizes the variables used to identify `loose` and `tight` photons with the range of the cut values given. Cuts set on these discriminant variables are optimized depending on photon η. The `tight` cuts are further optimized depending on photon p_{T} and treating unconverted and converted photons separately. The detailed cuts menu for the `loose` and `tight` criteria can be found in Tables 16 to 18 in Appendix Conclusion.

7.1.2.1 Isolation

In order to strengthen the background suppression, a further discriminant quantity has been introduced: the calorimeter isolation transverse energy E_{T}^{iso}.

The E_{T}^{iso} sums up all the positive energy deposits around the photon cluster in the 2nd EM layer, in a cone of radius $\Delta R = \sqrt{(\Delta\eta)^2 + (\Delta\phi)^2}$, which takes the barycenter of the cluster as center. Figure 7.5 schematically illustrates how the isolation variable, $TopoEtcone40$, is computed. The '40' refers to the $\Delta R < 0.40$ cone, shown as the yellow area in the fig-

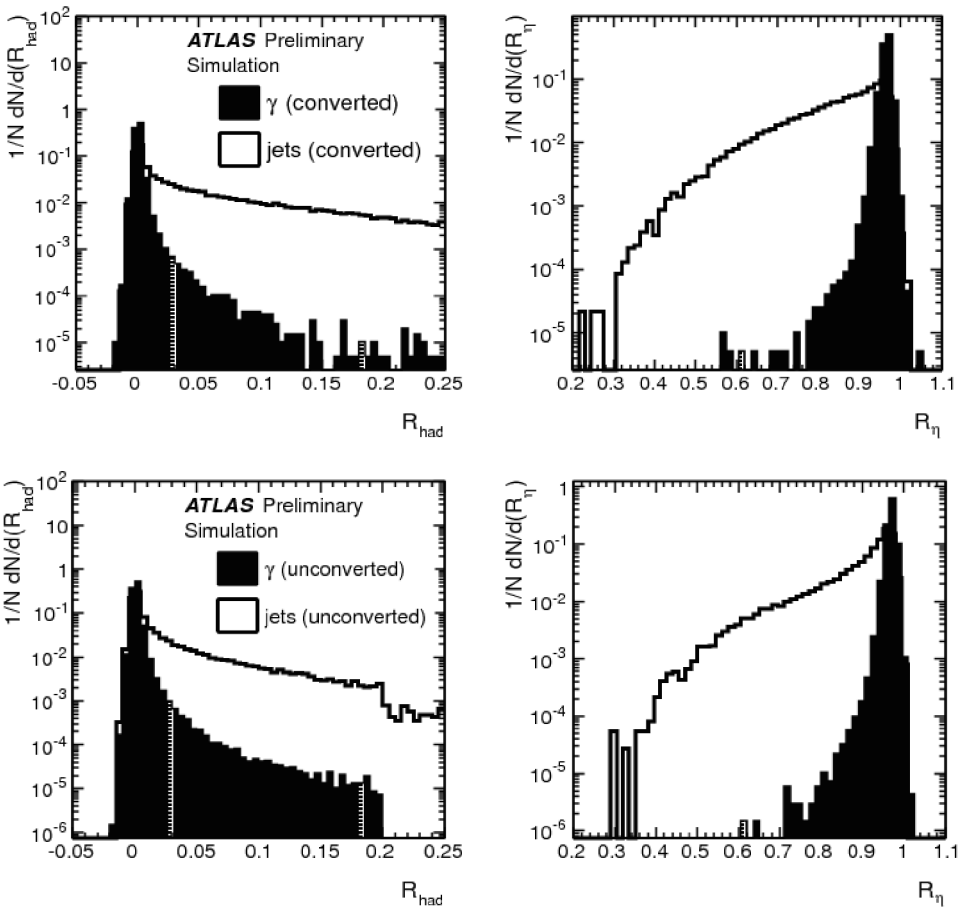

Fig. 7.3 Differences between photons and hadronic backgrounds are shown, with respect to the distributions of two shower shape variables: R_{had} is the hadronic leakage ratio, and R_η refers to the lateral width of the shower in the second EM layer. The upper two plots are for converted photons, and the lower two for unconverted photons; they are plotted in the region $0 < |\eta| < 0.6$ for $E_{\mathrm{T}} > 20\,\mathrm{GeV}$ before any selections [93].

ure. The core rectangle of the cone is removed to avoid counting the energy of the photon itself, which is a region of $N_\eta \times N_\phi = 5 \times 7$ cells. The 'topo' refers to the topological algorithm [89] to form the topological clusters (red areas in this figure) for the E_{T}^{iso} computation.

The topological algorithm starts from a seed cell with signal 4σ away from the the noise; then it groups all the neighbouring cells passing the threshold of 2σ on the signal significance over the noise; finally all the direct neighboring cells at the outer boundary will be included if the signal is more than 0σ away from the noise.

Although the clusters in the 2nd EM layer of many photon candidates are under a size of 5×7 cells, there exists a lateral leakage for energetic photons. As a result, the *TopoEtcone*40 variable has a large dependence on p_{T} and η of the photon. The energy

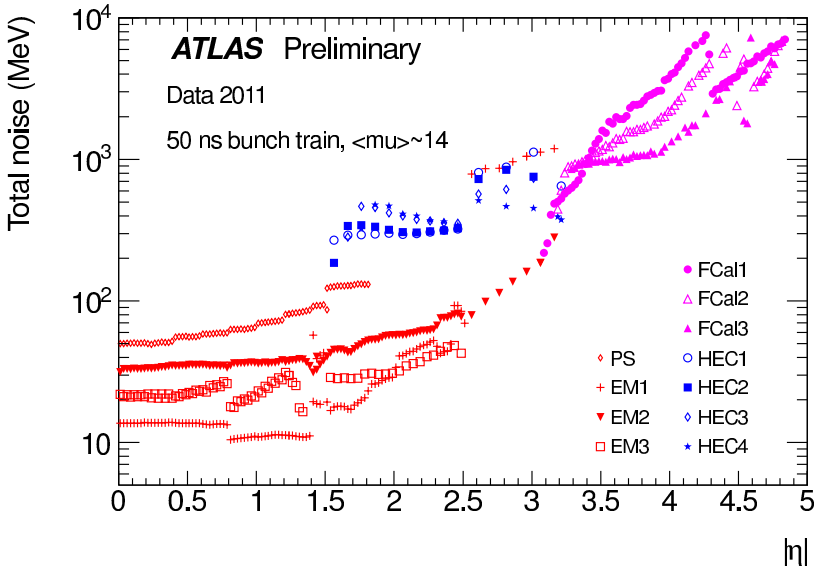

Fig. 7.4 Total noise (electronics and pileup) as a function of $|\eta|$ for each LAr calorimeter layer [95].

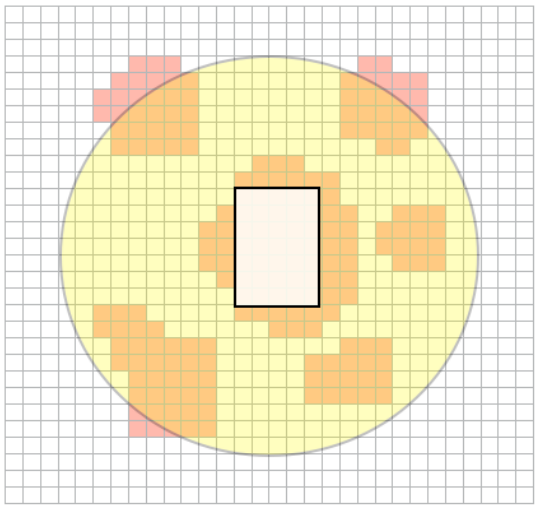

Fig. 7.5 An isolation cone of $\Delta R < 0.4$ illustrated by a circle is shown in a segmented $\eta \times \phi$ plane of the 2nd EM layer, where the central rectangle of 5×7 cells contains most of the energy deposit of the photon candidate. The red areas refer to the topological clusters used to compute the *TopoEtcone*40 variable [96].

Description		Loose	Tight
Acceptance			
$\|\eta\| < 2.37$ excluding $1.37 < \|\eta\| < 1.52$		✓	✓
Hadronic leakage			
$R_{had1} = \frac{E_{\mathrm{T}}^{\text{1st had. sampling}}}{E_{\mathrm{T}}^{\text{EM cluster}}}$, if $\|\eta\| < 0.8$ or $\|\eta\| > 1.37$	$<$	0.01975 or 0.02575	0.01525-0.01975
$R_{had} = \frac{E_{\mathrm{T}}^{\text{had. sampling}}}{E_{\mathrm{T}}^{\text{EM cluster}}}$, if $0.8 < \|\eta\| < 1.37$	$<$	0.02275-0.02725	0.01825-0.02575
2nd EM layer			
$E_{s2}^{7\times7}$	$>$	0.1 MeV	0.1 MeV
$R_\eta = E_\eta^{3\times7}/E_\eta^{7\times7}$	$>$	0.750-0.9025	0.910-0.9025
$w_{\eta 2}$ lateral width of the cluster	$<$	0.013-0.016	0.011-0.0130
$R_\phi = E_\phi^{3\times3}/E_\phi^{3\times7}$	$>$	-	0.57-0.93
1st EM layer			
$f_1 = E_{s1}^{tot}/E_{shower}^{tot}$	$>$	-	0.005
$w_{\eta 1}^3$ lateral width of 3 strips around the max. strip	$<$	-	0.645-0.75
$w_{\eta 1}^{tot}$ total lateral shower width	$<$	-	1.8-3.5
$f_{side} = \frac{E_{s1}^{7\times1} - E_{s1}^{3\times1}}{E_{s1}^{7\times1}}$	$<$	-	0.24-0.52
$\Delta E = E_{s1}^{\text{2nd max strip}} - E_{s1}^{\text{min strip}}$	$<$	-	$120-560$ MeV
$E_{ratio} = \frac{E_{\mathrm{s1}}^{\text{max strip}} - E_{\mathrm{s1}}^{\text{2nd max strip}}}{E_{\mathrm{s1}}^{\text{max strip}} + E_{\mathrm{s1}}^{\text{2nd max strip}}}$	$>$	-	0.76-0.88

Table 7.1 The variables used for `loose`/`tight` photon identification [94]. The superscripts in the form $N_\eta \times N_\phi$ refer to the cells (or strips) centering around the most energetic cell (or strip), while the $s1$ and $s2$ subscripts refer to the 1st and 2nd EM samplings.

leakage issue was fixed after applying corrections binned in p_{T} as a function of η derived from studies on single particle simulation samples with converted and unconverted photons treated differently as described in Reference [96]. However, a discrepancy was observed in higher p_{T} bins between the results obtained from simulation and from data. A data-driven method to further correct the photon energy leakage is introduced [97], and the corresponding isolation variable $TopoEtcone40_{corr}$ is used in this thesis.

7.1.2.2 Identification efficiency

The simplest photon identification efficiency can be estimated using MC samples only. It is defined as the ratio of the number of reconstructed photons passing a given criterion ($N_{\gamma}^{\text{reco,pass cut}}$) divided by the associated truth photon multiplicity, where the reconstructed photons are checked to be associated with a truth photon to avoid counting fake photons. As the efficiency depends on the η and E_{T} of the photon, it is measured as a function of E_{T} in different η bins, thus forming a map of efficiency.

The photon identification efficiency can also be derived from data [94]. A discrepancy between simulation and data is found for the efficiency result in some (η, E_{T}) bins. Specific corrections are thus derived by applying small modification to the simulated EM shower shapes in the simulation samples, called fudge factors. The fudge factors give a good agreement between the simulation and the data-driven results at $\pm 5\%$. Since the fudge factors change the identification results, they should be applied before the photon identification. Figure 7.6 shows four η bins of converted photon identification efficiency (ε_{ID}) as a function of E_{T}, comparing the combined data-driven measurements with the nominal and corrected simulation predictions. Especially, the bottom two figures show the residual $\pm 5\%$ fluctuation between the data-driven and the corrected results.

7.1.3 Calibration

The energies of electrons and photons measured by the EM Calo are calibrated with a multi-step scheme, shown in Figure 7.7. It derives an overall scale factor by comparing MC simulation to data with respect to the Z boson resonance reconstructed using events of $Z \to e^+e^-$, referring to the **Step 5** in the figure. In parallel, an effective constant term c, referring to Equation (5.3), is extracted to smear the energy resolution of MC simulation to be consistent with the data. The final results are validated in **Step 6** with events of $Z \to ll\gamma$ for photons, and $J/\Psi \to e^+e^-$ events for electrons.

Before comparing energy response between the data and simulation for the $Z \to e^+e^-$ events, corrections are applied to both data and MC simulated samples as a function of $|\eta|$ in bins of E_{T}^{calo} in **Step 3**, for the lateral and longitudinal leakages introduced in Section 7.1.1. This correction is based on MC simulation samples using a multivariate algorithm (MVA) [98], discussed in detail in Reference [92]. The MVA method has been trained in **Step 1** treating electrons, converted and unconverted photons separately. As the EM Calo is longitudinally divided, the scales of different layers have to be equalized in **Step 2**, in order to apply an uniform scale factor at the end. The layer inter-calibration includes the calibration between first and second EM layers, and the presampler energy scale determination.

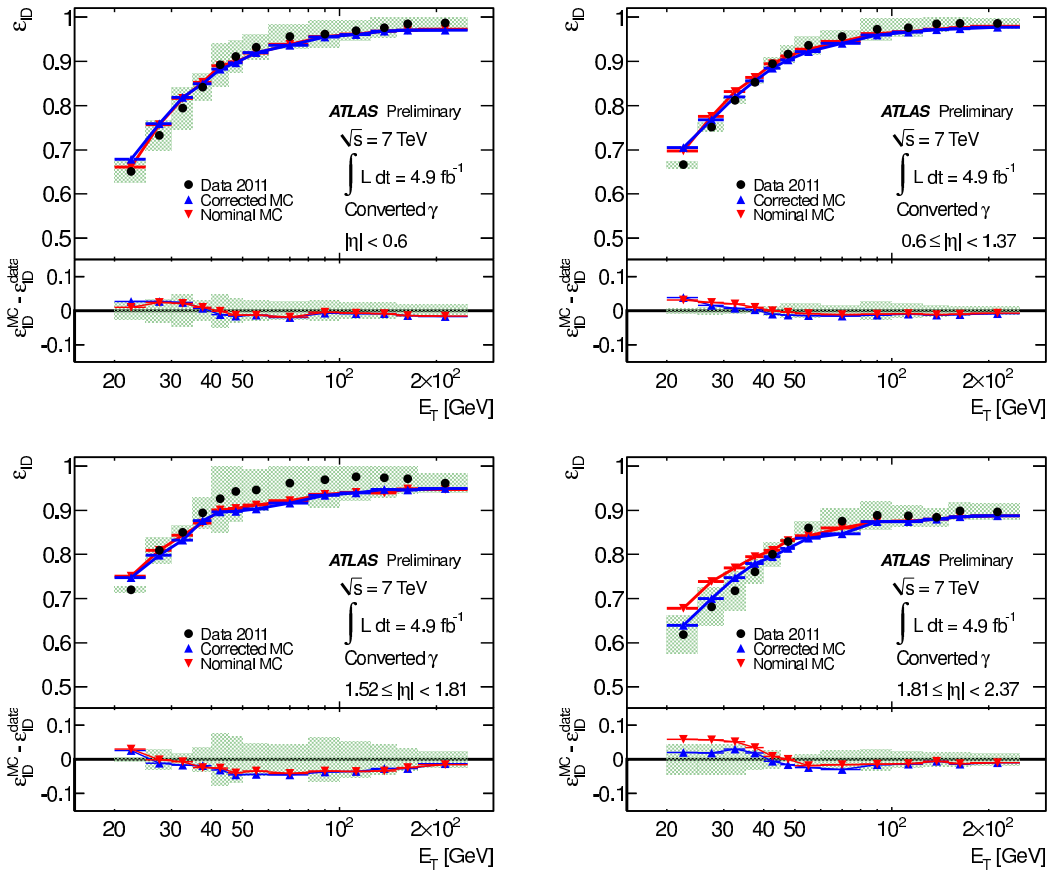

Fig. 7.6 Comparison of weighted mean of the data-driven measurements of converted photon identification (ε_{ID}) to the nominal and corrected MC predictions in the region 15 GeV $< E_{\mathrm{T}} <$ 300 GeV. The ε_{ID} curves are shown in four different η regions. The green uncertainty band refers to the total uncertainties estimated for the combination of the data-driven methods. Only the statistical uncertainties are shown for the MC predictions [94].

The third layer is not included as its contribution is proven negligible in current studies [92].

Various systematic uncertainties will be introduced during the electron and photon energy calibration. Well-described detector geometry and good physics lists for MC simulation are needed for the MC-based calibration in **Step 3**. They rely on material distribution measurements in data linked to the inter-calibration of first and second EM layers. The variation of the energy response related to the material distribution measurement will lead to a source of systematic uncertainty considered in this thesis, noted as material uncertainty in Section 11.5. Besides, the presampler energy scale determination process described in Reference [92] will introduce another independent uncertainty on the final electron/photon energy response.

All other uncertainties on the calibration introduced in Reference [92] will be treated as two independent systematic uncertainty sources: one on the energy resolution and the other one on the energy scale.

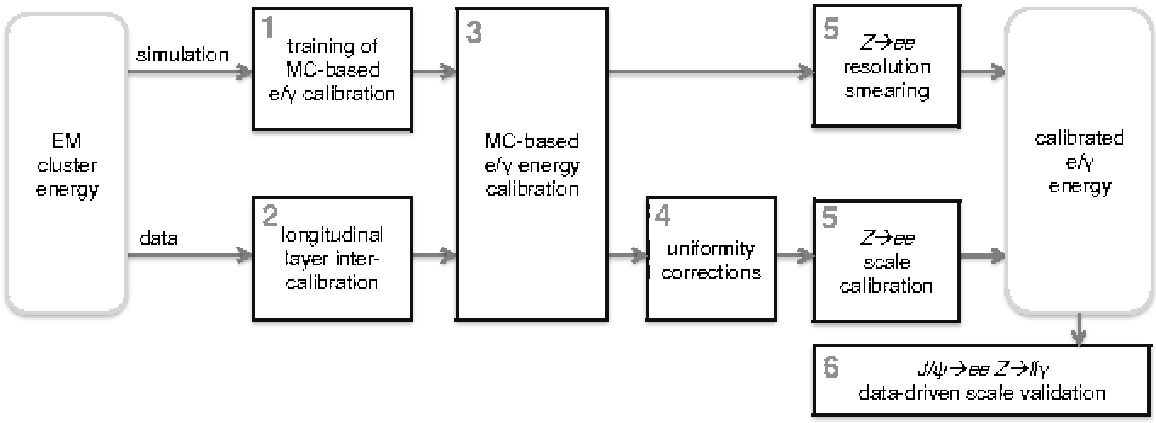

Fig. 7.7 The procedure flow for energy calibration of photons and electrons in ATLAS [92].

7.2 Electrons

Electrons will leave a track in the ID and deposit energy in the EM Calo, as illustrated in Figure 5.3. Therefore, they are reconstructed from the EM clusters ($N_\eta \times N_\phi = 3 \times 5$) in the 2nd EM Calo layer, which must be associated with a well reconstructed track in the ID. Reconstructed electrons cover region up to $|\eta| = 2.5$, as the ID. Forward electrons ($2.5 < |\eta| < 4.9$) are not considered here.

Electrons and photons have a very similar detector response, thus sharing a lot in common with respect to reconstruction, identification, isolation and calibration. The unconverted photons differ from the electrons since they must not have an associated track. Low–p_{T} ($p_{\mathrm{T}}^e < 20$ GeV) electrons are included in this thesis. Their calibration is improved with a specific energy-momentum combination algorithm defined in Reference [92], based on $J/\Psi \to e^+e^-$ events. A relevant systematic uncertainty is taken into account in Section 11.5.

In addition to the variables of shower shape and hadronic leakage used for photon identification, see Table 7.1, more variables describing the track quality and the track-cluster matching are selected as discriminant variables to identify electrons. Electron identification is based on cuts and three sets of cuts are graded according to the background rejection power, labeled as `loose`, `medium` and `tight`. It is interesting to note that these three criteria require the electrons to be reconstructed in the central region of the detector with $|\eta| < 2.47$. Detailed studies on electron identification can be found in Reference [99].

The electron identification efficiency ε_{ID}^e is measured as a function of $|\eta|$ in bins of E_{T} from both data and MC simulation using three independent channels of $W \to e\nu$, $Z \to e^+e^-$ and $J/\psi \to e^+e^-$, as described in Reference [99]. Scale factors which depend on E_{T} and η are derived from a global χ^2 test to combine the results of the three channels. For the `medium` electron, the identification efficiency increases from about 80% at 7 GeV to 90% at 50 GeV [99].

The identification efficiency has a large dependence to the number of reconstructed primary vertices N_{PV} with the cut-based menu used at 7 TeV. For the data taking in 2012 at $\sqrt{s} = 8$ GeV, the N_{PV} increases up to 40 as indicated from Figure 4.4. In order to cope with this effect, an optimized cut-based menu [100] is used to identify electrons for data collected at $\sqrt{s} = 8$ GeV. These criteria can be noted with '++' added at the end, such as `medium++` used in this thesis. This 'plus' menu keeps the variation of the efficiency below 4% from 1 to 30 vertices, and the improvement can be seen in Figure 7.8, which shows the `loose`, `medium` and `tight` identification efficiencies as a function of the number of reconstructed primary vertices (N_{PV}) measured in data at 7 TeV and at 8 TeV.

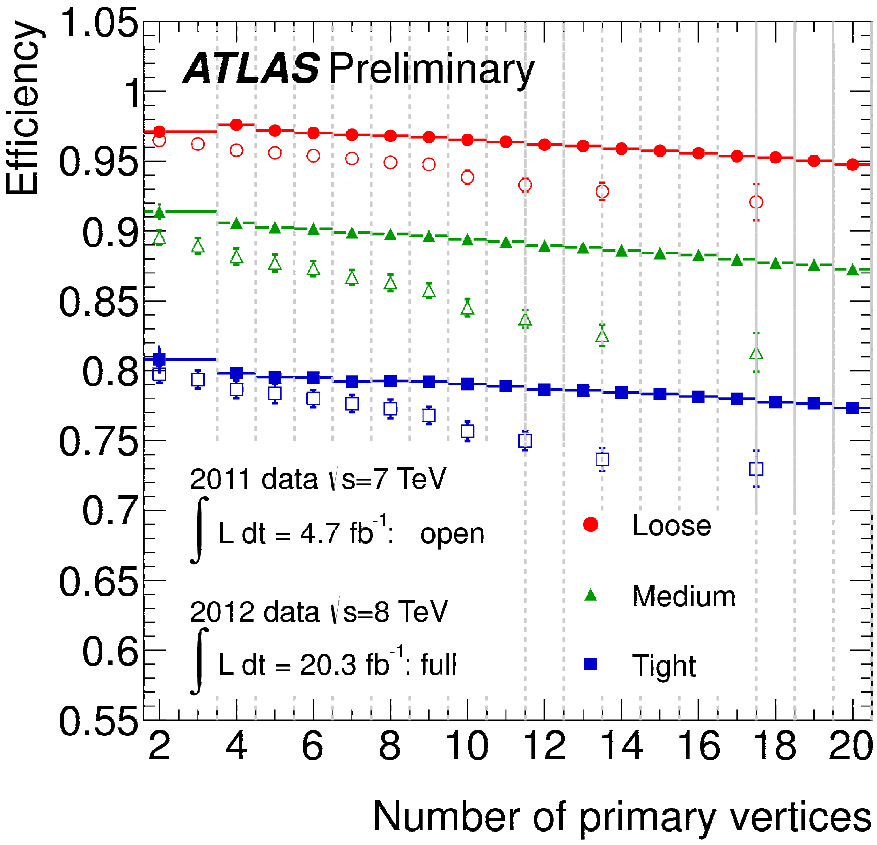

Fig. 7.8 The electron identification efficiency for `loose`, `medium` and `tight` cut-based selections measured in data at 7 TeV and at 8 TeV as a function of the number of reconstructed primary vertices [100].

7.3 Muons

Muons will pass through the detector and interact with the ID and muons chambers, leaving tracks as shown in Figure 5.3. The reconstruction of muons is based on information from MS, ID and calorimeters. The ideal situation to identify a muon passing through ATLAS is when it leaves matched tracks found in both ID and MS, which is called a *combined* (CB) muon [101, 102]. Muons can only be found in the ID if their transverse momenta are too low to leave a complete track in the MS. They can be recognized if one ID track can be extrapolated to be associated to at least one tagged segment in MS; these muons are called *segment-tagged* (ST) muons [101, 102]. These two types of muons are reconstructed up to region $|\eta| < 2.5$ following the coverage of ID.

The CB muons are tagged as `tight` muons, whilst the ST muons can be classified as `loose`, `medium` and `tight` according to the MS chambers segment reconstruction, and the tracking quality. Muons with different reconstruction methods have a different efficiency as a function of $|\eta|$, as shown in Figure 7.9. This was obtained with muons measured in $Z \to \mu^+\mu^-$ events with $p_{\mathrm{T}} > 10$ GeV. The 'CaloTag' in the Figure refers to muons reconstructed by combining information from the ID and the calorimeters. Due to the lack of MS installed in region $1.1 < \eta < 1.3$ and $\eta = 0$, the figure shows an inefficiency in these two regions for both CB and ST muons. Figure 7.10 shows the efficiency as a function of the muon p_{T}, indicating that the efficiency starts to be maximal at $p_{\mathrm{T}} \geq 20$ GeV. There is a steep increase for the low–p_{T} muons because muons need a minimum p_{T} of approximately 3 GeV to arrive at the MS and to satisfy the reconstruction requirements of CB and ST muons.

7.4 Jets

The QCD final states in the proton-proton collisions will pass through the ID and EM Calo, and leave energy in the hadronic calorimeters to be reconstructed as jets as shown in Figure 5.3. The reconstruction is implemented based on an algorithm using calorimeter energy deposits as input. The jet finding algorithm groups the energetic inputs into subsets (jets) defined by the algorithm. The algorithm used in this thesis to define jets is the "anti-k_{t}" algorithm, which is the default in ATLAS since 2009.

The default anti-k_{t} algorithm [103] uses positive-energy calorimeter topological clusters (TopoClusters) as input. A prior separation between EM and hadronic TopoClusters must be applied based on shower shape parameters; more studies on the topoclusters can be found in [89]. The input four-momenta are grouped within a distance parameter R, which is chosen

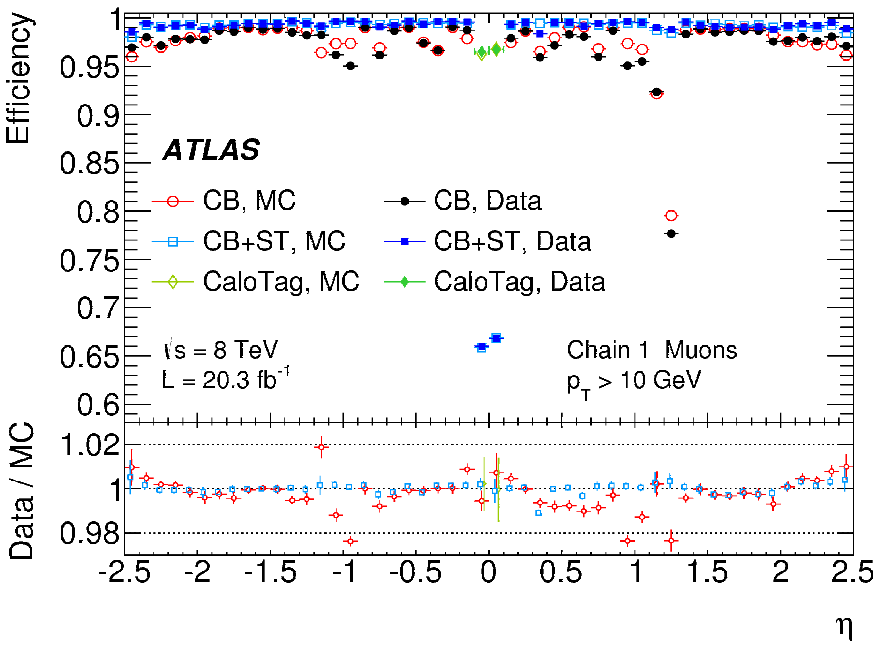

Fig. 7.9 Muon reconstruction efficiency as a function of $|\eta|$ for various muon types [102].

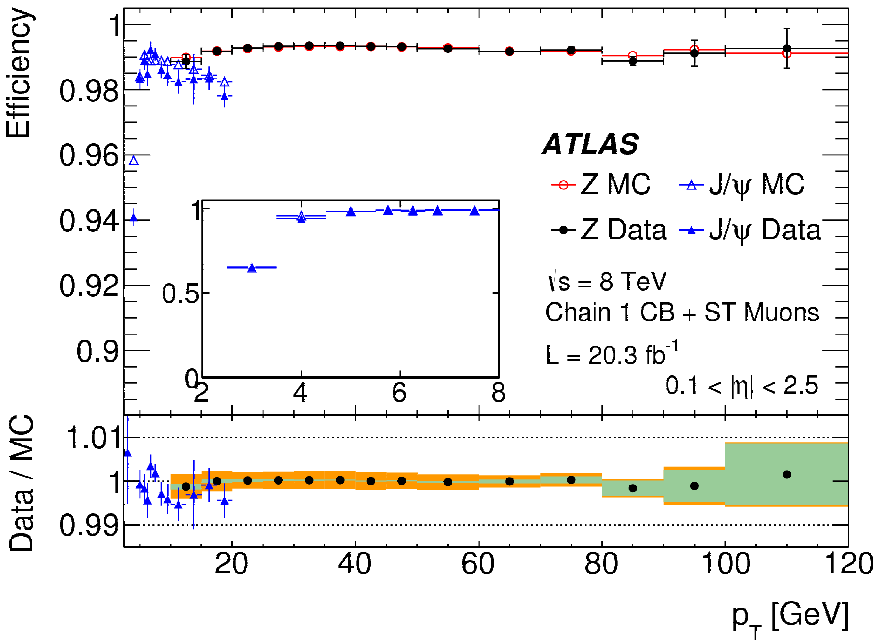

Fig. 7.10 Muon reconstruction efficiency as a function of p_{T} for CB and ST muons [102].

to be 0.4 in this thesis, by introducing a new distance quantity d_{ij}:

$$d_{ij} = min(k_{\mathrm{t,i}}^{2p}, k_{\mathrm{t,j}}^{2p}) \frac{\Delta_{ij}^2}{R^2}, \tag{7.2}$$

where i and j refer to the candidate TopoClusters; $k_{\mathrm{t,i}}$ and $k_{\mathrm{t,j}}$ are the transverse momentum of the TopoClusters; $\Delta_{ij}^2 = (y_i - y_j)^2 + (\phi_i - \phi_j)^2$ (y is the rapidity of the TopoCluster).

The parameter p is set to be -1 in the anti-k_{t} algorithm, so that the jet algorithm always starts from the most energetic input to merge the input pairs within the distance R, and ends up with the jet candidate when d_{ij} equals to $k_{\mathrm{t,i}}^{2p}$. The jet will be reconstructed as long as it has a momentum above 7 GeV.

A multi-level set of cleaning cuts has been devised to reject jets due to calorimeter noise and non-collision backgrounds such as cosmic rays, leading to several quality criteria labeled as "Loose", "Medium" and "Tight", which are described in details in [104]. In addition to the three criteria recommended for 7 TeV studies, a new "VeryLoose" (or "Looser") criterion was developed as the default baseline for jet cleaning criteria for 8 TeV studies [105].

The jet calibration is essential for jet energy measurement as the un-calibrated jet energy might be polluted by additional interaction vertices, or affected by detector effects such as calorimeter non-compensation response or signal losses due to noise thresholds. There are many methods to calibrate jets, introduced in [104]. In this thesis the LCW+JES calibration is adopted.

A local cluster weighting (LCW) calibration method [106, 107] is applied at TopoCluster level. The calibration depends on whether the cluster is classified as EM or hadronic, and the values are derived from MC and data studies.The LCW is dedicated to eliminate the detector effects, and jets can then be built with these LCW calibrated clusters using a given jet algorithm. As incident particles from pile-up are distributed uniformly in the η, ϕ plane, the jet energy measurements are then corrected by subtracting contributions from pile-up, which is evaluated using in-situ data based on a concept of jet area [108, 109] This pile-up suppression is computed event by event. Further calibration is derived from a comparison between the jets measured in data and the Monte Carlo simulated truth jets, and is known as jet energy scale, or JES [104, 110].

7.5 Missing transverse energy

The missing transverse energy, $E_{\mathrm{T}}^{\mathrm{miss}}$, is a crucial object in many analyses searching for new physics. For example, the WIMP particles, $\tilde{\chi}^0$, will definitely contribute to this $E_{\mathrm{T}}^{\mathrm{miss}}$ term. For a given physics event, the $E_{\mathrm{T}}^{\mathrm{miss}}$ is reconstructed in basis of calibrated calorimeter cells and the muon spectrometers, and is computed as the square root of the quadratic sum of the x and y terms:

$$E_{x(y)}^{\mathrm{miss}} = E_{x(y)}^{\mathrm{miss,calo}} + E_{x(y)}^{\mathrm{miss},\mu}, \tag{7.3}$$

where the term contributed by muons is computed from the momenta as

$$E_{x(y)}^{\mathrm{miss},\mu} = -\sum p_{x(y)}^{\mu}. \tag{7.4}$$

A refined scheme classifies the candidate cells into physics objects to be calibrated in the following order, to avoid double counting clusters or tracks due to the similar detector response of physics objects: electrons, photons, hadronic taus, jets and muons. Besides, the energy of topological clusters or tracks which are not classified in the above classification sequence will be summed up as a so-called *SoftTerm* entering the $E_{\mathrm{T}}^{\mathrm{miss}}$ calculation, using an energy-flow algorithm [111]. The regular $E_{\mathrm{T}}^{\mathrm{miss}}$ computation can be written as

$$E_{x(y)}^{\mathrm{miss}} = E_{x(y)}^{\mathrm{miss},e} + E_{x(y)}^{\mathrm{miss},\gamma} + E_{x(y)}^{\mathrm{miss},\tau} + E_{x(y)}^{\mathrm{miss,jets}} + E_{x(y)}^{\mathrm{miss,SoftTerm}} + E_{x(y)}^{\mathrm{miss},\mu}, \tag{7.5}$$

where each term is calculated as the negative sum of the calibrated reconstructed objects, projected to the x and y directions. A prior cut on pseudorapidity of $|\eta| < 4.5$ is applied before the summation due to the fact that the MC does not provide a good description in the very forward region [111]. The muon term only accounts for muons within the pseudorapidity range up to 2.7, limited by the MS.

Physics objects can be identified via different criteria introduced above. At the same time the $E_{\mathrm{T}}^{\mathrm{miss}}$ computation can even omit some of them, and hence various different $E_{\mathrm{T}}^{\mathrm{miss}}$ algorithms were developed satisfying specific usage. For a given $E_{\mathrm{T}}^{\mathrm{miss}}$ algorithm, a relevant computation is defined to store all the classified physics objects. As an example, a generic $E_{\mathrm{T}}^{\mathrm{miss}}$ computation, called `MET_RefFinal`, serves as a baseline to build up customized computations. It contains all the well-calibrated standard terms in Equation (7.5) [112].

The $E_{\mathrm{T}}^{\mathrm{miss}}$ performance has been studied in References [111, 112]. The $E_{\mathrm{T}}^{\mathrm{miss}}$ resolution σ follows a function of $\sum E_{\mathrm{T}}$ as:

$$\sigma = k \cdot \sqrt{\sum E_{\mathrm{T}}}, \tag{7.6}$$

where the k factor value is obtained from a fit and varies from $0.42\,\mathrm{GeV}^{1/2}$ for $Z \to \ell^+\ell^-$ events to $0.51\,\mathrm{GeV}^{1/2}$ for di-jet events [111]. Figure 7.11 shows the two component of $E_{\mathrm{T}}^{\mathrm{miss}}$, E_x^{miss} and E_y^{miss}, as a function of the total transverse energy E_{T} measured in different channels at 7 GeV; the fitted k value for each channel is also given.

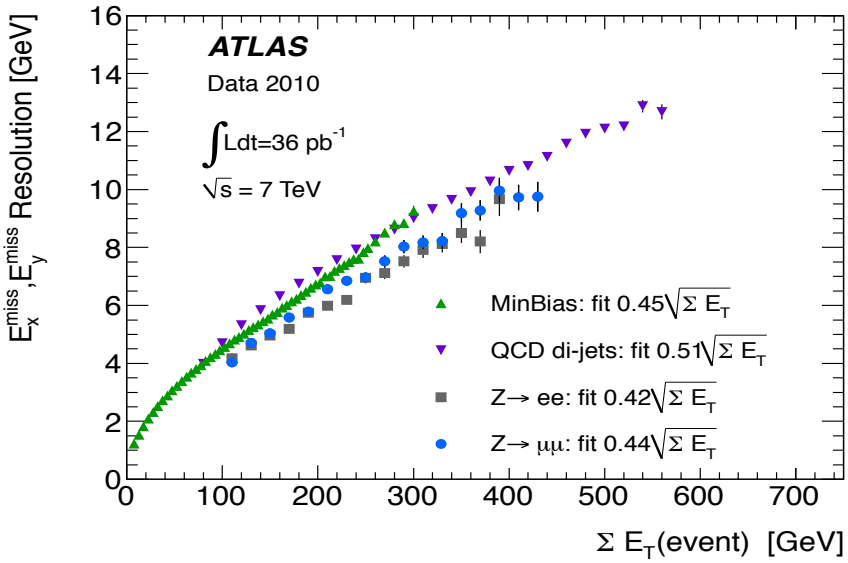

Fig. 7.11 The two component of $E_{\mathrm{T}}^{\mathrm{miss}}$, E_x^{miss} and E_y^{miss}, measured as a function of the total transverse energy E_{T} in different channels at 7 GeV; the fitted k value for each channel is also given [111].

A specific computation used in this thesis is the `MET_Egamma10NoTau_RefFinal`, which will not identify taus; they will thus be regarded as jets. Furthermore, a customized requirement is implemented to the $E_{\mathrm{T}}^{\mathrm{miss}}$ computation to treat the muons as invisible, which will be discussed in Section 10.1, leading to the $E_{\mathrm{T}}^{\mathrm{miss}}$ being computed as:

$$E_{x(y)}^{\mathrm{miss}} = E_{x(y)}^{\mathrm{miss},e} + E_{x(y)}^{\mathrm{miss},\gamma} + E_{x(y)}^{\mathrm{miss,jets}} + E_{x(y)}^{\mathrm{miss,SoftTerm}}. \tag{7.7}$$

In the Equation (7.7), $E_{x(y)}^{\mathrm{miss},e}$ comes from standard calibrated [92] electrons identified with the `medium++` criteria ($|\eta| < 2.47$) and satisfying $p_{\mathrm{T}}^{e} > 10$ GeV; $E_{x(y)}^{\mathrm{miss},\gamma}$ refers to the photons passing the `tight` criteria, calibrated using the electromagnetic scale [66] with $p_{\mathrm{T}}^{\gamma} > 10\,\mathrm{GeV}$; $E_{x(y)}^{\mathrm{miss,jets}}$ is made up of jets reconstructed using the anti-k_{t} algorithm with distance parameter $R = 0.4$, and calibrated using the LCW+JES scheme; besides, an extra transverse momentum cut is applied to reject calibrated soft jets with $p_{\mathrm{T}}^{\mathrm{jet}} < 20\,\mathrm{GeV}$. The SoftTerm is summing over all the un-associated topoclusters (including the soft jets).

Part III

Data Analysis

Chapter 8

Introduction

8.1 Motivation of the monophoton analysis

Particles from models beyond the Standard Model (BSM), such as dark matter particles, can be produced in pairs at collider. Particles which interact only weakly are invisible to the ATLAS detector, and thus a pair production of such particles at the LHC, as shown in Figure 8.1a, is not measurable. As discussed in Chapter 2, a solution is to look for an initial state radiation (ISR) signature in the photon and $E_{\mathrm{T}}^{\mathrm{miss}}$ final state, as shown in Figure 8.1b.

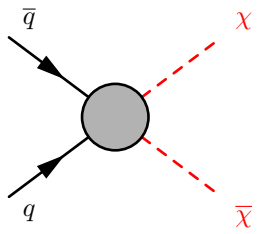

(a) Undetectable

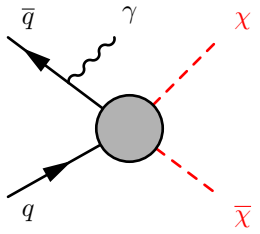

(b) Detectable with an ISR single photon

Fig. 8.1 Feynman diagrams for dark matter pair production at the LHC, assuming the EFT approach (see Chapter 2).

Various BSM models can produce an excess of events in the monophoton final state competing with the Standard Model backgrounds which are mainly electroweak processes, such as large extra dimensions theories, dark matter models, and supersymmetric models. There are two new physics models of interest which will be considered in this thesis.

One is a dark matter model inspired by the gamma-ray line seen in the Fermi-LAT data as introduced in Section 2.2. This gamma-ray line may come from the annihilation of dark matter particles with $m_\chi = 130$ GeV, $\chi\bar{\chi} \to \gamma\gamma$, at a rate of $\langle\sigma v\rangle = 10^{-27}\,\mathrm{cm}^3\mathrm{s}^{-1}$ [30, 34]. A model was suggested in Reference [113] which would allow to confront this line with the

search for $pp \to \gamma^*/Z \to \gamma\chi\bar{\chi}$ at the LHC as illustrated in Figure 8.2. This model uses an *effective field theory* (EFT) [37, 39], in which the mediator is integrated out of the propagator to give a contact interaction with a suppression scale M^*.

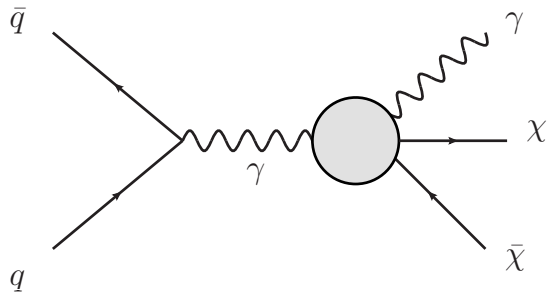

Fig. 8.2 Production of a pair of dark-matter particles ($\chi - \bar{\chi}$) via an effective $\gamma - \gamma - \chi - \bar{\chi}$ vertex.

The effective operator of interest has dimensions of energy of E^7 and involves fermionic WIMPs as described in Reference [114], where the coupling constants of the DM to different pairs of electroweak gauge bosons are given by:

$$\begin{aligned} g_{\gamma\gamma} &= \frac{1}{4\cos^2\theta_w}\frac{k_1+k_2}{M^{*3}}, \\ g_{Z\gamma} &= \frac{1}{2\cos\theta_w \sin\theta_w M^{*3}}\left(\frac{k_2}{\sin^2\theta_w} - \frac{k_1}{\cos^2\theta_w}\right), \end{aligned} \tag{8.1}$$

where θ_w is the weak mixing angle, and where k_1 and k_2 control the strength of the effective coupling of the WIMPs to the U(1) and SU(2) gauge sectors of the Standard Model, respectively.

As the cross section $\sigma_{\gamma^*/Z\to\gamma\chi\bar{\chi}}$ is proportional to $g^2_{\gamma\gamma,Z\gamma}$, the relevant suppression scale M^* is therefore related to the cross section via

$$\sigma(\gamma^*/Z \to \gamma\chi\bar{\chi}) \propto (1/M^*)^6. \tag{8.2}$$

For a given M^*, the cross section is determined by three parameters: the dark matter mass, and the electroweak coupling strengths k_1 and k_2.

The annihilation rate of $\chi\bar{\chi} \to \gamma\gamma$ can be computed [113, 114] as:

$$\langle\sigma v\rangle^{\gamma\gamma} = \frac{4(\hbar c)^2 m_\chi^4 v}{\pi M^{*6}}(k_1\cos^2\theta_w + k_2\sin^2\theta_w)^2, \tag{8.3}$$

where the dark matter velocity v is $\sim 10^{-3}c$. For given k_1 and k_2 values, one can compute the suppression scale M^* which corresponds to the $\langle\sigma v\rangle$ and m_χ given by the Fermi-LAT

result [30, 34], noted as M^*_{Fermi}. The values of k_i considered are 0.01, 0.25, 0.5, 0.75 and 1.0, where $i = 1$ and 2. The values of M^*_{Fermi} computed for each combination of k_1 and k_2 is shown in Figure 8.3. Therefore one can compare the limits on M^* obtained by the ATLAS analysis to M^*_{Fermi} for $m_\chi = 130$ GeV and for each value of k_1 and k_2 in order to probe the nature of the Fermi-LAT result.

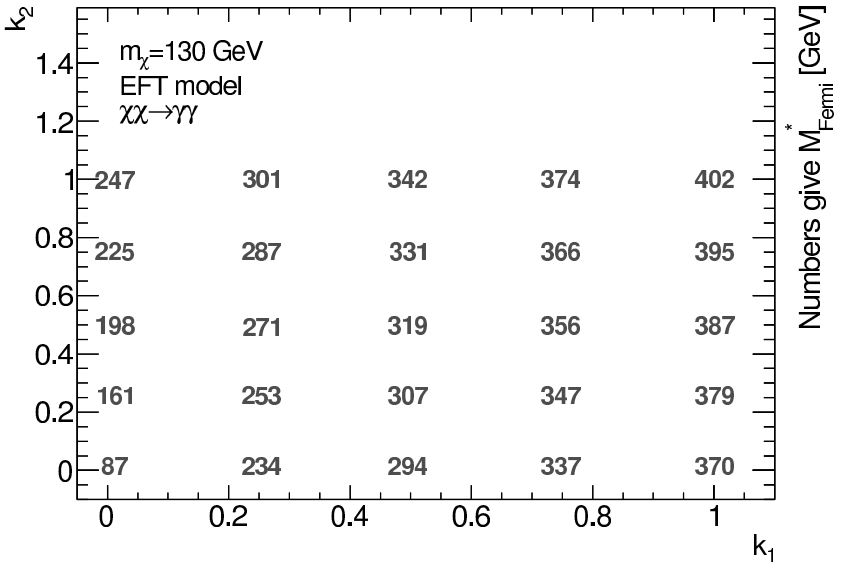

Fig. 8.3 The values of M^*_{Fermi} shown in plane of k_1 and k_2, computed using the Equation (8.3) with $\langle \sigma v \rangle = 10^{-27}\,\text{cm}^3\text{s}^{-1}$ and $m_\chi = 130$ GeV.

The other model considered here is the pair production of mass-degenerate left and right handed first and second generations squarks ($\tilde{q}\bar{\tilde{q}}$) in a R-parity conserving simplified supersymmetric model. In this model, squarks are set to decay directly to a quark (q) and the lightest neutralino ($\tilde{\chi}^0$) with a 100% branching ratio, see Figure 8.4a. All the other supersymmetric particles are decoupled apart from the ones considered in the diagram shown in this figure. This can lead to final states of multiple jets associated with $E_{\text{T}}^{\text{miss}}$ without any lepton; this final state is searched in the so-called "0–lepton" analysis [115]. Upper limits on the cross sections have been set as a function of the squark mass ($m_{\tilde{q}}$) and the lightest neutralino mass ($m_{\tilde{\chi}^0_1}$) by this analysis in this model, see Figure 8.5.

In Figure 8.5, the dashed diagonal indicates an interesting region in the plane of ($m_{\tilde{q}}$, $m_{\tilde{\chi}^0_1}$), where the mass difference between the $\tilde{q}$ and the $\tilde{\chi}^0$ is very small. In this compressed region, where $\Delta M = m_{\tilde{q}} - m_{\tilde{\chi}^0_1} \lesssim 10$ GeV the quarks produced from the squarks decay are often too soft to be reconstructed as jets. In this case, an additional photon radiated either from an initial-state quark or an intermediate squark, see Figure 8.4b, would lead to a final state of $\gamma + E_{\text{T}}^{\text{miss}}$.

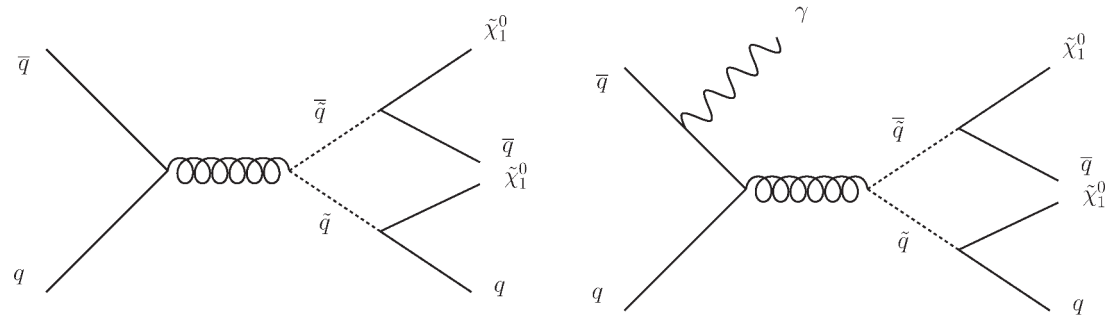

(a) In the 0–lepton analysis.

(b) In the monophoton analysis.

Fig. 8.4 The pair production of squarks in a R-parity conserving simplified supersymmetric model, with a subsequent decay into quarks and neutralinos. The photon in (b) can be radiated either from the initial-state quarks or from the intermediate squarks.

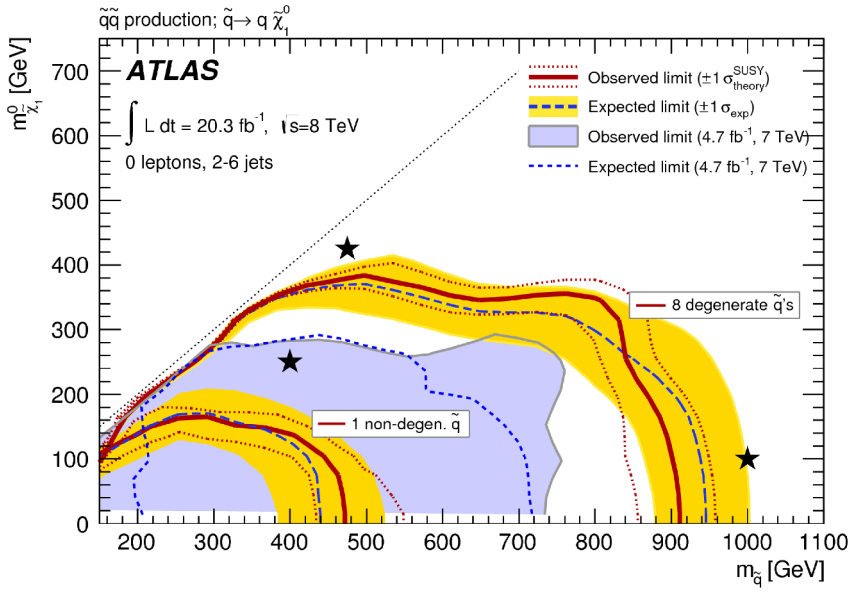

Fig. 8.5 Expected (blue dashed line) and observed (solid red line) exclusion limits at 95% CL are set in the plane of the squark mass ($m_{\tilde{q}}$) and the lightest neutralino mass ($m_{\tilde{\chi}_1^0}$), for the model described in Figure 8.4a using 20.3 fb^{-1} proton-proton collision data collected by ATLAS at 8 TeV. In addition, the limits for one species of non-degenerate squark is shown [115].

8.2 Overview of the monophoton analysis

A monophoton analysis has already been performed by the ATLAS collaboration using the 7 TeV data [116]. The 7 TeV analysis acts as a baseline to perform the monophoton analysis on the 8 TeV data [117]. The 7 TeV analysis defines a signal enriched region by

applying a set of selections to the kinematic observables, which is called *signal region* (SR). The events in the SR are required to have one high p_{T} photon and a large $E_{\mathrm{T}}^{\mathrm{miss}}$, with leptons vetoed. The possibility to have one ISR jet is retained to increase the signal acceptance and reduce the systematic uncertainties related to the modeling of initial-state radiation. The tools and data samples used in the 8 TeV monophoton analysis will be introduced in Chapter 9, and the SR studies are described in Chapter 10.

The irreducible Standard Model background in this monophoton final state is the process $Z(\to \nu\bar{\nu}) + \gamma$, since neutrinos are reconstructed as $E_{\mathrm{T}}^{\mathrm{miss}}$. The other reducible Standard Model background processes are W and Z boson production in association with a photon or a jet and decaying leptonically.

The Standard Model backgrounds with a real photon are dominated by:

- $\gamma + W(e\nu)$: when the electron is not reconstructed, or reconstructed as a photon;
- $\gamma + W(\mu\nu)$: when the muon is not reconstructed;
- $\gamma + W(\tau\nu)$: similarly to the two leptonic processes above, if the tau decays leptonically, or if the tau decays hadronically, as taus are reconstructed as jets in this analysis;
- $\gamma + Z(\ell^+\ell^-)$: when the two leptons are not reconstructed;
- $\gamma +$ jet: events can mimic the signal events via $E_{\mathrm{T}}^{\mathrm{miss}}$ faked from fully or partially mis-reconstructed jet. Although the cross-section of $\gamma +$ jet events is large at the LHC, this fake $E_{\mathrm{T}}^{\mathrm{miss}}$ background is strongly suppressed to be a minor background by the large $E_{\mathrm{T}}^{\mathrm{miss}}$ requirement and by requiring $E_{\mathrm{T}}^{\mathrm{miss}}$ to be far from the jet if there is any.

During the photon reconstruction, other objects, such as jets or electrons, can sometimes be mis-reconstructed as photons due to their similar detector responses; such mis-reconstructed photons are noted as 'fake photons'. The fake photon backgrounds are:

- jet $+ Z(\nu\bar{\nu})$: if the jet is mis-reconstructed as a photon;
- jet $+ W(\ell\nu)$ ($\ell = \mu, \tau$): if the jet is mis-reconstructed as a photon and the lepton is not reconstructed;
- jet $+ W(e\nu)$: if the electron fakes a photon or the jet fakes a photon and the electron is not reconstructed;
- $t\bar{t}$, single-t and diboson: as in the $W +$ jet processes;
- multi-jet and di-jet: if one jet is mis-reconstructed as a photon, and there is a large fake $E_{\mathrm{T}}^{\mathrm{miss}}$.

Backgrounds with a real photon ($V + \gamma$ backgrounds) are estimated using a semi-data-driven method, with three lepton *control regions* (CRs) defined. The CRs are defined to be enriched in a given background while have a strongly suppressed signal, in order to control the Monte Carlo predictions of the backgrounds using the observed data in a fit, called *background-only fit* (see more details in Chapter 11). The background-only fit neglects

any possible signal contamination in the CRs. The SR yield of real photon background are extrapolated from the CRs results. For backgrounds with a fake photon (dominated by $V+$jet backgrounds), they are estimated using data-driven methods since the Monte Carlo simulation does not describe well the faking mechanism. The background estimation technique is validated with a validation region (VR) which is defined to be kinematically close to the SR, acting as a trade-off between minimizing the signal contamination and maximizing statistics. The background estimation technique with its validation and results are described in Chapter 11.

A model-independent upper limit is set at 95% confidence level on the number of events beyond the expected background in the SR, derived from a *model-independent signal fit* (discovery fit) using both the SR and the lepton CRs. A background-only hypothesis is tested in the discovery fit. The model-independent limit setting is described in Chapter 12.

In this thesis, the result is also interpreted as upper limits in the parameter space of two new physics models. These limits are computed from a *model-dependent signal fit* (exclusion fit) which is performed in CRs and SR simultaneously similarly to the discovery fit but with a signal plus background hypothesis tested. One of the two physics models, described in Section 13.1, is an effective field theory of dark matter inspired by the Fermi-LAT results, in which dark matter particles couple to photons via a contact interaction vertex. The other one, described in Section 13.2, is a simplified supersymmetric model describing squark pair production with their subsequent decay into a quark and a neutralino.

Chapter 9

Analysis tools and samples

9.1 Analysis tools

This work is based on an analysis framework, known as **SUSYTools**, which is developed and maintained by the SUSY working group of the ATLAS collaboration. This set of tools is based on the **ROOTCORE** package within the **ROOT** framework [118]; it works in a stand-alone way outside the **Athena** framework.

The **SUSYTools** offer basic algorithms to define the physics objects and make it convenient to apply the latest corrections to the resolution, identification and calibration of these objects. Besides, it provides algorithms for event selections, which can easily be adapted. Adding further analysis tools, even customized packages, is flexible and convenient. Moreover, the variations of the event yields in analysis regions, caused by various sources of systematic uncertainties, can be easily operated with this tool.

9.2 Data and trigger selection

The experimental data used in this thesis were collected in proton-proton collisions at $\sqrt{s} = 8$ TeV by the ATLAS detector in 2012. Only the data taken during the periods when the calorimeters, inner detector and muon system were well functioning are used for physics analysis. These are selected by using good run lists (GRLs) which select the luminosity periods based on the data quality flags. The corresponding integrated luminosity is $20.3\,\text{fb}^{-1}$. The systematic uncertainty on the integrated luminosity is $\pm 2.8\%$, which is derived, following the same methodology as described in details in Reference [119], from a preliminary calibration of the luminosity scale obtained from beam-separation scans performed in November 2012.

The trigger used for signal events selection is an $E_{\mathrm{T}}^{\mathrm{miss}}$ trigger, `EF_xe80_tclcw_tight`, indicating a nominal threshold on $E_{\mathrm{T}}^{\mathrm{miss}}$ of 80 GeV [120]. This trigger computes the value of $E_{\mathrm{T}}^{\mathrm{miss}}$ without considering the muons, as the $E_{\mathrm{T}}^{\mathrm{miss}}$ computation used in this analysis. The trigger efficiency can be expressed as a function of the reconstructed $E_{\mathrm{T}}^{\mathrm{miss}}$, and this trigger is found to be fully efficient for the events selected in this analysis.

9.3 Monte Carlo samples

9.3.1 Event generation

The Monte Carlo (MC) samples for all the considered SM backgrounds are summarized in Table 9.1, where the generators and PDFs used are shown, as well as the cross section information. The SM backgrounds can be classified as $V+\gamma$, $V+$jet and minor backgrounds including top productions, di–boson and $\gamma+$jet.

At parton-level of the event generation, a photon transverse momentum filter is applied to $V+\gamma$ backgrounds, which is set to $p_{\mathrm{T}}^{\gamma} > 70$ GeV for $Z+\gamma$ samples and $p_{\mathrm{T}}^{\gamma} > 80$ GeV for $W+\gamma$ samples, respectively. Besides, the di-lepton invariant mass, $m_{\ell^+\ell^-}$, is required to be larger than 40 GeV in $Z(\to \ell^+\ell^-)+\gamma$ MC samples. The relevant cross sections are given directly from the generator SHERPA which are computed at leading-order (LO) only.

The $V+$jet backgrounds are generated by SHERPA [121] as well, and they are binned in the transverse momentum of the W/Z boson, which are $0 < p_{\mathrm{T}}^{W/Z} < 70$ GeV, $70 < p_{\mathrm{T}}^{W/Z} < 140$ GeV, $140 < p_{\mathrm{T}}^{W/Z} < 280$ GeV, $280 < p_{\mathrm{T}}^{W/Z} < 500$ GeV, and $p_{\mathrm{T}}^{W/Z} > 500$ GeV, respectively. Cross sections given in Table 9.1 for $V+$jet backgrounds are computed at next-to-next-to-leading order (NNLO) in QCD perturbation theory, as described in Reference [122], using the MSTW2008NNLO [78] PDFs.

The $t\bar{t}$ background is generated by POWHEG [123], and its cross section is computed at NNLO with resummation accuracy up to next-to-next-to-leading logarithm (NNLL) [124, 125]. An inclusive MC sample of the single-top production in t-channel is used, which is generated by ACERMC [126]. Single-top productions via Wt-channel and s-channel are generated exclusively by MC@NLO [127, 128]; they are split by the decay mode of the W boson. Cross sections of all the single-top quark productions are computed at NNLO with NNLL accuracy, as detailed in References [129–131].

Three di-boson (WW, WZ and ZZ) samples generated by HERWIG [132, 133] are used, and their cross sections are computed at NLO [134, 135].

The $\gamma+$jet events are generated in three bins of photon transverse momentum, which are respectively $80 < p_{\mathrm{T}}^{\gamma} < 150$ GeV, $150 < p_{\mathrm{T}}^{\gamma} < 300$ GeV, and $p_{\mathrm{T}}^{\gamma} > 300$ GeV. The cross

section of these γ+jet samples are given directly from their generator, PYTHIA 8 [84, 136].

HERWIG version 6.520 is used for simulating the parton shower and fragmentation processes in combination with JIMMY [137] for underlying-event MC for the MC@NLO samples, while PYTHIA 6 version 4.2.6 is used for the POWHEG and ACERMC samples. The proton PDFs used are CTEQ6L1 [79] for the PYTHIA 8 and ACERMC samples, and CT10 [80] for the MC@NLO , SHERPA , and POWHEG samples. The ATLAS underlying-event tune AUET2 [138] is used, except for the $t\bar{t}$ sample, which uses the new Perugia 2011C tune [139]. SHERPA uses its own parton shower, fragmentation and underlying-event model.

Channel	Generator	PDF set	Cross section normalization	Cross section [pb]
$Z(\nu\bar{\nu})+\gamma$	SHERPA 1.4.1	CT10	LO	0.762
$W(e\nu)+\gamma$	SHERPA 1.4.1	CT10	LO	0.719
$W(\mu\nu)+\gamma$	SHERPA 1.4.1	CT10	LO	0.718
$W(\tau\nu)+\gamma$	SHERPA 1.4.1	CT10	LO	0.720
$Z(e^+e^-)+\gamma$	SHERPA 1.4.1	CT10	LO	0.186
$Z(\mu^+\mu^-)+\gamma$	SHERPA 1.4.1	CT10	LO	0.186
$Z(\tau^+\tau^-)+\gamma$	SHERPA 1.4.1	CT10	LO	0.186
$W(e\nu)+$jet	SHERPA 1.4.1	CT10	NNLO	12192.8
$W(\mu\nu)+$jet	SHERPA 1.4.1	CT10	NNLO	12188.0
$W(\tau\nu)+$jet	SHERPA 1.4.1	CT10	NNLO	12170.0
$Z(\nu\bar{\nu})+$jet	SHERPA 1.4.1	CT10	NNLO	6706.4
$Z(e^+e^-)+$jet	SHERPA 1.4.1	CT10	NNLO	1237.9
$Z(\mu^+\mu^-)+$jet	SHERPA 1.4.1	CT10	NNLO	1243.8
$Z(\tau^+\tau^-)+$jet	SHERPA 1.4.1	CT10	NNLO	1245.3
$t\bar{t}$	POWHEG r2129	CT10	NNLO+NNLL	137.38
Single-t Wt-channel	MC@NLO 4.06	CT10	NNLO+NNLL	22.373
Single-t s-channel	MC@NLO 4.06	CT10	NNLO+NNLL	1.818
Single-t t-channel	ACERMC 3.8	CTEQ6L1	NNLO+NNLL	28.393
$\gamma+$jet, $p_{\mathrm{T}}^{\gamma} > 80$ GeV	PYTHIA 8	CTEQ6L1	LO	932.91
WW	HERWIG 6.520	CT10	NLO	20.864
ZZ	HERWIG 6.520	CT10	NLO	1.539
WZ	HERWIG 6.520	CT10	NLO	6.970

Table 9.1 Cross sections for the Standard Model backgrounds at $\sqrt{s} = 8$ GeV considered in this analysis. The generator efficiency is included in the cross-section. Only semi-leptonic decays are considered for the diboson and $t\bar{t}$ samples and the W is requested to decay leptonically in the s- and t-channel single-top samples.

The EFT DM signal samples are generated using MADGRAPH 5 1.4.2 [140] with PYTHIA 8 using the LO PDF set CTEQ6L1. M^* is set at a nominal value of 175 GeV. In addition to the 130 GeV WIMP mass compatible to the Fermi line, two other masses (10 GeV

and 1000 GeV) are also generated in order to also test a more generic dark matter model not necessarily connected with the Fermi-LAT result. For each WIMP mass, 25 independent samples were produced with different k_1 and k_2, where $k_i \in 0.01, 0.25, 0.5, 0.75, 1.0$ and $i = 1, 2$. All the signal samples are asked to have photon with $p_{\mathrm{T}} > 120$ GeV and $|\eta| > 2.5$ at generator level.

The compressed squark signal samples are generated with MADGRAPH 5 [140] version 1.5.11 with showering and hadronization modeled by PYTHIA 6 [136] version 4.2.7 using CTEQ6L1 [79] PDFs; the radiated photon is required at parton-level with $p_{\mathrm{T}} > 80$ GeV and $|\eta| < 2.5$. The signal samples are generated on the basis of the existing grid used in the "0–lepton" analysis in the phase space of $m_{\tilde{q}}$ and $m_{\tilde{\chi}_1^0}$, and they are extended to the more compressed region of the mass spectrum.

9.3.2 Detector simulation

All the $V + \gamma$, di-boson, $\gamma +$ jet, the Wt-channel and s-channel of the single-top productions use the full detector simulation chain based on `Geant4`. The MC samples of single-top t-channel production and the inclusive top pair production are based on a fast simulation, `Atlfast-II` , introduced in Section 6.1. For the $V +$ jet backgrounds, some of them uses the `Atlfast-II` simulation for larger statistics, whilst the rest are simulated with the full simulation chain.

All signal samples are produced with the `Atlfast-II` simulation.

In-time pile-up is simulated by overlaying minimum bias events, which are generated by PYTHIA 8 with MSTW2008LO PDF set and A2 tune, onto the hard scattering event with $\langle\mu\rangle$ (the mean number of interactions per crossing, see Chapter 4) ranging from 0 to 40. The overlaying process also covers the impact of out-of-time pile-up.

As the distribution of $\langle\mu\rangle$ differs between simulation and data, it is necessary to apply further corrections to the pile-up overlaid process in the simulation samples by re-weighting $\langle\mu\rangle$ according to the data measurement. Besides, another re-weighting is implemented for the simulated events which corrects the MC description of the vertex position along the z–axis to that observed in the data.

Atlfast–II and full simulation samples comparison

Both `Atlfast-II` and full `GEANT4` simulation samples are used in this analysis. Since this analysis is sensitive to the objects reconstructed in the calorimeters which is parameterized in fast simulation, it is important to validate the fast simulation samples against the fully simulated samples.

The validation study compares a sample produced with `Atlfast-II` to its corresponding fully simulated sample. The study is based on the SR defined in the 7 TeV analysis, which is detailed in Section 10.3.1.

The cutflow is checked, which indicates which fraction of the events in the dataset survives each SR selection cut. Four pairs of samples were checked which are all dark matter signal samples. The cutflows of the `Atlfast-II` and full `Geant4` samples show good agreement within one standard statistical deviation. The cutflow is further checked by quantifying the difference on the number of events left after each selection cut as $R = |N_{Full} - N_{Atlfast}|/N_{Full}$. All the differences are less than 5%.

The following discriminant kinematic variables used to define the SR are also checked just before implementing the corresponding selection cut:

- distribution of the $E_{\mathrm{T}}^{\mathrm{miss}}$ and the transverse momentum of the most energetic (leading) photon;
- the photon isolation variable, TopoEtcone40$_{corr}$;
- the numbers of photons, jets, electrons and muons per event;
- the azimuthal angle (ϕ) between the leading jet and $E_{\mathrm{T}}^{\mathrm{miss}}$;
- the azimuthal angle (ϕ) between the leading photon and $E_{\mathrm{T}}^{\mathrm{miss}}$.

For a given discriminant variable, the `Atlfast-II` and full `Geant4` distributions are compared. As an example, Figure 9.1 shows the comparisons of the distributions of $E_{\mathrm{T}}^{\mathrm{miss}}$ and the photon isolation variable, with one pair of `Atlfast-II` and full `Geant4` samples. In the bottom part of each plot, a ratio between the number of events in the `Atlfast-II` and the full `Geant4` samples is shown. All the variables show good agreement between `Atlfast-II` and full `Geant4` samples with a ratio of 1 within one standard statistical deviation, except for the the photon isolation variable, which needs to be further checked. This conclusion is cross checked for the other three pairs of `Atlfast-II` and full `Geant4` samples; they give the same results.

Central photon study

The distribution of the photon isolation variable, TopoEtcone40$_{corr}$, in Figure 9.1 seems to indicate a discrepancy between the `Atlfast-II` and full `Geant4` samples.

In order to understand better this potential discrepancy, TopoEtcone40$_{corr}$ is checked for central ($|\eta^{\gamma}| < 1.37$) and end-cap ($|\eta^{\gamma}| > 1.52$) photons, separately. The photon candidates are `tight` photons with $p_{\mathrm{T}}^{\gamma} > 125$ GeV.

Figure 9.2 presents the distributions of the isolation variable with its statistical uncertainty, where the top histogram accounts for the central photons and the bottom one for the end-cap photons. The top histogram shows a good agreement between the `Atlfast-II` and

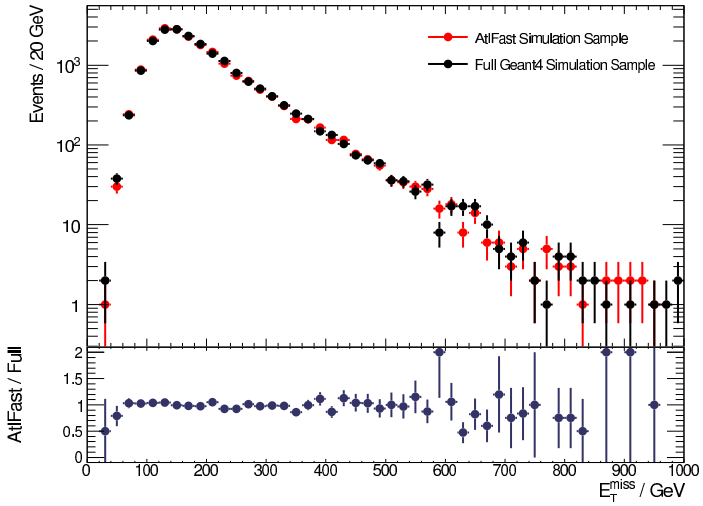

(a) Comparison of $E_{\mathrm{T}}^{\mathrm{miss}}$ between an `Atlfast-II` sample and the relevant full Geant4 sample.

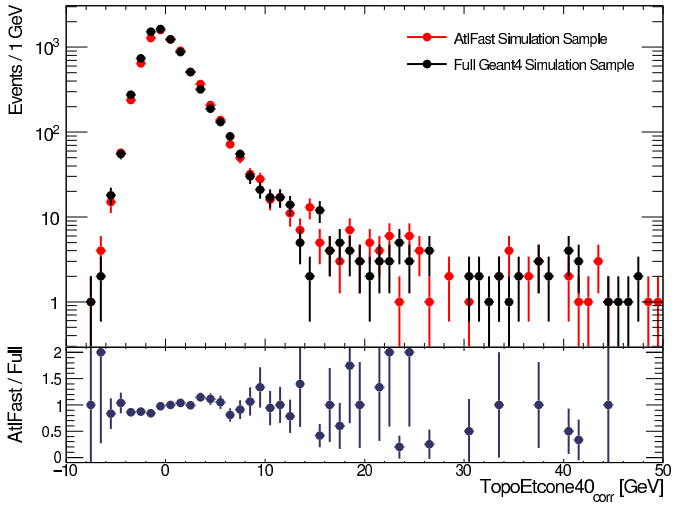

(b) Comparison of the photon isolation variable, TopoEtcone40$_{corr}$, between an `Atlfast-II` sample and the relevant full Geant4 sample.

Fig. 9.1 Comparison of `Atlfast-II` and full Geant4, based on one dark matter signal sample.

the full Geant4 samples. However, a significant difference is shown in the bottom histogram: the end-cap photons from the Atlfast-II events are reconstructed with larger values of the isolation variable compared to that of the full Geant4 events.

The Atlfast-II simulation can hence only be used in the monophoton analysis if one requests central photons ($|\eta| < 1.37$).

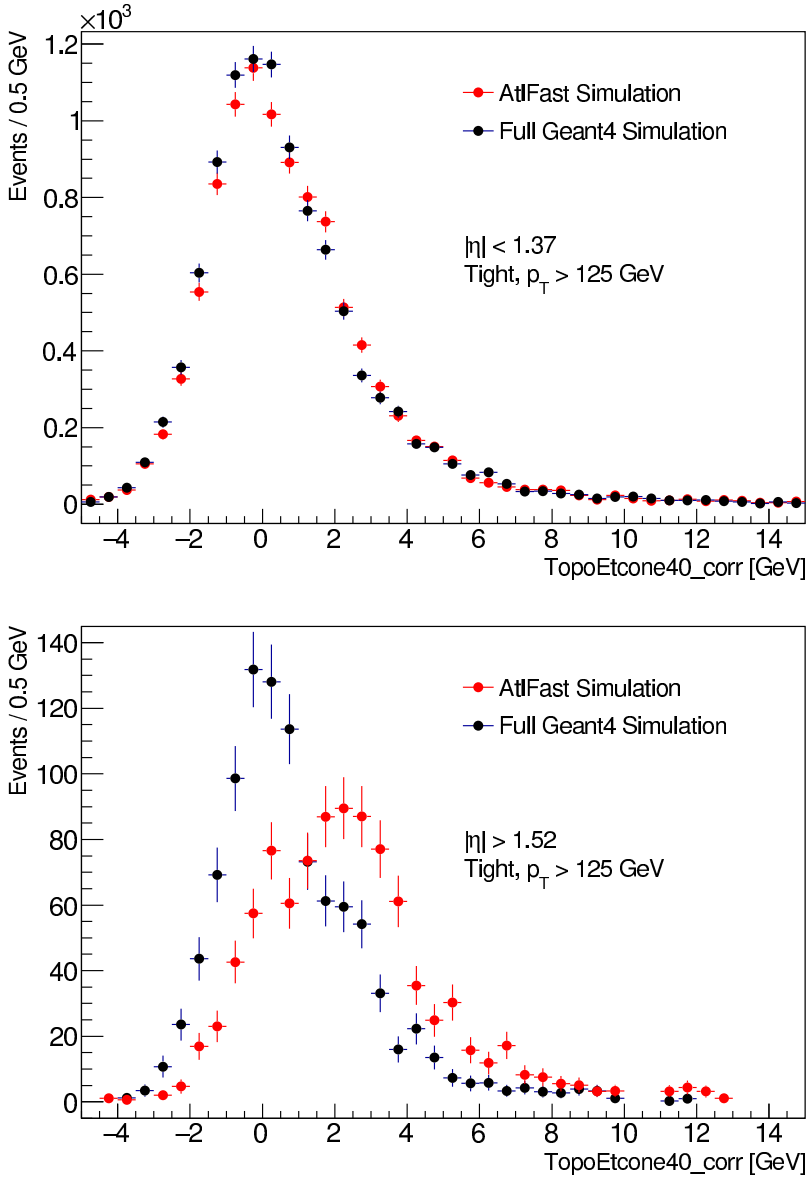

Fig. 9.2 TopoEtcone40$_{corr}$ distributions is compared from samples of Atlfast-II to full simulation, where the top plot is for central photons ($\eta < 1.37$) and the bottom one, for end-cap photons ($\eta > 1.52$).

Chapter 10

Signal region definition

The signal region used in the monophoton analysis at 8 TeV is defined in this chapter. The definition of the object candidates will be introduced in Section 10.1. Mis-reconstructed events are rejected in a pre-selection step introduced in Section 10.2. The full optimization study to define the SR with improved signal sensitivity is introduced in Section 10.3.

10.1 Object candidates definition

Both converted and un-converted photons are considered in this analysis. They are reconstructed following the standard ATLAS reconstruction algorithms and identified with `loose` requirements; besides, recommended procedures for calibrations on energy scale and resolution are applied; see more details in Section 7.1. Further cleaning cuts are applied to reject bad quality photons arising from instrumental issues, see Section 7.1. The photon candidates must satisfy $p_{\mathrm{T}}^{\gamma} > 10$ GeV and $|\eta^{\gamma}| < 2.37$, while being outside the calorimeter transition region $1.37 < |\eta^{\gamma}| < 1.52$.

Electrons used in this analysis are reconstructed and identified using the `medium++` criterion, and their energy calibrated as described in Section 7.2. Similarly to photons, electrons can be mis-reconstructed due to instrumental issues, thereby relevant quality cuts are applied to reject such bad electrons, see Section 7.2. The η of the electron (η^{el}) is derived from its associated track when the track is reconstructed from at least 4 hits found in the pixel detector and SCT, otherwise, the TopoCluster used to reconstruct the electron is used. The electron candidates are further required to have $p_{\mathrm{T}}^{el} > 7$ GeV and $|\eta^{el}| < 2.47$.

The CB and ST muons, as introduced in Section 7.3, are taken into account in this analysis. Further quality requirements are applied on the ID track matched to the reconstructed muon:

- the sum of the number of hits found in the pixel detector and the number of dead pixel sensors crossed by the track is asked to be at least one;
- more than five hits must be found in the SCT;
- the number of holes in the SCT and pixel detectors which are crossed by the track must be no more than three;
- in the region $0.1 < |\eta| < 1.9$, there must be more than five TRT hits, out of which the outlier hits must be less than 90%.

Moreover, the muon candidates are required to have $p_{\mathrm{T}}^{\mu} > 6$ GeV and $|\eta^{\mu}| < 2.5$.

The jet candidates are reconstructed from TopoClusters using the default anti-k_{t} algorithm with a radius parameter $R = 0.4$. The energy calibration has been done at cluster level via LCW (see Section 7.4). Further calibrations are applied after the jet area offset corrections, which are an η direction correction and a jet energy scale (JES) calibration. Throughout the 8 TeV data collection, some tile modules needed to be temporarily or permanently masked. Therefore, a correction to the energy scale needs to be applied for jets containing such modules. The jet candidates are required to have $p_{\mathrm{T}} > 30$ GeV and $|\eta| < 4.5$. In order to avoid double counting energy from an electron or a photon as a jet, an overlap removal is applied to the jet candidates by requiring that the distance between the jets and the closest electron or photon candidates must be no less than $\Delta R = 0.2$.

The missing transverse energy $E_{\mathrm{T}}^{\mathrm{miss}}$ computation is introduced in Section 7.5 as a variant of the `MET_Egamma10NoTau_RefFinal`. The energy of all the physics objects used in the $E_{\mathrm{T}}^{\mathrm{miss}}$ computation are re-calibrated as described above.

10.2 The event pre-selection

Events are preselected by the following quality cuts:

1. Data quality: The events must be recorded during periods when the detector performed well according to the Good Run List(GRL);
2. Trigger: The events must pass the `EF_xe80_tclcw_tight` trigger requirement;
3. Good vertex: The primary vertex of the events must be reconstructed with at least five associated tracks. The primary vertex is defined as the vertex with the highest sum of the squared transverse momenta of its associated tracks;
4. Event cleaning:
   (a) Events recorded with noise bursts in the LAr calorimeters are rejected;
   (b) Incomplete events coming from a reset of the readout system are rejected.
   (c) Events are rejected if they are recorded with data corruption from tile channels;
   (d) As introduced in Section 10.1, a correction is applied to the jet energy scale to

account for the influence of masked tile modules. However, since not all the masked modules are simulated in the standard ATLAS MC samples, any event containing a jet candidate falling in a masked tile module was removed;

(e) Events with any jet candidate identified as VeryLoose bad jet (see Section 7.4) are rejected to reduce the fake $E_{\mathrm{T}}^{\mathrm{miss}}$ contribution;

10.3 The signal region event selection

The SR is defined for $\sqrt{s} = 8$ TeV by applying further selections on the preselected events. It is developed based on the selections used in the published $\sqrt{s} = 7$ TeV monophoton analysis introduced in Section 10.3.1. The full SR development first focused on optimizing the signal over background ratio, and later on increasing the statistics by loosening specific criteria without affecting the significance (see Section 10.3.2).

10.3.1 The 7 TeV event selection

The SR selection used in the 7 TeV analysis is described here. They will be used as a baseline in the next section.

- The trigger used to select data is a $E_{\mathrm{T}}^{\mathrm{miss}}$ trigger with a threshold of 70 GeV and it does not include muons in the $E_{\mathrm{T}}^{\mathrm{miss}}$ computation;
- Events are asked to have a large transverse missing energy with $E_{\mathrm{T}}^{\mathrm{miss}} > 150$ GeV;
- The event must contain a photon candidate with $p_T^{\gamma} > 150\,\mathrm{GeV}$;
- In order to reduce the possibility to select events with a signal photon mis-reconstructed from an electron or a jet, the highest p_{T} (leading) photon is required to pass the tight identification criteria and isolation requirement of $TopoEtcone40_{corr} < 5$ GeV;
- As in the signal the photon and $E_{\mathrm{T}}^{\mathrm{miss}}$ are expected to be more in a back-to-back configuration, the leading photon is then required to be well separated from the $E_{\mathrm{T}}^{\mathrm{miss}}$ in the transverse plane by $\Delta\phi(\gamma, E_{\mathrm{T}}^{\mathrm{miss}}) > 0.4$;
- It is introduced in Chapter 8 that events are allowed to have at most one jet. The fake $E_{\mathrm{T}}^{\mathrm{miss}}$ backgrounds, such as $\gamma+$jet and di-jet productions, can mimic the signal events if one jet is mis-reconstructed or partially mis-reconstructed as $E_{\mathrm{T}}^{\mathrm{miss}}$. Such backgrounds are suppressed mainly because of the large $E_{\mathrm{T}}^{\mathrm{miss}}$ requirement. A further suppression is implemented by requesting events with one jet candidate to pass the jet–$E_{\mathrm{T}}^{\mathrm{miss}}$ separation cut of $\Delta\phi(\mathrm{jet}, E_{\mathrm{T}}^{\mathrm{miss}}) > 0.4$, since the fake $E_{\mathrm{T}}^{\mathrm{miss}}$ backgrounds usually have a single jet close to the fake $E_{\mathrm{T}}^{\mathrm{miss}}$;
- Electrons with $p_T^{el} > 20$ GeV and muons with $p_T^{\mu} > 10$ GeV are vetoed to suppress

the leptonic backgrounds, such as $W(l\nu)+\gamma$.

10.3.2 The event selection optimization

In order to maximize the signal to background ratio in the SR, some optimization studies are performed based on the nominal SR definition from the 7 TeV analysis. The signal samples used in this study are from a simplified supersymmetric model (which will be described in Section 13.2) describing squark pair production with their subsequent decay into a quark and a neutralino. The mass spectrum of the squark and the neutralino is considered to be so compressed that the quark is too soft to be reconstructed as a jet. Four signal samples with different kinematic profiles are used, and will be referred to as 'squark' or 'compressed squark' in the following description. All the backgrounds used in this study are estimated directly from MC simulation.

The discriminant variables checked are the jet multiplicity N_{jets}, $E_{\text{T}}^{\text{miss}}$ and η^{γ}. Their distributions in the 7 TeV SR (nominal SR) are first checked by comparing the signal to the backgrounds. The distributions are normalized to 1 in order to compare their shapes directly. The normalized distributions of all the three variables are shown in Figures 10.1 – 10.3. A specific loose nominal SR is defined with the SR jet multiplicity requirement released from $N_{\text{jets}} \leq 1$ to $N_{\text{jets}} \leq 10$.

Figure 10.1 shows that the squark signal events tend to have more central photons than the backgrounds. The $E_{\text{T}}^{\text{miss}}$ distributions, shown in Figure 10.2, also differ between the squark signal events and the backgrounds, suggesting that an increased $E_{\text{T}}^{\text{miss}}$ cut may help to strengthen the signal significance. Figure 10.3 contains the jet multiplicity distributions, which indicate that the squark signal events with larger $m_{\tilde{q}} - m_{\tilde{\chi}_1^0}$ contain more jets with respect to the backgrounds. This is because the quark from the $\tilde{q}$ decay is more likely to be reconstructed as a jet when $m_{\tilde{q}} - m_{\tilde{\chi}_1^0}$ increases.

In order to quantify the signal strength in the SR, the following significance computation is used:

$$\begin{aligned} &\text{Zn} = \text{erf}^{-1}\left(1 - 2 \times p\right) \times \sqrt{2}, \\ &p = \text{P}(N \geq N_{\text{observed}} | \text{ background only hypothesis }), \end{aligned} \tag{10.1}$$

where N follows a Gaussian probability density function with the Standard Model background expectation N_{SM} as the mean value, and its overall systematic uncertainty ΔN_{SM} as one standard deviation; $N_{observed}$ is the result of a counting experiment following a Poisson probability density function, treating the sum of the signal and background MC estimates as the mean value.

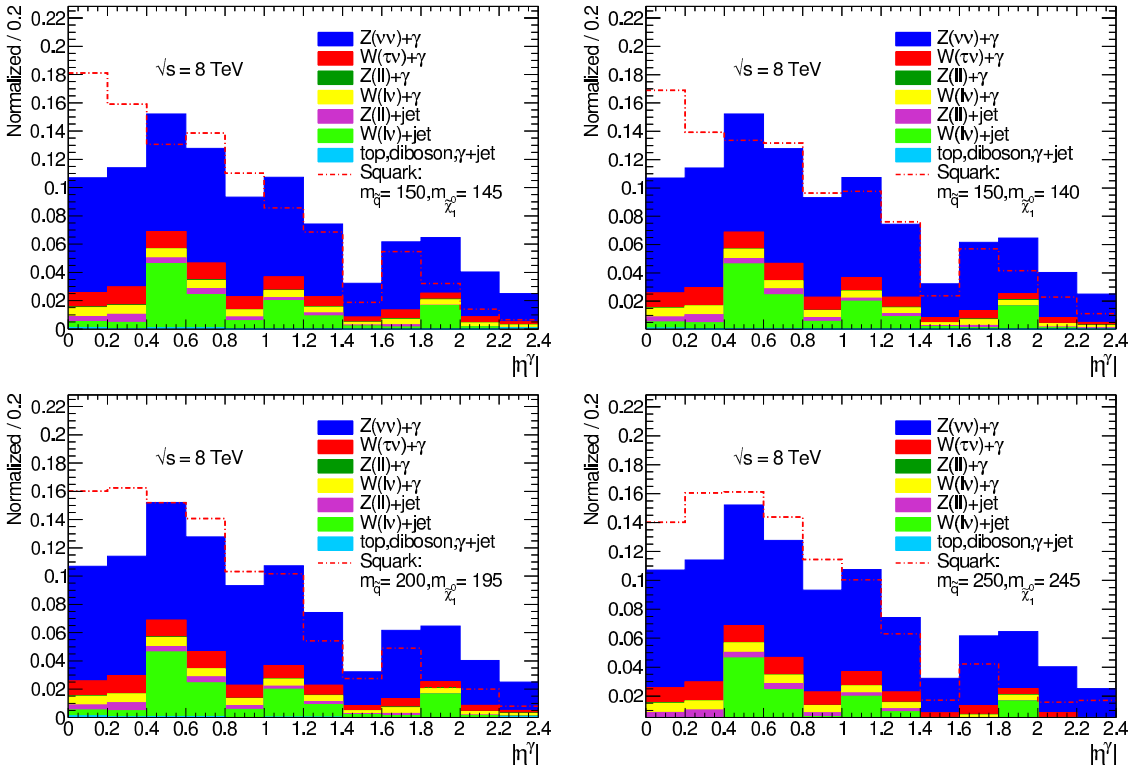

Fig. 10.1 The normalized distributions of $|\eta^{\gamma}|$ of all the backgrounds and different compressed squark signal points in the nominal 7 TeV SR (with $|\eta^{\gamma}| < 2.37$ and $|p_{\mathrm{T}}^{\gamma}| > 150$ GeV). The masses shown in the legend are expressed in GeV.

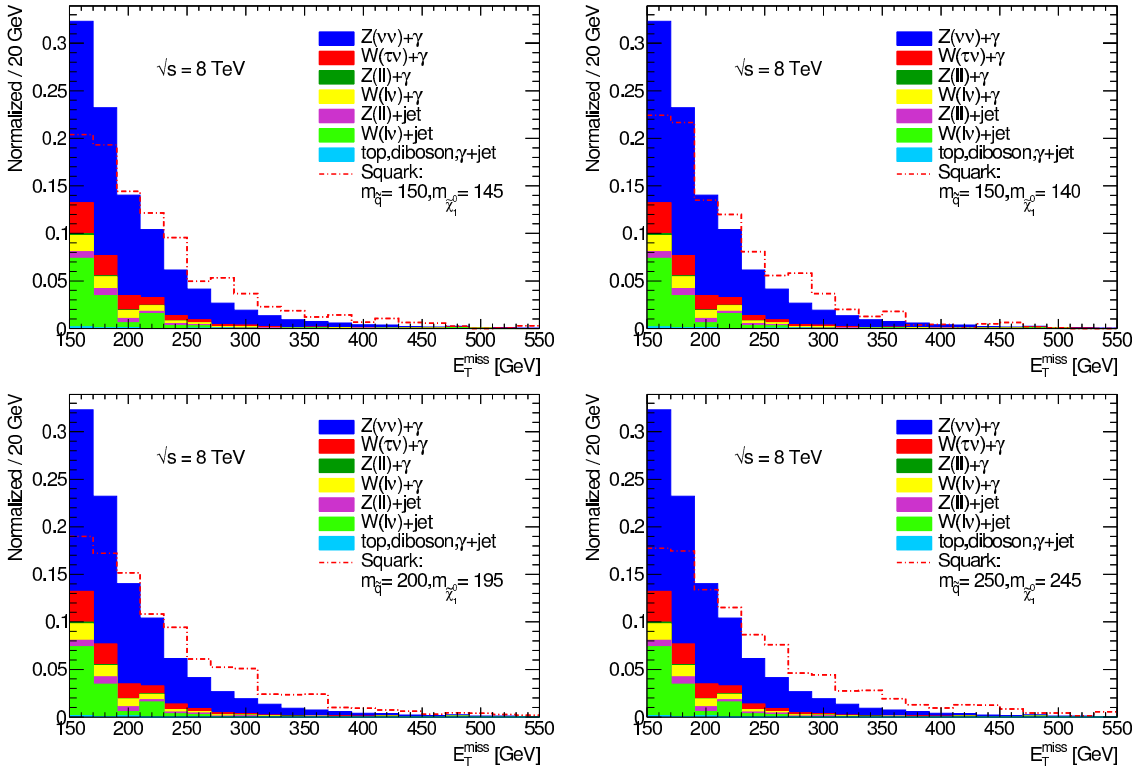

Fig. 10.2 The normalized distributions of $E_{\mathrm{T}}^{\mathrm{miss}}$ of all the backgrounds and a compressed squark signal in the nominal 7 TeV SR (with $|\eta^{\gamma}| < 2.37$ and $|p_{\mathrm{T}}^{\gamma}| > 150$ GeV). The masses shown in the legend are expressed in GeV.

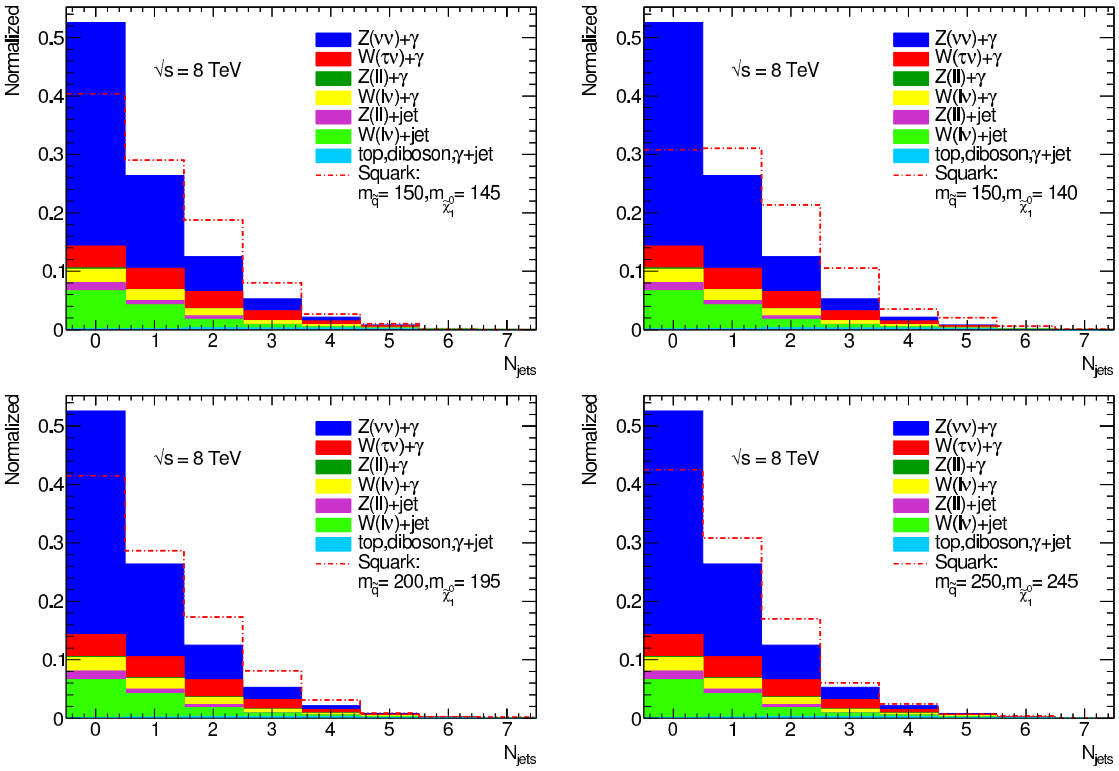

Fig. 10.3 The normalized distributions of N_{jets} in a loose nominal SR (with the jet multiplicity cut released to allow up to 10 jets) of all the backgrounds and a compressed squark signal (with $|\eta^{\gamma}| < 2.37$ and $|p_{\mathrm{T}}^{\gamma}| > 150$ GeV). The masses shown in the legend are expressed in GeV.

Figures 10.4 – 10.6 compare the selected signal (red dash line) to the backgrounds for an integrated luminosity of 20.3 fb^{-1}. The bottom panels illustrate the significance (Zn) as a function of different cuts on the discriminant variables. The overall systematic uncertainty on the background used to compute the significance is set to a nominal value of 10%, as inspired by the overall 7.3% systematic uncertainty from the 7 TeV analysis [116]. It suggests that the signal strength would increase by tightening cuts on $|\eta^{\gamma}|$ and $E_{\mathrm{T}}^{\mathrm{miss}}$, and loosening the cut on N_{jets}.

The jet multiplicity cut will not be loosened, because other signal processes considered in this analysis do not have as many jets as the squark scenario, such as dark matter models (see description in Section 10.3.3 with Figure 10.10). Besides, allowing more jets can lead to an increase of backgrounds like $\gamma+$jet, and thus change the background estimation strategy.

According to the background estimation strategy introduced in Section 11, the final systematic uncertainty estimated in the SR is proportional to the data statistics in the control region (CR). The statistics in the CRs decrease when tightening the SR cuts, as the CRs are built to be as close as possible to the SR. This will influence the significance computed above, which takes a nominal systematic uncertainty of 10%. In this case, two independent and complementary studies were performed on tighter SRs, in order to determine if a tighter SR would indeed increase the significance or not. The tighter SRs are defined with a lower $|\eta^{\gamma}|$ requirement and higher $E_{\mathrm{T}}^{\mathrm{miss}}$ requirement.

The photon $|\eta^{\gamma}|$ requirement is lowered to $|\eta^{\gamma}| < 1.37$ in the SR for the following reasons. First of all, it improves the signal sensitivity as shown in Figure 10.4. Secondly, since the $|\eta^{\gamma}|$ is well described by the MC in the CRs, the cut can be kept at 2.37 in the CRs so as to maintain the statistics for background estimation. One can also note that lowering the $|\eta|$ cut allows the use of `Atlfast-II` for simulating the signal samples, as discussed in Section 9.3.2.

Therefore, tighter SRs to be checked are defined with the maximal $|\eta^{\gamma}|$ requirement ranging from 1 to 1.37, and the minimal $E_{\mathrm{T}}^{\mathrm{miss}}$ from 160 GeV to 200 GeV. A 3×5 grid of tighter SRs were checked in the phase space of minimal $E_{\mathrm{T}}^{\mathrm{miss}}$ and maximal $|\eta^{\gamma}|$ in both studies.

In a first study, the significance of the tighter SRs are computed with the systematic uncertainty varied to determine the maximal systematic uncertainty for a given tighter SR to maintain the improved significance. The other study evaluates the increase in statistical uncertainty of the data in the CRs, assuming that the loss of events in the CRs is proportional to the one in the SR for a given tighter SR. The SR data for 20.3 fb^{-1} is estimated from the MC prediction of backgrounds only.

Figure 10.7 shows the statistical uncertainty in each tighter SR estimated by $1/\sqrt{N_{SM}}$,

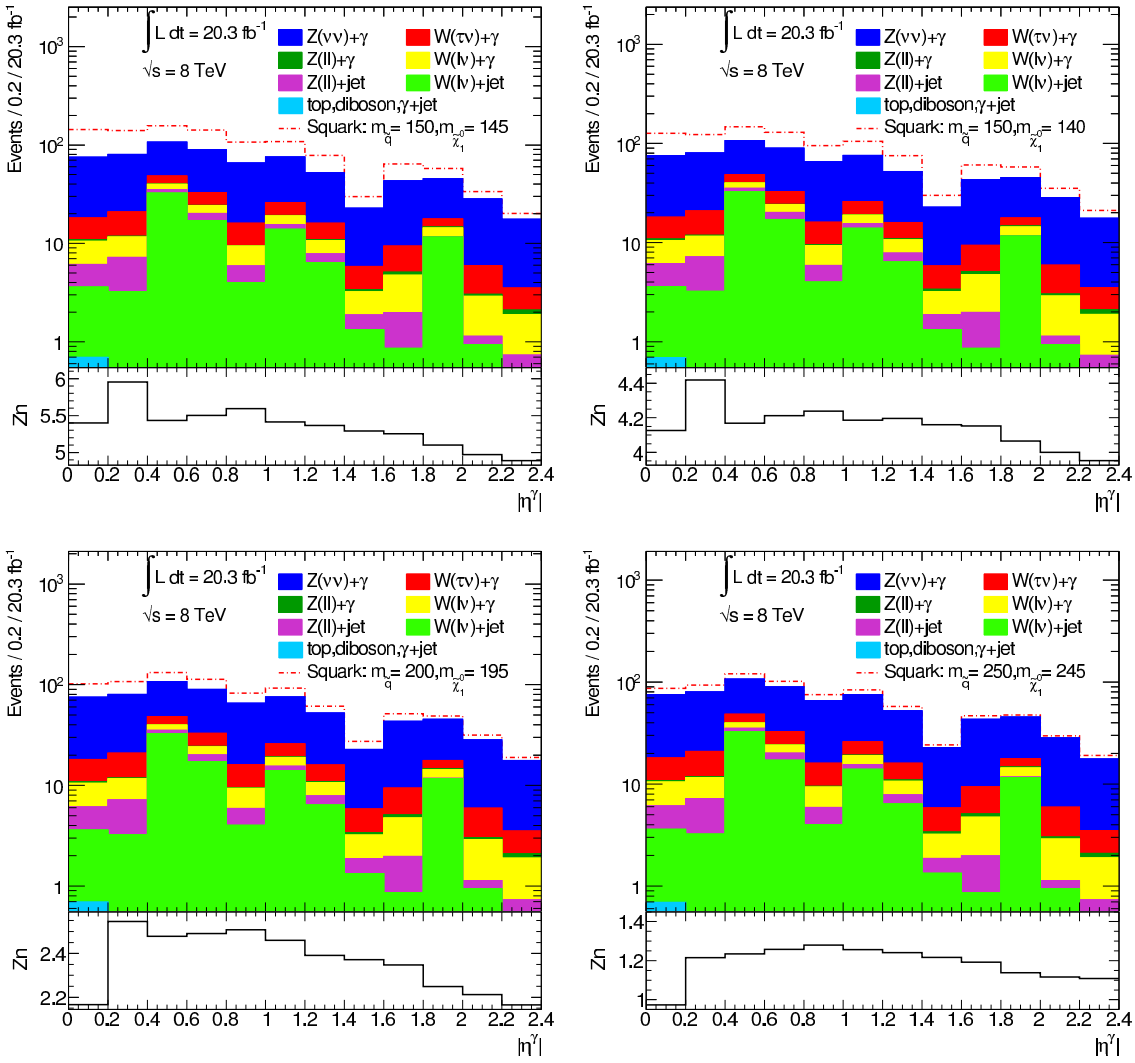

Fig. 10.4 The distributions of $|\eta^{\gamma}|$ in the SR of all the backgrounds with a compressed squark signal. The bottom panel shows how the significance changes as a function of the cut value on this variable. The masses shown in the legend are expressed in GeV.

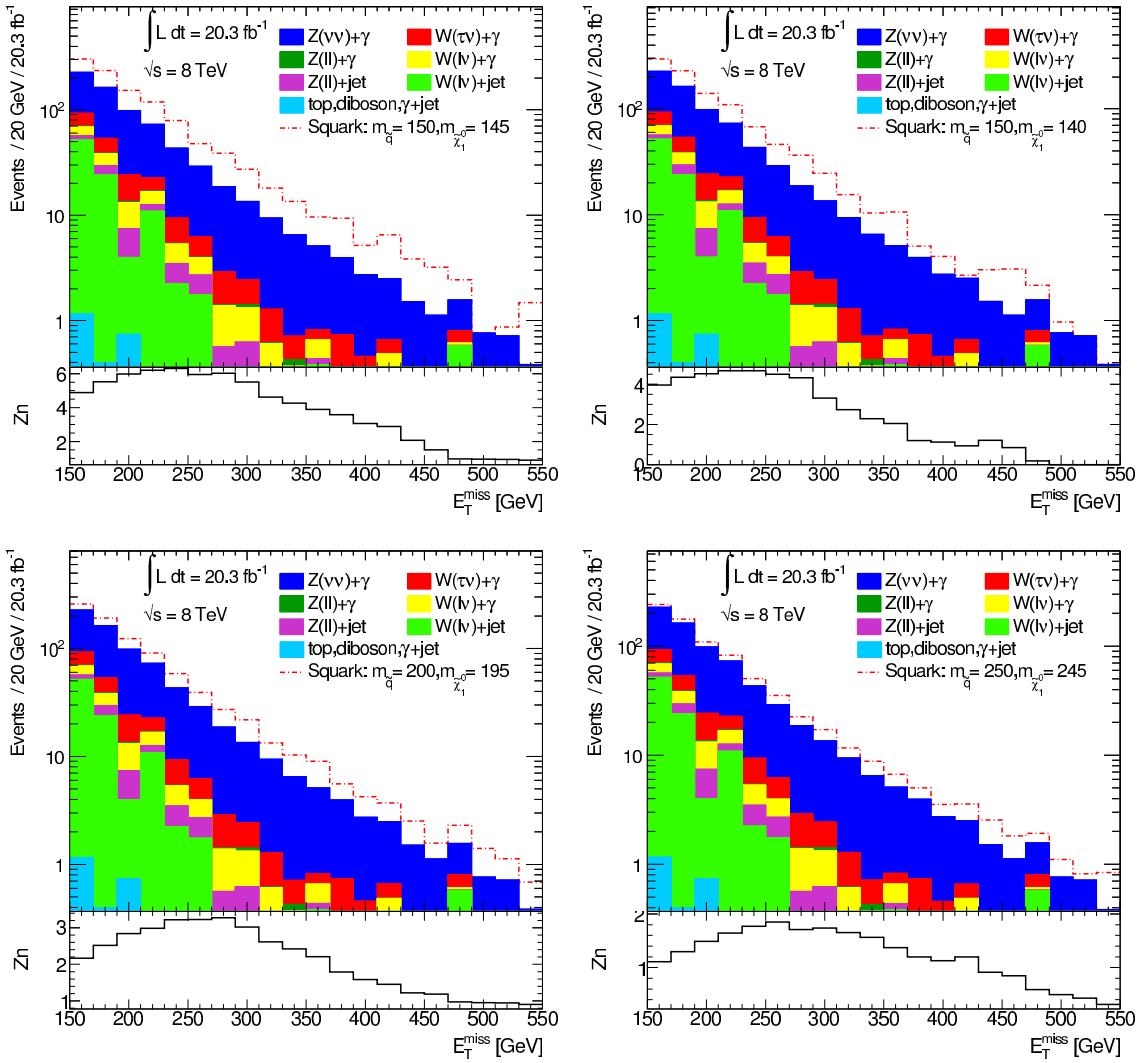

Fig. 10.5 The distributions of $E_{\mathrm{T}}^{\mathrm{miss}}$ in the SR of all the backgrounds with a compressed squark signal. The bottom panel shows how the significance changes as a function of the cut value on this variable. The masses shown in the legend are expressed in GeV.

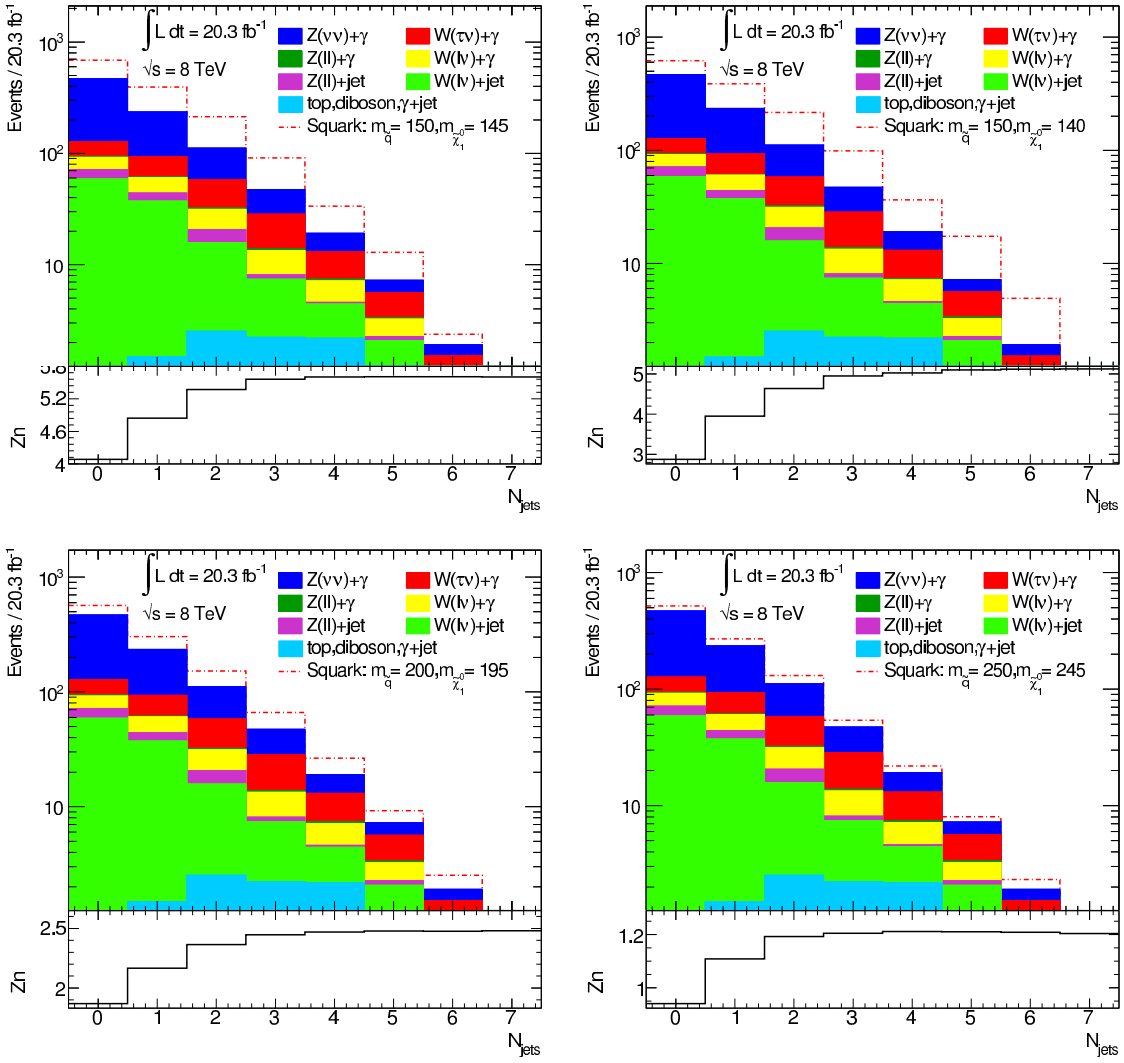

Fig. 10.6 The distributions of N_{jets} in a loose nominal SR (with the jet multiplicity cut released to 10) of all the backgrounds and a compressed squark signal. The bottom panel shows how the significance changes as a function of the cut value on this variable. The masses shown in the legend are expressed in GeV.

to be compared to the 3.8% statistical uncertainty of the nominal SR. In order to decide on the best SR definition, one then needs to check whether or not, for a given tighter cut, the increase in the CR statistical uncertainty brings the total systematic uncertainty above the value for which no gain in significance is obtained. The full compressed squark signal grid is used, which is in the parameter space of the squark mass $m_{\tilde{q}}$ and the mass difference between the squark and the neutralino $\Delta M = m_{\tilde{q}} - m_{\tilde{\chi}_1^0}$.

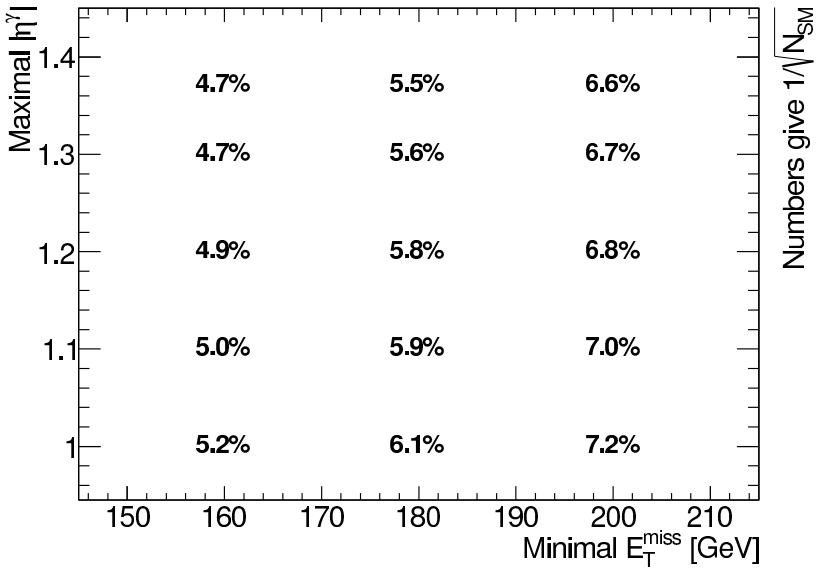

Fig. 10.7 The statistical uncertainty in various tight SRs in a 3×5 grid of minimal $E_{\mathrm{T}}^{\mathrm{miss}}$ and maximal $|\eta^{\gamma}|$. The nominal SR has a 3.8% statistical uncertainty.

For example, for the tighter SR point with $E_{\mathrm{T}}^{\mathrm{miss}} > 180$ GeV and $|\eta^{\gamma}| < 1.37$ in the figure, the uncertainty is increased by a factor of ~ 1.45 (by comparing 5.5% to the nominal 3.8%). Figure 10.8 shows the change in significance in this tighter SR with respect to the nominal SR (computed with an overall 10% systematic uncertainty) for all the SUSY signal samples. The tighter SR significance is computed with an overall systematic uncertainty of 12% (top) and 14% (bottom), respectively.

Most of the ratios in the squark signal samples of interest (with $\Delta M \leq 10$ GeV) are positive for 12% (top figure) while they become negative for 14% (bottom figure). The signal points at $m_{\tilde{q}} = 100$ GeV in the compressed region expect to have very high significance ($Zn > 8$), while they do not expect to have large significance ($Zn < 1$) for large squark mass ($m_{\tilde{q}} \sim 300$ GeV); therefore one can still conclude that the maximal systematic uncertainty allowed in this tighter SR is 12–14%, which is 1.2–1.4 times the nominal 10% systematic uncertainty. This tighter SR is excluded as the systematic uncertainty is allowed to be increased by a factor smaller than the expected ~ 1.45.

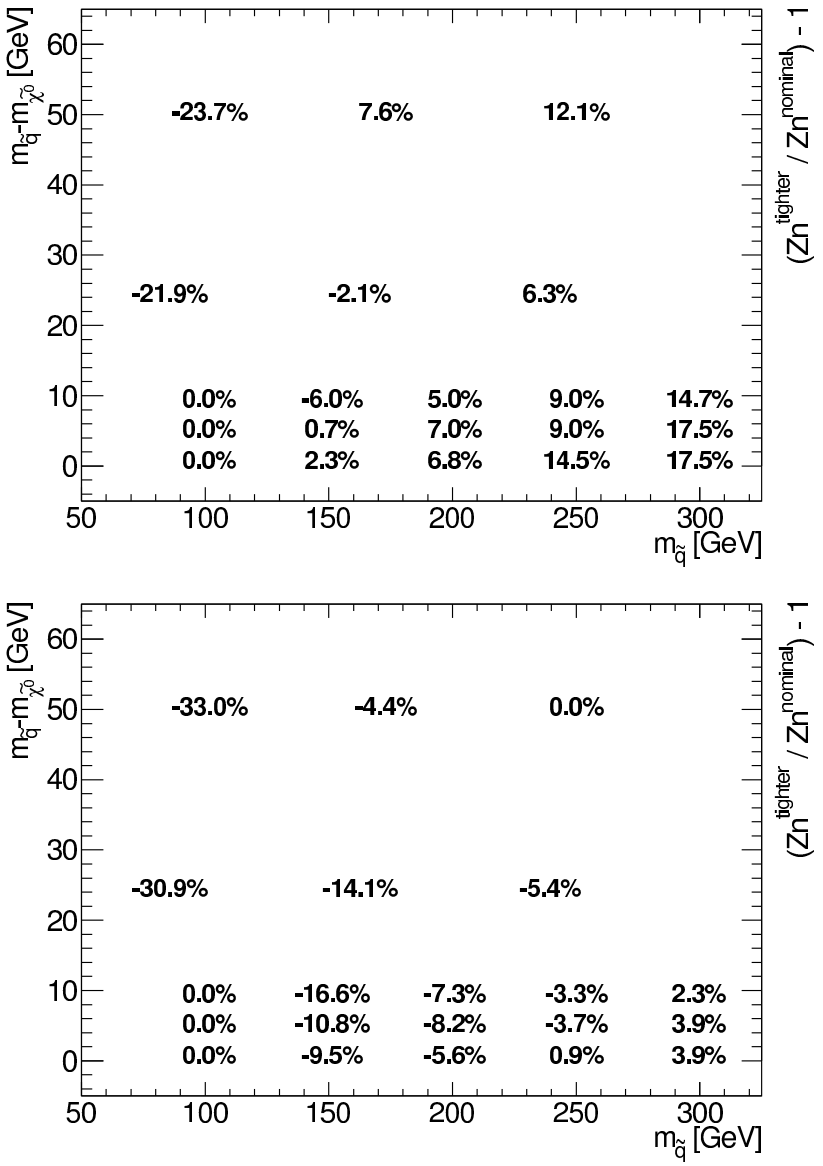

Fig. 10.8 In the tight SR with $|\eta^{\gamma}| < 1.37$ and $E_{\mathrm{T}}^{\mathrm{miss}} > 180$ GeV, the change in significance with respect to the nominal SR is shown for all the SUSY signal samples in the plane of the squark mass $m_{\tilde{q}}$ and the mass difference between the squark and the lightest neutralino $m_{\tilde{q}} - m_{\tilde{\chi}^0}$. The tighter SR significance is computed with an overall systematic uncertainty of 12% (top) and 14% (bottom), respectively.

All the 15 tighter SRs shown in Figure 10.8 are excluded, as they significantly lower the number of events in the CRs for background estimation, leading to an increase of the systematic uncertainty beyond that allowed to have an improved signal significance. Finally, the SR is optimized only by tightening the cut on $|\eta^{\gamma}|$ from 2.37 to 1.37.

Lower–p_{T} photon study

The possibility to loosen the p_{T}^{γ} threshold from 150 GeV to 125 GeV was also explored in order to increase the statistics for background estimation. In the new SR with $|\eta^{\gamma}| < 1.37$, the number of background events increases by $\approx 20\%$ when loosening the cut on p_{T}^{γ} to 125 GeV. Such statistics enhancement is useful for the background estimation, but one needs to check if the signal significance is affected or not.

Given a significance computed via $N_{Signal}/\sqrt{N_{Background}}$, the number of signal events needs to increase by at least $\approx 10\%$ when going to $p_{\mathrm{T}}^{\gamma} > 125$ GeV to maintain the significance. Figure 10.9 (top) shows that most of the SUSY signal points do get a more than 10% increase in the number of SR events. This leads to an increased significance as shown in Figure 10.9 (bottom).

It can be concluded that loosening the cut on p_{T}^{γ} from 150 GeV to 125 GeV improves the sensitivity for the squark scenario.

10.3.3 The 8 TeV event selection

The signal region (SR) event selection for the 8 TeV analysis after the pre-selection (see Section 10.2) is built upon the object candidates defined in Section 10.1, in which the leptons have lower p_{T} cuts than the ones used in the 7 TeV analysis; and follows the suggestions from the SR definition studies (see Section 10.3.2) on lowering the thresholds on p_{T}^{γ} and η^{γ} with respect to the ones used in the 7 TeV analysis. The SR event selection used in this analysis after the Preselections is summarized below:

1. Events must have $E_{\mathrm{T}}^{\mathrm{miss}} > 150$ GeV (muons are treated as invisible particles in the $E_{\mathrm{T}}^{\mathrm{miss}}$ computation);
2. Each event must contain at least one photon candidate (`loose`, $|\eta| < 2.37$, excluding the calorimeter transition (crack) region $1.37 < |\eta| < 1.52$) with $p_{\mathrm{T}} > 125$ GeV;
3. The highest p_{T} (leading) photon must pass the `tight` identification criterion and $|\eta^{\gamma}| < 1.37$;
4. The leading photon must be isolated by requiring $TopoEtcone40_{corr} < 5$ GeV;
5. The leading photon must be sufficiently far from $E_{\mathrm{T}}^{\mathrm{miss}}$ by requiring $\Delta\phi(\gamma, E_{\mathrm{T}}^{\mathrm{miss}}) > 0.4$;

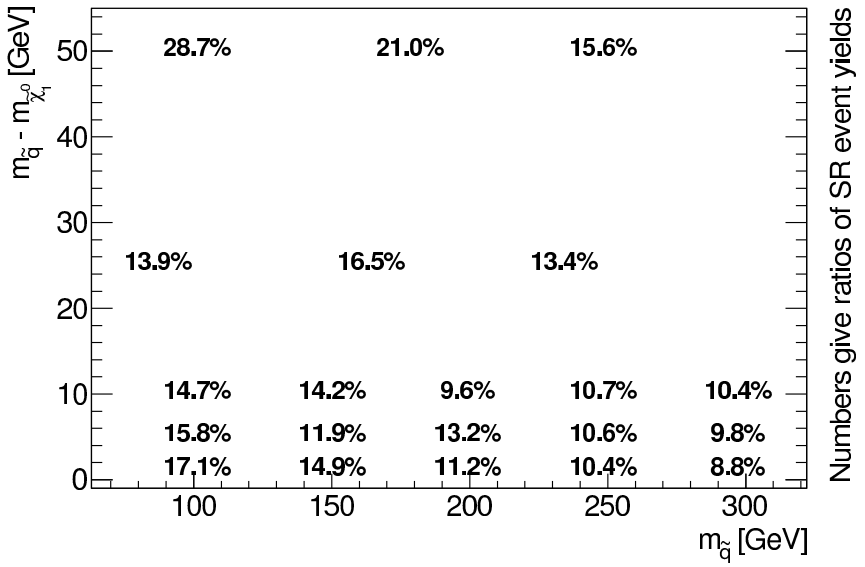

(a) Relative increase of the event yield in the signal region

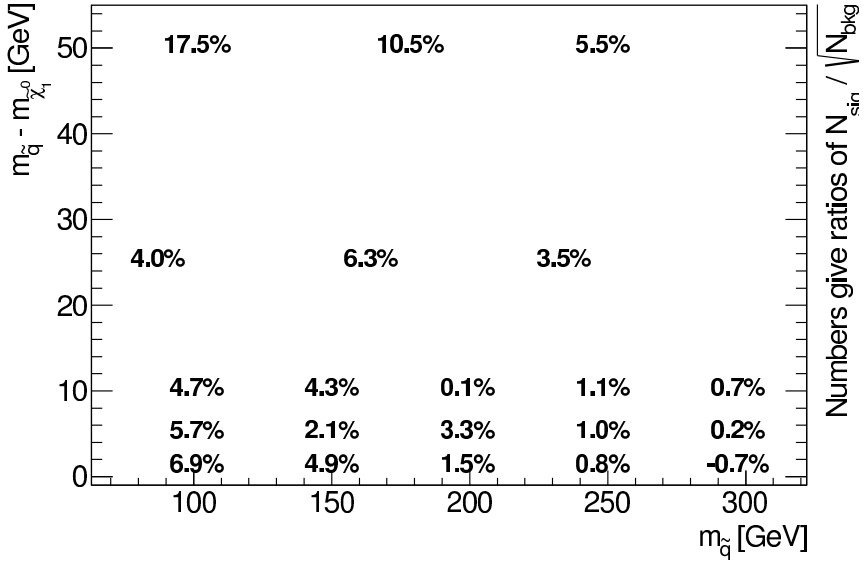

(b) Relative increase in $N_{Signal}/\sqrt{N_{Background}}$

Fig. 10.9 Comparisons of the event yields (top) and the significance ($N_{Signal}/\sqrt{N_{Background}}$) when going from $p_{\mathrm{T}}^{\gamma} > 125$ GeV to the $p_{\mathrm{T}}^{\gamma} > 150$ GeV using the full compressed squark signal grid in the plane of $m_{\tilde{q}}$ and $m_{\tilde{q}} - m_{\tilde{\chi}_1^0}$.

6. The jet 'veto' requirement asks each event to contain at most one jet candidate ($p_{\mathrm{T}}^{\mathrm{jet}} > 30$ GeV, $|\eta^{\mathrm{jet}}| < 4.5$). If there is a jet, this jet must be away from $E_{\mathrm{T}}^{\mathrm{miss}}$ with $\Delta\phi(E_{\mathrm{T}}^{\mathrm{miss}},\mathrm{jet}) > 0.4$;
7. A lepton veto cut is applied to all the events by requiring no electron (`medium++`, $p_{\mathrm{T}} > 7$ GeV) and no muon ($p_{\mathrm{T}} > 6$ GeV).

Table 10.1 shows the SR cutflow for the main backgrounds, based on the MC samples introduced in Section 9.2. The first requirement on a large $E_{\mathrm{T}}^{\mathrm{miss}}$ efficiently suppress most of the background events, including the irreducible background of $Z(\to \nu\bar{\nu}) + \gamma$, The criteria on the photon from cut 2 to 5 remove most of events without a real photon, such as the fake photon background, $W(e\nu)+\mathrm{jet}$. The last two cuts, the 'jet veto' and 'lepton veto' strongly suppress events with leptons or extra jets reconstructed, such as the real photon backgrounds $Z(\to \ell^+\ell^-) + \gamma$ and $W(\to \ell\nu) + \gamma$ (noted as $V + \gamma$ in the table).

Cutflow	$Z(\nu\bar{\nu}) + \gamma$	$V + \gamma$	$W(e\nu)+\mathrm{jet}$
0. Pre-Selection	100%	100%	100%
1. $E_{\mathrm{T}}^{\mathrm{miss}} > 150$ GeV	33%	31%	45%
2. ≥ 1 loose photon with $p_{\mathrm{T}} > 125$ GeV ($\lvert\eta\rvert < 2.37$)	21%	18%	2.5%
3. the leading photon is tight with $\lvert\eta\rvert < 1.37$	15%	13%	0.33%
4. the leading photon is isolated	13%	10%	0.24%
5. $\Delta\phi(\gamma^{\mathrm{leading}}, E_{\mathrm{T}}^{\mathrm{miss}}) > 0.4$	13%	9.4%	0.15%
6. Jet veto: $N_{\mathrm{jet}} \leq 1$ and $\Delta\phi(\mathrm{jet}, E_{\mathrm{T}}^{\mathrm{miss}}) > 0.4$	10%	5.8%	0.12%
7. Lepton veto	10%	1.1%	0.05%

Table 10.1 The SR cutflow for the main backgrounds, based on MC samples, where the $V + \gamma$ refers to $Z(\to \ell^+\ell^-) + \gamma$ and $W(\to \ell\nu) + \gamma$.

Figure 10.10 shows the distributions of four discriminant kinematic variables in the SR, including the jet multiplicity, photon $|\eta|$, photon p_{T} and $E_{\mathrm{T}}^{\mathrm{miss}}$. The irreducible background $Z(\to \nu\bar{\nu}) + \gamma$ (blue) is shown compared to one compressed squark signal (red) and an EFT dark matter model (green) inspired by Fermi-LAT results, in which dark matter particles couple to photons via a contact interaction vertex (see Chapter 13). This dark matter model is referred as 'EFT DM' in the figure and in the following description. As the photon is not an ISR photon in the EFT DM model, the photon p_{T} and the consequential reconstructed $E_{\mathrm{T}}^{\mathrm{miss}}$ of this model are expected to be larger than the compressed squark model, as shown in Figure 10.10 (bottom plots).

The compressed squark model tends to have more jets because the quarks from the squarks decay product can be reconstructed if they are energetic enough. This is found in the SR studies shown in Section 10.3.2. Events in the EFT DM model and in the irreducible background only have jets coming from ISR; the jet multiplicity distribution in both cases

thus agree quite well, as shown in Figure 10.10 (top left). This is also the reason why the jet veto in the SR is not loosened.

Both signal models show a preference for central photons, which is shown in Figure 10.10 (top right). Therefore, the signal significance in both models is improved by the tightened photon $|\eta|$ cut.

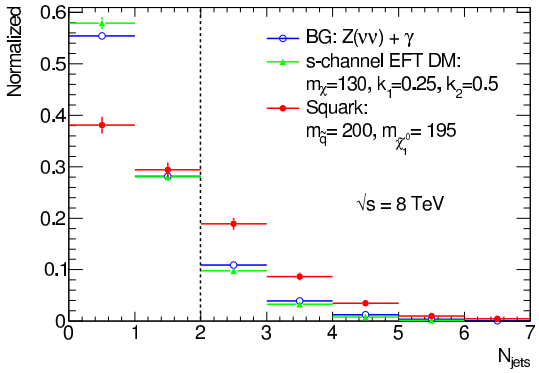

(a) Jet multiplicity in the signal region with a loosened jet veto.

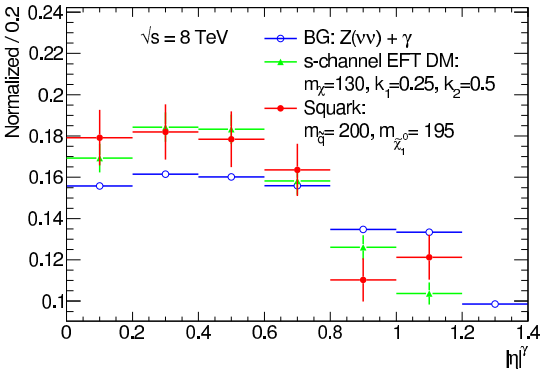

(b) Photon $|\eta|$ distribution in the SR

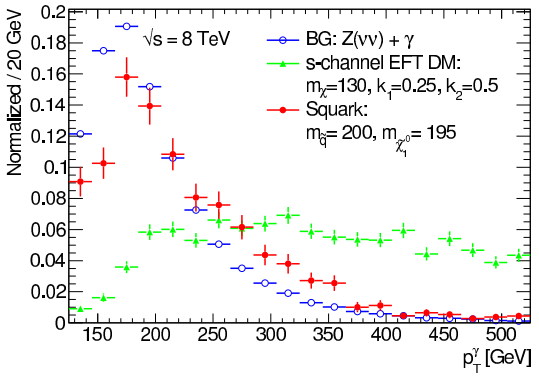

(c) Photon p_{T} distribution in the SR

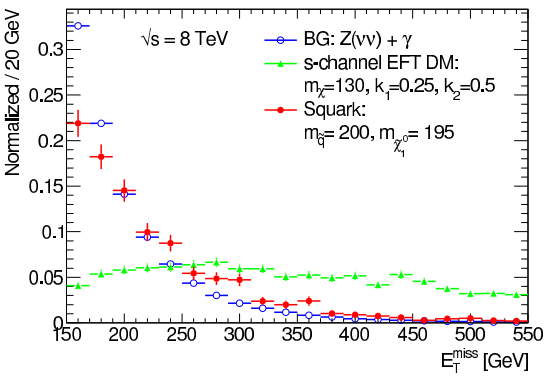

(d) $E_{\mathrm{T}}^{\mathrm{miss}}$ distribution in the SR

Fig. 10.10 Kinematic distributions in the SR for various signal samples compared with the main irreducible background process $Z(\to \nu\bar{\nu}) + \gamma$. The black dash line in the jet multiplicity distribution indicates the SR cut.

Chapter 11

Background estimation

11.1 Background estimation scheme

The $V+\gamma$ background in the SR is estimated from a background-only fit [141] based on the profile likelihood method [142]. This fit only takes into account the CRs and assumes no signal contamination. The following inputs from each CR are used: the number of events observed in the data, the number of events predicted by MC simulation for the $V+\gamma$ background, the number of events yields estimated by the data-driven method for the other backgrounds, and the number of events predicted by MC simulation for the $\gamma+$jet background. In order to implement this fit, a customized statistical tool is derived from the `HistFitter` [141] framework.

The numbers of observed and predicted events in each region is described using Poisson probability density functions (pdf):

$$N_R(\text{data}) \propto \text{Pois}\left(N_R(\text{data})|\sigma \times (A \times \varepsilon)_R \times L + \sum N_R(B)\right), \tag{11.1}$$

where R refers to a specific analysis region; $\sigma \times (A \times \varepsilon)_R \times L$ stands as the signal yield for $\int L dt = 20.3\,\text{fb}^{-1}$, which is zero in the control regions; $N_R(B)$ refers to each background estimate.

The systematic uncertainties (see Section 11.5) on the predicted numbers of events and the statistical uncertainties on the MC predictions are treated as nuisance parameters. Each systematic uncertainty is constrained by a Gaussian pdf with its width referring to the size of the uncertainty, whilst each statistical uncertainty is constrained by a Poisson pdf. Each background is allowed to vary within its respective uncertainties.

The real photon backgrounds, $Z\gamma$ and $W\gamma$, in the SR are estimated by normalizing the

MC prediction with two actual normalization factors obtained in the aforementioned likelihood fit to the data in the CRs. The CRs are built to be enriched in these specific backgrounds. The two normalization factors, referred as the k factors, are applied to the $Z+\gamma$ and $W+\gamma$ backgrounds respectively. Therefore the Equation (11.1) becomes:

$$\begin{aligned} N_R(\text{data}) \propto \text{Pois}\Bigg(& N_R(\text{data}) | \sigma \times (A \times \varepsilon)_R \times L \\ & + k_{Z\gamma} N_R(Z(\to \nu\bar{\nu}) + \gamma) \\ & + k_{W\gamma} N_R(W(\to \ell\nu) + \gamma) \\ & + k_{Z\gamma} N_R(Z(\to \ell^+\ell^-) + \gamma) \\ & + \sum_{B \neq V\gamma, Z\gamma} N_R(B) \Bigg), \end{aligned} \tag{11.2}$$

where the R refers to the specific CR; $N_R(Z(\to \nu\bar{\nu}) + \gamma)$, $N_R(W(\to \ell\nu) + \gamma)$ and $N_R(Z(\to \ell^+\ell^-) + \gamma)$ are the MC prediction for each of these processes; $N_R(B)$ refers to the fake photon background estimates together with the $\gamma+$jet background; $\sigma \times (A \times \varepsilon)_R \times L$ is zero in these CRs; $k_{W\gamma}$ and $k_{Z\gamma}$ are the free parameters in the fit, which will be applied to the MC yields of the $W+\gamma$ and $Z+\gamma$ backgrounds in the SR. The observed data in the CRs are hence used to evaluate the real photon background contributions in the SR.

The product of the various pdfs forms the likelihood, built with the HistFactory [143] package in the customized statistical tool, and the correlations of the parameters are taken into account. The fit adjusts the various parameters in order to maximize the likelihood.

The definitions of the CRs together with the estimation of the real photon backgrounds are given in Section 11.2. The data-driven methods which are used to determine the fake photon backgrounds are described in Section 11.3. The last component of the considered background is the $\gamma+$jet; its estimate is given directly by the MC prediction, described in Section 11.4. In this section, further potential background sources are checked to ensure the completeness of the current background composition.

The scheme to estimate the background in the SR is validated in a validation region (VR) which is described in Section 11.6.

At the end of this chapter (Section 11.7), the final estimation results in both SR and VR are given.

11.2 $Z\gamma$ and $W\gamma$ backgrounds

The $Z\gamma$ and $W\gamma$ backgrounds are estimated by normalizing the MC expectations to data with a likelihood fit to several control regions (CRs), as introduced in Section 11.1.

Three lepton control regions are constructed by inverting the SR 'lepton veto' cut to enrich these regions with $Z(\to \mu^+\mu^-)+\gamma$, $Z(\to e^+e^-)+\gamma$ and $W(\to \ell\nu)+\gamma$ events respectively. The $W(\to \mu\nu)+\gamma$ CR is built by requiring one extra muon, whilst the $Z(\to \ell^+\ell^-)+\gamma$ CRs are asking for the presence of either a pair of muons ($Z(\to \mu^+\mu^-)+\gamma$ CR) or a pair of electrons ($Z(\to e^+e^-)+\gamma$ CR).

The CRs must be as similar as possible to the SR, especially for the distribution of the main objects, in order to be able to extrapolate the k factors to the SR. The $E_{\mathrm{T}}^{\mathrm{miss}}$ distribution for CRs with extra muons required are ensured to be similar to the SR since the muons are treated as invisible particles in the $E_{\mathrm{T}}^{\mathrm{miss}}$ calculation. For the $Z(\to e^+e^-)+\gamma$ CR, electrons are also removed in order to mimic the $Z(\to \nu\bar{\nu})+\gamma$ background when computing $E_{\mathrm{T}}^{\mathrm{miss}}$. The $E_{\mathrm{T}}^{\mathrm{miss}}$ trigger used in the SR is therefore not suitable for the di-electron CR, and a photon trigger `EF_g120_loose` is used in this CR.

The leptons in the CRs are selected using the same requirements as the lepton candidates in the SR 'lepton veto'. In order to insure that real leptons are selected in the CRs, they are further required to be isolated by asking the scalar sum of the tracks p_{T} within a cone of radius $\Delta R = 0.2$ around the lepton to be less than 15% of the lepton p_{T}. The electrons in the CRs are required to have $p_{\mathrm{T}}^{el} > 10$ GeV as that in the $E_{\mathrm{T}}^{\mathrm{miss}}$ computation. Furthermore, the distance between the lepton and photon is asked to be $\Delta R(\ell,\gamma) > 0.5$ (as in the MC requirement at generator level). In the dilepton CRs, the dilepton invariant mass $m_{\ell^+\ell^-}$ is required to be greater than 50 GeV to match the generator-level requirement.

Since the shape of the photon η from the simulation is found to agree with data in the CRs the CRs are allowed to relax the photon pseudorapidity requirement to $|\eta| < 2.37$ (excluding the calorimeter barrel and end-cap transition region $1.37 < |\eta| < 1.52$) in order to increase the number of events in the CRs. Furthermore, this is also viable as all the MC samples used in the CRs are simulated with full `Geant4`.

The $E_{\mathrm{T}}^{\mathrm{miss}}$ distribution in each of these CRs is shown in Figure 11.1 compared to that of the post-fit background expectation. In Figure 11.1, one can see that all the CRs are enriched in the background process of interest with a high purity. Besides, the lower panel of each histogram in Figure 11.1 shows the ratio of data to the post-fit MC estimate, indicating a good agreement in each region between the data and the post-fit background estimate within the global uncertainty. The k factors obtained in the background only fit are $k_{W\gamma} = 0.81 \pm 0.05(\mathrm{stat.}) \pm 0.06(\mathrm{syst.})$ and $k_{Z\gamma} = 0.89 \pm 0.08(\mathrm{stat.}) \pm 0.08(\mathrm{syst.})$.

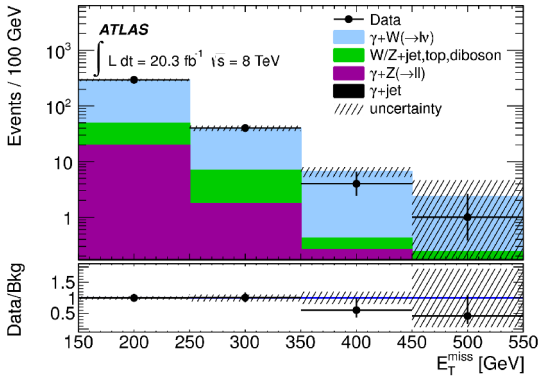

(a) The one-muon control region, in which 340 events are observed, is enriched in the $W \to \mu\nu$ process with a 87% purity.

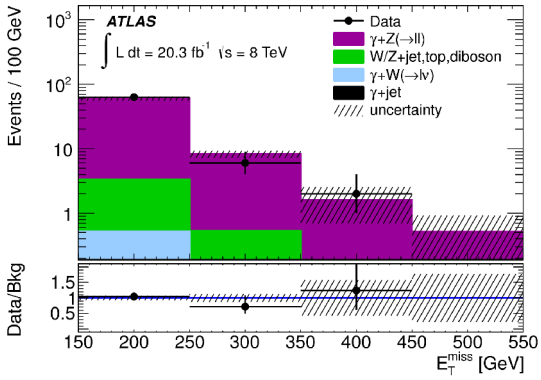

(b) The two-muon control region, in which 77 events are observed, is enriched in the $Z \to \mu\mu$ process with a 97% purity.

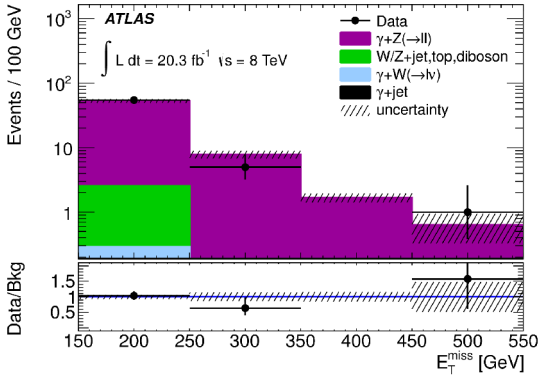

(c) The two-electron control region, in which 61 events are observed, is enriched in the $Z \to ee$ process with a 94% purity.

Fig. 11.1 $E_{\mathrm{T}}^{\mathrm{miss}}$ distribution for the data and compared to the background expectation in the three lepton CRs. The dashed band includes the statistical and systematic uncertainties. Overflows are included in the final bin. The lower part of each figure shows the ratios of data to the post-fit background estimate.

11.3 Fake photon background

The Standard Model processes without real photon such as $W/Z+\text{jet}$ can yield events in the signal region, if photons are mis-reconstructed from objects with similar detector responses, such as electrons or jets. As the MC simulation is believed to be unable to describe well such fake photon processes, two different data-driven methods are adopted to extract the distribution of these backgrounds in the SR, which are described below.

11.3.1 Fake photons from mis-identified electrons

Background contributions in the SR from processes in which an electron is mis-identified as a photon are estimated by scaling event yields of $e + E_{\mathrm{T}}^{\mathrm{miss}}$ (mono-electron) events with a factor describing the probability of the electron-to-photon mis-identification. Similarly, the fake photon contribution in the CRs are estimated by applying the mis-identification factor to the event yields of regions similar to the CRs, but in which an electron is required instead of a photon.

The electron-to-photon fake probability can be measured by comparing the number of events in which there is one good electron (tag) and one electron (probe) to that with one tag electron and one probe photon, requiring the 'tag-and-probe' mass to be compatible with Z mass within $m_Z \pm 10$ GeV.

The tag electrons are selected with $|\eta| < 2.37$ and outside the calorimeter transition region ($1.37 < |\eta| < 1.52$). They are required to be identified with the `Tight++` criterion with $E_{\mathrm{T}} > 20$ GeV, TopoEtcone40$_{corr} < 5$ GeV and TopoEtcone40$_{corr}/E_{\mathrm{T}} < 0.1$. The probe photons are selected as the signal photons (see Chapter 10). The probe electrons are selected with the same kinematic and isolation cuts as the signal photons, passing the `Tight++` electron criterion.

The electron can also come from the $W(\to e\nu) + \gamma$ events, therefore $E_{\mathrm{T}}^{\mathrm{miss}}$ is asked to be less than 40 GeV to suppress this potential background. As a result, the trigger used in this study is the photon trigger `EF_g120_loose` rather than the $E_{\mathrm{T}}^{\mathrm{miss}}$ trigger used in the SR. The side-bands of $|M_{inv} - m_Z| \in [10, 20]$ GeV are used to estimate the QCD background which will be subtracted.

The invariant mass reconstructed by a pair of tag and probe electrons, as measured in data, is shown as the black dotted curve in Figure 11.2; in this figure, the red dotted curve shows the invariant mass reconstructed by a pair of tag electron and probe photon. The mis-identification factor is computed as the ratio of probe photon events to the probe electron events within the window of $m_Z \pm 10$ GeV after subtracting the QCD background.

The following three systematic uncertainty sources are considered when estimating the fake photon backgrounds using a 'tag-and-probe' method. The first source comes from the potential bias of the 'tag-and-probe' method, which is estimated by comparing the 'tag-and-probe' result with the real value from $Z \to e^+e^-$ MC simulation samples. The second one comes from the bias to estimate the fake photon SR events with the mis-identification factor derived using only Z events. This is evaluated by comparing the difference of the real electron-to-photon mis-identification factor between the $Z \to e^+e^-$ and the $W \to e\nu$ MC simulation samples. The last one is contributed from the variation of the $|M_{int} - m_Z|$ 'window' size, this is evaluated by varying the 'window' size with the side-bands changed

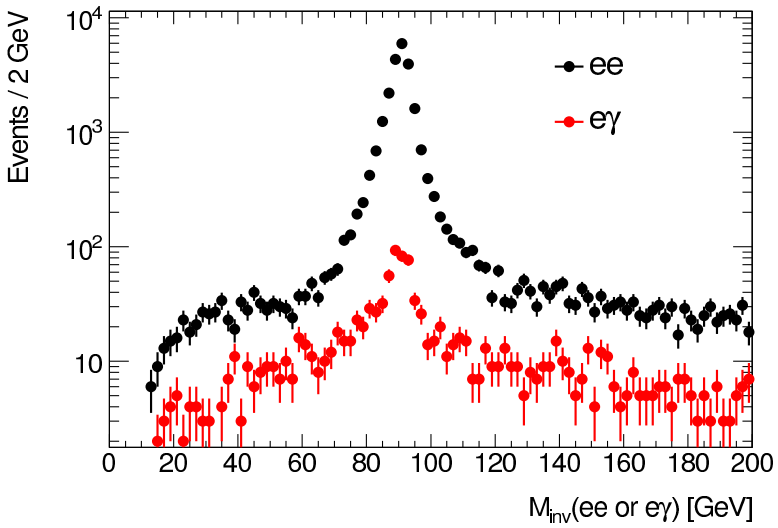

Fig. 11.2 Invariant mass, M_{inv} of the 'tag' electron with the 'probe' electron or 'probe' photon as measured in data [144].

accordingly for the QCD background subtraction.

This mis-identification factor is found to depend on η and p_{T}, and is therefore measured as a function of p_{T} in three pseudorapidity bins: $|\eta| \leq 0.8$, $0.8 < |\eta| \leq 1.37$ and $|\eta| > 1.52$. The mis-identification factors measured from data for each combination of η and p_{T} bins are shown in Table 11.1 with the uncertainties. The measured mean value of the mis-identification factors varies from 1.1% to 3.9%, with the maximum in the end-cap region and the minimum in the central region, and the factors generally decrease with increasing p_{T}.

E_T bins [GeV]	$\lvert\eta\rvert \leq 0.8$	$0.8 < \lvert\eta\rvert \leq 1.37$	$\lvert\eta\rvert \geq 1.52$
$[125, 150)$	$2.1 \pm 0.3 \pm 0.6\%$	$2.5 \pm 0.4 \pm 0.8\%$	$3.3 \pm 0.5 \pm 0.4\%$
$[150, 200)$	$1.1 \pm 0.3 \pm 0.3\%$	$1.5 \pm 0.4 \pm 0.4\%$	$3.9 \pm 0.7 \pm 1.0\%$
$[200, -)$	$1.1 \pm 0.4 \pm 0.2\%$	$1.3 \pm 0.5 \pm 1.1\%$	$3.6 \pm 1.3 \pm 1.0\%$

Table 11.1 The electron-fake-photon mis-identification factor measured from the data with the statistic uncertainty followed by the systematic one [144].

The tag-and-probe control region used to estimate the electron-fake-photon events in the SR selects $e + E_{\text{T}}^{\text{miss}}$ events as in the SR, but with the 'probe' electron instead of the signal photon. The electron-to-photon mis-identification factor is applied to electrons event-by-event according to η and p_{T}, in the mono-electron CR. In order to estimate the fake electron background in the lepton CRs and the validation region (see Section 11.6), the mono-electron control region is rebuilt correspondingly.

11.3.2 Fake photons from mis-identified jets

The background from events containing a jet mis-identified as a photon is mainly suppressed by the tight identification criteria and isolation requirement of the signal photon. The remaining contributions in the SR from these events are estimated from a measurement in a control region normalized by the jet-to-photon fake factor measured in data.

This control region is built to be orthogonal to the SR by inverting the photon isolation cut. Considering that some true photon events could leak in this control region if it is kinematically too close to the SR, the inverted isolation cut is therefore set to be 10 GeV $<$ TopoEtcone40$_{corr}$ $<$ 45 GeV, as a trade-off between minimizing the true photon leakage and keeping sufficient statistics.

The isolation requirement can be treated independently from the following shape variables in the first EM layer used for the 'tight' identification criterion:

- The lateral EM shower width for the three central strips around the maximum strip;
- The fraction of the energy in the seven strips centered around the first maximum which is outside of the three cells centered around the maximum strip;
- The difference between the energy of the strip with the second largest energy deposit and the energy of the strip with the smallest energy deposit between the two leading strips;
- The difference between the maximum and the second maximum strips of the cluster.

One can therefore derive the jet-to-photon fake factor from data in a 'non-tight' region by inverting the `tight` photon criterion to a customized 'non-tight' criterion based on the above discriminant variables.

All the four regions, including the SR, are shown in Figure 11.3 in a two dimensional plane defined by the photon isolation variable and a subset of the photon identification variables. The number of events measured in the non-isolated control region is noted as N^B, and that of the two 'non-tight' regions are M^A and M^B. The jet-to-photon fake factor is computed as the ratio M^A/M^B. The superscript indicates the two isolation quality, whilst M and N refers to the `tight` and 'non-tight' identification criteria, respectively. The true photon leakage in the non-isolated control region is estimated using MC samples and noted as $N^{B,leakage}$. The jet-to-photon fake event count in the SR N^A is therefore computed by $N^A = (N^B - N^{B,leakage}) \times M^A/M^B$.

There are two sources of systematic uncertainty in this data-driven method. First, a potential bias comes from the variation of the MC estimation to subtract the real photon leakage in the control region. The second bias comes from the fact that the subset of the photon identification variables is considered to be independent from the isolation variable, in order to apply the fake rate measured from 'non-tight' regions to the 'tight' regions. Both

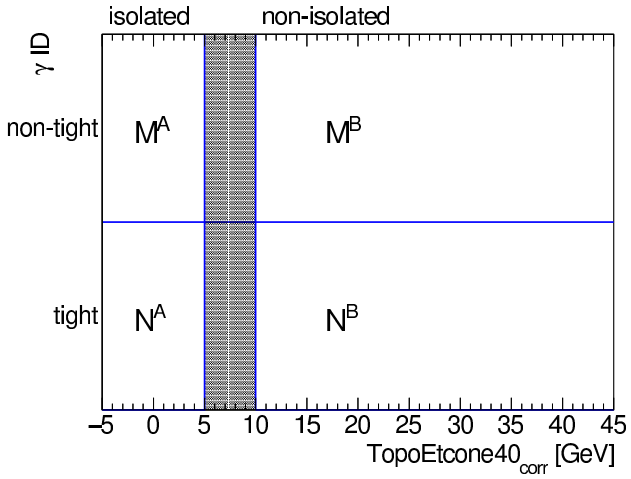

Fig. 11.3 The four regions used to estimate the jet-fake-photon background in the signal region, illustrated in a two dimensional plane defined by the photon isolation variable and a subset of the photon identification variables. The jet fake photon background in the signal region N^A is estimated from the three control regions N^B, M^A and M^B.

systematic uncertainty sources are studied with MC samples, and the combination gives the final systematic uncertainty to the estimate of this background.

The fake factor is computed by comparing the measurements from M^A to M^B, and it is measured as a function of $E_{\mathrm{T}}^{\mathrm{miss}}$ in the central ($|\eta| < 1.37$) and end-cap ($|\eta| > 1.52$) regions separately. The fake factor measured from data for each combination of $E_{\mathrm{T}}^{\mathrm{miss}}$ and $|\eta|$ is shown in Table 11.2 with its uncertainties. The end-cap region is found more likely to have jet-fake-photon than the central region: in the central region, the fake factor varies from 0.24 to 0.14 decreasing with $E_{\mathrm{T}}^{\mathrm{miss}}$, while it varies from 0.24 to 0.30 in the end-cap region.

$E_{\mathrm{T}}^{\mathrm{miss}}$ bins [GeV]	$\lvert\eta\rvert < 1.37$	$\lvert\eta\rvert > 1.52$
$[110, 150)$	$0.24 \pm 0.03 \pm 0.16$	$0.30 \pm 0.07 \pm 0.58$
$[150, -)$	$0.14 \pm 0.02 \pm 0.03$	$0.24 \pm 0.06 \pm 0.10$

Table 11.2 The jet fake photon factor measured from data as a function of $E_{\mathrm{T}}^{\mathrm{miss}}$ for different $|\eta|$ bins with the statistic uncertainty followed by the systematic one [144].

This estimate also covers the estimation of the contribution from multi-jets events, which can mimic the monophoton signature if one jet is mis-reconstructed as a photon and one or more of the other jets are poorly reconstructed, resulting in a large fake $E_{\mathrm{T}}^{\mathrm{miss}}$.

11.4 Other minor backgrounds

11.4.1 Fake $E_{\mathrm{T}}^{\mathrm{miss}}$ background

Events from the $\gamma+$jet process can contribute to the background in the SR when the jet is poorly reconstructed and partially lost, creating fake $E_{\mathrm{T}}^{\mathrm{miss}}$. Though they are produced at a large rate, this background is suppressed due to the requirements of large $E_{\mathrm{T}}^{\mathrm{miss}}$ and a good jet-$E_{\mathrm{T}}^{\mathrm{miss}}$ separation ($\Delta\phi(\mathrm{jet}, E_{\mathrm{T}}^{\mathrm{miss}}) > 0.4$).

This background is estimated from MC simulation only, as a result, $0.4^{+0.3}_{-0.4}$ events are predicted in the SR. A potential data-driven estimate has been tested by defining a control region with events selected as in the SR but inverting the $\Delta\phi(\mathrm{jet}, E_{\mathrm{T}}^{\mathrm{miss}})$ requirement to enrich the sample in events with a large $E_{\mathrm{T}}^{\mathrm{miss}}$ mis-reconstructed from the aligned jet. The result was found to be compatible with the estimate derived from the MC simulation, but with a large statistical uncertainty due to only 23 events observed in this potential control region.

11.4.2 Study of other potential backgrounds in the SR

A few further potential backgrounds, in which there is a real photon produced, are checked to see if they should be taken into account for the background estimation in this analysis. Contributions from these backgrounds are checked in the SR at the reconstruction and the generator level. Table 11.3 shows each process considered, along with the generator used, the cross-section computed at NLO (except for the di-photon production), the size of the samples, the product of acceptance and efficiency (acceptance) in the SR, and the SR yield using reconstructed objects (real objects) for $20.3\,\mathrm{fb}^{-1}$ of data at a center-of-mass energy of 8 TeV.

The check at the reconstruction level does not subtract fake-photon contributions sourced from electrons or jets, which are already estimated by the data-driven methods described in Section 11.3. Consequently, the yield predicted for samples such as $t\bar{t}+\gamma$ may be overestimated as the goal of this check is to find further sources of true γ background.

This study is performed on MC samples which were produced with an older version for object calibration and have a worse resolution for $E_{\mathrm{T}}^{\mathrm{miss}}$ compared to the MC samples used in the analysis, due to a bug fixed when reprocessing the samples. Therefore, the reconstruction-level yields should be considered as the upper limit on the number of expected events in the SR Summing up the yield of all the processes listed in Table 11.3 would add a maximal contribution of 0.2% to the full background estimate in the SR. It can hence be concluded from this study that the SM background composition already considered in this thesis is sufficient for the background expectation study.

Channel	Generator	Sample size [fb^{-1}]	σ [fb]	Real Level A[%]	Real Level Yield	Reconstruction Level $A \times \varepsilon$[%]	Reconstruction Level Yield
$t\bar{t}+\gamma$							
tops are not both hadronic decay	MADGRAPH	1063	188	0.004	0.15	0.0175	0.67
tops are both hadronic decay	MADGRAPH	2915494	68.6	0.0	0.0	0.0	0.0
$\gamma+\gamma$, $\eta^{\gamma} < 2.7$, $p_{\mathrm{T}}^{\gamma} > 20$ GeV	SHERPA	20576	485.45	0.0	0.0	0.0	0.0
Single-$t+\gamma$							
leptonic t-channel,γ in production	Whizard	48147188143	22.85	0.017	0.08	0.0545	0.25
leptonic t-channel,γ in decay	Whizard	4929330	4.057	0.0	0.0	0.005	0.004
dileptonic tW-channel, γ in production	Whizard	4710673	2.123	0.0	0.0	0.03	0.013
dileptonic tW-channel, γ in t-decay	Whizard	11963484	0.4179	0.02	0.0017	0.02	0.0017
dileptonic tW-channel, γ in W-decay	Whizard	6365671	0.7855	0.02	0.0032	0.0	0.0
semi-leptonic tW-channel, γ in production	Whizard	4767565	4.195	0.02	0.017	0.015	0.012
semi-leptonic tW-channel, γ in t-decay	Whizard	6226803	0.8030	0.0	0.0	0.0	0.0
semi-leptonic tW-channel, γ in W-decay	Whizard	6664568	0.7502	0.04	0.0061	0.08	0.012
semi-leptonic tW-channel, γ in production	Whizard	4788499	4.177	0.0	0.0	0.0	0.0
semi-leptonic tW-channel, γ in t-decay	Whizard	5918062	0.8449	0.0	0.0	0.04	0.00686
semi-leptonic tW-channel, γ in W-decay	Whizard	3175645	1.574	0.0	0.0	0.0	0.0
Higgs$\rightarrow \gamma+\gamma$							
$m_H = 125$ GeV, $\gamma\gamma$-channel	POWHEG	68160900	43.94	0.0	0.0	0.0	0.0
$m_H = 125$ GeV, WH-channel	PYTHIA 8	18679950	1.606	0.033	0.011	0.1	0.0326
$m_H = 125$ GeV, ZH-Channel	PYTHIA 8	31682332	0.9469	0.41	0.079	0.577	0.11
$m_H = 125$ GeV, ttH-Channel	PYTHIA 8	1017615319	0.2948	0.002	0.00014	0.006	0.00036

Table 11.3 The generator, sample size in fb^{-1}, cross section, product of acceptance and efficiency in the SR (or acceptance at true level) and event yield for 20.3 fb^{-1} of data are given for other potential backgrounds in the Standard Model. The SR yield given at the reconstruction level should be regarded as an upper expectation due to the worse $E_{\mathrm{T}}^{\mathrm{miss}}$ description in the MC samples used with respect to the nominal samples used in this analysis.

11.5 Systematic uncertainties

At particle level, the processes of reconstruction, identification and calibration of each interesting physics object (see Chapter 7) introduce various systematic uncertainties, which affect the final event yields in all the analysis regions. These systematic uncertainties are studied by dedicated combined performance (CP) groups in ATLAS . Recommendations are given by the CP groups on how to take into account the variation of each uncertainty source. These systematic uncertainties are introduced below according to the relevant particle type.

At the event level, uncertainties related to the integrated luminosity and the trigger efficiency can also affect the final event yields; they are also introduced in the following text.

Various sources of systematic uncertainties are uncorrelated, and can hence be summed in quadrature. Each source of systematic uncertainty can bring a variation to the event yield giving a value greater or smaller than the nominal. All the systematic sources giving an upward fluctuation are summed up to give the final upward variation on the yield. The same is implemented for the systematic sources giving a downward fluctuation.

Photons and electrons

The uncertainties on the photon identification efficiency, introduced in Section 7.1, is applied to all the photons in each event in the full `Geant4` simulation samples. For all the full-simulated samples, the photon identification efficiency variations are taken into account to recompute the event yields. For the `Atlfast-II` samples, an overall conservative $\pm 5\%$ uncertainty is applied to the event yield. It is a conservative uncertainty coming from the preliminary studies which were available at that time. This conservative uncertainty was validated when the recommendation became available. The final recommendation gives a variation of $\pm 2\%$ on the event yield, which is well covered by the $\pm 5\%$ considered here.

An uncertainty on the photon isolation efficiency ($\varepsilon^{\gamma}_{iso}$) is also applied. It is obtained in this analysis by comparing various MC simulation samples to the data in the central and the end-cap regions. The MC simulation considered includes samples of background ($Z+\gamma$ and $\gamma+$jet) and signal. In order to take into account the effect brought by different generators, two simulated $\gamma+$jet samples are checked, which are generated with SHERPA and PYTHIA 8, respectively. As all the validated MC samples are found to agree with data within 4%, an overall symmetric uncertainty of 4% is applied to all the simulation samples in this thesis.

As introduced in Section 7.1.3, electrons and photons share a common energy calibration process. Therefore, the corresponding uncertainties introduced from this calibration process are introduced together here. Five uncertainties of this type are taken into account in this thesis, and each type can be varied up and down. These five uncertainties are studied in

details in Reference [92]. They are respectively:

- the uncertainty on the material distribution related to the inter-calibration of the first and second EM layers, for electrons and photons;
- the uncertainty on the presampler energy scale for both electrons and photons;
- an additional scale uncertainty applied for low-p_{T} (< 20 GeV) electrons;
- the uncertainty on the energy resolution smearing procedure;
- the uncertainty on the energy scale, given by the study of $Z \to e^+e^-$ events for electrons and photons.

In addition to the systematic uncertainties coming from the electron/photon energy calibration process, further uncertainties, described in Reference [99], are applied to electrons, concerning the electron identification and reconstruction efficiency scale factors. The scale factor comes from the combined efficiency measurement from three channels: $Z \to e^+e^-$, $W \to e\nu$ and $J/\Psi \to e^+e^-$.

Jets

Systematic uncertainties related to the jets can be classified into two categories: one refers to the jet energy resolution ('JER') and is described in details in Reference [145]; the other is coming from the jet calibration, including variations from the jet energy scale ('JES') and from the pile-up suppression. All the uncertainty sources can be varied up and down, except for the JER uncertainty.

The JES uncertainties are described in Reference [110], and ten different sources are considered in this analysis, including the reduced set of nuisance parameters from in-situ analyses, uncertainties in the η inter-calibration and the single hadron (corresponding to a high p_{T} jet) response measurements. Uncertainties due to the use of different simulation conditions in Monte Carlo samples such as the fast simulation samples are also considered.

The pile-up conditions used in the pile-up corrections to calibrate the jet energy (see Section 7.4) is sensitive to the distribution of the average number of interactions per bunch crossing, $\langle\mu\rangle$, and the number of reconstructed vertices in the event, N_{PV}. Therefore, uncertainty sources related to the pile-up corrections are included into the JES uncertainties.

Muons

Eight sources of systematic uncertainties related to the muons are taken into consideration. They are linked to the momentum scale and the resolution, as well as to the reconstruction efficiency. The momentum resolution uncertainties considered include uncertainties

coming from the measurement of the momentum in the muon spectrometer and the inner detector.

Missing transverse energy

For the $E_{\mathrm{T}}^{\mathrm{miss}}$ computation introduced in Section 7.5, energy deposits in the ATLAS detector are associated to various physics objects which are specifically calibrated. All the uncertainties related to the physics objects introduced above are propagated to the $E_{\mathrm{T}}^{\mathrm{miss}}$ computation. In addition, uncertainties on the energy scale and resolution of the SoftTerm (see Section 7.5) are also taken into account.

Luminosity

As introduced in Chapter 9, an overall symmetric uncertainty of 2.8% [119] on the integrated luminosity $20.3\,\mathrm{fb}^{-1}$ is applied to all the number of events given by the MC prediction, including $\gamma+$jet events and the signal samples (see Chapter 13).

Trigger efficiency

Two different triggers are used in this analysis: the $E_{\mathrm{T}}^{\mathrm{miss}}$ trigger, EF_xe80_tclcw_tight and the photon trigger EF_g120_loose. The uncertainties are obtained in the three lepton CRs and the VR by comparing the efficiency measurement as a function of $E_{\mathrm{T}}^{\mathrm{miss}}$, measured in the data to the one obtained in MC simulation. The trigger efficiency from MC simulation is given as the average of the integrated efficiencies of background samples composed of $Z(\to \nu\bar{\nu})+\gamma$, $W(\to \mu\nu)+\gamma$ and $Z(\to \mu^{+}\mu^{-})+\gamma$, weighted by the yield of the sample in that region.

A conservative symmetric uncertainty of 1% is derived from this study and will be applied to all the MC event yields. This study shows a 0.99 ± 0.01 efficiency of the $E_{\mathrm{T}}^{\mathrm{miss}}$ trigger in the SR, and an efficiency of $1.00^{+0.00}_{-0.01}$ for the photon trigger in the lepton CRs.

Theory uncertainties

At the generator level, the uncertainties related to the PDF can lead to variations of both the cross-section (σ) and the acceptance times efficiency ($A \times \varepsilon$). They are evaluated by following the PDF4LHC recommendations [146]. The PDF uncertainties can be classified into two categories:

- **The inter-PDF uncertainties** are computed as the difference between the mean value of PDFs from different families. They are evaluated as the symmetric uncertainty around the center of an *envelope* of two PDFs, shown in Figure 11.4.
- **The intra-PDF uncertainties** are computed from the systematic uncertainties from the fit process using all the PDF sets within a given PDF family. They are evaluated using either the Hessian method [147, 148] or the standard deviation depending on the PDF family: uncertainties on CTEQ6L1 and CT10 are computed using the symmetric Hessian method with a 68% confidence level; while uncertainties on MSTW2008lo68cl are derived from the asymmetric Hessian method; the uncertainties on NNPDF2.1LO are given simply as the standard deviation of the PDFs.

Another source of theoretical uncertainty for the MC simulated background samples is the scale uncertainty, which comes from the uncertainties on the renormalization and factorization scales. It can impact both the cross-section and the acceptance times efficiency, and it is estimated by increasing and decreasing the scale factors by a factor of 2.

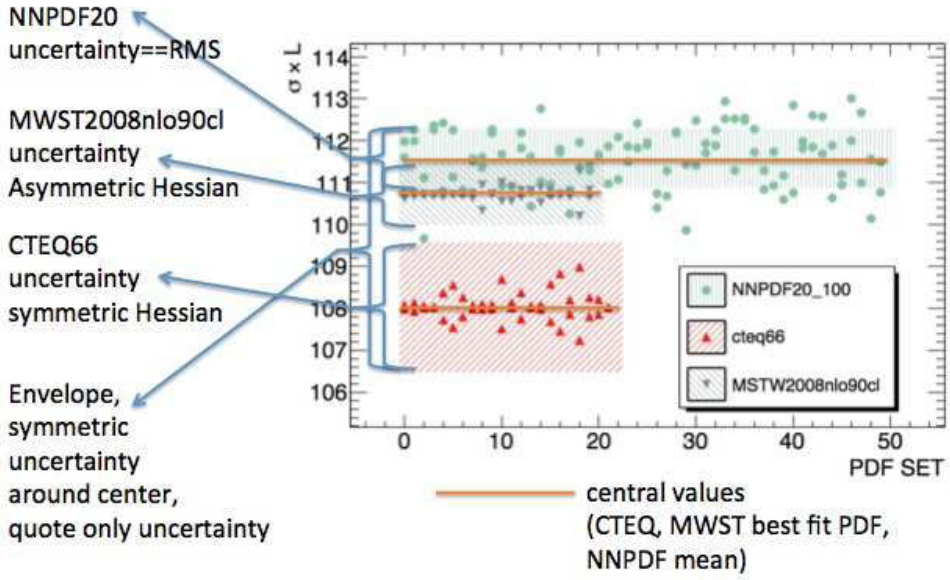

Fig. 11.4 Conceptual illustration of the PDF uncertainties.[149]

11.6 Background estimate validation

The techniques used to estimate the $V + \gamma$ backgrounds are checked in a VR, which is similar but orthogonal to the SR.

The VR events are selected with the same criteria as the SR, but lowering the $E_{\mathrm{T}}^{\mathrm{miss}}$ to the region of $(110, 150)$ GeV and enlarging the photon pseudorapidity range to $|\eta| < 2.37$ (excluding the calorimeter barrel and end-cap transition region $1.37 < |\eta| < 1.52$) to increase statistics.

There are two more specific cuts added to the VR. Given the fact that $\gamma+$jet and fake photon backgrounds will be increased when loosening the $E_{\mathrm{T}}^{\mathrm{miss}}$ cut, the first additional cut is set to suppress these backgrounds to a level similar to that in the SR. This is implemented for the selected events with a jet by asking the azimuthal angle between the photon and the jet to be $\Delta\phi(\gamma,\mathrm{jet}) < 2.7$. The other additional cut is applied on the azimuthal angle between the photon and $E_{\mathrm{T}}^{\mathrm{miss}}$ with $\Delta\phi(\gamma, E_{\mathrm{T}}^{\mathrm{miss}}) < 3.0$, in order to minimize the contamination of the signal events in the VR. The signal suppression power with the cut $\Delta\phi(\gamma, E_{\mathrm{T}}^{\mathrm{miss}}) < 3.0$ applied has been validated by comparing the signal significance from the VR to the SR rescaled to the 7 TeV data size for all the signal samples. The signal significance in the VR is below that in the rescaled SR.

The three lepton CRs are rebuilt to be consistent with the VR definition in order to derive the VR Standard Model expectation. The $\Delta\phi(\gamma, E_{\mathrm{T}}^{\mathrm{miss}})$ cut reduces too much statistics in these CRs in which no signal event is expected, therefore this cut is not applied in these CRs. This was proven not to bias the estimation, since the distribution shape of $\Delta\phi(\gamma, E_{\mathrm{T}}^{\mathrm{miss}})$ is found to agree well between MC and data in these CRs. The fake photon backgrounds based on data-driven estimation methods are recomputed accordingly.

In the VR, 307 events are observed in data. The total background estimate, obtained from the background fit (see Section 11.1) gives $272 \pm 17(stat.) \pm 14(syst.)$ events expected in the VR. The post-fit background estimate in the VR is in reasonable agreement with the observed data within two standard derivation (2σ). Table 11.4 shows the post-fit expectation for each of the background processes in the VR, where the irreducible background $Z(\rightarrow \nu\bar{\nu}) + \gamma$ represents 56% of the whole background.

The discriminant kinematic distributions are also checked from data to the background estimation in the VR. Figure 11.5 shows the comparison of the measured and expected $E_{\mathrm{T}}^{\mathrm{miss}}$ distribution in the VR; in the lower panel the ratio of the data and the background expectation is given. A good agreement between the estimation and measurement is shown in this figure for $E_{\mathrm{T}}^{\mathrm{miss}}$, and it is the same for the other variables checked.

Process	Event yield
$Z(\to \nu\bar{\nu}) + \gamma$	$153 \pm 16 \pm 10$
$W(\to \ell\nu) + \gamma$	$67 \pm 5 \pm 5$
$W/Z + \text{jet}, t\bar{t}, \text{diboson}$	$47 \pm 2 \pm 14$
$Z(\to \ell^+\ell^-) + \gamma$	$2.9 \pm 0.3 \pm 0.6$
$\gamma + \text{jet}$	$2.5^{+4.0}_{-2.5}$
Total background	$272 \pm 17 \pm 14$
Data	307

Table 11.4 Observed and expected event yields from Standard Model backgrounds in the validation region (VR). The uncertainties given are the statistical uncertainty followed by the systematic one. In the case of the $\gamma+$jet process, a global uncertainty is given.

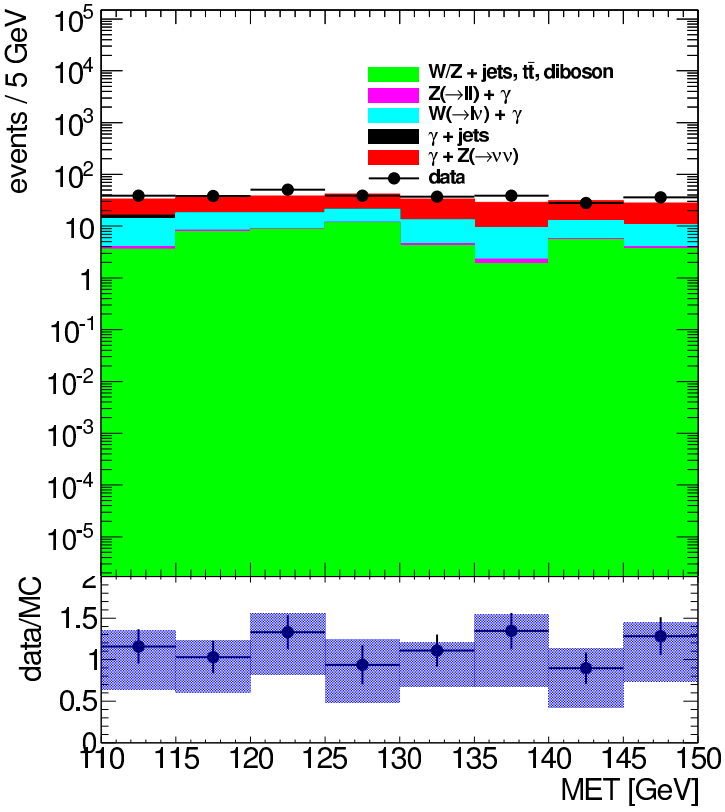

Fig. 11.5 The $E_{\mathrm{T}}^{\mathrm{miss}}$ distribution in the validation region (VR), where the bottom panel shows the ratio of data and background expectation [150].

11.7 Background estimate results

In the SR, there are 521 events observed in data, and the total Standard Model background expectation in the SR after the background-only fit is $557 \pm 36(stat.) \pm 27(syst.)$. Table 11.5 shows the post-fit expectation for each of the background processes in the SR. The total background expectation is dominated by $Z(\to \nu\bar{\nu}) + \gamma$ which represents approximately 70% of the background in the SR.

Process	Event yield
$Z(\to \nu\bar{\nu}) + \gamma$	$389 \pm 36 \pm 10$
$W(\to \ell\nu) + \gamma$	$82.5 \pm 5.3 \pm 3.4$
$W/Z + \text{jet}, t\bar{t}, \text{diboson}$	$83 \pm 2 \pm 28$
$Z(\to \ell^+\ell^-) + \gamma$	$2.0 \pm 0.2 \pm 0.6$
$\gamma + \text{jet}$	$0.4^{+0.3}_{-0.4}$
Total background	$557 \pm 36 \pm 27$
Data	521

Table 11.5 Observed and expected event yields from Standard Model backgrounds in the signal region (SR). The uncertainties given are the statistical uncertainty followed by the systematic one. In the case of the $\gamma+$jet process, a global uncertainty is given.

The systematic uncertainties shown in Table 11.5 are obtained from the background-only fit, considering all the uncertainty sources. The post-fit value of each uncertainty source is listed in Table 11.6. The dominant systematic uncertainty (4.6%) comes from the electron fake rate. Uncertainties from the reconstruction and identification efficiency corrections applied to the electrons and muons in the MC samples, give relative uncertainties of 1.3% and 0.7% respectively. The anti-correlation between the SR and the lepton CRs are taken into account, with respect to the uncertainties related to the lepton identification and reconstruction efficiency. This comes from the fact that leptons are vetoed in the SR but identified in the CRs. A 0.6% relative uncertainty comes from the uncertainties on the energy scale calibration for simulated electrons and photons. The photon energy resolution, isolation and identification efficiencies together give a relatively small uncertainty of 0.1%. The JES and JER uncertainties contribute 0.1% and 0.5% respectively. The uncertainties associated to the SoftTerm in the $\boldsymbol{E}_{\mathrm{T}}^{\mathrm{miss}}$computation give a relative uncertainty of 0.3%. The theoretical uncertainties related to the PDF and scale factors in the simulation samples at the generator level gives in total a 0.7% uncertainty on the background estimate in the SR. Besides, the uncertainty on the jet energy scale for pile-up suppression, and the uncertainties on the trigger efficiency and luminosity, are found to have negligible effects on the background estimation.

Uncertainty source	Relative effect in SR
Electron id/reco efficiency	$-1.3\% + 1.3\%$
E/γ energy scale	$-0.6\% + 0.4\%$
E/γ energy resolution	$-0.1\% + 0.01\%$
Photon identification efficiency	$-0.04\% + 0.05\%$
Photon isolation efficiency	$-0.0\% + 0.01\%$
Jet energy resolution	$-0.5\% + 0.5\%$
Jet energy scale	$-0.0\% + 0.1\%$
Jet energy corrections related to pile-up	$-0.0\% + 0.06\%$
Luminosity	$-0.0\% + 0.01\%$
$E_{\mathrm{T}}^{\mathrm{miss}}$ SoftTerms scale and resolution	$-0.3\% + 0.1\%$
Muon reco efficiency	$-0.7\% + 0.7\%$
Muon momentum scale	$-0.0\% + 0.01\%$
Muon momentum resolution	$-0.0\% + 0.01\%$
Theoretical uncertainty	$-0.7\% + 0.7\%$
Trigger efficiency	$-0.0\% + 0.01\%$
Electron fake photon	$-4.5\% + 4.6\%$
Jet fake photon	$-0.1\% + 0.1\%$
Statistical error	$-6.4\% + 6.4\%$
Total	$557 \pm 36(\mathrm{stat}) \pm 27(\mathrm{syst})$

Table 11.6 The relative effect of the various uncertainty sources on the total background in the SR [151]. Results are shown for $V\gamma$ backgrounds estimated with the simultaneous fit technique. Uncertainties are the sum in quadrature of the corresponding individual contributions.

All the systematic uncertainties are treated as orthogonal, giving a total systematic uncertainty on the post-fit background estimate in the SR of $\sim 5\%$, with a statistical uncertainty of $\sim 6\%$.

The $E_{\mathrm{T}}^{\mathrm{miss}}$ distribution in the SR is shown in Figure 11.6 compared to that of the post-fit background expectation, and the similar comparisons in the three lepton CRs are shown in Figure 11.1. In Figure 11.1, one can see that the CRs are indeed enriched in the background process of interest as introduced in Section 11.2. Besides, the lower panel of each histogram in Figures 11.6 and 11.1 shows the ratio of data to the post-fit MC estimate, indicating a good agreement in each region between the data and the post-fit background estimate within the global uncertainty.

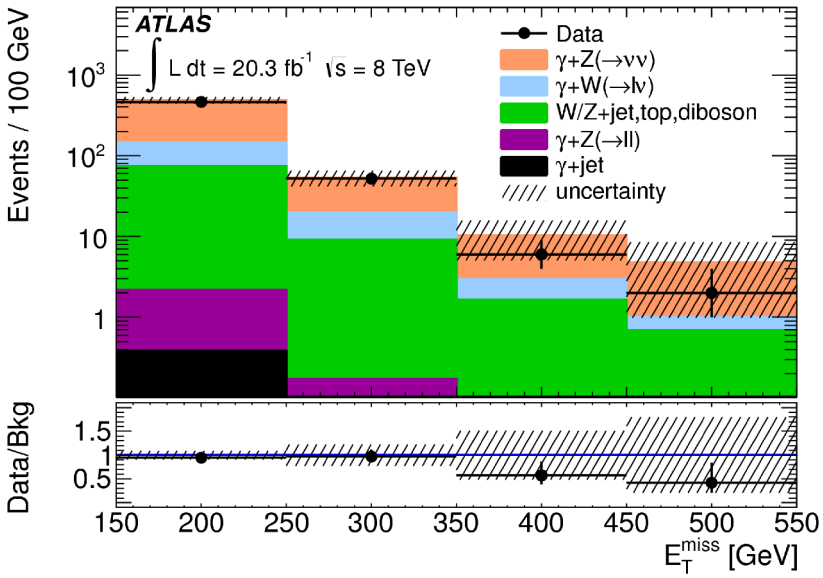

Fig. 11.6 Distribution of $E_{\mathrm{T}}^{\mathrm{miss}}$ in the signal region measured in data compared to the background expectation normalized by the background-only fit. The dashed band includes the statistical and systematic uncertainties. Overflows are included in the final bin. The lower part of the figure shows the ratios of data to the post-fit background estimate.

Chapter 12

Model-independent results

If an excess of $\gamma + E_{\mathrm{T}}^{\mathrm{miss}}$ events is found with respect to the Standard Model expectation, it can be noted as N_{sig} and presented as:

$$\mathrm{N}_{sig} = \sigma_{vis} \times \int L\mathrm{d}t, \tag{12.1}$$

where $\int L\mathrm{d}t$ is the integrated luminosity equal to $20.3\,\mathrm{fb}^{-1}$, and σ_{vis} is the *visible cross section* produced by any BSM physics, defined as the product of acceptance (A), selection efficiency (ε) and production cross section (σ): $\sigma \times A \times \varepsilon$.

As indicated in Table 11.5, the number of events observed in the SR is consistent with the post-fit SM background expectation. A model-independent upper limit at 95% confidence level (CL) will be set on the number of events in the SR, N_{sig}, which could come from any BSM physics in the SR. This model-independent result can be applied to models of new physics, by comparing this limit to their predicted yield in the SR.

A model-independent signal fit [141] is used in this case. It is similar to the background-only fit introduced in Section 11.1, but with the likelihood being constructed from both the SR and the CRs. The observed and expected numbers of events in the SR follow Poisson pdfs. The correlations of the parameters are also taken into account. The number of signal events in the SR is treated as a free parameter of interest (POI) in the fit, and no signal contamination is considered in the CRs.

After the fit, the upper limit is derived based on the CL_S method described in Reference [152]. The one-sided p-value is computed for each tested N_{sig} using the distribution of the test statistic, which is obtained by throwing pseudo experiments. The test statistic is defined as the profile likelihood ratio, shown in Equation 12.2, where the likelihood function is constructed from the model-independent signal fit. In the numerator, $\hat{\mathrm{N}}_{sig}$ and $\hat{\theta}$ are the values which maximize the likelihood function, whilst $\hat{\hat{\theta}}$ maximizes the likelihood for each

test value of N_{sig} in the denominator.

$$q_{\mu_{\text{sig}}} = -2\log\left(\frac{\mathscr{L}(N_{sig}\,,\,\hat{\hat{\theta}})}{\mathscr{L}(\hat{N}_{sig}\,,\,\hat{\theta})}\right) \tag{12.2}$$

As the distribution of the test statistic is well behaving for a sample of large data statistics, asymptotic formulae [142] are used to compute the result instead of using pseudo experiments. The expected p-values are computed using likelihoods obtained using the background-only fit. The observed and expected p-values are shown as a function of $\sigma_{vis} = \sigma \times A \times \varepsilon$ in Figure 12.1. The 1σ and 2σ uncertainty bands on the expected p-values are also shown in this figure. The value of $\sigma \times A \times \varepsilon$ for which the p-value reaches 0.05 (0.10) is the upper limit on the visible cross section for new physics production at 95% (90%) CL.

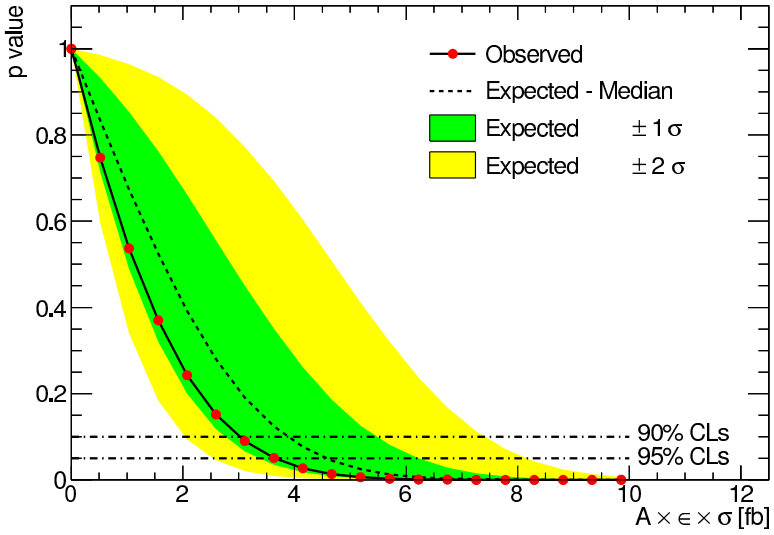

Fig. 12.1 Evolution of the p-values for the signal hypothesis (CLs) as a function of the visible cross section ($\sigma \times A \times \varepsilon$) of new physics. The $\sigma \times A \times \varepsilon$ values with observed p-values below the 95% (90%) CL line are excluded at 95% (90%) CL.

The upper limits are also given on the fiducial cross section, $\sigma \times A$, in order to present the model-independent result in a format better suited for re-interpretation. The selection efficiency ε is determined from signal samples (the EFT DM samples described in Section 9.3) with pure $\gamma + E_{\text{T}}^{\text{miss}}$ final state giving a conservative estimate of 69%. The upper limits on the visible cross section and fiducial cross section at 95% CL are shown in Table 12.1.

	$\sigma \times A \times \varepsilon$ [fb]	$\sigma \times A$ [fb]
95% CL, observed	3.64	5.3
95% CL, expected	4.68	6.8

Table 12.1 The observed and expected upper limits at 95% CL on the visible cross section $\sigma \times A \times \varepsilon$, in fb. The fiducial cross section ($\sigma \times A$) limits shown in the third column are obtained by using a conservative estimate of $\varepsilon = 69\%$.

Chapter 13

Model interpretation

The monophoton analysis results presented in Section 11.7 can also be interpreted in the two models introduced in Section 8.1. They are a EFT dark matter model describing the WIMP pair production coupling with two photons, and a R-parity conserving simplified supersymmetric model describing a pair of left and right handed first and second generation mass degenerate squark pair production. The result interpretation to put constraints to the parameter space of these two models will be described in Section 13.1 and 13.2, respectively

13.1 Dark matter model inspired by the Fermi-LAT results

In the monophoton analysis, one can compute an upper limit on the cross section σ_{excluded} of the process $\chi\bar{\chi} \to \gamma\gamma$ as shown in Figure 8.2, for given m_χ, M^*, k_1 and k_2. According to the Equation (8.2), one can use σ_{excluded} to compute the lower limit on the suppression scale, M^*_{excluded}. For $m_\chi = 130$ GeV, an excluded area can then be drawn in the plane of k_1 and k_2, by comparing M^*_{excluded} to M^*_{Fermi}.

13.1.1 Signal cross section

The cross sections (σ) for all the samples introduced in Section 9.3 are taken directly from the generator; they are shown as a function of k_1 and k_2 for different masses of dark matter particles in Figure 13.1. It shows that cross sections decrease with the increase of the mass of dark matter particles since it is harder to produce heavier particles at the LHC. For a given mass of dark matter particles, the cross sections increases more rapidly with k_2 than with k_1 resulting from their different ratios in the coupling of dark matter particles to

a photon and a Z boson, as shown in Equation (8.1). The theoretical uncertainties on the cross section are given in Section 13.1.2, they will be considered when setting the observed exclusion limits in Section 13.1.3.

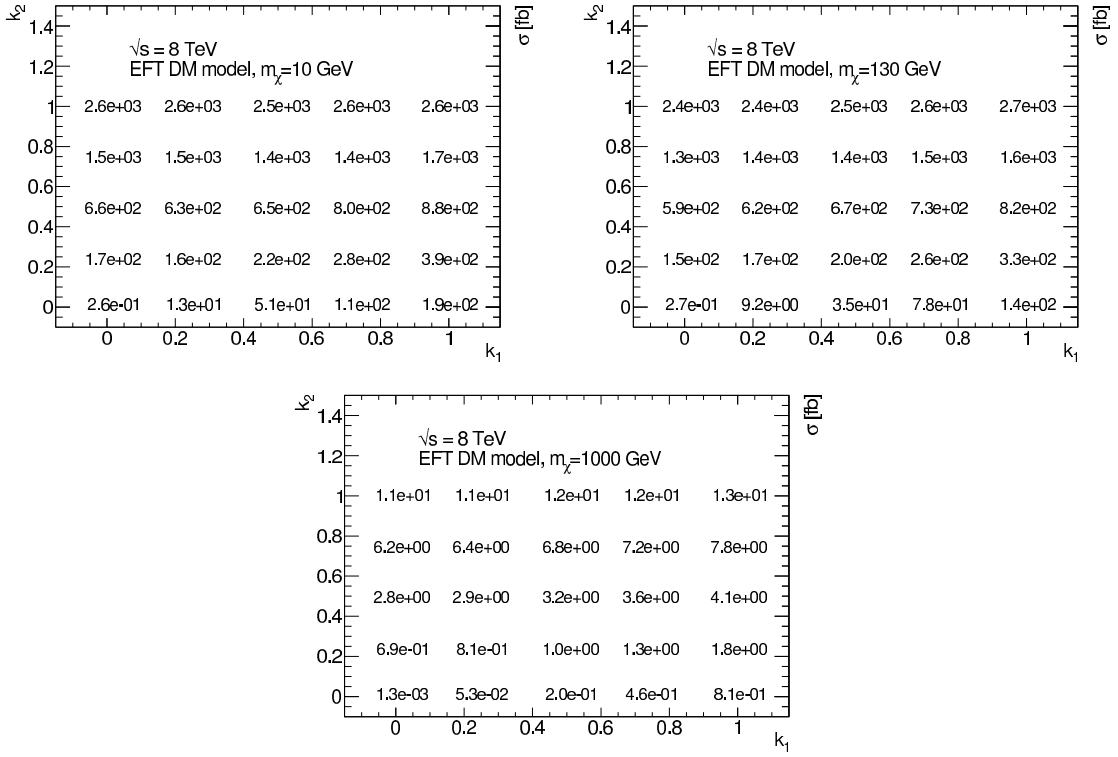

Fig. 13.1 Cross sections in fb as a function of k_1 and k_2 for the EFT DM samples with $m_\chi = 10$ GeV (top left), $m_\chi = 130$ GeV (top right) and $m_\chi = 1000$ GeV (bottom).

13.1.2 SR yields and uncertainties

The SR event yields for all the signal samples for $20.3\,\text{fb}^{-1}$ at $\sqrt{s} = 8$ TeV are shown in Figure 13.2 in the plane of k_1 and k_2 for each WIMP mass. Similarly, the product of acceptance and efficiency ($A \times \varepsilon$) for each signal sample in the SR are shown in Figure 13.3. This figure shows that $A \times \varepsilon$ is mostly independent of k_1 and k_2, which mainly affect the cross section, as these parameters control the interaction of the dark matter particles with photon and Z boson.

Figure 13.4 shows how the distribution of $E_{\text{T}}^{\text{miss}}$ changes with the dark matter mass for a given k_1 and k_2. The $E_{\text{T}}^{\text{miss}}$ distribution shifts to higher value as the dark matter mass increases, leading to an increased $A \times \varepsilon$, as shown in Figure 13.3.

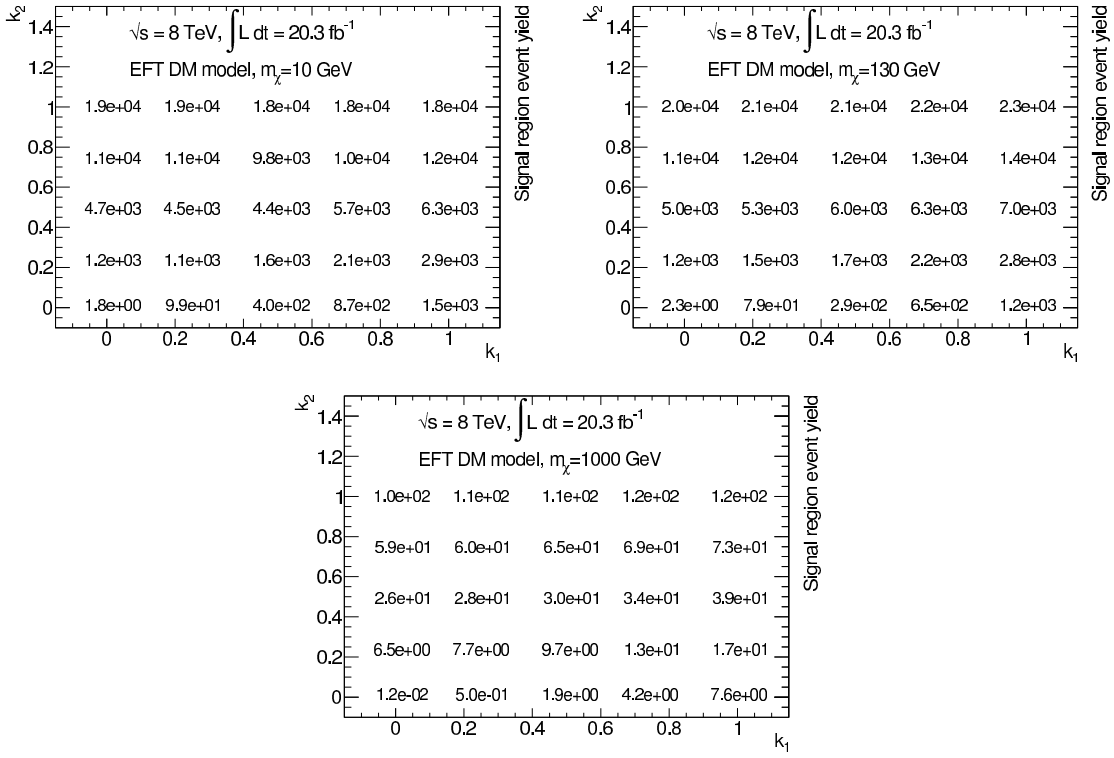

Fig. 13.2 Event yield in the signal region for $20.3\,\text{fb}^{-1}$ of data as a function of k_1 and k_2 for the EFT DM samples with $m_\chi = 10$ GeV (top left), $m_\chi = 130$ GeV (top right) and $m_\chi = 1000$ GeV (bottom).

Theory uncertainties

At the generator level, three independent categories of theory uncertainties are taken into account, which will be added up in quadrature to estimate their effect on the cross section or $A \times \varepsilon$.

Two of the uncertainties, the PDF uncertainties and the scale uncertainties, are introduced in Section 11.5. They are computed using LHAPDF [153, 154].

The third category is the ISR/FSR uncertainties which affect the $A \times \varepsilon$. They are evaluated in PYTHIA 8 by varying the parameters such as the strong coupling strength α_S or the kinematic parameters, which control the ISR or FSR development in PYTHIA 8 . The considered parameters are varied up and down with respect to their default values. Further information can be found in References [84, 136, 155].

For all the signal samples, the PDF (scale) uncertainties on the cross section is approximately $\pm 8\%$ ($^{+10\%}_{-8\%}$). They will be shown as a variation of the observed upper limits in Section 13.1.3. The PDF and scale uncertainties on the cross section for each signal sample are listed in Tables 2 to 4 in Appendix Conclusion.

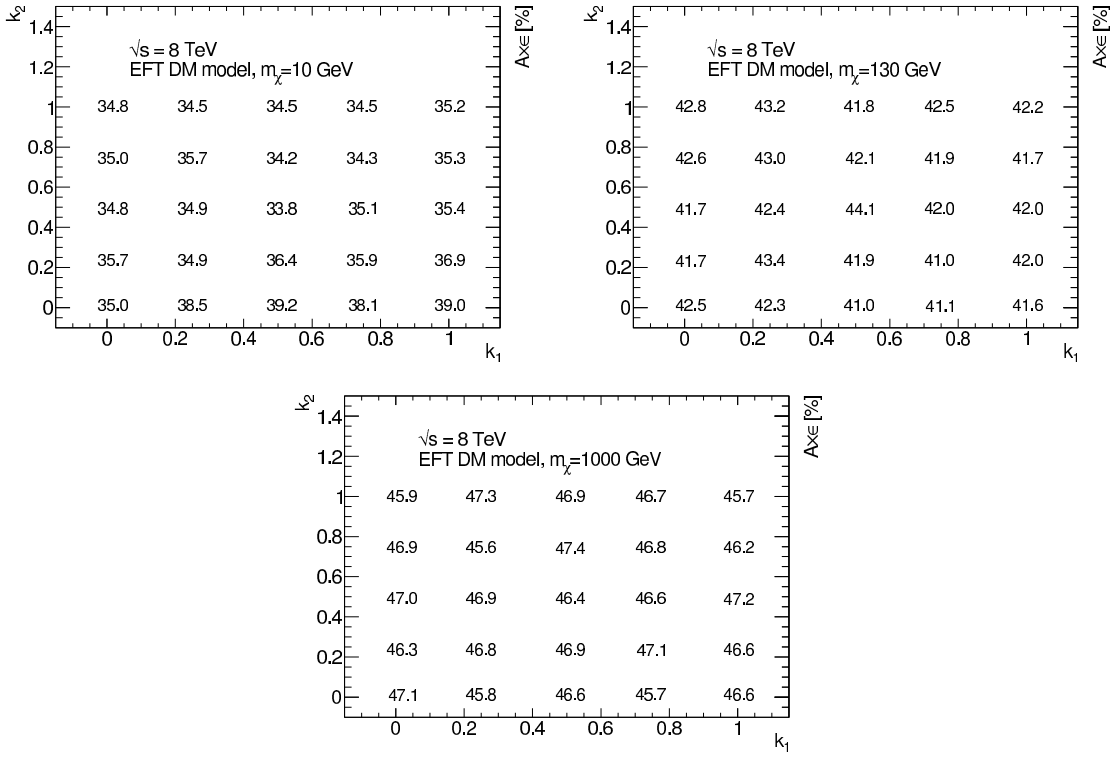

Fig. 13.3 The product of the acceptance and the efficiency [%] in the SR as a function of k_1 and k_2 for the EFT DM samples with $m_\chi = 10$ GeV (top left), $m_\chi = 130$ GeV (top right) and $m_\chi = 1000$ GeV (bottom).

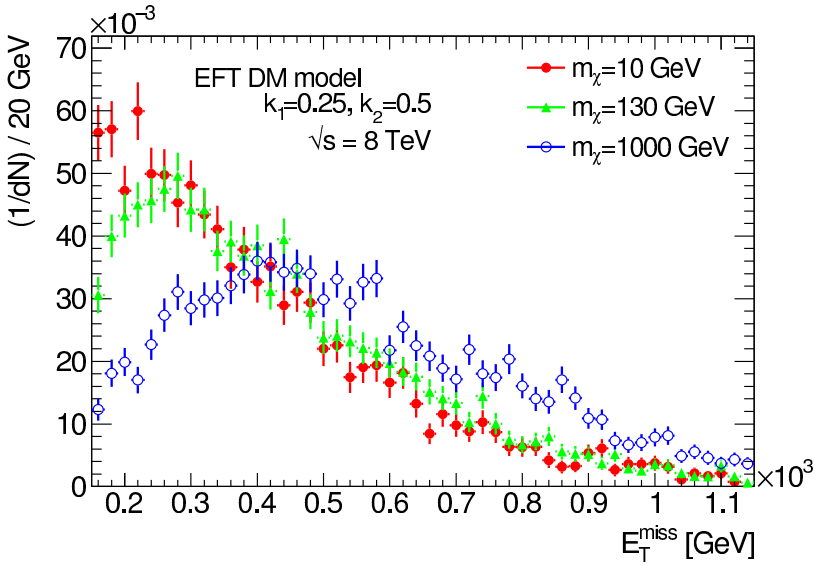

Fig. 13.4 The $E_{\mathrm{T}}^{\mathrm{miss}}$ distribution for three EFT DM signal samples in the signal region.

The uncertainties on $A \times \varepsilon$ vary among all the signal samples up to approximately 3%, and are dominated by the ISR/FSR uncertainties. They will be treated as a nuisance parameter in the model-dependent fit procedure, as the other systematic uncertainties introduced in Section 11.5. The PDF, scale and ISR/FSR uncertainties on the product of acceptance and efficiency in the SR for each signal sample are listed in Tables 5 to 7 in Appendix Conclusion.

Other systematic uncertainties

Beside the theoretical uncertainties, the systematic uncertainties introduced in Section 11.5 are also computed for each signal sample. The final uncertainties on the SR yield of each signal sample are dominated by the 5% symmetric uncertainty from the photon identification efficiency, the 4% symmetric uncertainty from the photon isolation efficiency and the 2.8% symmetric uncertainty from the integrated luminosity. The absolute values of the systematic uncertainties for all the signal samples are approximately $\sim$ 7-8% as listed in Tables 8 to 10 in Appendix Conclusion.

13.1.3 Results

As no excess of events is observed in this analysis, the results shown in Section 11.7 are used to compute lower limits on M^* for all the signal samples of this model via an exclusion fit.

The exclusion fit [141] procedure is similar to the model-independent signal fit (discovery fit) introduced in Chapter 12, but it takes the systematic and theoretical uncertainties on the signal $A \times \varepsilon$ as input in the SR.

According to the Equation (8.2), the lower limits on the suppression scale ($M^*_{excluded}$) are translated from the upper limits on the cross section ($\sigma_{excluded}$) via

$$M^*_{excluded} = \left(\frac{\mathrm{N}_{expected}}{\mathrm{N}_{excluded}} \right)^{\frac{1}{6}} \times M^*_{nominal}, \tag{13.1}$$

where $\mathrm{N}_{expected}$ refers to the expected event yields shown in Figure 13.1, and $\mathrm{N}_{excluded} = \sigma_{excluded} \times 20.3\,\mathrm{fb}^{-1}$. The lower limits are computed at 95% CL on M^* for all the signal points. The results are shown as the numbers in Figures 13.5 to 13.7 in the plane of k_1 and k_2 for $m_\chi = 130, 10, 1000$ GeV. As indicated by these three figures, $M^*_{excluded}$ decreases with m_χ for a given k_1 and k_2 whilst it increases with k_1 and k_2 for a given m_χ, as expected.

As introduced in Section 2.2, the EFT can be valid for a s-channel model when $M_* > \frac{m_\chi}{2\pi}$. Therefore some lower limits on the suppression scale M^* with small k_1 and k_2 for $m_\chi =$

1000 GeV may not be valid in this case. However, the procedure to insure EFT validity for this specific model is still under discussion within the ATLAS-CMS Dark Matter Forum [1]; it was therefore not implemented neither in the published paper, nor in this thesis.

The results for $m_\chi = 130$ GeV are shown in Figure 13.5, where the observed and expected exclusion boundaries on M^* are also given by comparing the $M^*_{excluded}$ to the value required to explain the Fermi-LAT results (see Section 8.1). A large area of the parameter space of k_1 and k_2 is excluded in this model by comparing to the Fermi-LAT results.

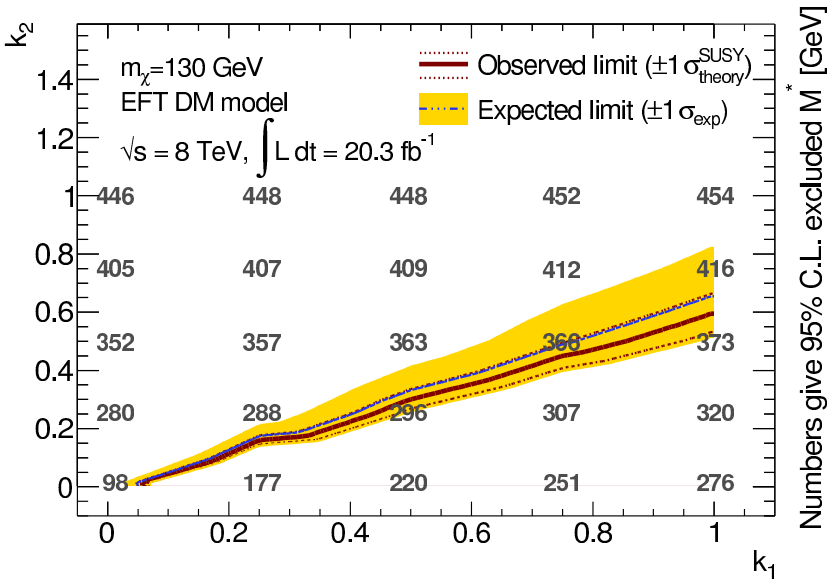

Fig. 13.5 The 95% CL observed lower limits on M^* as a function of k_1 and k_2 for the EFT dark matter model inspired by Fermi-LAT ($m_{DM} = 130$ GeV). The limits are proportional to the expected number of event yields in the SR, which increase with k_1 and k_2. The observed (expected) exclusion boundary indicates that the upper region is excluded at 95% CL by comparing to the Fermi-LAT line results.

[1] The forum aims at harmonizing the dark matter benchmarks used in both experiments for the next LHC run.

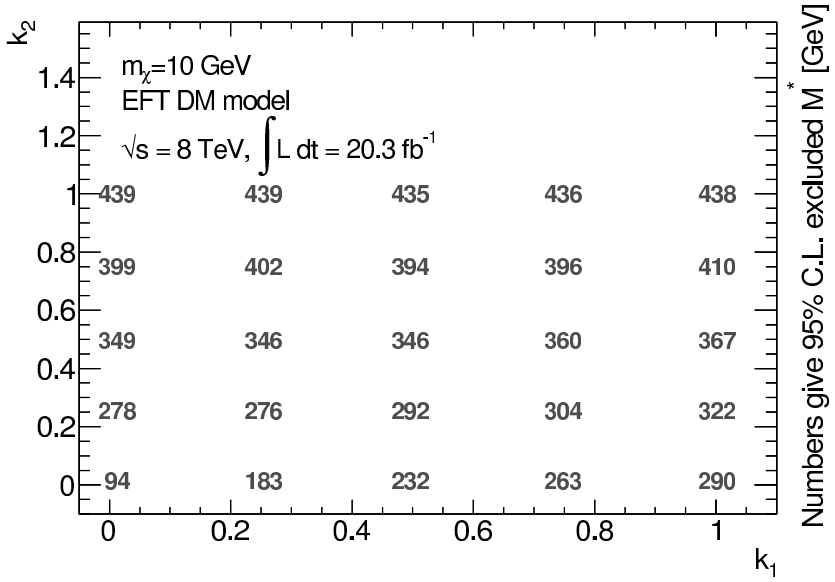

Fig. 13.6 The 95% CL observed lower limits on M^* as a function of k_1 and k_2 for the EFT dark matter model inspired by Fermi-LAT ($m_{DM} = 10$ GeV).

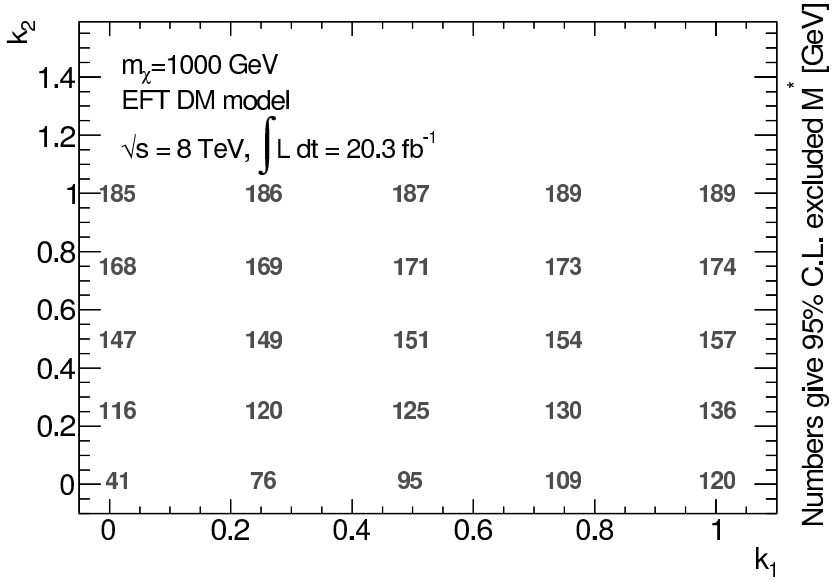

Fig. 13.7 The 95% CL observed lower limits on M^* as a function of k_1 and k_2 for the EFT dark matter model inspired by Fermi-LAT ($m_{DM} = 1000$ GeV).

13.2 Squarks in a compressed mass spectrum scenario

In the monophoton analysis, one can compute the upper limits on the cross sections for given $m_{\tilde{q}}$ and $m_{squark} - m_{\tilde{\chi}^0}$ in this compressed squark model. One can put an exclusion boundary in the plane of $m_{\tilde{q}}$ and $m_{squark} - m_{\tilde{\chi}^0}$ by comparing the upper limits on the cross section to the theoretical values.

13.2.1 Signal cross section

Cross sections for the signal samples introduced in Section 9.3 are calculated at next-to-leading order in the strong coupling constant including the resummation of soft gluon emission at next-to-leading-logarithm accuracy when available [156–160]. The nominal cross section and its uncertainty are taken from an envelope of cross-section predictions using different PDF sets and factorization and renormalization scales, as described in Reference [161].

The simulated signal points with their cross sections are shown in Figure 13.8, and the most compressed region shown in these figures is at $\Delta M = 5$ GeV.

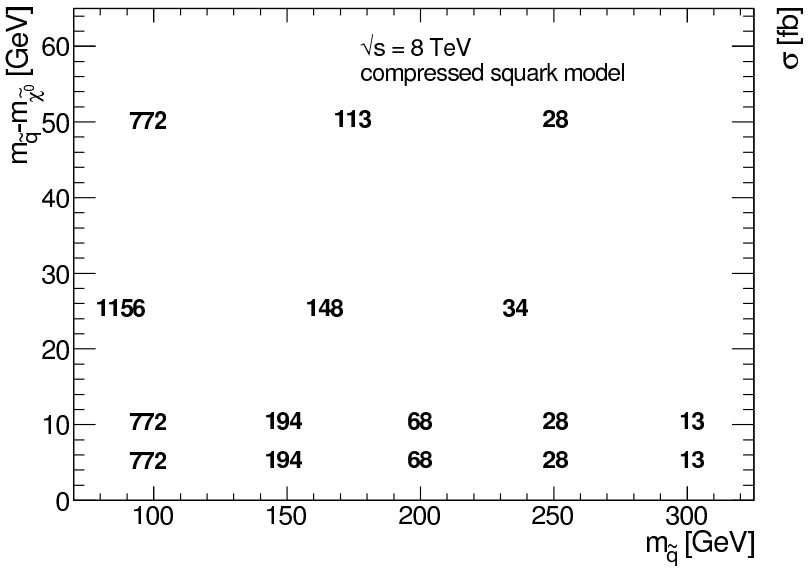

Fig. 13.8 Cross section in fb for each signal of the squark model, shown in the plane of $m_{\tilde{q}}$ and $m_{\tilde{q}} - m_{\tilde{\chi}_1^0}$.

13.2.2 SR yields and uncertainties

Figure 13.9 contains four signal grids showing various SR quantities computed at each signal point, including the SR event yield for 20.3 fb^{-1}at $\sqrt{s} = 8$ GeV (top left), the acceptance and efficiency in the SR (top right), the SR acceptance obtained with truth information given by the MC simulation (bottom left), and the SR selection efficiency which is computed from the measurement of the $A \times \varepsilon$ and A (bottom right).

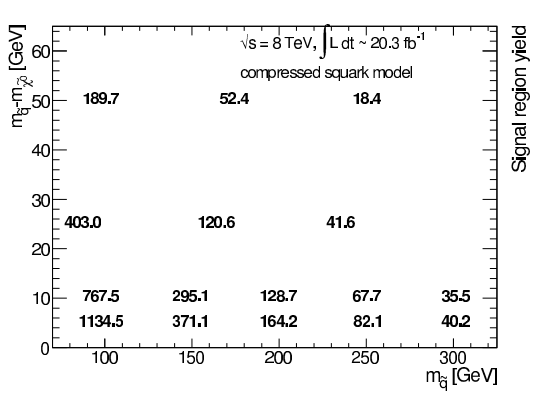

(a) Event yield for 20.3 fb^{-1}of data

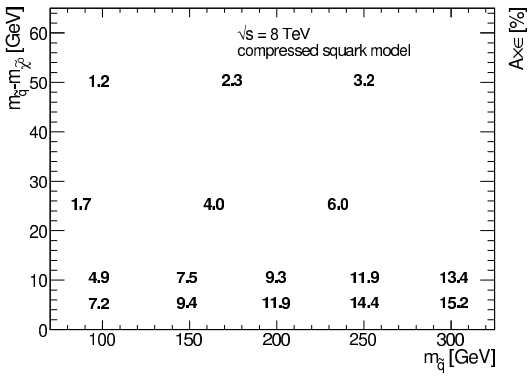

(b) The product of the acceptance and the efficiency (%)

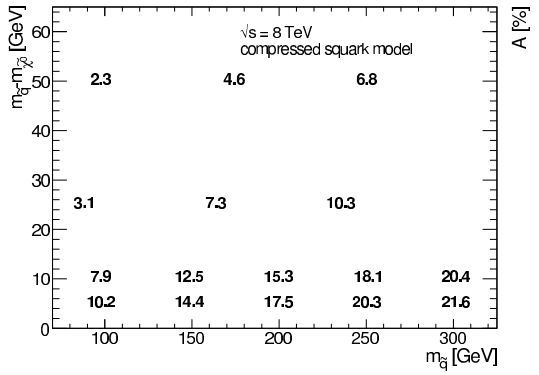

(c) Truth acceptance (%).

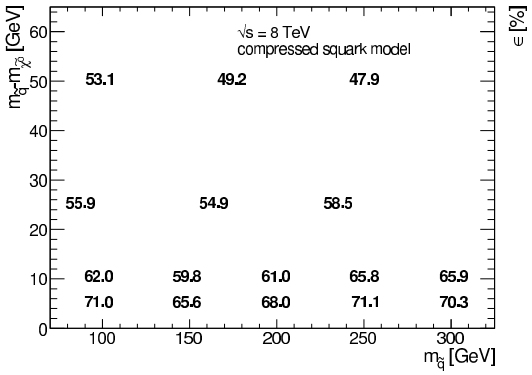

(d) Selection efficiency (%)

Fig. 13.9 Various quantities in the SR is shown as a function of $m_{\tilde{q}}$ and $m_{\tilde{q}} - m_{\tilde{\chi}_1^0}$, for all the signal points of the supersymmetric simplified model in a compressed squark scenario. Only the first and second generation squarks are considered and are degenerate in mass.

$A \times \varepsilon$ is found to decrease with increasing ΔM in Figure 13.9. This is expected as, for signal events with larger ΔM, the quarks from the decay product of the squarks are more likely to be reconstructed as jets, and thus to contain more than one jet in the final state. This can be seen in the distribution of the jet multiplicity before the 'jet veto' cut, shown in Figure 10.10 (top left). For the events with quarks more likely to be reconstructed as jets ,

the corresponding $E_{\mathrm{T}}^{\mathrm{miss}}$ distribution shifts slightly to lower values as shown in Figure 13.10 (top).

Figure 13.9 also shows that $A \times \varepsilon$ increases with $m_{\tilde{q}}$, which is expected as the signals with higher squark mass produce larger $E_{\mathrm{T}}^{\mathrm{miss}}$, as shown in Figure 13.10 (bottom). As discussed in the SR optimization studies shown in Section 10.3.2, having exclusive SRs with different $E_{\mathrm{T}}^{\mathrm{miss}}$ cut could increase the sensitivity at higher masses if the statistics in the CRs with higher $E_{\mathrm{T}}^{\mathrm{miss}}$ cut was sufficient. This could potentially be done in the monophoton analysis performed in the next LHC run, as will be discussed in Chapter 15.

Cutflow

Table 13.1 shows an example of the cutflow for one signal point with $m_{\tilde{q}} = 200$ GeV and $m_{\tilde{\chi}_1^0} = 195$ GeV. This cutflow along with the efficiency, acceptance, σ and uncertainties for all squark samples shown in Figure 13.9 are published on HepData [162], which offers auxiliary information for external users to re-implement the analysis result. This information has been used in Reference [163], which has reproduced and validated this analysis using the MadAnalysis5 [164, 165] framework.

Nominal	9989
Pre-selection:	
1. Trigger	8582
2. Good vertex	8574
3. Cleaning cuts	8213
SR selection:	
1. $E_{\mathrm{T}}^{\mathrm{miss}} > 150$ GeV	4131
2. At least one loose photon with $p_{\mathrm{T}} > 125$ GeV ($\lvert\eta\rvert < 2.37$)	2645
3. The leading photon is tight with $\lvert\eta\rvert < 1.37$	2068
4. The leading photon is isolated	1898
5. $\Delta\phi(\gamma^{\mathrm{leading}}, E_{\mathrm{T}}^{\mathrm{miss}}) > 0.4$	1887
6. Jet veto: $N_{\mathrm{jet}} \leq 1$ and $\Delta\phi(\mathrm{jet}, E_{\mathrm{T}}^{\mathrm{miss}}) > 0.4$	1219
7. Lepton veto	1188

Table 13.1 Example cutflow for the SUSY compressed squark signal point with $m_{\tilde{q}} = 200$ GeV and $m_{\tilde{\chi}_1^0} = 195$ GeV; 10,000 events were generated.

Theory uncertainties

The theory uncertainties on the cross sections come from the uncertainties on the PDFs, renormalization and factorization scales and ISR/FSR. They are computed with a package based on Prospino 2.1 [166] and developed by the SUSY working group in ATLAS, which is

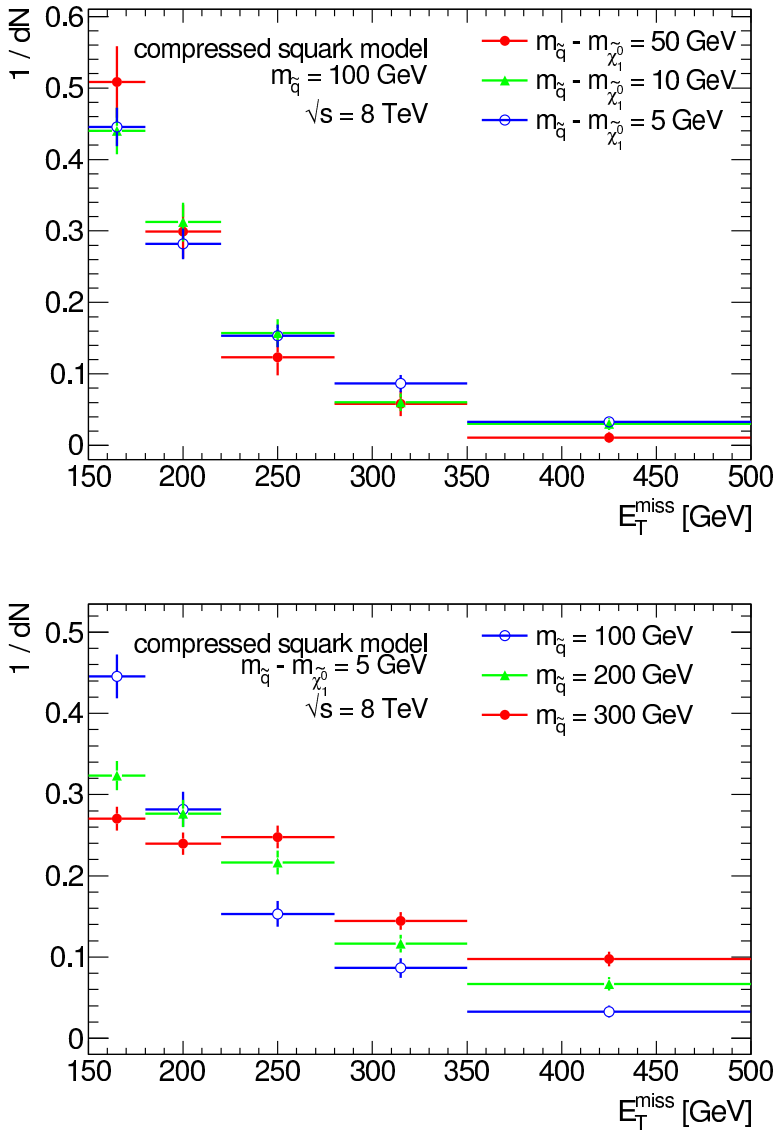

Fig. 13.10 The $E_{\mathrm{T}}^{\mathrm{miss}}$ distributions of various squark signal points, for $m_{\tilde{q}} = 100$ GeV with different $m_{\tilde{q}} - m_{\tilde{\chi}_1^0}$ (top) and for $m_{\tilde{q}} - m_{\tilde{\chi}_1^0} = 5$ GeV with different $m_{\tilde{q}}$ (bottom).

known as `SUSYSignalUncertainties`. These uncertainties are symmetric and are $\sim 15\%$ for different signal points. They will be used to compute the variation of the observed model exclusion limits in Section 13.2.3.

The theoretical uncertainty on the SR acceptance (A) for each signal point is estimated by varying the value of the strong coupling strength α_S, the renormalization and factorization scales, and the generator (MADGRAPH and PYTHIA 6) matching parameters. These uncertainties vary from 0 to 9% and are treated as symmetric uncertainties on the SR event

yields; they are treated as nuisance parameters in the exclusion fit with a Gaussian distribution as described in Section 13.2.3. The overall theoretical uncertainties on cross section and SR acceptance for each signal point are shown in Table 14 in Appendix Conclusion.

Other systematic uncertainties

All the systematic uncertainties introduced in Section 11.5 are computed for each signal sample. The final systematic uncertainties do not differ much from one signal point to another for $\Delta M < 10$ GeV, and the absolute values of the uncertainties vary from 7% to 9%. The dominant uncertainties come from the identification and isolation efficiencies of the photon. For signal points with $\Delta M = 25$ GeV and 50 GeV, the uncertainties are dominated by the uncertainties related to the jet, varying from 7.5% to 11.7%.

Figure 13.11 shows the maximum [%] from the up and down systematic uncertainties on $A \times \varepsilon$ for each signal point of the compressed squark model, including the theoretical uncertainties.

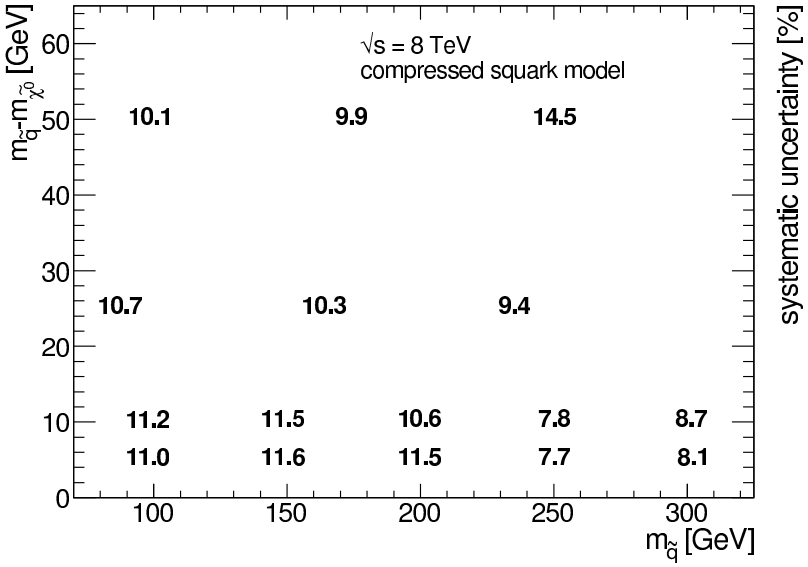

Fig. 13.11 The maximum [%] from the up and down systematic uncertainties on $A \times \varepsilon$ for each signal point of the compressed squark model, including the theoretical uncertainties.

13.2.3 Results

Mass degenerate limits

The upper limits at 95% CL on the cross section are computed using the exclusion fit. All the uncertainties on $A \times \varepsilon$ introduced in Section 13.2.2 are treated as nuisance parameters,

and the visible cross section is set as the free parameter of interest in the fit.

The expected and observed upper limits on the cross section for all the signal points are shown in the plane of $m_{\tilde{q}}$ and $m_{\tilde{q}} - m_{\tilde{\chi}_1^0}$ in Figure 13.12. By comparing these to the cross sections shown in Figure 13.8, one can derive the expected and observed exclusion areas in the phase space of $m_{\tilde{q}}$ and $m_{\tilde{q}} - m_{\tilde{\chi}_1^0}$. They are shown in Figure 13.12 along with the uncertainty band on the expected limit and the uncertainty band on the observed exclusion line coming from the theoretical uncertainties on the cross section introduced in Section 13.2.2.

As introduced in Section 8.1, the very compressed region in the mass spectrum of this model is particularly interesting for the monophoton analysis. For the most compressed region in Figure 13.12, the monophoton analysis is able to exclude the squark mass, $m_{\tilde{q}}$, up to 250 GeV. This result is included in the summary plot of the ATLAS SUSY working group, see Figure 3.3.

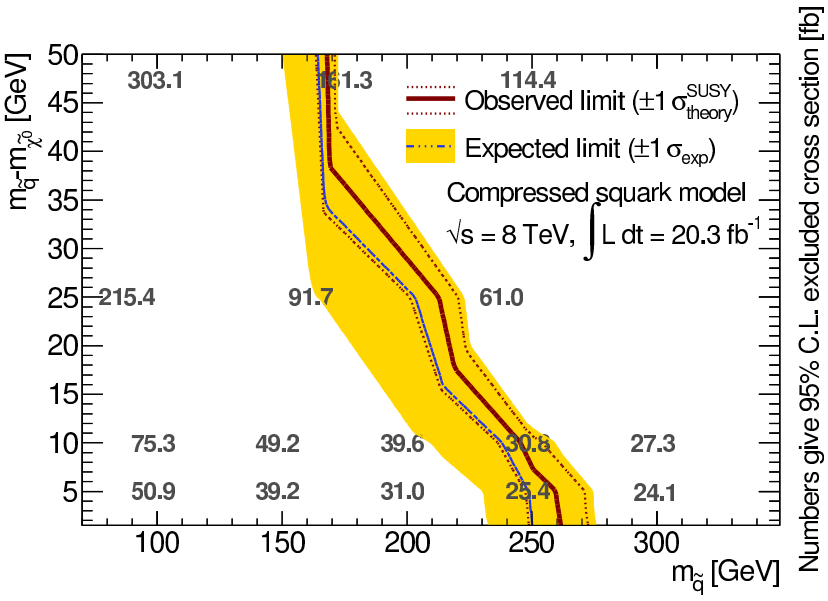

Fig. 13.12 Upper limits at 95% CL on the cross section for the compressed squark model, as a function of the squark mass, $m_{\tilde{q}}$, and of the difference between the squark mass and the mass of the neutralino, $m_{\tilde{q}} - m_{\tilde{\chi}_1^0}$, in the compressed region of $m_{\tilde{q}} - m_{\tilde{\chi}_1^0} < 50$ GeV. The observed (solid line) and expected (dashed line) upper limits from this analysis are shown; the upper limit on the cross section (in fb) is indicated for each model point.

Non-degenerate limits

As discussed in Section 8.1, the photon in the model considered here can be radiated from either the initial-state quarks or the intermediate squarks. The cross sections therefore

differ for the up-type squark ($\tilde{u}$) and the down-type squark ($\tilde{d}$), which makes it possible for the monophoton analysis to probe the squark charge if any signal is observed.

In order to obtain the exclusion boundaries for non-degenerate $\tilde{u}$ and $\tilde{d}$ (the left and right handed sparticles are still mass degenerate), the cross sections for all the signal points are recomputed by allowing one or the other component to be generated in MADGRAPH 5. Their $A \times \varepsilon$ are obtained from the signal samples described in Section 13.2.1 by requiring the squark to be of the appropriate type in the SR events. The kinematic distributions were checked and found to be in good agreement between the up and the down type squark production. Both the theoretical and the systematic uncertainties to compute the final exclusion boundaries follow the results from the degenerate signals. The upper limits at 95% CL in the phase space of $m_{\tilde{q}}$ versus $m_{\tilde{q}} - m_{\tilde{\chi}_1^0}$ for the up and the down type $\tilde{q}$ are shown in Figure 13.13, along with the mass degenerate squark results already presented in Figure 13.12.

The non-degenerate limits differentiate the up-type squark from the down-type squark, as shown in Figure 13.13. If there is a signal observed, one possible way to exploit this monophoton feature to probe the charge information of the squark is to compare its result with other channels which have the same model interpretation but which are not sensitive to the charge. Such channel can be the monojet analysis, which will be introduced in Section 14.2.

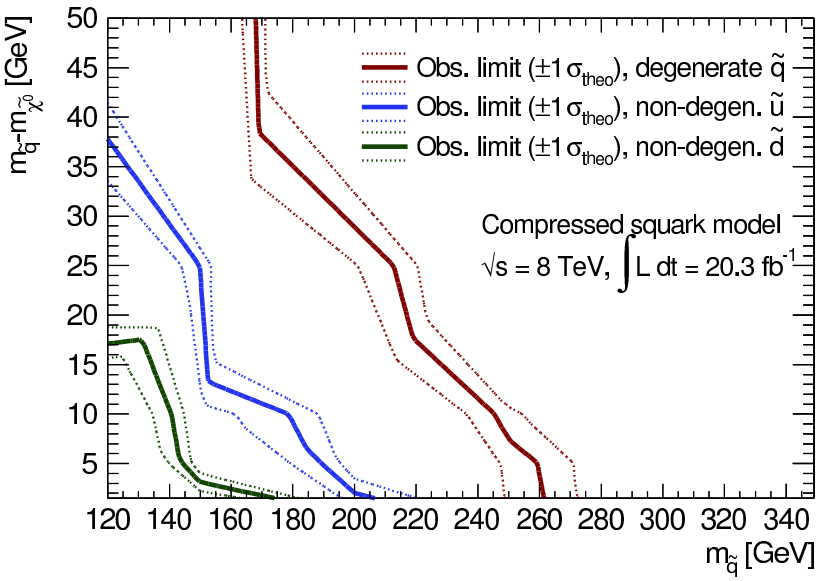

Fig. 13.13 The observed upper limits at 95% CL on the compressed squark model as a function of $m_{\tilde{q}}$ and $m_{\tilde{q}} - m_{\tilde{\chi}_1^0}$. The limits with mass degenerate squarks (red) are shown compared with two non-degenerate scenarios: $\tilde{u}$ (blue) and $\tilde{d}$ (green).

Chapter 14

Comparison to similar analyses at LHC

The monophoton final state is studied not only in ATLAS, but also in CMS. The CMS monophoton analysis will be introduced in Section 14.1 where it will be compared to the monophoton analysis in ATLAS.

There are many other analyses performed by the ATLAS collaboration which are looking for new physics with a missing transverse energy signature. For example, one can look for dark matter in a $H(\gamma\gamma) + E_{\mathrm{T}}^{\mathrm{miss}}$ final state [167], in a final state composed of a large missing transverse energy and at least one b-jet [168], or in a final state consisting of a single charged lepton and missing transverse energy [169]. The last example can also used to search for a new heavy vector W' boson.

For the compressed squark model described in Chapter 8, instead of having a photon one can have a jet accompanying large $E_{\mathrm{T}}^{\mathrm{miss}}$, which results in a monojet analysis. Although this model is not included in the published monojet analysis at $\sqrt{s} = 8\,\mathrm{TeV}$ the re-interpretation is ongoing. For the other model considered in this thesis, the EFT dark matter model inspired by the Fermi-LAT result can also be probed in the mono-Z analyses.

The analyses which can provide constraints on the models considered in this thesis, namely the monojet and mono-Z analyses, will be introduced in Section 14.2 and Section 14.3 respectively.

14.1 The monophoton analysis in CMS

A monophoton analysis has also been performed by the CMS collaboration using $19.6\,\mathrm{fb}^{-1}$ of data at center-of-mass energy of 8 TeV; it is published in Reference [170].

CMS is the other general purpose detector at the LHC, as mentioned in Chapter 5. Its design differs from the ATLAS detector. The electromagnetic calorimeters in the barrel

($|\eta| < 1.479$) and in the end-caps ($1.479 < |\eta| < 3.0$) are lead tungstate crystal calorimeters, whilst the hadronic calorimeter covering the same regions is a brass and scintillator calorimeter. The tracking system consists of silicon tracking detectors only, which are embedded in a magnetic field of 3.8 T provided by a superconducting solenoid which also surrounds the calorimeters. The muon spectrometer of CMS is composed of drift tubes, cathode strip chambers (CSC's) and resistive plate chambers (RPC's) which are interleaved with steel return yoke plates [66], in order to provide good measurement of high–p_{T} muons. The physics objects are reconstructed and identified using a particle flow algorithm [171, 172],

The SR event selections are listed in Table 14.1, compared to the ones used in the ATLAS analysis as described in Chapter 10. As in the ATLAS analysis, the CMS analysis also requires a high p_{T} central photon, a large transverse missing momentum and vetoes leptons in the SR; both analyses allow at most one jet with $p_{\mathrm{T}}^{\mathrm{jet}} > 30$ GeV which is well separated from the photon. The exact value of the cuts in the CMS analysis differ slightly from the ATLAS analysis, as shown in Table 14.1. In this SR, the number of events observed in data is 630.

CMS	ATLAS
$E_{\mathrm{T}}^{\mathrm{miss}} > 140$ GeV	$E_{\mathrm{T}}^{\mathrm{miss}} > 150$ GeV
≥ 1 isolated photon with $p_{\mathrm{T}} > 145$ GeV, $\|\eta\| < 1.44$	≥ 1 isolated photon with $p_{\mathrm{T}} > 125$ GeV, $\|\eta\| < 1.37$
$\Delta\phi(\gamma, E_{\mathrm{T}}^{\mathrm{miss}}) > 2.0$	$\Delta\phi(\gamma, E_{\mathrm{T}}^{\mathrm{miss}}) > 0.4$
≤ 1 jet with $p_{\mathrm{T}}^{\mathrm{jet}} > 30$ GeV, $\Delta R(\gamma, \mathrm{jet}) > 0.5$	≤ 1 jet with $p_{\mathrm{T}}^{\mathrm{jet}} > 30$ GeV, $\Delta R(\gamma, \mathrm{jet}) \geq 0.2$
leptons vetoed with $p_{\mathrm{T}}^{\ell} > 10$ GeV, $\Delta R(\gamma, \ell) > 0.5$	leptons vetoed with $p_{\mathrm{T}}^{\mu} > 6$ GeV, $p_{\mathrm{T}}^{el} > 7$ GeV
A χ^2 test to reduce fake $E_{\mathrm{T}}^{\mathrm{miss}}$ from jets	$\Delta\phi(\mathrm{jet}, E_{\mathrm{T}}^{\mathrm{miss}}) > 0.4$

Table 14.1 The SR selections for the monophoton analysis in CMS compared to that in ATLAS. The 'isolated' photon criteria in both analyses use different discriminant variables according to the reconstruction methods, in a slightly different cone size ($\Delta R < 0.3$ in CMS and $\Delta R < 0.4$ in ATLAS). Jets are both reconstructed using a default anti–k_{t} algorithm but with slightly different radius parameters of $R = 0.5$ in CMS and of $R = 0.4$ in ATLAS. The 'leptons' here refers to muons and electrons.

For the estimation of the fake photon background, the CMS and the ATLAS monophoton analyses both use similar data-driven methods.

For the real photon background, different methods are used in these two analyses. The CMS analysis uses MC prediction only to estimate the contribution of the real photon backgrounds ($Z(\to \nu\bar{\nu}) + \gamma$ and $W(\to \ell\nu) + \gamma$). The estimates are then normalized with an

overall factor $F = 0.94 \pm 0.06$ which corrects for different cut efficiencies between data and MC. The results are then cross checked using a $Z(\to \ell^+\ell^-) + \gamma$ CR. As described in Chapter 11, the ATLAS monophoton analysis normalizes the real photon SR contribution using data from CRs in a simultaneous fit.

The final background estimation result is given in Table 14.2, where the 'Others' term refers to the small contributions from events of $W \to \mu\nu$, $Z(\to \ell^+\ell^-) + \gamma$, $\gamma\gamma$ and $\gamma +$jet.

In the CMS analysis, the contribution from non-collision backgrounds is non-negligible, including events from anomalous signals, cosmic ray muons and beam halo. Its estimate is obtained from a data-driven method, and is found to come mainly from beam halo events. In the ATLAS analysis, the non-collision backgrounds are checked in data [173] but found to be negligible.

The total expected number of events predicted from Standard Model only is 614 ± 63, in good agreement with the observed 630 events.

Process	SR yield
$Z(\to \nu\nu) + \gamma$	345 ± 43
$W(\to \ell + \nu) + \gamma$	103 ± 21
$W(\to e\nu)$	60 ± 6
jet $\to \gamma$ MisID	45 ± 14
Beam halo	25 ± 6
Others	36 ± 3
Total background	614 ± 63
Data	630

Table 14.2 Summary of the estimated backgrounds and observed number of events in the SR, given by the CMS monophoton analysis [170]. > Backgrounds labeled as "Others" refer to the small contributions from events of $W \to \mu\nu$, $Z(\to \ell^+\ell^-) + \gamma$, $\gamma\gamma$ and $\gamma +$jet. Uncertainties include both statistical and systematic contributions.

Figure 14.1 compares the E_{T}^{γ} distribution measured in data to the SM background expectation. The measured data is found to be consistent with the SM background expectation only.

The model-independent limit on the product of the cross section and the SR acceptance ($\sigma \times A$) is 14 fb at 95% CL (13 fb expected). It is higher than 4.7 fb set in ATLAS (6.8 fb expected), which is linked to the fact that both of the expected number of events (614) and the uncertainty (10.2%) are larger than the ones (557 and 8.1%) obtained in ATLAS.

The E_{T}^{γ} spectrum shown in Figure 14.1 is used to set the model-dependent limits. Although none of the two models described in this thesis is covered by the CMS analysis, one can nevertheless compare limits on some other EFT dark matter models which are common

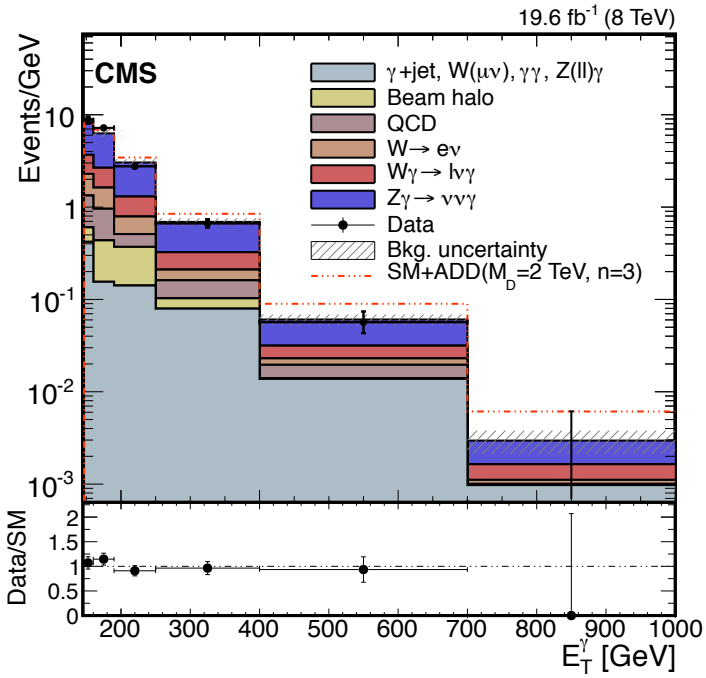

Fig. 14.1 The measured E_{T}^{γ} distribution in the SR is compared to the SM background prediction [170]. The red dashed line shows the effect of a potential signal.

to both analyses, but which were not the focus of the work presented in this thesis. For these models, the ATLAS expected limits are more stringent at lower dark matter mass (as expected from the looser model-independent limit set by CMS) while the CMS expected limits are more stringent at higher masses. This is expected as CMS uses a shape fit to the E_{T}^{γ} spectrum to place exclusions on models, while the ATLAS analysis is a cut-and-count analysis in one signal region. The higher mass models tend to populate the highest E_{T}^{γ} bins (see Figure 10.10), which have less background; the shape fit is therefore more powerful for high-mass models.

In order to give an idea on how the limits vary with the E_{T}^{γ} cut, the model-independent limits at 95% CL are given as a function of the E_{T}^{γ} cut in Figure 14.2. The relative uncertainty to the expected limits increases with E_{T}^{γ}. The tightest SR with $E_{\mathrm{T}}^{\gamma} > 700$ GeV sets the strongest observed limit of 0.22 fb at 95% CL.

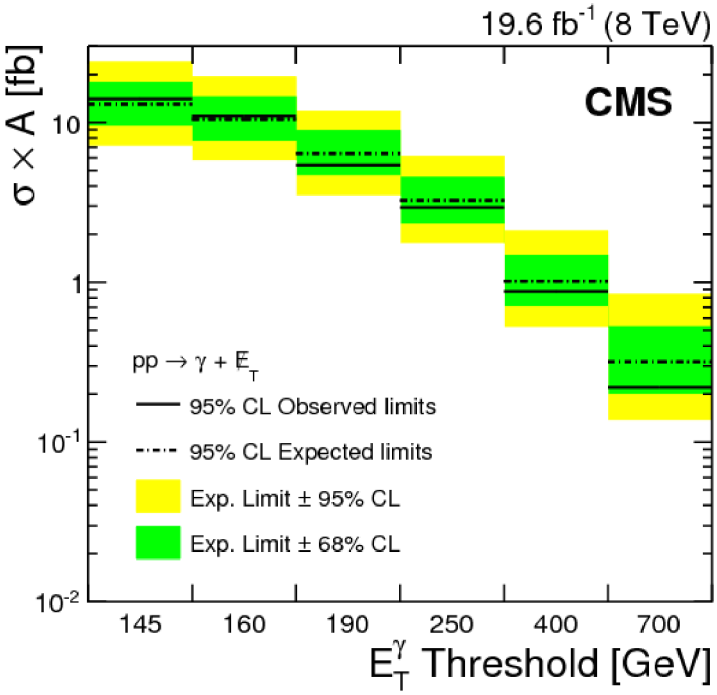

Fig. 14.2 The observed and expected upper limits on the product of cross section and acceptance ($\sigma \times A$) at 95% confidence level (CL) are shown as a function of the E_{T}^{γ} threshold [170].

14.2 The ATLAS monojet analysis

Pair production of invisible BSM particles, such as dark matter particles, can be probed with an ISR signature, such as an ISR photon as described in this thesis. Another example can be an ISR jet, leading to a production of $q\overline{q} \to \chi\overline{\chi}g$ as shown in Figure 14.3. The corresponding event yield is higher than the one in the monophoton analysis due to the strong coupling constant versus the electroweak coupling constant. A monojet analysis was performed by ATLAS on 20.3 fb^{-1} of proton-proton collisions data at $\sqrt{s} = 8$ TeV [174].

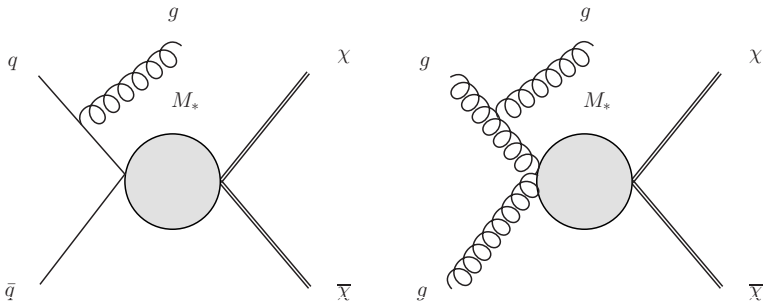

Fig. 14.3 Feynman diagrams for dark matter pair production leading to a monojet final state.

The monojet analysis defines nine signal regions which differ by their $E_{\mathrm{T}}^{\mathrm{miss}}$ cuts. The SRs are ordered with the $E_{\mathrm{T}}^{\mathrm{miss}}$ cut increasing from 150 GeV to 400 GeV with an interval of 50 GeV and from 400 GeV to 700 GeV by 100 GeV. The dominant backgrounds are coming from $W(\to \ell\nu) + \text{jet}$ and $Z(\to \nu\bar{\nu}) + \text{jet}$. These backgrounds are estimated by normalizing the MC prediction in control regions. Other backgrounds include multijet, $Z(\to \ell^+\ell^-) + \text{jet}$, diboson and top. Apart from the multijet background , which is estimated from a data-driven method, the other small backgrounds are given directly by the MC simulation. The estimated and observed distributions of $E_{\mathrm{T}}^{\mathrm{miss}}$ in SR1 ($E_{\mathrm{T}}^{\mathrm{miss}} > 150$ GeV) are illustrated in Figure 14.4, where the composition of the background is also shown. The total observed events in SR1 is 364378, and the expectation is 372100 ± 9900. The model-independent limit set on the visible cross section ($\sigma \times A \times \varepsilon$) in SR1 is 726 fb at 95% CL. For the tightest signal region, SR9 ($E_{\mathrm{T}}^{\mathrm{miss}} > 700$ GeV), 126 events are observed and the background expectation is 97 ± 14. SR9 gives an observed model-independent limit of 3.4 fb at 95% CL.

For the models probed by both the monojet and monophoton analyses, such as some EFT dark matter models, the monojet analysis produces tighter limits than the monophoton analysis The monojet limit could in principle also be interpreted as a limit on the squark production in the very compressed mass spectrum scenario, as shown in Figure 14.5. The monojet analysis should be able to set more stringent limits on the squark mass in the very

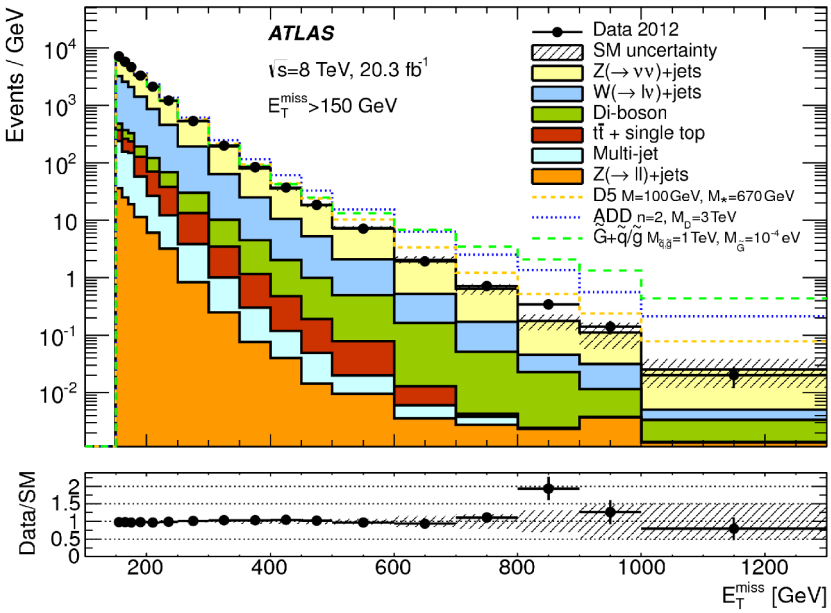

Fig. 14.4 The observed distribution of $E_{\mathrm{T}}^{\mathrm{miss}}$ in SR1 ($E_{\mathrm{T}}^{\mathrm{miss}} > 150$ GeV) compared to the SM background estimate [174]. The SM uncertainty band includes statistical and systematic uncertainties from background estimation.

compressed mass region, and this interpretation is currently being studied in ATLAS. Although the monojet analysis has a better sensitivity than the monophoton analysis on the models which can lead to both signatures, it is still interesting to implement the monophoton analysis as it is complementary. In case of discovery, it would be useful to have as many probes as possible on the new signal to confirm it and determine its properties. Furthermore, if there is any signal observed, the ratio of the monojet and monophoton analyses could be used to probe the charge information of the signal as described in Section 13.2.3.

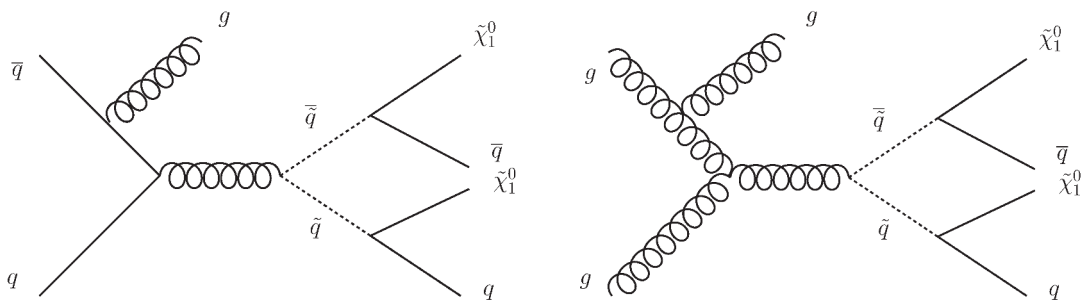

Fig. 14.5 Feynman diagrams illustrating the process of the pair production of squarks with subsequent decay to quarks and neutralinos with a jet radiated from initial-state.

14.3 The ATLAS mono-Z analysis

The EFT DM model discussed in Section 8.1 predicts the couplings of dark matter to either photons or Z bosons. As the relative couplings are controlled by the coupling constants k_1 and k_2, one can also search for this model in a complementary way in the $Z + E_{\mathrm{T}}^{\mathrm{miss}}$ final state. This final state can either be probed using a hadronically decaying Z boson or a leptonically decaying one.

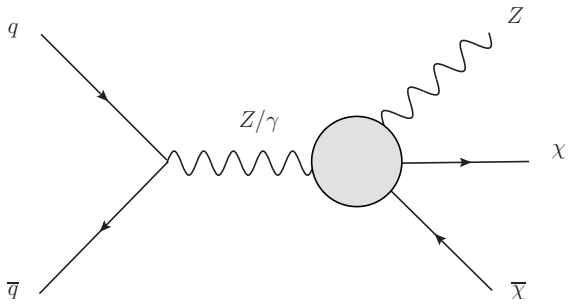

Fig. 14.6 Production of a pair of dark-matter particles via an effective $ZZ\chi\overline{\chi}$ vertex at the LHC.

A mono–Z analysis was performed using $20.3\,\mathrm{fb}^{-1}$ of data at $\sqrt{s} = 8$ GeV by probing a leptonically decaying Z ($Z \to \ell^+\ell^-$) [175], where ℓ refers to electron or muon. The DM model shown in Figure 14.6 is considered in this analysis. Two different operators were taken into account, one is a dimension–5 operator mediated by Z exchange only, and the other one refers to the dimension–7 operator used in the monophoton analysis.

Two mixtures of k_1 and k_2 for the dimension–7 operator were considered in this mono–Z analysis which is introduced in Reference [176]. One is $k_1 = k_2$, leading to the maximal contribution from γ exchange, while the other one, with $k_1 = \cos^2\theta_w / \sin^2\theta_w k_2$, has a negligible contribution from γ exchange.

Different signal regions with different $E_{\mathrm{T}}^{\mathrm{miss}}$ cuts are used in this mono–Z analysis, which are $E_{\mathrm{T}}^{\mathrm{miss}} > 150$ GeV, $E_{\mathrm{T}}^{\mathrm{miss}} > 250$ GeV, $E_{\mathrm{T}}^{\mathrm{miss}} > 350$ GeV and $E_{\mathrm{T}}^{\mathrm{miss}} > 450$ GeV. Given the fact that no excess of events over the background is observed, lower limits are set on the mass scale of the $ZZ\chi\bar{\chi}$ EFT operators at 95% CL, and the SR with the best expected limit is used to calculate the observed limit for each operator and mass point. Figure 14.7 shows the results, where the dot-dash red line ($ZZ\chi\chi$ max. γ) and the dotted cyan line ($ZZ\chi\chi$ no γ) correspond to the EFT model configured with $k_1 = k_2$ and $k_1 = \cos^2\theta_w / \sin^2\theta_w k_2$, respectively; the other lines correspond to other DM models which are not considered in this thesis.

The monophoton analysis and this mono–Z analysis are looking at orthogonal final

states, but one can nevertheless compare the limits on the mass scale (M^*) of the EFT operator with similar k_1 and k_2 configuration. For the dark masses m_χ at 10 GeV and 1000 GeV which are common in both analyses, the mono–Z analysis obtains more stringent limits on M^* than the ones set by the monophoton analysis (see diagonals of Figures 13.6 and 13.7) regardless of the value of k_1 ($= k_2$); however, the monophoton results are still complementary as the final states are orthogonal.

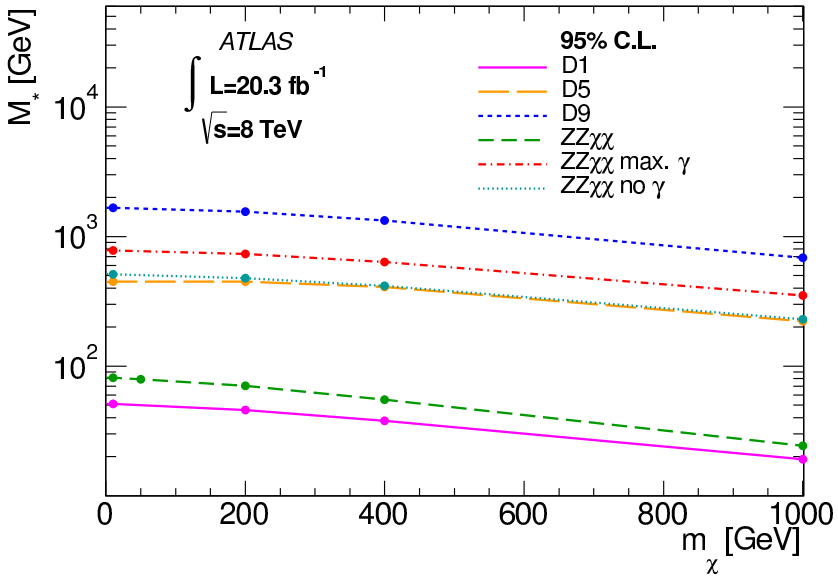

Fig. 14.7 Observed 95% CL lower limits on the mass scale, M^*, of the considered effective field theory as a function of m_χ. For each operator, the values below the corresponding line are excluded [177].

Another mono–W/Z analysis performed in ATLAS was searching for a hadronically decaying Z (or W) boson with 20.3 fb^{-1} of data at 8 GeV [178]. The EFT DM model considered here is not studied in this analysis, but it is very likely to be considered in the next LHC run following the recommendations [42] given by the ATLAS-CMS dark matter forum.

Chapter 15

Prospects

15.1 Long–term LHC schedule

The LHC has collided proton beams at a center-of-mass energy of 7 and 8 TeV from 2010 to 2012. A long shutdown (LS1) has been operated from 2013 to 2014 in order to maintain and adjust the machine for the next LHC run (run 2), which started at a center-of-mass energy of 13 TeV on June 3^{rd}, 2015. A higher peak luminosity of $1.7 \times 10^{34}\,\mathrm{cm}^{-2}\mathrm{s}^{-1}$ should be reached during run 2 compared to the $7.7 \times 10^{33}\,\mathrm{cm}^{-2}\mathrm{s}^{-1}$ [63] achieved during run 1 in 2012. The integrated luminosity expected during run 2 is on the order of $150\,\mathrm{fb}^{-1}$.

Another long shutdown (LS2) is planned to start in July 2018 and continue until the end of 2019, during which maintenance and upgrades will be carried out onto the machine and the detectors, in order to perform the run 3 from 2020 to 2022 at 14 TeV with luminosity peaking at $2.0 \times 10^{34}\,\mathrm{cm}^{-2}\mathrm{s}^{-1}$. In run 3, the integrated luminosity delivered by the LHC is expected to be $300\,\mathrm{fb}^{-1}$.

The LHC is scheduled to shut down again in 2023 for LS3, in order to prepare the High-Luminosity Large Hadron Collider (HL-LHC) stage. The HL-LHC project is expected to increase the total number of proton-proton collisions from run 3 by a factor of ten [179].

The long–term LHC schedule introduced above is summarized in Figure 15.1, where the main features of each LS and run are shown.

15.2 Projection to the next LHC run

As suggested in the SR optimization study in Chapter 10, the monophoton analysis could be optimized with more statistics by having various SRs with increasing $E_{\mathrm{T}}^{\mathrm{miss}}$ cuts.

As the expected total integrated luminosity in run 2 is approximately six times that of run

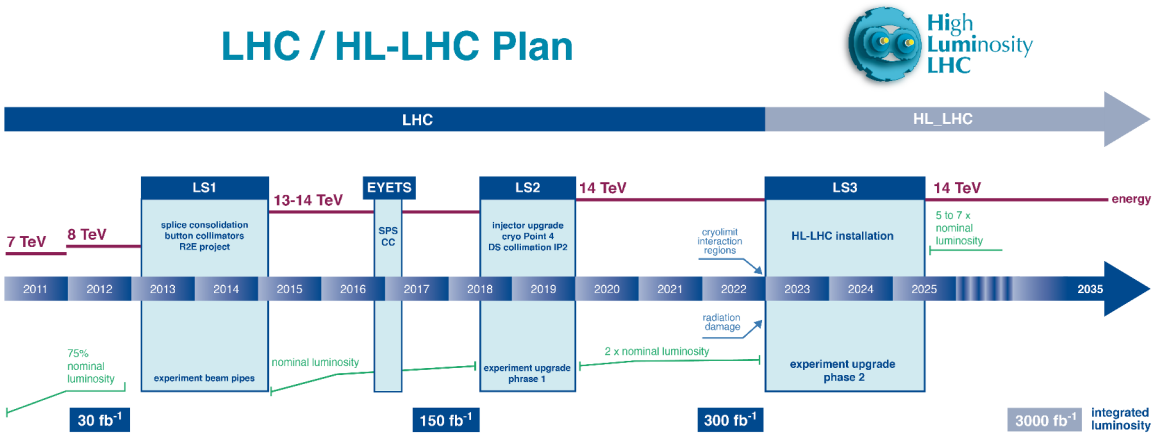

Fig. 15.1 The LHC schedule [179].

1, it may become possible to have several inclusive/exclusive SRs with different $E_{\mathrm{T}}^{\mathrm{miss}}$ cuts for the monophoton analysis while maintaining reasonable statistics in the CRs. Therefore, the analysis results could be optimized in run 2 by using the shape information of $E_{\mathrm{T}}^{\mathrm{miss}}$.

The center-of-mass energy increases from 8 TeV to 13 TeV in run 2, therefore, the cross sections to produce particles, especially those at high masses, will increase with respect to run 1. This is shown in Figure 15.2, which shows the ratios of LHC parton luminosities when going from 8 TeV to 13 TeV using the MSTW2008NLO PDF set, as described in Reference [78]. It shows that the cross section to produce new particles with mass of 2 TeV at the LHC should increase roughly by a factor of ten, i.e. the signal strength will increase significantly.

A preliminary study is carried out to check the search sensitivity of the monophoton analysis at 13 TeV. This is estimated by checking the minimal integrated luminosity needed at 13 TeV to obtain results comparable to that of the 8 TeV analysis. This pre-study uses the same SR as defined in the 8 TeV analysis. However, the photon p_{T} cut is tightened from 125 GeV to 150 GeV, because the trigger which will be used for the 13 TeV monophoton analysis has a requirement of $p_{\mathrm{T}}^{\gamma} > 140$ GeV.

This study is performed with the squark model introduced in Section 13.2. All the simulated signal samples described in Section 13.2.1 are reweighted at event level, by changing the beam energy of the nominal PDF set, CTEQ6L1, from 8 TeV to 13 TeV. By comparing the number of events before any cut is applied between the reweighted samples and the nominal ones, one can derive scale factors on the cross section, λ_{13TeV}^{σ}, which vary from 3.4 to 4.8 depending on the squark mass. By comparing the SR prediction of reweighted samples to the one of the nominal samples, one can derive the scale factor on the $A \times \varepsilon$, $\lambda_{13TeV}^{A\times\varepsilon}$,

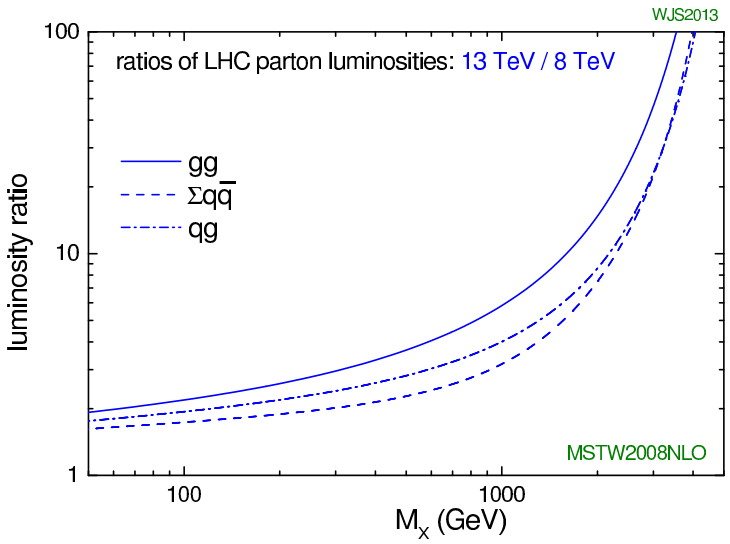

Fig. 15.2 Ratios of LHC parton luminosities from 8 TeV to 13 TeV [180].

which varies from 0.8 to 1.0; the ratio is below or around unity because of the increase in the photon p_{T} cut.

The simulated events of the irreducible background process, $Z(\to \nu\bar{\nu})+\gamma$, are reweighted as well. Its MC prediction in the SR is increased by a factor of 2.1 from 8 TeV to 13 TeV. As a simplifying assumption, all the other backgrounds are also scaled by this factor. Table 15.1 shows the post-fit expectation for each of the background processes in the SR ($p_{\mathrm{T}}^{\gamma} > 150$ GeV) at 13 TeV. The total background estimate from the background-only fit is 290 events for $5\,\mathrm{fb}^{-1}$ data at 13 TeV.

Process	$5\,\mathrm{fb}^{-1}$
$Z(\to \nu\bar{\nu})+\gamma$	203
$W(\to \ell\nu)+\gamma$	43
$W/Z+\mathrm{jet}, t\bar{t}, \mathrm{diboson}$	43
$Z(\to \ell^+\ell^-)+\gamma$	1.1
$\gamma+\mathrm{jet}$	0.2
Total background	290

Table 15.1 Expected event yields from Standard Model backgrounds in the SR ($p_{\mathrm{T}}^{\gamma} > 150$ GeV) for $5\,\mathrm{fb}^{-1}$ data at 13 TeV.

The expected upper limits at 95% CL on the squark model are shown in Figure 15.3. In the very compressed region, the result with $5\,\mathrm{fb}^{-1}$ of data at 13 TeV is expected to exclude $m_{\tilde{q}}$ up to around 275 GeV, which is 10% better than that of 8 TeV analysis. According to

the LHC schedule, this amount of data is expected to be ready after less than 2 months of running with a beam bunch interval of 25 ns.

This study was repeated with an increased luminosity of $15\,\text{fb}^{-1}$. For this luminosity, a squark mass of $m_{\tilde{q}} = 300$ GeV is expected to be excluded at 95% CL in the very compressed region.

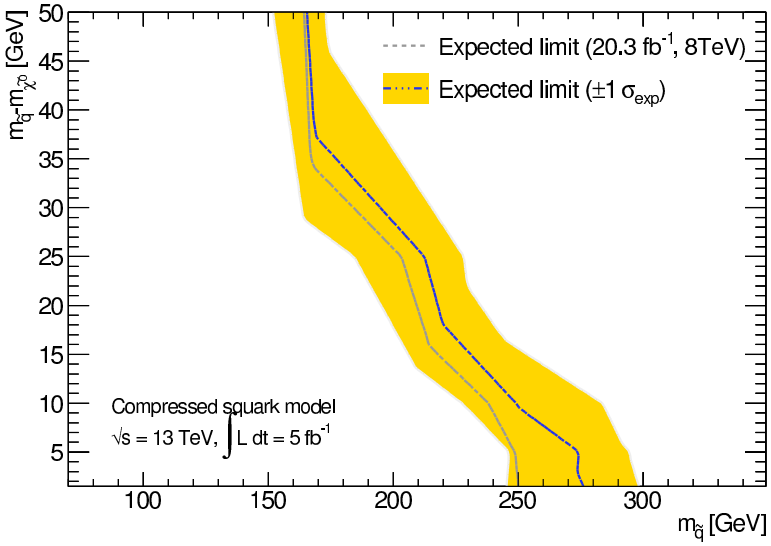

Fig. 15.3 The expected upper limits at 95% CL for the compressed squark scenario with $5\,\text{fb}^{-1}$ of data at 13 TeV (blue) is compared to the ones obtained in the 8 TeV analysis (gray) performed on $20.3\,\text{fb}^{-1}$ of data.

Conclusion

This thesis presents a search for new physics in the final state of a single high p_{T} photon with large missing transverse momentum, performed on $20.3\,\mathrm{fb}^{-1}$ of proton-proton collisions data at a center-of-mass energy of 8 TeV collected by the ATLAS detector at the LHC.

The final state is able to probe the production of particles predicted by new physics models, which are in themselves undetectable, by relying on the presence of a visible object, the photon which can come from initial state radiation (ISR).

Signal events are selected if they contain one isolated central ($|\eta| < 1.37$) photon with transverse momentum above 125 GeV, a missing transverse momentum larger than 150 GeV and no lepton (electron and muon). In order to increase the signal acceptance and reduce the systematic uncertainties related to the ISR modeling, the events are allowed to contain at most one jet with transverse momentum above 30 GeV. The number of events in the SR from data is 521.

The SR contains background from various Standard Model sources: an irreducible component from $Z(\rightarrow \nu\bar{\nu}) + \gamma$ events, and some reducible ones, such as events from leptonically decaying W and Z bosons produced in association with a photon or a jet. Backgrounds with a real photon ($V + \gamma$ events) are estimated by normalizing the MC prediction by scale factors obtained from a fit using three lepton control regions (CRs), which are enriched in background processes of interest. Backgrounds with a fake photon (dominated by $V +$ jet events) are estimated using data-driven methods, since the Monte Carlo simulation is not reliable. A small amount of $\gamma +$ jet events can also enter the SR by faking $E_{\mathrm{T}}^{\mathrm{miss}}$, and its estimate is given directly by the MC prediction. The final Standard Model expectation in the SR is $557 \pm 36(stat.) \pm 27(syst.)$ events. The background estimation technique is validated using a validation region, in which the background expectation is in reasonable agreement with the observed data.

As the Standard Model expectation in the SR is in good agreement with the observed event count from data, an observed upper limit on the visible cross section, σ_{vis}, is computed using a Modified Frequentist (CL_S) method: it is 3.64 fb at 95% confidence level.

The results are also interpreted into the parameter space of two new physics models in this thesis. One is an effective field theory predicting a contact interaction between pairs of dark matter particles and photons. This model is inspired by the Fermi-LAT result issued in 2012, which hinted at a dark matter particle with mass of 130 GeV. The limits are set to the effective mass scale in the phase space of the coupling constants; they provide an effective constraint on the parameter space of the theory compatible with the Fermi-LAT result. The Fermi-LAT peak result is now highly disfavored, but this dark matter model can still be of interest, it will thus be studied for various dark matter masses in the next LHC run.

The other model studied here is a simplified supersymmetric model describing the pair production of mass degenerate squarks in a compressed spectrum scenario. The limits are set to the cross-section in the plane of the squark mass versus the mass difference between the neutralino and the squark. In the very compressed part of this plane, the analysis excludes a mass degenerate first and second generation squark mass up to 250 GeV. As the photon in the final state can be irradiated by the intermediate squark in this model, this search can provide the possibility to probe the charge information of the squark in case of an excess.

A preliminary study has also been carried out to show the monophoton search sensitivity with 13 TeV data. It indicates that the limits presented in this thesis can already be improved by 10% with $5\,\text{fb}^{-1}$ which will be cumulated in the next few months.

References

[1] Particle Data Group Collaboration, K. Olive et al., *Review of Particle Physics*, Chin. Phys. **C38** (2014) 090001.

[2] D. Griffiths, *Introduction to Elementary Particles*. WILEY-VCH, second, revised ed., 2008.

[3] P. W. Higgs, *Broken Symmetries and the Masses of Gauge Bosons*, Phys.Rev.Lett. **13** (1964) 508–509.

[4] F. Englert and R. Brout, *Broken Symmetry and the Mass of Gauge Vector Mesons*, Phys.Rev.Lett. **13** (1964) 321–323.

[5] G. S. Guralnik, C. R. Hagen, and T. W. B. Kibble, *Global Conservation Laws and Massless Particles*, Phys. Rev. Lett. **13** (1964) 585–587.

[6] S. Weinberg, *A Model of Leptons*, Phys. Rev. Lett. **19** (1967) 1264–1266.

[7] L. Alvarez-Gaume and J. Ellis, *Eyes on a prize particle*, Nature Physics **7** (2011) no. 1, 2–3.

[8] ATLAS, CMS Collaboration, G. Aad et al., *Combined Measurement of the Higgs Boson Mass in pp Collisions at $\sqrt{s} = 7$ and 8 TeV with the ATLAS and CMS Experiments*, Phys.Rev.Lett. **114** (2015) 191803.

[9] S. Troitsky, *Unsolved problems in particle physics*, Phys.Usp. **55** (2012) 72–95.

[10] E. Gildener, *Gauge-symmetry hierarchies*, Phys. Rev. D **14** (1976) 1667.

[11] S. Weinberg, *Gauge hierarchies*, Physics Letters B **82** (1979) 387–391.

[12] G. F. Giudice, *Naturally Speaking: The Naturalness Criterion and Physics at the LHC*, `arXiv:0801.2562 [hep-ph]`.

[13] S. P. Martin, *A Supersymmetry primer*, Adv.Ser.Direct.High Energy Phys. **21** (2010) 1–153.

[14] K. G. Begeman, A. H. Broeils, and R. H. Sanders, *Extended rotation curves of spiral galaxies - Dark haloes and modified dynamics*, Monthly Notices of the Royal Astronomical Society **249** (1991) 523–537.

[15] Planck Collaboration, *Planck 2013 results. XVI. Cosmological parameters*, Astron.Astrophys. **571** (2014) A16.

[16] G. R. Blumenthal, S. Faber, J. R. Primack, and M. J. Rees, *Formation of Galaxies and Large Scale Structure with Cold Dark Matter*, Nature **311** (1984) 517–525.

[17] J. R. Primack, *Dark matter and structure formation*, `arXiv:astro-ph/9707285 [astro-ph]`.

[18] Planck Collaboration, *Planck 2015 results. XIII. Cosmological parameters*, `arXiv:1502.01589 [astro-ph.CO]`.

[19] SuperCDMS Collaboration, R. Agnese et al., *Search for Low-Mass Weakly Interacting Massive Particles with SuperCDMS*, Phys.Rev.Lett. **112** (2014) 241302.

[20] LUX Collaboration, D. Akerib et al., *The Large Underground Xenon (LUX) experiment*, Nuclear Instruments and Methods in Physics Research A **704** (2013) 111–26.

[21] EDELWEISS Collaboration, E. Armengaud et al., *A search for low-mass WIMPs with EDELWEISS-II heat-and-ionization detectors*, Phys.Rev. **D86** (2012) 051701.

[22] XENON100 Collaboration, E. Aprile et al., *Dark Matter Results from 225 Live Days of XENON100 Data*, Phys.Rev.Lett. **109** (2012) 181301.

[23] PICASSO Collaboration, *Constraints on low-mass WIMP interactions on 19F from PICASSO*, Phys.Lett.B **711** (2012) 153–161.

[24] LUX Collaboration, D. Akerib et al., *First results from the LUX dark matter experiment at the Sanford Underground Research Facility*, Phys.Rev.Lett. **112** (2014) 091303.

[25] XENON Collaboration, S. Orrigo, *Direct Dark Matter Search with XENON100*, 2015. `arXiv:1501.03492 [astro-ph.CO]`.

[26] F. Halzen and S. R. Klein, *IceCube: An instrument for neutrino astronomy*, Review of Scientific Instruments **81** (2010) 081101.

[27] AMS Collaboration, M. Aguilar et al., *First Result from the Alpha Magnetic Spectrometer on the International Space Station: Precision Measurement of the Positron Fraction in Primary Cosmic Rays of 0.5–350 GeV*, Phys.Rev.Lett. **110** (2013) 141102.

[28] Fermi–LAT Collaboration, *The Large Area Telescope on the Fermi Gamma-Ray Space Telescope Mission*, Astrophys.J. **697** (2009) 1071–1102.

[29] G. Bertone, D. Hooper, and J. Silk, *Particle dark matter: Evidence, candidates and constraints*, Phys.Rept. **405** (2005) 279–390.

[30] C. Weniger, *Tentative observation of a gamma-ray line at the Fermi LAT*, AIP Conf.Proc. **1505** (2012) 470–473.

[31] Fermi-LAT Collaboration, M. Ackermann et al., *Search for Gamma-ray Spectral Lines with the Fermi Large Area Telescope and Dark Matter Implications*, Phys.Rev. **D88** (2013) 082002.

[32] B. Hensley, J. Siegal-Gaskins, and V. Pavlidou, *The Detectability of Dark Matter Annihilation with Fermi Using the Anisotropy Energy Spectrum of the Gamma-ray Background*, Astrophys.J. **723** (2010) 277–284.

[33] Fermi-LAT Collaboration, M. Ackermann et al., *Dark matter constraints from observations of 25 Milky Way satellite galaxies with the Fermi Large Area Telescope*, Phys.Rev. **D89** (2014) 042001.

[34] C. Weniger, *A Tentative Gamma-Ray Line from Dark Matter Annihilation at the Fermi Large Area Telescope*, JCAP **1208** (2012) 007.

[35] J. Goodman, M. Ibe, A. Rajaraman, W. Shepherd, T. M. Tait, et al., *Constraints on Light Majorana dark Matter from Colliders*, Phys.Lett. **B695** (2011) 185–188.

[36] Y. Bai, P. J. Fox, and R. Harnik, *The Tevatron at the Frontier of Dark Matter Direct Detection*, JHEP **1012** (2010) 048.

[37] M. Beltran, D. Hooper, E. W. Kolb, and Z. A. C. Krusberg, *Deducing the nature of dark matter from direct and indirect detection experiments in the absence of collider signatures of new physics*, Phys. Rev. D **80** (2009) 043509.

[38] M. Beltran, D. Hooper, E. W. Kolb, Z. A. Krusberg, and T. M. Tait, *Maverick dark matter at colliders*, JHEP **1009** (2010) 037.

[39] J. Goodman, M. Ibe, A. Rajaraman, W. Shepherd, T. M. Tait, et al., *Constraints on Dark Matter from Colliders*, Phys.Rev. **D82** (2010) 116010.

[40] J.-Y. Chen, E. W. Kolb, and L.-T. Wang, *Dark matter coupling to electroweak gauge and Higgs bosons: an effective field theory approach*, Phys.Dark Univ. **2** (2013) 200–218.

[41] G. Busoni, A. De Simone, J. Gramling, E. Morgante, and A. Riotto, *On the Validity of the Effective Field Theory for Dark Matter Searches at the LHC, Part II: Complete Analysis for the s-channel*, JCAP **1406** (2014) 060.

[42] D. Abercrombie et al., *Dark Matter Benchmark Models for Early LHC Run-2 Searches: Report of the ATLAS/CMS Dark Matter Forum*, `arXiv:1507.00966 [hep-ex]`.

[43] S. Coleman and J. Mandula, *All Possible Symmetries of the S Matrix*, Physical Review **159** (1967) 1251–1256.

[44] M. Carena, S. Pokorski, and C. Wagner, *On the unification of couplings in the minimal supersymmetric Standard Model*, Nucl.Phys. **B406** (1993) 59–89.

[45] P. Fayet, *Supersymmetry and Weak, Electromagnetic and Strong Interactions*, Phys. Lett. **B64** (1976) 159.

[46] P. Fayet, *Spontaneously Broken Supersymmetric Theories of Weak, Electromagnetic and Strong Interactions*, Phys. Lett. **B69** (1977) 489.

[47] G. R. Farrar and P. Fayet, *Phenomenology of the Production, Decay, and Detection of New Hadronic States Associated with Supersymmetry*, Phys. Lett. **B76** (1978) 575–579.

[48] P. Fayet, *Relations Between the Masses of the Superpartners of Leptons and Quarks, the Goldstino Couplings and the Neutral Currents*, Phys. Lett. **B84** (1979) 416.

[49] S. Dimopoulos and H. Georgi, *Softly Broken Supersymmetry and SU(5)*, Nucl. Phys. **B193** (1981) 150.

[50] M. Dine and W. Fischler, *A Phenomenological Model of Particle Physics Based on Supersymmetry*, Phys. Lett. **B110** (1982) 227.

[51] L. Alvarez-Gaume, M. Claudson, and M. B. Wise, *Low-Energy Supersymmetry*, Nucl. Phys. **B207** (1982) 96.

[52] C. R. Nappi and B. A. Ovrut, *Supersymmetric Extension of the SU(3) x SU(2) x U(1) Model*, Phys. Lett. **B113** (1982) 175.

[53] M. Dine and A. E. Nelson, *Dynamical supersymmetry breaking at low-energies*, Phys. Rev. **D48** (1993) 1277–1287.

[54] M. Dine, A. E. Nelson, and Y. Shirman, *Low-energy dynamical supersymmetry breaking simplified*, Phys. Rev. **D51** (1995) 1362–1370.

[55] M. Dine, A. E. Nelson, Y. Nir, and Y. Shirman, *New tools for low-energy dynamical supersymmetry breaking*, Phys. Rev. **D53** (1996) 2658–2669.

[56] A. H. Chamseddine, R. Arnowitt, and P. Nath, *Locally Supersymmetric Grand Unification*, Phys. Rev. Lett. **49** (1982) 970.

[57] R. Barbieri, S. Ferrara, and C. A. Savoy, *Gauge Models with Spontaneously Broken Local Supersymmetry*, Phys. Lett. **B119** (1982) 343.

[58] L. E. Ibanez, *Locally Supersymmetric SU(5) Grand Unification*, Phys. Lett. **B118** (1982) 73.

[59] L. J. Hall, J. D. Lykken, and S. Weinberg, *Supergravity as the Messenger of Supersymmetry Breaking*, Phys. Rev. **D27** (1983) 2359–2378.

[60] N. Ohta, *Grand Unified Theories Based on Local Supersymmetry*, Prog. Theor. Phys. **70** (1983) 542.

[61] G. L. Kane, C. F. Kolda, L. Roszkowski, and J. D. Wells, *Study of constrained minimal supersymmetry*, Phys. Rev. **D49** (1994) 6173–6210.

[62] ATLAS Collaboration, *Summary plots from the ATLAS Supersymmetry physics group*, tech. rep., CERN, Geneva, February, 2015. http://atlas.web.cern.ch/Atlas/GROUPS/PHYSICS/CombinedSummaryPlots/SUSY/index.html#ATLAS_SUSY_Summary.

[63] M. Lamont, *Status of the LHC*, Journal of Physics: Conference Series **455** (2013) 012001.

[64] M. Lamont, *2010–2013: the LHC's first long run*, CERN Courier **53** (2013) no. 7, 25. http://cds.cern.ch/record/1734981/files/vol53-issue7-p025-e.pdf.

[65] ATLAS Collaboration, *ATLAS Luminosity Public Results*, tech. rep., CERN, Geneva, September, 2013. http://twiki.cern.ch/twiki/bin/view/AtlasPublic/LuminosityPublicResults?cover=print.

[66] A. Breskin and R. Voss, *The CERN Large Hadron Collider: Accelerator and Experiments: LHC machine, ALICE, and ATLAS*, vol. 1. CERN, Geneva, 2009. http://cds.cern.ch/record/1244506.

[67] G. Aad, B. Abbott, J. Abdallah, A. A. Abdelalim, A. Abdesselam, O. Abdinov, B. Abi, M. Abolins, H. Abramowicz, H. Abreu, and et al., *The ATLAS Inner Detector commissioning and calibration*, European Physical Journal C **70** (2010) 787–821.

[68] J. Pequenao and P. Schaffner, *A computer generated image representing how ATLAS detects particles*, Online, Jan, 2013. http://cds.cern.ch/record/1505342.

[69] ATLAS Collaboration, *Alignment of the ATLAS Inner Detector and its Performance in 2012*, Tech. Rep. ATLAS-CONF-2014-047, CERN, Geneva, Jul, 2014. http://cds.cern.ch/record/1741021.

[70] ATLAS Collaboration, *Expected Performance of the ATLAS Experiment - Detector, Trigger and Physics (Reconstruction of Photon Conversions)*. CERN, 2009. http://cds.cern.ch/record/1125884.

[71] ATLAS Collaboration, *Performance of the ATLAS Inner Detector Track and Vertex Reconstruction in the High Pile-Up LHC Environment*, Tech. Rep. ATLAS-CONF-2012-042, CERN, Geneva, Mar, 2012. http://cds.cern.ch/record/1435196.

[72] ATLAS Collaboration, *Performance of primary vertex reconstruction in proton-proton collisions at $\sqrt{s}$ =7 TeV in the ATLAS experiment*, Tech. Rep. ATLAS-CONF-2010-069, CERN, Geneva, Jul, 2010. http://cds.cern.ch/record/1281344.

[73] ATLAS Collaboration, G. Aad et al., *Electron performance measurements with the ATLAS detector using the 2010 LHC proton-proton collision data*, Eur.Phys.J. **C72** (2012) 1909.

[74] ATLAS Collaboration, G. Aad et al., *Jet energy resolution in proton-proton collisions at $\sqrt{s} = 7$ TeV recorded in 2010 with the ATLAS detector*, Eur.Phys.J. **C73** (2013) no. 3, 2306.

[75] ATLAS Collaboration, *Studies of the performance of the ATLAS detector using cosmic-ray muons*, The European Physical Journal C **71** (2011) 1–36.

[76] ATLAS Collaboration, M. S. Neubauer, *A Fast Hardware Tracker for the ATLAS Trigger System*, (2011) , `arXiv:1110.1910 [hep-ex]`.

[77] S. Lloyd, *ATLAS Computing Workbook*, private communication within the ATLAS collaboration, September, 2012.

[78] A. Martin, W. Stirling, R. Thorne, and G. Watt, *Parton distributions for the LHC*, Eur.Phys.J. **C63** (2009) 189–285.

[79] J. Pumplin et al., *New generation of parton distributions with uncertainties from global QCD analysis*, JHEP **0207** (2002) 012.

[80] H.-L. Lai et al., *New parton distributions for collider physics*, Phys. Rev. **D82** (2010) 074024.

[81] DELPHI Collaboration, P. Abreu et al., *Tuning and test of fragmentation models based on identified particles and precision event shape data*, Z.Phys. **C73** (1996) 11–60.

[82] The GEANT4 Collaboration, *GEANT4: A Simulation toolkit*, Nucl.Instrum.Meth. **A506** (2003) 250–303.

[83] E. Richter-Was, D. Froidevaux, and L. Poggioli, *ATLFAST 2.0 a fast simulation package for ATLAS*, Tech. Rep. ATL-PHYS-98-131, CERN, Geneva, Nov, 1998. http://cds.cern.ch/record/683751.

[84] T. Sjostrand, S. Mrenna, and P. Skands, *A Brief Introduction to PYTHIA 8.1*, Comput. Phys. Comm. **178** (2008) 852.

[85] ATLAS Collaboration, *The ATLAS Simulation Infrastructure*, Eur.Phys.J.C **70** (2010) 823–874.

[86] ATLAS Collaboration, *ATLAS Computing: technical design report*. Technical Design Report ATLAS. CERN, Geneva, 2005. http://cds.cern.ch/record/837738.

[87] M. Capeans, G. Darbo, K. Einsweiller, M. Elsing, T. Flick, M. Garcia-Sciveres, C. Gemme, H. Pernegger, O. Rohne, and R. Vuillermet, *ATLAS Insertable B-Layer Technical Design Report*, Tech. Rep. CERN-LHCC-2010-013. ATLAS-TDR-19, CERN, Geneva, Sep, 2010. http://cds.cern.ch/record/1291633/.

[88] ATLAS Collaboration, *Photon Conversions at* $\sqrt{s} = 900$ GeV *measured with the ATLAS Detector*, Tech. Rep. ATLAS-CONF-2010-007, CERN, Geneva, Jun, 2010. http://cds.cern.ch/record/1274001.

[89] W. Lampl, S. Laplace, D. Lelas, P. Loch, H. Ma, S. Menke, S. Rajagopalan, D. Rousseau, S. Snyder, and G. Unal, *Calorimeter Clustering Algorithms: Description and Performance*, Tech. Rep. ATL-LARG-PUB-2008-002. ATL-COM-LARG-2008-003, CERN, Geneva, Apr, 2008. http://cds.cern.ch/record/1099735.

[90] ATLAS Collaboration, *Electron and photon reconstruction and identification in ATLAS: expected performance at high energy and results at 900 GeV*, tech. rep., CERN, Geneva, 2010. http://inspirehep.net/record/1203984.

[91] ATLAS Collaboration, *Expected Performance of the ATLAS Experiment - Detector, Trigger and Physics (Calibration and Performance of the Electromagnetic Calorimeter)*. CERN, 2009. http://cds.cern.ch/record/1125884.

[92] ATLAS Collaboration, ATLAS, *Electron and photon energy calibration with the ATLAS detector using LHC Run 1 data*, Eur.Phys.J. **C74** (2014) no. 10, 3071.

[93] ATLAS Collaboration, *Expected photon performance in the ATLAS experiment*, tech. rep., CERN, Geneva, Apr, 2011. http://cds.cern.ch/record/1345329.

[94] ATLAS Collaboration, *Measurements of the photon identification efficiency with the ATLAS detector using 4.9 fb^{-1} of pp collision data collected in 2011*, Tech. Rep. ATLAS-CONF-2012-123, CERN, Geneva, Aug, 2012.

[95] ATLAS Collaboration, *Public Liquid-Argon Calorimeter Plots on Detector Status*, tech. rep., CERN, Geneva, July, 2014. http://twiki.cern.ch/twiki/bin/view/AtlasPublic/LArCaloPublicResultsDetStatus.

[96] S. Laplace and J. de Vivie, *Calorimeter isolation and pile-up*, Tech. Rep. ATL-COM-PHYS-2012-467, CERN, Geneva, May, 2012. ATLAS Internal.

[97] B. Lenzi, C. Royon, and M. Saimpert, *Data-driven corrections for the calorimeter isolation energy of photons computed from topological clusters*, tech. rep., CERN, Geneva, Apr, 2015.

[98] A. Hoecker, P. Speckmayer, J. Stelzer, J. Therhaag, E. von Toerne, and H. Voss, *TMVA: Toolkit for Multivariate Data Analysis*, PoS **ACAT** (mar, 2007) 040.

[99] ATLAS Collaboration, *Electron reconstruction and identification efficiency measurements with the ATLAS detector using the 2011 LHC proton-proton collision data*, Eur.Phys.J. **C74** (2014) no. 7, 2941.

[100] ATLAS Collaboration, *Electron efficiency measurements with the ATLAS detector using the 2012 LHC proton-proton collision data*, tech. rep., CERN, Geneva, Jun, 2014. http://cds.cern.ch/record/1706245.

[101] R. Nicolaidou, L. Chevalier, S. Hassani, J. Laporte, E. Le Menedeu, et al., *Muon identification procedure for the ATLAS detector at the LHC using Muonboy reconstruction package and tests of its performance using cosmic rays and single beam data*, J.Phys.Conf.Ser. **219** (2010) 032052.

[102] ATLAS Collaboration, *Measurement of the muon reconstruction performance of the ATLAS detector using 2011 and 2012 LHC proton-proton collision data*, Eur.Phys.J. **C74** (2014) no. 11, 3130.

[103] M. Cacciari, G. P. Salam, and G. Soyez, *The Anti-k(t) jet clustering algorithm*, JHEP **0804** (2008) 063.

[104] ATLAS Collaboration, *Jet energy measurement with the ATLAS detector in proton-proton collisions at $\sqrt{s} = 7$ TeV*, Eur.Phys.J. **C73** (2013) no. 3, 2304.

[105] ATLAS Collaboration, *Selection of jets produced in proton-proton collisions with the ATLAS detector using 2011 data*, Tech. Rep. ATLAS-CONF-2012-020, CERN, Geneva, Mar, 2012. http://cds.cern.ch/record/1430034.

[106] ATLAS Collaboration, *Jet energy measurement with the ATLAS detector in proton-proton collisions at* $\sqrt{s} = 7$ *TeV*, Eur.Phys.J. **C73** (2013) no. 3, 2304.

[107] C. Issever, K. Borras, and D. Wegener, *An Improved weighting algorithm to achieve software compensation in a fine grained LAr calorimeter*, Nucl.Instrum.Meth. **A545** (2005) 803–812.

[108] M. Cacciari and G. P. Salam, *Pileup subtraction using jet areas*, Phys.Lett. **B659** (2008) 119–126.

[109] ATLAS Collaboration, *Pile-up subtraction and suppression for jets in ATLAS*, tech. rep., CERN, Geneva, 2013. http://cds.cern.ch/record/1570994.

[110] ATLAS Collaboration, *Jet energy scale and its systematic uncertainty in proton-proton collisions at sqrt(s)=7 TeV with ATLAS 2011 data*, Tech. Rep. ATLAS-CONF-2013-004, CERN, Geneva, Jan, 2013.

[111] ATLAS Collaboration, *Performance of Missing Transverse Momentum Reconstruction in Proton-Proton Collisions at 7 TeV with ATLAS*, Eur. Phys. J. **C72** (2012) 1844.

[112] ATLAS Collaboration, *Performance of Missing Transverse Momentum Reconstruction in ATLAS studied in Proton-Proton Collisions recorded in 2012 at 8 TeV*, Tech. Rep. ATLAS-CONF-2013-082, CERN, Geneva, Aug, 2013. https://cds.cern.ch/record/1570993.

[113] A. Nelson, L. M. Carpenter, R. Cotta, A. Johnstone, and D. Whiteson, *Confronting the Fermi Line with LHC data: an Effective Theory of Dark Matter Interaction with Photons*, Phys.Rev. **D89** (2014) no. 5, 056011.

[114] A. Rajaraman, T. M. Tait, and A. M. Wijangco, *Effective Theories of Gamma-ray Lines from Dark Matter Annihilation*, Phys.Dark Univ. **2** (2013) 17–21.

[115] ATLAS Collaboration, *Search for squarks and gluinos with the ATLAS detector in final states with jets and missing transverse momentum using* $\sqrt{s} = 8$ *TeV proton–proton collision data*, JHEP **1409** (2014) 176.

[116] ATLAS Collaboration, *Search for dark matter candidates and large extra dimensions in events with a photon and missing transverse momentum in* pp *collision data at* $\sqrt{s} = 7$ *TeV with the ATLAS detector*, Phys.Rev.Lett. **110** (2013) no. 1, 011802.

[117] (ATLAS) Collaboration, *Search for new phenomena in events with a photon and missing transverse momentum in* pp *collisions at* $\sqrt{s} = 8$ TeV *with the ATLAS detector*, Phys. Rev. D **91** (2015) 012008.

[118] I. Antcheva, M. Ballintijn, B. Bellenot, M. Biskup, R. Brun, et al., *ROOT: A C++ framework for petabyte data storage, statistical analysis and visualization*, Comput.Phys.Commun. **180** (2009) 2499–2512.

[119] ATLAS Collaboration, *Improved luminosity determination in pp collisions at $\sqrt{s}$ = 7 TeV using the ATLAS detector at the LHC*, Eur.Phys.J. **C73** (2013) no. 8, 2518.

[120] ATLAS Collaboration, *The ATLAS transverse-momentum trigger performance at the LHC in 2011*, Tech. Rep. ATLAS-CONF-2014-002, CERN, Geneva, Feb, 2014. http://cds.cern.ch/record/1647616.

[121] T. Gleisberg et al., *Event generation with SHERPA 1.1*, JHEP **0902** (2009) 007.

[122] S. Catani, L. Cieri, G. Ferrera, D. de Florian, and M. Grazzini, *Vector boson production at hadron colliders: a fully exclusive QCD calculation at NNLO*, Phys.Rev.Lett. **103** (2009) 082001.

[123] S. Frixione, P. Nason, and G. Ridolfi, *A Positive-weight next-to-leading-order Monte Carlo for heavy flavour hadroproduction*, JHEP **0709** (2007) 126.

[124] M. Czakon and A. Mitov, *Top++: A Program for the Calculation of the Top-Pair Cross-Section at Hadron Colliders*, Comput.Phys.Commun. **185** (2014) 2930.

[125] M. Czakon, P. Fiedler, and A. Mitov, *Total Top-Quark Pair-Production Cross Section at Hadron Colliders Through $O(\mathrm{ff}\frac{4}{S})$*, Phys.Rev.Lett. **110** (2013) 252004.

[126] B. P. Kersevan and E. Richter-Was, *The Monte Carlo event generator AcerMC versions 2.0 to 3.8 with interfaces to PYTHIA 6.4, HERWIG 6.5 and ARIADNE 4.1*, Comput.Phys.Commun. **184** (2013) 919–985.

[127] S. Frixione and B. R. Webber, *Matching NLO QCD computations and parton shower simulations*, JHEP **0206** (2002) 029.

[128] S. Frixione, P. Nason, and B. R. Webber, *Matching NLO QCD and parton showers in heavy flavor production*, JHEP **0308** (2003) 007.

[129] N. Kidonakis, *Next-to-next-to-leading-order collinear and soft gluon corrections for t-channel single top quark production*, Phys. Rev. D **83** (2011) 091503.

[130] N. Kidonakis, *NNLL resummation for s-channel single top quark production*, Phys. Rev. D **81** (2010) 054028.

[131] N. Kidonakis, *Two-loop soft anomalous dimensions for single top quark associated production with a W- or H-*, Phys. Rev. D **82** (2010) 054018.

[132] G. Corcella, I. Knowles, G. Marchesini, S. Moretti, K. Odagiri, et al., *HERWIG 6: An Event generator for hadron emission reactions with interfering gluons (including supersymmetric processes)*, JHEP **0101** (2001) 010.

[133] G. Corcella, I. Knowles, G. Marchesini, S. Moretti, K. Odagiri, et al., *HERWIG 6.5 release note*, `arXiv:hep-ph/0210213 [hep-ph]`.

[134] J. M. Campbell and R. K. Ellis, *An Update on vector boson pair production at hadron colliders*, Phys.Rev. **D60** (1999) 113006.

[135] J. M. Campbell, R. K. Ellis, and C. Williams, *Vector boson pair production at the LHC*, JHEP **1107** (2011) 018.

[136] T. Sjostrand, S. Mrenna, and P. Skands, *PYTHIA 6.4 physics and manual*, JHEP **05** (2006) 026.

[137] J. Butterworth, J. R. Forshaw, and M. Seymour, *Multiparton interactions in photoproduction at HERA*, Z.Phys. **C72** (1996) 637–646.

[138] ATLAS Collaboration, *New ATLAS event generator tunes to 2010 data*, tech. rep., CERN, Geneva, Apr, 2011. http://cds.cern.ch/record/1345343.

[139] B. Cooper, J. Katzy, M. Mangano, A. Messina, L. Mijovic, et al., *Importance of a consistent choice of alpha(s) in the matching of AlpGen and Pythia*, Eur.Phys.J. **C72** (2012) 2078.

[140] J. Alwall, M. Herquet, F. Maltoni, O. Mattelaer, and T. Stelzer, *MadGraph 5 : Going Beyond*, JHEP **1106** (2011) 128.

[141] M. Baak, G. Besjes, D. Côte, A. Koutsman, J. Lorenz, et al., *HistFitter software framework for statistical data analysis*, Eur.Phys.J. **C75** (2015) no. 4, 153.

[142] G. Cowan, K. Cranmer, E. Gross, and O. Vitells, *Asymptotic formulae for likelihood-based tests of new physics*, Eur. Phys. J. **C71** (2011) 1554.

[143] ROOT Collaboration, K. Cranmer, G. Lewis, L. Moneta, A. Shibata, and W. Verkerke, *HistFactory: A tool for creating statistical models for use with RooFit and RooStats*, Tech. Rep. CERN-OPEN-2012-016, New York U., New York, Jan, 2012. http://cds.cern.ch/record/1456844.

[144] N. Zhou. Private communication within the ATLAS monophoton analysis group.

[145] ATLAS Collaboration, *Jet energy resolution and selection efficiency relative to track jets from in-situ techniques with the ATLAS Detector Using Proton-Proton Collisions at a Center of Mass Energy sqrts = 7 TeV*, Tech. Rep. ATLAS-CONF-2010-054, CERN, Geneva, Jul, 2010. http://cds.cern.ch/record/1281311.

[146] M. Botje, J. Butterworth, A. Cooper-Sarkar, A. de Roeck, J. Feltesse, et al., *The PDF4LHC Working Group Interim Recommendations*, (2011) , `arXiv:1101.0538 [hep-ph]`.

[147] J. Pumplin, D. Stump, R. Brock, D. Casey, J. Huston, et al., *Uncertainties of predictions from parton distribution functions. 2. The Hessian method*, Phys.Rev. **D65** (2001) 014013.

[148] J. Pumplin, D. Stump, and W. Tung, *Multivariate fitting and the error matrix in global analysis of data*, Phys.Rev. **D65** (2001) 014011.

[149] T. Duc Bao. Private communication within the ATLAS collaboration, Jan, 2011.

[150] V. Ippolito. Private communication within the ATLAS monophoton analysis group.

[151] F. Wang. Private communication within the ATLAS monophoton analysis group.

[152] A. L. Read, *Presentation of search results: The CL(s) technique*, J. Phys. G **G28** (2002) 2693–2704.

[153] A. Buckley, J. Ferrando, S. Lloyd, K. Nordstrom, B. Page, et al., *LHAPDF6: parton density access in the LHC precision era*, (2014) , arXiv:1412.7420 [hep-ph].

[154] *Les Houches 2013: Physics at TeV Colliders: Standard Model Working Group Report*. 2014. arXiv:1405.1067 [hep-ph].

[155] T. Sjostrand and P. Z. Skands, *Transverse-momentum-ordered showers and interleaved multiple interactions*, Eur.Phys.J. **C39** (2005) 129–154.

[156] W. Beenakker, R. Hopker, M. Spira, and P. Zerwas, *Squark and gluino production at hadron colliders*, Nucl. Phys. **B492** (1997) 51–103.

[157] A. Kulesza and L. Motyka, *Threshold resummation for squark-antisquark and gluino-pair production at the LHC*, Phys. Rev. Lett. **102** (2009) 111802.

[158] A. Kulesza and L. Motyka, *Soft gluon resummation for the production of gluino-gluino and squark-antisquark pairs at the LHC*, Phys. Rev. **D80** (2009) 095004.

[159] W. Beenakker et al., *Soft-gluon resummation for squark and gluino hadroproduction*, JHEP **0912** (2009) 041.

[160] W. Beenakker et al., *Squark and gluino hadroproduction*, Int. J. Mod. Phys. **A26** (2011) 2637–2664.

[161] M. Kramer et al., *Supersymmetry production cross sections in pp collisions at* $\sqrt{s}$ = *7 TeV*, arXiv:1206.2892 [hep-ph].

[162] ATLAS Collaboration, *Search for new phenomena in final states with an energetic jet and large missing transverse momentum in pp collisions at* $\sqrt{s} = 8$ *TeV with the ATLAS detector* , Online, February, 2015.
http://hepdata.cedar.ac.uk/view/ins1326409.

[163] D. Barducci, *MadAnalysis 5 implementation of ATLAS-EXOT-2014-06*, .

[164] E. Conte, B. Fuks, and G. Serret, *MadAnalysis 5, A User-Friendly Framework for Collider Phenomenology*, Comput.Phys.Commun. **184** (2013) 222–256.

[165] E. Conte, B. Dumont, B. Fuks, and C. Wymant, *Designing and recasting LHC analyses with MadAnalysis 5*, Eur.Phys.J. **C74** (2014) no. 10, 3103.

[166] W. Beenakker, R. Hopker, and M. Spira, *PROSPINO: A Program for the production of supersymmetric particles in next-to-leading order QCD*, arXiv:hep-ph/9611232 [hep-ph].

[167] ATLAS Collaboration, G. Aad et al., *Search for Dark Matter in Events with Missing Transverse Momentum and a Higgs Boson Decaying to Two Photons in pp Collisions at $\sqrt{s} = 8$ TeV with the ATLAS Detector*, arXiv:1506.01081 [hep-ex].

[168] ATLAS Collaboration, G. Aad et al., *Search for dark matter in events with heavy quarks and missing transverse momentum in pp collisions with the ATLAS detector*, Eur. Phys. J. **C75** (2015) 92.

[169] ATLAS Collaboration, G. Aad et al., *Search for new particles in events with one lepton and missing transverse momentum in pp collisions at $\sqrt{s}$ = 8 TeV with the ATLAS detector*, JHEP **09** (2014) 037.

[170] CMS Collaboration, V. Khachatryan et al., *Search for new phenomena in monophoton final states in proton-proton collisions at $\sqrt{s}$ = 8 TeV*, (2014) , arXiv:1410.8812 [hep-ex].

[171] CMS Collaboration, *Commissioning of the Particle-flow Event Reconstruction with the first LHC collisions recorded in the CMS detector*, tech. rep., CERN, Geneva, 2010. http://cds.cern.ch/record/1247373.

[172] CMS Collaboration, *Particle-Flow Event Reconstruction in CMS and Performance for Jets, Taus, and MET*, Tech. Rep. CMS-PAS-PFT-09-001, CERN, Geneva, Apr, 2009. http://cds.cern.ch/record/1194487.

[173] ATLAS Collaboration, *Characterisation and mitigation of beam-induced backgrounds observed in the ATLAS detector during the 2011 proton-proton run*, JINST **8** (2013) P07004.

[174] ATLAS Collaboration, G. Aad et al., *Search for new phenomena in final states with an energetic jet and large missing transverse momentum in pp collisions at $\sqrt{s} = 8$ TeV with the ATLAS detector*, Eur. Phys. J. **C75** (2015) 299.

[175] ATLAS Collaboration, G. Aad et al., *Search for dark matter in events with a Z boson and missing transverse momentum in pp collisions at $\sqrt{s}$=8 TeV with the ATLAS detector*, Phys.Rev. **D90** (2014) no. 1, 012004.

[176] L. M. Carpenter, A. Nelson, C. Shimmin, T. M. Tait, and D. Whiteson, *Collider searches for dark matter in events with a Z boson and missing energy*, Phys.Rev. **D87** (2013) no. 7, 074005.

[177] ATLAS Collaboration, *Search for dark matter in events with a Z boson and missing transverse momentum in pp collisions at $\sqrt{s}$=8 TeV with the ATLAS detector*, tech. rep., CERN, Geneva, March, 2014. http://atlas.web.cern.ch/Atlas/GROUPS/PHYSICS/PAPERS/EXOT-2012-26/. Public auxilliary material for Phys.Rev.D.90,012004(2014).

[178] ATLAS Collaboration, *Search for dark matter in events with a hadronically decaying W or Z boson and missing transverse momentum in pp collisions at $\sqrt{s} =$ 8 TeV with the ATLAS detector*, Phys.Rev.Lett. **112** (2014) 041802.

[179] *HL-LHC: High Luminosity Large Hadron Collider*, Online, March, 2015. http://hilumilhc.web.cern.ch/about/hl-lhc-project.

[180] W. Stirling. Private communication.
http://www.hep.ph.ic.ac.uk/~wstirlin/plots/plots.html.

Auxiliary material for signal interpretation

This appendix includes the auxiliary information on the two new physics models introduced in Section 8.1.

Tables 2 to 13 show information for the EFT DM model. Tables 2 to 4 list all the theoretical uncertainties on the cross section for each signal sample; whilst Tables 5 to 7 show these uncertainties on the product of acceptance and efficiency in the SR. The statistic and systematic uncertainties for each signal sample are listed in Tables 8 to 10. The expected and observed lower limits on the suppression scale M^* at 95% CL for each signal sample are shown in Tables 11 to 13

Tables 14 and 15 show the overall theoretical uncertainties on cross section and SR acceptance, and the upper limits on the cross section at 95% CL for each signal point in the compressed squark model.

Sample		$\Delta\sigma$ [%]	
k_1	k_2	PDF uncertainty	scale uncertainty
0.01	0.01	$\pm$8.29	$+10.3, -8.77$
0.01	0.25	$\pm$8.26	$+10.4, -8.86$
0.01	0.50	$\pm$8.30	$+10.5, -8.92$
0.01	0.75	$\pm$8.22	$+10.4, -8.82$
0.01	1.00	$\pm$8.22	$+10.5, -8.89$
0.25	0.01	$\pm$9.15	$+10.4, -8.86$
0.25	0.25	$\pm$8.30	$+10.3, -8.77$
0.25	0.50	$\pm$8.18	$+10.4, -8.8$
0.25	0.75	$\pm$8.25	$+10.4, -8.85$
0.25	1.00	$\pm$8.13	$+10.4, -8.81$
0.50	0.01	$\pm$9.18	$+10.4, -8.82$
0.50	0.25	$\pm$8.51	$+10.4, -8.86$
0.50	0.50	$\pm$8.25	$+10.3, -8.77$
0.50	0.75	$\pm$8.16	$+10.2, -8.71$
0.50	1.00	$\pm$8.13	$+10.3, -8.78$
0.75	0.01	$\pm$9.22	$+10.5, -8.88$
0.75	0.25	$\pm$8.72	$+10.5, -8.87$
0.75	0.50	$\pm$8.37	$+10.4, -8.81$
0.75	0.75	$\pm$8.38	$+10.3, -8.76$
0.75	1.00	$\pm$8.16	$+10.2, -8.67$
1.00	0.01	$\pm$9.22	$+10.4, -8.86$
1.00	0.25	$\pm$8.82	$+10.4, -8.84$
1.00	0.50	$\pm$8.52	$+10.4, -8.85$
1.00	0.75	$\pm$8.37	$+10.4, -8.82$
1.00	1.00	$\pm$8.28	$+10.4, -8.79$

Table 2 Two theoretical uncertainties on the cross section for the EFT DM model with $m_\chi = 10$ GeV and different k_1 and k_2.

Sample		$\Delta\sigma$ [%]	
k_1	k_2	PDF uncertainty	scale uncertainty
0.01	0.01	$\pm$9.57	$+11.8, -9.9$
0.01	0.25	$\pm$9.59	$+11.8, -9.93$
0.01	0.50	$\pm$9.57	$+11.8, -9.9$
0.01	0.75	$\pm$9.59	$+11.8, -9.92$
0.01	1.00	$\pm$9.51	$+11.8, -9.9$
0.25	0.01	$\pm$10.6	$+11.6, -9.72$
0.25	0.25	$\pm$9.60	$+11.8, -9.88$
0.25	0.50	$\pm$9.59	$+11.7, -9.84$
0.25	0.75	$\pm$9.59	$+11.8, -9.87$
0.25	1.00	$\pm$9.69	$+11.8, -9.91$
0.50	0.01	$\pm$10.6	$+11.6, -9.74$
0.50	0.25	$\pm$9.81	$+11.8, -9.89$
0.50	0.50	$\pm$9.58	$+11.8, -9.9$
0.50	0.75	$\pm$9.68	$+11.8, -9.91$
0.50	1.00	$\pm$9.55	$+11.7, -9.85$
0.75	0.01	$\pm$10.6	$+11.5, -9.71$
0.75	0.25	$\pm$9.94	$+11.7, -9.86$
0.75	0.50	$\pm$9.79	$+11.8, -9.89$
0.75	0.75	$\pm$9.58	$+11.8, -9.88$
0.75	1.00	$\pm$9.64	$+11.8, -9.89$
1.00	0.01	$\pm$10.7	$+11.6, -9.77$
1.00	0.25	$\pm$10.1	$+11.7, -9.81$
1.00	0.50	$\pm$9.79	$+11.7, -9.86$
1.00	0.75	$\pm$9.66	$+11.8, -9.9$
1.00	1.00	$\pm$9.58	$+11.8, -9.87$

Table 3 Two theoretical uncertainties on the cross section for the EFT DM model with $m_\chi = 130$ GeV and different k_1 and k_2.

Sample		$\Delta\sigma$ [%]	
k_1	k_2	PDF uncertainty	scale uncertainty
0.01	0.01	$\pm$24.8	+19.6, −15.5
0.01	0.25	$\pm$24.5	+19.6, −15.5
0.01	0.50	$\pm$24.5	+19.5, −15.4
0.01	0.75	$\pm$26.1	+19.5, −15.4
0.01	1.00	$\pm$24.4	+19.5, −15.4
0.25	0.01	$\pm$24.7	+19.5, −15.4
0.25	0.25	$\pm$25.0	+19.6, −15.5
0.25	0.50	$\pm$24.5	+19.5, −15.4
0.25	0.75	$\pm$24.3	+19.6, −15.5
0.25	1.00	$\pm$24.4	+19.6, −15.5
0.50	0.01	$\pm$26.8	+19.5, −15.4
0.50	0.25	$\pm$24.9	+19.5, −15.4
0.50	0.50	$\pm$24.9	+19.6, −15.5
0.50	0.75	$\pm$24.5	+19.5, −15.4
0.50	1.00	$\pm$24.5	+19.5, −15.4
0.75	0.01	$\pm$25.2	+19.5, −15.5
0.75	0.25	$\pm$25.6	+19.5, −15.4
0.75	0.50	$\pm$25.1	+19.6, −15.5
0.75	0.75	$\pm$24.8	+19.6, −15.5
0.75	1.00	$\pm$24.8	+19.5, −15.4
1.00	0.01	$\pm$26.9	+19.5, −15.4
1.00	0.25	$\pm$25.8	+19.5, −15.4
1.00	0.50	$\pm$25.0	+19.5, −15.4
1.00	0.75	$\pm$24.5	+19.5, −15.4
1.00	1.00	$\pm$24.8	+19.6, −15.5

Table 4 Two theoretical uncertainties on the cross section for the EFT DM model with $m_\chi = 1000$ GeV and different k_1 and k_2.

Sample		$\Delta A \times \varepsilon$ [%]		
k_1	k_2	PDF uncertainty	scale uncertainty	ISR/FSR uncertainty
0.01	0.01	± 0.648	$+0.293, -0.277$	$+0.46, -1.27$
0.01	0.25	± 1.04	$+0.396, -0.373$	$+0.39, -2.56$
0.01	0.50	± 0.937	$+0.377, -0.352$	$+1.93, -1.10$
0.01	0.75	± 0.859	$+0.304, -0.288$	$+2.94, -0.00$
0.01	1.00	± 0.946	$+0.321, -0.305$	$+0.90, -0.61$
0.25	0.01	± 0.778	$+0.248, -0.239$	$+0.44, -0.89$
0.25	0.25	± 0.653	$+0.287, -0.279$	$+2.59, -0.70$
0.25	0.50	± 0.852	$+0.307, -0.288$	$+2.00, -0.45$
0.25	0.75	± 0.811	$+0.319, -0.301$	$+2.00, -0.21$
0.25	1.00	± 0.851	$+0.418, -0.396$	$+0.31, -0.57$
0.50	0.01	± 0.706	$+0.268, -0.255$	$+1.81, -0.00$
0.50	0.25	± 0.836	$+0.308, -0.288$	$+2.41, -0.60$
0.50	0.50	± 0.957	$+0.379, -0.359$	$+0.00, -1.20$
0.50	0.75	± 0.718	$+0.229, -0.222$	$+1.00, -0.61$
0.50	1.00	± 0.642	$+0.302, -0.287$	$+0.23, -1.36$
0.75	0.01	± 0.714	$+0.276, -0.262$	$+1.14, -0.57$
0.75	0.25	± 0.676	$+0.261, -0.25$	$+3.37, -0.60$
0.75	0.50	± 0.855	$+0.358, -0.34$	$+1.60, -0.00$
0.75	0.75	± 0.8	$+0.374, -0.355$	$+0.28, -0.86$
0.75	1.00	± 0.809	$+0.33, -0.313$	$+3.07, -0.00$
1.00	0.01	± 0.634	$+0.21, -0.2$	$+0.53, -0.31$
1.00	0.25	± 0.702	$+0.224, -0.212$	$+0.00, -2.64$
1.00	0.50	± 0.651	$+0.366, -0.345$	$+0.18, -0.92$
1.00	0.75	± 0.677	$+0.233, -0.226$	$+0.88, -0.75$
1.00	1.00	± 0.699	$+0.308, -0.291$	$+0.14, -0.67$

Table 5 The PDF, scale and ISR/FSR theoretical uncertainties on the product of acceptance and efficiency in the SR for the EFT DM model with $m_\chi = 10$ GeV and different k_1 and k_2.

Sample		$\Delta A \times \varepsilon$ [%]		
k_1	k_2	PDF uncertainty	scale uncertainty	ISR/FSR uncertainty
0.01	0.01	± 0.372	$+0.0291, -0.0295$	$+1.27, -0.54$
0.01	0.25	± 0.455	$+0.0792, -0.076$	$+1.67, -0.00$
0.01	0.50	± 0.389	$+0.0833, -0.0769$	$+1.16, -0.85$
0.01	0.75	± 0.475	$+0.0547, -0.053$	$+1.01, -0.61$
0.01	1.00	± 0.477	$+0.116, -0.109$	$+1.09, -1.32$
0.25	0.01	± 0.515	$+0.0655, -0.0664$	$+1.06, -0.55$
0.25	0.25	± 0.434	$+0.0824, -0.0786$	$+2.31, -0.00$
0.25	0.50	± 0.572	$+0.0701, -0.0677$	$+1.46, -1.06$
0.25	0.75	± 0.532	$+0.0559, -0.0544$	$+1.79, -0.86$
0.25	1.00	± 0.497	$+0.0883, -0.0864$	$+0.98, -1.24$
0.50	0.01	± 0.586	$+0.0688, -0.0639$	$+0.55, -1.04$
0.50	0.25	± 0.621	$+0.0648, -0.0617$	$+0.00, -2.00$
0.50	0.50	± 0.447	$+0.108, -0.102$	$+0.79, -0.99$
0.50	0.75	± 0.545	$+0.0835, -0.0789$	$+0.80, -0.52$
0.50	1.00	± 0.407	$+0.0655, -0.0671$	$+2.16, -0.00$
0.75	0.01	± 0.436	$+0.0434, -0.0421$	$+0.00, -1.51$
0.75	0.25	± 0.457	$+0.0147, -0.0192$	$+1.47, -0.00$
0.75	0.50	± 0.399	$+0.11, -0.104$	$+1.35, -0.68$
0.75	0.75	± 0.438	$+0.0587, -0.0554$	$+1.98, -0.00$
0.75	1.00	± 0.509	$+0.148, -0.141$	$+1.80, -0.50$
1.00	0.01	± 0.455	$+0.00859, -0.00814$	$+0.00, -0.80$
1.00	0.25	± 0.331	$+0.0801, -0.0784$	$+2.11, -0.00$
1.00	0.50	± 0.391	$+0.102, -0.0957$	$+0.15, -3.70$
1.00	0.75	± 0.522	$+0.0386, -0.0377$	$+0.20, -0.63$
1.00	1.00	± 0.648	$+0.0748, -0.0717$	$+1.91, -0.00$

Table 6 The PDF, scale and ISR/FSR theoretical uncertainties on the product of acceptance and efficiency in the SR for the EFT DM model with $m_\chi = 130$ GeV and different k_1 and k_2.

Sample		$\Delta A \times \varepsilon$ [%]		
k_1	k_2	PDF uncertainty	scale uncertainty	ISR/FSR uncertainty
0.01	0.01	±0.447	+0.0274, −0.0257	+0.07, −0.70
0.01	0.25	±0.466	+0.0188, −0.0207	+0.21, −0.51
0.01	0.50	±0.287	+0.0248, −0.0205	+0.56, −0.76
0.01	0.75	±0.503	+0.00286, −0.00341	+0.67, −1.08
0.01	1.00	±0.553	+0.039, −0.0444	+0.87, −0.21
0.25	0.01	±0.223	+0.0692, −0.0761	+0.63, −0.38
0.25	0.25	±0.365	+0.0334, −0.0311	+0.00, −1.53
0.25	0.50	±0.4	+0.0257, −0.0315	+0.92, −0.29
0.25	0.75	±0.191	+0.0056, −0.00211	+0.00, −2.64
0.25	1.00	±0.613	+0.0061, −0.00722	+0.96, −0.89
0.50	0.01	±0.61	+0.0782, −0.0757	+0.70, −0.12
0.50	0.25	±0.309	+0.0262, −0.0284	+0.91, −0.32
0.50	0.50	±0.358	+0.0128, −0.00998	+0.33, −0.56
0.50	0.75	±0.553	+0.00875, −0.0134	+0.94, −0.73
0.50	1.00	±0.359	+0.0493, −0.0535	+1.55, −0.83
0.75	0.01	±0.141	+0.0104, −0.0198	+0.00, −1.92
0.75	0.25	±0.295	+0.00437, −0.00103	+2.94, −0.00
0.75	0.50	±0.364	+0.01, −0.0155	+0.19, −2.23
0.75	0.75	±0.433	+0, −0.00335	+1.40, −0.12
0.75	1.00	±0.552	+0.0284, −0.0287	+0.44, −1.09
1.00	0.01	±0.407	+0.0374, −0.034	+0.06, −1.14
1.00	0.25	±0.257	+0.00157, −0.0015	+1.23, −0.00
1.00	0.50	±0.426	+0.0208, −0.0225	+1.80, −0.00
1.00	0.75	±0.385	+0.024, −0.0274	+1.06, −0.45
1.00	1.00	±0.456	+0.0913, −0.0992	+1.43, −1.30

Table 7 The PDF, scale and ISR/FSR theoretical uncertainties on the product of acceptance and efficiency in the SR for the EFT DM model with $m_\chi = 1000$ GeV and different k_1 and k_2.

Sample		ΔN^{SR}_{events} [%]	
k_1	k_2	statistical	systematic
0.01	0.01	±1.70	+7.34, −7.30
0.01	0.25	±1.68	+7.46, −7.34
0.01	0.50	±1.69	+7.28, −7.30
0.01	0.75	±1.70	+7.27, −7.17
0.01	1.00	±1.70	+7.46, −7.33
0.25	0.01	±1.61	+7.34, −7.32
0.25	0.25	±1.70	+7.25, −7.27
0.25	0.50	±1.70	+7.27, −7.19
0.25	0.75	±1.68	+7.35, −7.27
0.25	1.00	±1.70	+7.35, −7.42
0.50	0.01	±1.60	+7.28, −7.34
0.50	0.25	±1.66	+7.29, −7.35
0.50	0.50	±1.73	+7.42, −7.29
0.50	0.75	±1.71	+7.29, −7.23
0.50	1.00	±1.71	+7.23, −7.24
0.75	0.01	±1.63	+7.34, −7.50
0.75	0.25	±1.68	+7.25, −7.31
0.75	0.50	±1.69	+7.41, −7.35
0.75	0.75	±1.71	+7.25, −7.27
0.75	1.00	±1.71	+7.33, −7.30
1.00	0.01	±1.60	+7.50, −7.39
1.00	0.25	±1.65	+7.20, −7.40
1.00	0.50	±1.68	+7.23, −7.21
1.00	0.75	±1.69	+7.18, −7.15
1.00	1.00	±1.69	+7.35, −7.58

Table 8 The global systematic uncertainty (not including the theoretical ones) on the event yields for 20.3 fb^{-1} of data for the EFT DM model with $m_\chi = 10$ GeV and different k_1 and k_2.

Sample		ΔN_{events}^{SR} [%]	
k_1	k_2	statistical	systematic
0.01	0.01	±1.54	+7.30, −7.21
0.01	0.25	±1.55	+7.43, −7.27
0.01	0.50	±1.55	+7.31, −7.22
0.01	0.75	±1.54	+7.40, −7.49
0.01	1.00	±1.53	+7.39, −7.25
0.25	0.01	±1.54	+7.51, −7.52
0.25	0.25	±1.52	+7.26, −7.35
0.25	0.50	±1.54	+7.22, −7.31
0.25	0.75	±1.53	+7.33, −7.41
0.25	1.00	±1.52	+7.38, −7.35
0.50	0.01	±1.56	+7.35, −7.26
0.50	0.25	±1.54	+7.35, −7.40
0.50	0.50	±1.51	+7.36, −7.44
0.50	0.75	±1.55	+7.32, −7.28
0.50	1.00	±1.55	+7.28, −7.36
0.75	0.01	±1.56	+7.48, −7.53
0.75	0.25	±1.56	+7.46, −7.52
0.75	0.50	±1.55	+7.27, −7.29
0.75	0.75	±1.55	+7.20, −7.21
0.75	1.00	±1.54	+7.24, −7.29
1.00	0.01	±1.55	+7.44, −7.54
1.00	0.25	±1.55	+7.21, −7.12
1.00	0.50	±1.55	+7.36, −7.25
1.00	0.75	±1.56	+7.34, −7.30
1.00	1.00	±1.54	+7.22, −7.21

Table 9 The global systematic uncertainty (not including the theoretical ones) on the event yields for 20.3 fb^{-1} of data for the EFT DM model with $m_\chi = 130$ GeV and different k_1 and k_2.

Sample		ΔN_{events}^{SR} [%]	
k_1	k_2	statistical	systematic
0.01	0.01	±1.46	+7.29, −7.31
0.01	0.25	±1.48	+7.27, −7.35
0.01	0.50	±1.46	+7.18, −7.26
0.01	0.75	±1.47	+7.32, −7.32
0.01	1.00	±1.48	+7.28, −7.28
0.25	0.01	±1.48	+7.25, −7.25
0.25	0.25	±1.46	+7.19, −7.25
0.25	0.50	±1.46	+7.41, −7.32
0.25	0.75	±1.48	+7.37, −7.29
0.25	1.00	±1.46	+7.25, −7.34
0.50	0.01	±1.47	+7.19, −7.28
0.50	0.25	±1.46	+7.22, −7.26
0.50	0.50	±1.48	+7.30, −7.38
0.50	0.75	±1.45	+7.35, −7.39
0.50	1.00	±1.46	+7.31, −7.44
0.75	0.01	±1.48	+7.38, −7.26
0.75	0.25	±1.46	+7.28, −7.33
0.75	0.50	±1.47	+7.30, −7.45
0.75	0.75	±1.46	+7.41, −7.32
0.75	1.00	±1.47	+7.27, −7.27
1.00	0.01	±1.47	+7.32, −7.35
1.00	0.25	±1.47	+7.37, −7.32
1.00	0.50	±1.46	+7.26, −7.32
1.00	0.75	±1.47	+7.20, −7.19
1.00	1.00	±1.48	+7.32, −7.34

Table 10 The global systematic uncertainty (not including the theoretical ones) on the event yields for 20.3 fb^{-1} of data for the EFT DM model with $m_\chi = 1000$ GeV and different k_1 and k_2.

Sample		95% CL limit on M^* [GeV]	
k_1	k_2	expected	observed
0.01	0.01	92.3	94.4
0.01	0.25	272.0	278.0
0.01	0.50	341.1	348.6
0.01	0.75	390.7	399.2
0.01	1.00	429.5	439.0
0.25	0.01	179.4	183.3
0.25	0.25	270.0	275.9
0.25	0.50	338.6	346.0
0.25	0.75	392.9	401.5
0.25	1.00	429.3	438.7
0.50	0.01	226.8	231.8
0.50	0.25	286.2	292.5
0.50	0.50	338.3	345.8
0.50	0.75	386.0	394.5
0.50	1.00	425.9	435.3
0.75	0.01	257.8	263.4
0.75	0.25	297.8	304.3
0.75	0.50	352.5	360.2
0.75	0.75	388.0	396.5
0.75	1.00	426.7	436.1
1.00	0.01	283.7	289.9
1.00	0.25	315.0	321.9
1.00	0.50	358.8	366.7
1.00	0.75	401.1	409.9
1.00	1.00	429.1	438.5

Table 11 The expected and observed lower limits of the suppression scale M^* at 95% CL for the EFT DM model with $m_\chi = 10$ GeV and different k_1 and k_2.

Sample		95% CL limit on M^* [GeV]	
k_1	k_2	expected	observed
0.01	0.01	95.9	98.0
0.01	0.25	273.7	279.7
0.01	0.50	344.8	352.4
0.01	0.75	396.1	404.8
0.01	1.00	436.4	445.9
0.25	0.01	172.8	176.6
0.25	0.25	281.5	287.7
0.25	0.50	348.9	356.5
0.25	0.75	398.6	407.4
0.25	1.00	438.6	448.2
0.50	0.01	214.8	219.5
0.50	0.25	289.4	295.8
0.50	0.50	355.6	363.4
0.50	0.75	400.6	409.4
0.50	1.00	438.6	448.3
0.75	0.01	245.5	250.9
0.75	0.25	300.1	306.7
0.75	0.50	358.4	366.3
0.75	0.75	403.5	412.3
0.75	1.00	442.4	452.1
1.00	0.01	270.4	276.3
1.00	0.25	313.5	320.4
1.00	0.50	364.8	372.8
1.00	0.75	407.5	416.5
1.00	1.00	444.6	454.4

Table 12 The expected and observed lower limits of the suppression scale M^* at 95% CL for the EFT DM model with $m_\chi = 130$ GeV and different k_1 and k_2.

Sample		95% CL limit on M^* [GeV]	
k_1	k_2	expected	observed
0.01	0.01	40.1	41.0
0.01	0.25	114.0	116.5
0.01	0.50	144.0	147.1
0.01	0.75	164.7	168.3
0.01	1.00	180.6	184.5
0.25	0.01	74.3	75.9
0.25	0.25	117.2	119.7
0.25	0.50	145.4	148.6
0.25	0.75	165.0	168.6
0.25	1.00	182.3	186.3
0.50	0.01	93.2	95.3
0.50	0.25	121.9	124.6
0.50	0.50	147.4	150.7
0.50	0.75	167.5	171.2
0.50	1.00	183.1	187.1
0.75	0.01	106.2	108.5
0.75	0.25	127.7	130.5
0.75	0.50	150.3	153.6
0.75	0.75	168.9	172.7
0.75	1.00	184.5	188.5
1.00	0.01	117.1	119.7
1.00	0.25	133.2	136.2
1.00	0.50	153.8	157.2
1.00	0.75	170.6	174.4
1.00	1.00	185.3	189.4

Table 13 The expected and observed lower limits of the suppression scale M^* at 95% CL for the EFT DM model with $m_\chi = 1000$ GeV and different k_1 and k_2.

Sample		Theory Uncertainties [%]	
$m_{\tilde{q}}$ [GeV]	$m_{\tilde{q}} - m_{\tilde{\chi}_1^0}$ [GeV]	$\Delta\sigma$	$\Delta(A \times \varepsilon)$
100	1	$\pm$14.4	$+0.00, -1.03$
100	5	$\pm$14.4	$+8.19, -3.63$
100	10	$\pm$14.4	$+8.07, -3.63$
150	1	$\pm$14.5	$+9.07, -3.63$
150	5	$\pm$14.5	$+8.07, -3.63$
150	10	$\pm$14.4	$+8.54, -3.63$
200	1	$\pm$14.6	$+7.61, -3.63$
200	5	$\pm$14.6	$+8.07, -3.63$
200	10	$\pm$14.6	$+5.74, -5.46$
250	1	$\pm$14.6	$+8.46, -3.63$
250	5	$\pm$14.6	$+0.00, -0.00$
250	10	$\pm$14.6	$+0.00, -1.03$
300	1	$\pm$14.8	$+0.00, -0.00$
300	5	$\pm$14.8	$+0.00, -2.84$
300	10	$\pm$14.8	$+0.00, -1.03$
87	25	$\pm$14.5	$+0.00, -1.46$
162	25	$\pm$14.5	$+0.00, -0.00$
237	25	$\pm$14.5	$+2.76, -0.00$
100	50	$\pm$14.4	$+0.00, -0.00$
175	50	$\pm$14.5	$+0.00, -1.03$
250	50	$\pm$14.6	$+8.55, -0.00$

Table 14 The theoretical uncertainties on cross section and the product of acceptance and efficiency in the SR for all the signal samples used in the compressed squark model with different squark mass and mass difference between the squark and the neutralino.

Sample		95% CL limit on cross section [fb]	
$m_{\tilde{q}}$ [GeV]	$m_{\tilde{q}} - m_{\tilde{\chi}_1^0}$ [GeV]	expected	observed
100	1	35.8	42.8
100	5	42.6	50.9
100	10	63.0	75.3
150	1	28.2	33.7
150	5	32.8	39.2
150	10	41.2	49.2
200	1	24.3	29.0
200	5	25.9	31.0
200	10	33.2	39.6
250	1	20.6	24.6
250	5	21.3	25.4
250	10	25.8	30.8
300	1	20.1	23.9
300	5	20.2	24.1
300	10	22.9	27.3
87	25	180.1	215.4
162	25	76.8	91.7
237	25	51.1	61.0
100	50	254.0	303.1
175	50	135.0	161.3
250	50	95.6	114.4

Table 15 The upper limits on the cross section at 95% CL for all the signal samples used in the compressed squark model with different squark mass and mass difference between the squark and the neutralino.

Photon identification cuts

This appendix gives the detailed photon identification cuts in different $|\eta|$ and p_{T} bins. Table 16 shows the cuts used to identify a `loose` photon. The cuts used to identify an unconverted and a converted `tight` photon are listed in Tables 17 and 18.

$\|\eta\|$ bins		0-0.6	0.6-0.8	0.8-1.15	1.15-1.37	1.52-1.81	1.81-2.01	2.01-2.37
R_{had}	$<$	0.02425	0.02275	-	-	0.02725	0.02725	0.02725
R_{had1}	$<$	-	-	0.02575	0.01975	-	-	-
$E_{s2}^{7\times7}$	$>$				0.1 MeV			
R_{η}	$>$	0.8825	0.8825	0.8575	0.8575	0.8575	0.9025	0.8875
$w_{\eta 2}$	$<$	0.013	0.014	0.015	0.015	0.016	0.015	0.015

Table 16 The `loose` cut menu used for photon identification.

$\lvert\eta\rvert$ bins		0-0.6	0.6-0.8	0.8-1.15	1.15-1.37	1.52-1.81	1.81-2.01	2.01-2.37
R_{had}	$<$	0.020	0.020	-	-	0.02425	0.02575	0.02325
	or	0.01825	0.01975	-	-	0.02125	0.02275	0.01975
R_{had1}	$<$	-	-	0.01975	0.01825	-	-	-
	or	-	-	0.01525	0.01675	-	-	-
$E_{s2}^{7\times7}$	$>$				0.1 MeV			
R_η	$>$	0.92	0.92	0.93	0.925	0.925	0.925	0.910
$w_{\eta 2}$	$<$	0.011	0.0115	0.0115	0.0115	0.012	0.012	0.0128
R_ϕ	$>$	0.93	0.93	0.93	0.92	0.93	0.93	0.93
f_1	$>$				0.005			
ΔE[MeV]	$<$	180	170	165	160	425	500	560
E_{ratio}	$>$	0.80	0.80	0.76	0.82	0.78	0.80	0.80
$w_{\eta 1}^{tot}$	$<$	3.0	3.0	3.3	3.5	3.3	2.3	2.0
f_{side}	$<$	0.28	0.33	0.38	0.425	0.42	0.255	0.24
$w_{\eta 1}^{3}$	$<$	0.67	0.69	0.69	0.715	0.72	0.66	0.645

Table 17 The `tight` cut menu used for unconverted photon identification. The numbers shown in rows starting with 'or' are applied to photon candidates with $p_{\text{T}}^{\gamma} \geq 80$ GeV.

$\lvert\eta\rvert$ bins		0-0.6	0.6-0.8	0.8-1.15	1.15-1.37	1.52-1.81	1.81-2.01	2.01-2.37
R_{had}	$<$	0.020	0.018	-	-	0.02425	0.024	0.024
	or	0.01825	0.01975	-	-	0.02125	0.02275	0.01975
R_{had1}	$<$	-	-	0.01975	0.018	-	-	-
	or	-	-	0.01525	0.01675	-	-	-
$E_{s2}^{7\times7}$	$>$				0.1 MeV			
R_η	$>$	0.92	0.9125	0.915	0.91	0.908	0.917	0.903
$w_{\eta 2}$	$<$	0.011	0.0117	0.012	0.0120	0.0130	0.012	0.0127
R_ϕ	$>$	0.57	0.60	0.60	0.64	0.68	0.72	0.72
f_1	$>$				0.005			
ΔE[MeV]	$<$	160	160	120	125	350	520	525
E_{ratio}	$>$	0.85	0.85	0.80	0.78	0.82	0.86	0.88
$w_{\eta 1}^{tot}$	$<$	2.8	2.9	3.1	3.3	3.5	2.2	1.8
f_{side}	$<$	0.33	0.38	0.46	0.52	0.52	0.31	0.25
$w_{\eta 1}^{3}$	$<$	0.73	0.715	0.74	0.75	0.75	0.69	0.66

Table 18 The `tight` cut menu used for converted photon identification. The numbers shown in rows starting with 'or' are applied to photon candidates with $p_{\text{T}}^{\gamma} \geq 80$ GeV.